LEABHARLANN CHOLÁISTE NA TRÍONÓIDE, BAILE ÁTHA CLIATH | TRINITY COLLEGE LIBRARY DUBLIN
Ollscoil Átha Cliath | The University of Dublin

**Terms and Conditions of Use of Digitised Theses from Trinity College Library Dublin**

**Copyright statement**

All material supplied by Trinity College Library is protected by copyright (under the Copyright and Related Rights Act, 2000 as amended) and other relevant Intellectual Property Rights. By accessing and using a Digitised Thesis from Trinity College Library you acknowledge that all Intellectual Property Rights in any Works supplied are the sole and exclusive property of the copyright and/or other IPR holder. Specific copyright holders may not be explicitly identified. Use of materials from other sources within a thesis should not be construed as a claim over them.

A non-exclusive, non-transferable licence is hereby granted to those using or reproducing, in whole or in part, the material for valid purposes, providing the copyright owners are acknowledged using the normal conventions. Where specific permission to use material is required, this is identified and such permission must be sought from the copyright holder or agency cited.

**Liability statement**

By using a Digitised Thesis, I accept that Trinity College Dublin bears no legal responsibility for the accuracy, legality or comprehensiveness of materials contained within the thesis, and that Trinity College Dublin accepts no liability for indirect, consequential, or incidental, damages or losses arising from use of the thesis for whatever reason. Information located in a thesis may be subject to specific use constraints, details of which may not be explicitly described. It is the responsibility of potential and actual users to be aware of such constraints and to abide by them. By making use of material from a digitised thesis, you accept these copyright and disclaimer provisions. Where it is brought to the attention of Trinity College Library that there may be a breach of copyright or other restraint, it is the policy to withdraw or take down access to a thesis while the issue is being resolved.

**Access Agreement**

By using a Digitised Thesis from Trinity College Library you are bound by the following Terms & Conditions. Please read them carefully.

I have read and I understand the following statement: All material supplied via a Digitised Thesis from Trinity College Library is protected by copyright and other intellectual property rights, and duplication or sale of all or part of any of a thesis is not permitted, except that material may be duplicated by you for your research use or for educational purposes in electronic or print form providing the copyright owners are acknowledged using the normal conventions. You must obtain permission for any other use. Electronic or print copies may not be offered, whether for sale or otherwise to anyone. This copy has been supplied on the understanding that it is copyright material and that no quotation from the thesis may be published without proper acknowledgement.

# Magnetism in dilute magnetic oxides and related materials

by

Robert Denis Gunning

A thesis submitted to the University of Dublin in application for the degree of Doctor of Philosophy

School of Physics
University of Dublin

September 2006

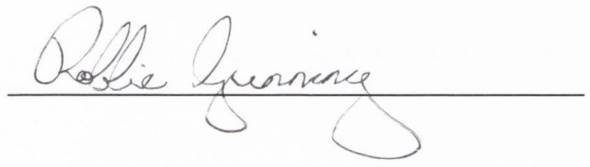
TRINITY COLLEGE
0 6 AUG 2007
LIBRARY DUBLIN
THESIS
8130

# DECLARATION

This thesis is submitted by the undersigned for examination for the degree of Doctor of Philosophy at the University of Dublin. It has not been submitted as an exercise for a degree at any other university.

This thesis, apart from the advice, assistance and joint effort mentioned in the acknowledgements and in the text, is entirely my own work.

I agree that the library may lend or copy this thesis freely on request.



October 2006

# Summary

The work in this thesis is focussed on the magnetic properties of dilute ferromagnetic semiconducting oxides and related materials. Since the first report of unexpected room temperature ferromagnetism in anatase and rutile Co-doped $TiO_2$ in 2001, there has been much research on the magnetic properties of transition-metal doped semiconducting oxides, such as $SnO_2$, ZnO and $In_2O_3$. While many research groups have observed room temperature ferromagnetism in these systems, there is no universal agreement on the origin of the ferromagnetism. Reports of ferromagnetism in $HfO_2$, hexaborides, graphite and sythentic carbon materials have demanded an explanation for the ferromagnetism that does not involve magnetic cations with a partially filled $3d$ or $4f$ electon shells.

To further investigate and understand the origins of the magnetism in these systems, thin films of transition-metal doped $TiO_2$ (reduced and oxidized), indium-tin oxide (ITO), $In_2O_3$, $SnO_2$ and Al-doped ZnO were formed by laser ablation of ceramic targets. Carbon-nitrgen whiskers were produced by the pyrolysis of 1,2-diaminopropane and allylamine. The magnetic, electrical and optical properties of these materials were investigated, as well of the properties of graphite powders of varying purity. Room temperature ferromangetism was observed in Fe-doped $TiO_2$ (reduced and oxidized), Fe-/Mn-/Cr-doped ITO, Cr-doped $In_2O_3$, Co-doped Al:ZnO, carbon-nitrogen whiskers produced from the pyrolysis of 1,2-diaminopropane and low purity graphite.

Careful examinations by means of x-ray diffractometry, Mössbauer spectroscopy and elemental analysis were performed on the thin films and powders that exhibited room temperature ferromagnetism to exclude the possibility of extrinsic mechanisms for the observed moments, such as ferromagnetic impurity phases and contamination. The room temperature ferromagnetism could be attributed, either partly or wholly to ferromagnetic impurity phases for reduced Fe-doped $TiO_2$, Fe-doped ITO, Fe-doped $SnO_2$ and low-purity graphite.

Impurity phases and contamination could explain the room temperature ferromagnetism for oxidized Fe-doped $TiO_2$, Mn- and Cr-doped ITO, Cr-doped $In_2O_3$, carbon-nitrogen whiskers and Co-doped Al:ZnO. The existing models for the mechanisms of ferromagnetism in oxides and semiconductors were unable to explain the observations of room temperature moments.

One of the most interesting finds of this thesis is that the transition-metal cation dopant does not contribute to the ferromagnetism of the thin films directly. The ferromagnetic films exhibit a paramagnetic susceptibility which corresponds to the $3d$ dopant concentrations. In the case of the iron-doped films of oxidized $TiO_2$, the paramagnetism of the dopant is confirmed by Mössbauer spectroscopy. Therefore, the materials presented as intrinsically ferromagnetic are not dilute magnetic semiconductors in the accepted sense.

# Acknowledgements

First of all, I would like to thank my supervisor, Mike Coey, for his guidance and support over the past four years.

In truth, I have received so much help, support and encouragement throughout my project that this should be the longest section of my thesis, but I can't pad this one out with figures, so it's not. Most helpful has been Venky, who has supervised my projects since I was a summer student. His vast practical and experimental knowledge was extremely useful and, in fairness, I would probably have killed myself and many others with some of the more "risky" experiments were it not for him. He performed many of the SQUID and resistivity measurements. I would like to thank Prof. James Lunney for his advice and PLD facilities. I must also thank Prof. David Grayson for his discussions on matters chemical. A great deal of my experimental training came from Dr. Ciara Fitzgerald, whose patience seemed, at times, infinite - despite the fact that she was finishing her own thesis at that time. My Mössbauer training came largely from the meticulous Dr. Alexis Douvalis. He's from Turkey or Greece or somewhere like that. I am indebted to Dr. Lucio Strazzabosco Dorneles for imparting much of his knowledge on the subjects of PLD and XRD on me. And how to chip the keeper. A big thanks must go to Plamen, whose knowledge and advice influenced almost every corner of my work for the better. He provided much assistance with the MPMS software for the Hall measurements and made the Hall measurements on the Al:ZnO thin films, and never blamed my dodgy soldered contacts when things went wrong. I would like to thank Nirina Randrianantoandro for the transition Mössbauer spectra on the $SnO_2$ thin films. I had many fruitful conversations with Dr. Sebastiaan van Dijken on the subjects of ITO and ZnO. It was also from his contract I was financed for many of my years here. Thanks for taking the broken rib in your stride.

I have had the pleasure of supervising summer students throughout my project, all of whom contributed most positively to my thesis. I must thank Béatrice Bernoux from INSA Toulouse, an excellent and versatile student - thanks Béa for *never complaining.* Another great contributor was Krisnendu Paul, from IT Mumbai. He may have been dilligent, eager and organised - but I can never forgive him for being part of the Brazilian-Asian soccer team that beat us in the cup. But I'm not bitter.

I would like to thank Zhu Diao for the last-minute AFM measurements (DART timetable dependent, of course), Dr. Ben Jones for the EPR data and rifle training, Dr. Richard Langford for FIB assistance, Greg for the Kerr stuff, and Maritathon (Marita and Jon) and for the help in the PLD lab.

The technical staff in the School of Physics provided invaluable help to me: John Kelly (not as funny as Henry, but has his moments), Ken, Mick, Dave, Jackie, Tracy, Pa "Reply-to-all" Murphy, Jemmer, Joe, Pat, Nigel, Una, Rebecca and Sandra. Oh, and Gillian - I think she printed a poster once for me.

Many thanks most go to the members of Group D and L who help make my experience most enjoyable: Cliff, Oscar, Mazhar, Fowley, Peter, Karsten, Chris, Adriele, Tony, Brendan, Donagh, Enrique and everyone else.

Outside of college, I would like to thank Tommy, Jon, Boz and Baz for the random nights out that helped release stress (yes, Tommy, postgradute students get stressed too). Though I have already thanked her, I would like to thank Gillian again, this time for being the light at the end of many a tunnel. Oh, she and Orla also gave me the crayons I used to colour in the figures of this thesis.

I would like to express my gratitude to Enterprise Ireland and Science Foundation Ireland for financing this work.

Finally, I would like to thank my parents, Denis and Marie, for their constant support and unwavering belief in me. Yes, Mom, the corrections are now done! If there are any spelling mistakes left, it is my father's fault, as he was chief spell-checker.

"I believe that what we become depends on what our fathers teach us at odd moments, when they aren't trying to teach us."

Umberto Eco, Foucault's Pendulum

# Table of contents

**Summary** ..... iii

**Acknowledgements** ..... v

**1 Introduction** ..... **11**

1.1 Spin electronics ..... 11
1.1.1 The Electron - Charge and Spin ..... 11
1.1.2 Moore's Law ..... 12
1.1.3 The Mechanisms Behind Spintronics ..... 12
1.1.4 Spin Accumulation, Spin Diffusion Lengths and Polarization ..... 14
1.1.5 Devices ..... 14
1.1.6 Materials ..... 16

1.2 Semiconductors ..... 18
1.2.1 Conductivity ..... 18
1.2.2 The Band Model ..... 18
1.2.3 Elemental and Compound Semiconductors ..... 19
1.2.4 Semiconductor Doping and Carrier Concentrations ..... 20
1.2.5 Doping Compound Semiconductors ..... 21
1.2.6 The Fermi Level ..... 21

1.3 Semiconducting Oxides ..... 24
1.3.1 Defects in Oxides ..... 24
1.3.2 Semiconducting Behaviour in Oxides ..... 27

1.4 Dilute Magnetic Semiconductors ..... 27
1.4.1 III-V Materials ..... 27
1.4.2 IV Materials ..... 28
1.4.3 Oxide semiconductors ..... 28

1.5 Transparent Conducting Oxides ..... 30
1.5.1 Uses of Transparent Conducting Oxides ..... 31
1.5.2 $p$-type Transparent Conducting Oxides ..... 32
1.5.3 Transparent Conducting Oxides in Spin Electronics ..... 33

1.6 Intrinsic vs. Extrinsic ..... 34
1.6.1 The "syndrome" ..... 34
1.6.2 $d^0$ Ferromagnetism ..... 35
1.6.3 Impurity Phases ..... 35
1.6.4 Methods of Determination ..... 36

References ..... 39

**2 Experimental Procedures** ..... **45**

2.1 Sample Preparation ..... 45
2.1.1 Ceramic Target Production ..... 45
2.1.2 Pulsed Laser Deposition ..... 45

2.2 Structural Characterization ..... 46

2.2.1 X-ray Diffraction (XRD) ..... 46
2.2.2 X-ray Reflectivity (XRR) ..... 48
2.2.3 Morphology ..... 51
2.2.4 FTIR spectroscopy ..... 52
2.2.5 Optical Spectroscopy ..... 52

2.3 Magnetic Measurements ..... 53
2.3.1 Vibrating Sample Magnetometry (VSM) ..... 53
2.3.2 Superconducting Quantum Interference Device Magnetometry (SQUID Magnetometry) ..... 53
2.3.3 MFM ..... 54
2.3.4 $^{57}$Fe Mössbauer Spectrometry ..... 54
2.3.5 Electronic Paramagnetic Resonance (EPR) ..... 61

2.4 Composition Determination ..... 63
2.4.1 Residual Gas Analysis (Mass Spectrometry) ..... 63
2.4.2 Combustion Analysis ..... 64
2.4.3 EDAX ..... 64

2.5 Electronic Measurements ..... 65
2.5.1 Transport Measurements ..... 65
2.5.2 The Hall effect ..... 66

References ..... 69

**3 $TiO_2$ ..... 70**

3.1 Introduction ..... 70
3.1.1 Applications ..... 71

3.2 Sample Preparation ..... 73

3.3 Sample Characterization ..... 74
3.3.1 SQUID Magnetometery ..... 74
3.3.2 X-Ray Diffraction ..... 75
3.3.3 X-Ray Reflectometry ..... 77
3.3.4 AFM ..... 78
3.3.5 EDAX Elemental analysis ..... 78
3.3.6 Mössbauer Spectrometry ..... 79
3.3.7 Optical Transmission ..... 80

3.4 Discussion ..... 83

References ..... 87

**4 $In_2O_3$ ..... 90**

4.1 Introduction ..... 90
4.1.1 Uses of Indium Oxide ..... 92
4.1.2 Ferromagnetism in Indium Oxide ..... 93

4.2 Sample Preparation ..... 94

4.3 Sample Characterization ..... 95
4.3.1 Structure ..... 96
4.3.2 Film Thickness ..... 98

4.3.3 Magnetization ..... 98
4.3.4 Electrical Conductivity ..... 100
4.3.5 MR measurements ..... 101
4.3.6 Magneto-Optical Kerr Effect (MOKE) ..... 101
4.4 Discussion ..... 101
References ..... 105
**5 Indium-Tin Oxide ..... 107**
5.1 Introduction ..... 107
5.1.1 Uses of ITO ..... 110
5.1.2 Ferromagnetism in ITO ..... 110
5.2 Sample Preparation ..... 112
5.3 Sample Characterization ..... 112
5.3.1 Structure ..... 113
5.3.2 Film Thickness ..... 115
5.3.3 Magnetization ..... 116
5.3.4 Mössbauer Spectroscopy ..... 117
5.3.5 Electrical Conductivity ..... 121
5.3.6 Magneto-Optical Kerr Effect (MOKE) ..... 122
5.3.7 Hall Effect ..... 122
5.3.8 Optical transmission ..... 125
5.4 Discussion ..... 128
References ..... 129
**6 Al-doped Co:ZnO ..... 133**
6.1 Introduction ..... 133
6.1.1 Conduction in Al-doped ZnO ..... 133
6.1.2 Burstein-Moss Shift ..... 135
6.1.3 Uses of ZnO ..... 137
6.1.4 Ferromagnetism in Co-doped ZnO ..... 137
6.2 Sample Preparation ..... 138
6.3 Sample Characterization ..... 139
6.3.1 X-ray Diffraction ..... 139
6.3.2 Magnetization ..... 139
6.3.3 Optical Spectroscopy ..... 140
6.3.4 Electrical Conductivity ..... 142
6.4 Discussion ..... 144
References ..... 146
**7 Carbon ..... 148**
7.1 Introduction ..... 148
7.2 Carbon Whiskers ..... 150
7.2.1 Pyrolysis ..... 150

7.2.2 Combustion Analysis ..... 152
7.2.3 ICP ..... 152
7.2.4 EDAX ..... 155
7.2.5 XRD ..... 155
7.2.6 Microscopy and SEM ..... 155
7.2.7 FTIR ..... 157
7.2.8 SQUID Magnetometry ..... 157
7.2.9 MFM ..... 159
7.2.10EPR ..... 159
7.2.11RGA ..... 160
7.2.12Gas Absorption Analysis ..... 161
7.2.13Transport ..... 161
7.2.14Hall Effect ..... 163

7.3 Carbon Manganese ..... 163
7.3.1 Sample Preparation ..... 163
7.3.2 XRD ..... 164
7.3.3 SEM/EDAX ..... 164
7.3.4 VSM ..... 164
7.3.5 SQUID Magnetometry ..... 165
7.3.6 $^{57}$Fe Mössbauer Spectrometry ..... 165

7.4 Discussion ..... 166
7.4.1 Whiskers ..... 166
7.4.2 C-Mn ..... 169

References ..... 172

**8 Discussion ..... 174**

8.1 Introduction ..... 174

8.2 Magnetization and Susceptibility ..... 174

8.3 Electrical Properties ..... 178

8.4 Optical Properties ..... 180

8.5 Extrinsic Mechanisms of Ferromagnetism ..... 182
8.5.1 Ferromagnetic Impurities ..... 182
8.5.2 Contamination ..... 185

8.6 Models for Ferromagnetism in Dilute Magnetic Semiconductors ..... 186
8.6.1 Superexchange ..... 186
8.6.2 Zener Double Exchange ..... 188
8.6.3 The RKKY Interaction ..... 188
8.6.4 Impurity Band Exchange and Magnetic Polarons ..... 189
8.6.5 Other Mechanisms ..... 190

References ..... 192

**9 Conclusions ..... 194**

9.1 Conclusions ..... 194

9.2 Future Work ..... 195

References ..... 197

Publications ..... 198

**A Units ..... 199**

A.1 The SI and cgs conventions ..... 199

**B Calculations and Derivations ..... 200**

B.1 Curie Susceptibility vs. Temperature to Obtain $p_{eff}^2$ ..... 200

B.2 Substrate Temperature ..... 201

**C Error calculation and analysis ..... 202**

C.1 Magnetization measurements ..... 202

C.1.1 Instrumental Error ..... 202

C.1.2 Sample variation ..... 203

C.2 Other measurements ..... 204

**D BASIC program for RGA spectrum acqisition ..... 205**

D.1 Program 1: Simple Control ..... 205

D.2 Program 2: Control, Display And Save ..... 205

# List of Figures


1.1 A graph illustrating Moore's Law . . . . . 13
1.2 A schematic diagram representing spin accumulation and spin scattering processes. . . . . 15
1.3 A schematic representation of a spin valve. . . . . 16
1.4 Band diagrams. . . . . 19
1.5 Donor and acceptor levels. . . . . 21
1.6 The probability of level occupation. . . . . 22
1.7 The four main point defect types. . . . . 25
1.8 The several different classes of crystal defects. . . . . 26
1.9 The energy levels of $p$TCO. . . . . 33
1.10 The change in energy levels of $d^{10}$ electrons with atomic number. . . . . 34
2.11 The laser ablating the ceramic target. . . . . 47
2.12 Bragg reflection. . . . . 48
2.13 The $\omega$-scan. . . . . 48
2.14 The method for alignment for an XRR measurement. . . . . 50
2.15 An x-ray reflectivity curve. . . . . 51
2.16 A transmission Mössbauer set-up. . . . . 54
2.17 Schematic representations of Mössbauer spectra altered due to hyperfine interactions. . . . . 56
2.18 The $^{57}$Fe Mössbauer decay scheme. . . . . 57
2.19 Absorption of a 14.4 keV $\gamma$-ray by the $^{57}$Fe nucleus. . . . . 58
2.20 The anomolous scattering coefficients of Fe x-rays. . . . . 59
2.21 Pulse height analyses. . . . . 60
2.22 The CEMS detector. . . . . 61
2.23 The electron penetration versus energy. . . . . 62
2.24 An EPR set-up. . . . . 63
2.25 RGA/Mass Spectrometer . . . . . 64
2.26 The acceptible methods of applying contact for a van der Pauw measurement. In case b), it is important that the contacts are at the corners an not inside the perimeters. . . . . 65
2.27 Contacts made to a whisker. . . . . 66
2.28 The Hall Effect. . . . . 67
3.29 The rutile $TiO_2$ crystal structure. . . . . 70
3.30 RT magnetization curves of $Ti_{0.99}Fe_{0.01}O_2$ thin films. . . . . 72
3.31 M-H loop of the oxidized and reduced $Ti_{1-x}Fe_xO_2$ thin films. . . . . 73
3.32 Magnetic moments of oxidized (red circles) and reduced (black squares) films plotted as a) $\mu_B$ per Fe and b) $\mu_B$ nm$^{-2}$ of substrate area. The dashed line shows the moment for metallic iron. . . . . 74
3.33 X-ray diffractograms $TiO_2$ thin films. . . . . 75
3.34 XRD pattern of reduced and oxidizedd thin films of $TiO_2$. . . . . 76
3.35 (101) rutile peaks of $TiO_2$ thin films. . . . . 77
3.36 Thickness monitoring using optical reflectivity of $TiO_2$. . . . . 78
3.37 XRR measurement of an undoped $TiO_2$ thin film. . . . . 79
3.38 AFM scan of an undoped $TiO_2$ thin film. . . . . 80
3.39 EDAX calibration. . . . . 81
3.40 Transition Mössbauer spectra of $Ti_{1-x}Fe_xO_2$ targets. . . . . 82
3.41 Conversion electron Mössbauer spectra of $Ti_{1-x}Fe_xO_2$. . . . . 83
3.42 Optical transmission spectra for $Ti_{1-x}Fe_xO_2$ thin films. . . . . 84

3.43 $\alpha^2$ versus photon energy for $Ti_{1-x}Fe_xO_2$ thin films. . . . . 84
4.44 The cubic bixbyite structure of $In_2O_3$. . . . . 90
4.45 Mmagnetization loops for granular $(In_{0.65}Fe_{0.35})_2O_3$ films. . . . . 92
4.46 Magnetization and Hall effect data for Fe- and Cu- codoped $In_2O_3$. . . . . 92
4.47 A graph of magnetization in $\mu_B$/dopant ion against dopant for $In_2O_3$ thin films. . . . . 93
4.48 Lattice parameter versus dopant concentration for $In_2O_3$. . . . . 94
4.49 Magnetic moment at versus substrate heater voltage. . . . . 95
4.50 Magnetization versus dopant concentration for $(In_{1-x}Cr_x)_2O_3$. . . . . 96
4.51 An x-ray diffractogram of an $(In_{0.95}Cr_{0.05})_2O_3$ thin film. . . . . 97
4.52 A x-ray diffractogram of a $(Cr_{0.95}In_{0.05})_2O_3$ thin film. . . . . 97
4.53 Moment of $(In_{0.9}Cr_{0.1})_2O_3$ thin films versus film thickness. . . . . 99
4.56 A plot of resistivity versus Cr doping concentration. The error bars are too small to be seen. . . . . 99
4.54 Parallel and perpendicular magnetization measurements of a $(In_{0.925}Cr_{0.075})_2O_3$ thin film. . . . . 100
4.55 A M-H loop of a $(Cr_{0.95}In_{0.05})_2O_3$ thin film. . . . . 101
4.57 Resistivity versus temperature measurements for $(In_{1-x}Cr_x)_2O_3$ thin films. . . . . 102
4.58 Magnetoresistance measurements for $(In_{1-x}Cr_x)_2O_3$ thin films. . . . . 103
5.59 The cubic bixbyite crystal structue of ITO. . . . . 108
5.60 The effect of Sn-doping on the lattice parameter of $In_2O_3$. . . . . 109
5.61 Mössbauer spectra of ITO samples with various Sn content. . . . . 109
5.62 Energy band ITO for light tin doping. . . . . 110
5.63 An XRD of undoped ITO thin film. . . . . 111
5.64 Pseudo-Voigt fit of a (222) $In_2O_3$ reflection grown on c-cut sapphire with fitting parameter in the inset . . . . . 113
5.65 X-ray diffractograms of $(In_{0.875}Sn_{0.1}Mn_{0.025})_2O_3$. . . . . 114
5.66 A plot of dopant concentration versus lattice constant x. . . . . 115
5.67 XRR measurement and simulation of nominal 18 nm thin film. . . . . 116
5.68 Measured magnetic moment versus heater voltage. . . . . 117
5.69 M-H loops for Mn- and Fe- doped ITO thin films. . . . . 118
5.70 $M_r$ versus temperature for $(In_{0.875}Sn_{0.1}Mn_{0.025})O_3$. . . . . 118
5.71 Moment versus $x$ for $(In_{0.9-x}Sn_{0.1}M_x)_2O_3$. . . . . 119
5.72 Magnetization curves for $(In_{0.875}Sn_{0.1}Mn_{0.025})O_3$. . . . . 120
5.73 Magnetization at 1 T versus temperature for a 2.5 at% Mn-doped film. . . . . 120
5.74 $^{57}Fe$ transmission Mössbauer spectra for Fe:ITO ceramic targets. . . . . 121
5.75 Resistance versus temperature for undoped and Mn-doped ITO. . . . . 122
5.76 CEMS spectra of $(In_{1-x}Sn_{0.1}Fe_x)_2O_3$ thin films. . . . . 123
5.77 Mössbauer and magnetization data for $Sn_{0.97}Fe_{0.03}O_2$ thin films. . . . . 124
5.78 Resistance versus temperature for an Fe-doped film and versus Fe at%. . . . . 125
5.81 Resistivity of the Mn-doped films and the temperature of minimum resistivity versus Mn at% for Mn-doped ITO thin films. . . . . 125
5.79 Hall effect measurements. . . . . 126
5.80 A plot of carrier concentration versus temperature for ITO thin films. . . . . 127
5.82 Optical bandgap measurements of the Mn-doped and Fe-doped thin films. . . . . 127
6.83 The wurtzite crystal structure of ZnO. . . . . 133
6.84 Dependence of conductivity, carrier concentration and mobility on Al content in ZnO films. . . . . 134
6.85 A schematic representation of the Burstein-Moss shift. . . . . 135

6.86 Schematic representation of the two competing mechanisms both widening and narrowing the bandgap . . . . . 136
6.87 X-ray diffractograms of the Al-doped ceramic $Zn_{0.95}Co_{0.05}O$ targets. . . . . 139
6.88 XRD of an Al-doped $Zn_{0.95}Co_{0.05}O$ thin film. . . . . 140
6.89 M-H curves Al-doped $Zn_{0.95}Co_{0.05}O$. . . . . 141
6.90 The saturation magnetization and $\mu_B$/Co against Al concentration. . . . . 141
6.91 A plot of the optical band gap versus the Al dopant concentration. . . . . 142
6.92 A graph of $\alpha^2$ against photon energy for Al-doped $Zn_{0.95}Co_{0.05}O$ thin films. . . . . 143
6.93 The Hall effect for Al-doped $Zn_{0.95}Co_{0.05}O$. . . . . 144
7.94 The scrolls on the unbroken tube surface. . . . . 148
7.95 A flake of soot broken in half and folded over itself. . . . . 149
7.96 An EDAX spectrum of the pyrolysis products of 1,2-diaminopropane. . . . . 150
7.97 X-ray diffractogram of the carbon-nitrogen scrolls . . . . . 151
7.98 An SEM image showing a carbon whisker. . . . . 152
7.99 SEM image of the soot showing agglomerates of $\sim 1\,\mu$m particles. . . . . 153
7.100 Cross-section of a whisker as viewed in the SEM. The diameter of this scroll is $\sim 25\,\mu$m, a typical value for the whisker. . . . . 154
7.101 An SEM of one layer of the whisker magnified. . . . . 154
7.102 Intercalated layers of graphite-like material. . . . . 155
7.103 Crystallite formation on tube surface. . . . . 156
7.104 M-H loop of soot product. . . . . 157
7.105 Magnetization measurements of a scroll sample at different temperatures. . . . . 158
7.106 Room temperature magnetization data for scroll and soot products of the two precursors . . . . . 159
7.107 AFM of scroll surface . . . . . 160
7.108 EPR spectrum of a soot sample from a 1,2 diaminopropane precursor. . . . . 161
7.109 Residual gas analysis of of the remaining gas following pyrolysis of 1,2-diaminopropane. . . . . 162
7.110 Residual gas analysis of of the remaining gas following pyrolysis of 1,2-diaminopropane. . . . . 162
7.111 A typical R(T) curve of a scroll . . . . . 163
7.112 Contacts made to a broken scroll to measure the Hall Effect. . . . . 164
7.113 Hall resistance of a scroll piece as a function of field. . . . . 165
7.114 X-ray diffraction pattern of C-Mn. . . . . 166
7.115 SEM image of the C-Mn . . . . . 167
7.116 EDAX of C-Mn . . . . . 167
7.117 VSM M-H loop of C-Mn . . . . . 168
7.118 M(H) loop from SQUID measurements of the C-Mn sintered at 600 °. . . . . 169
7.119 M(H) loops at different temperatures of "pure" graphite from Aldrich. . . . . 170
7.120 M-H loops at 300 K and 5 K for 99.9995% pure graphite from Aesar. . . . . 171
7.121 Transmission Mössbauer spectra of $C_{95}Mn_5$ and graphites. . . . . 171
8.122 A M-H loop of a thin film of $(In_{0.825}Sn_{0.1}Fe_{0.075})_2O_3$ at 300 K. . . . . 175
8.123 Susceptibility versus temperature measurements. . . . . 177
8.124 The narrow windows of deposition conditions that result in magnetic thin films. . . . . 179
8.125 The mobility as a function of temperature of a $(In_{0.875}Sn_{0.1}Mn_{0.025})_2O_3$ thin film. . . . . 180
8.126 The band gap shift of Al-doped $Zn_{0.95}Co_{0.05}O$ thin films as a function of carrier concentration. . . . . 181
8.127 A representative set of background room temperature SQUID measurements. . . . . 187

8.128 The superexchange. . . . . 188
8.129 Representation of magnetic polarons. . . . . 190
9.130 A plot of substrate temperature against heater voltage. . . . . 201
9.131 A plot of moment versus applied field for the "blank" materials. . . . . 202

# List of Tables

1 The properties of dilute magnetic semiconductors . . . . . 30
2 Properties of n-type TCOs . . . . . 31
3 The electrical properties of pTCOs . . . . . 33
4 Materials used for ceramic targets . . . . . 45
5 Fit parameters for transmission Mössbauer spectra of Fe-doped rutile ceramics . . . . . 79
6 Fit parameters for CEMS spectra for Fe-doped rutile . . . . . 85
7 Bond lengths for bulk indium oxide . . . . . 91
8 A table of $In_2O_3$ targets prepared. . . . . 95
9 A table summarising the properties of doped indium oxide films . . . . . 98
10 Transition-metal doped ITO ceramic targets. . . . . 112
11 Doped ZnO thin films prepared. . . . . 138
12 Elemental analysis of the soot and scrolls. . . . . 153
13 Fit parameters for the EPR spectra . . . . . 160
14 Common impurities phases in dilute magnetic semiconductors . . . . . 184
15 Materials that were found to exhibit ferromagnetic behaviour . . . . . 185
16 A table of cgs to SI and SI to cgs unit conversions . . . . . 199
17 The standard deviation of the noise measurements on the sample blanks and their average and standard deviation . . . . . 203
18 A table giving the measured magnetization of four different samples of five series of films. Also quoted is the average, the standard deviation and the ratio of the standard deviation to the average. . . . . 204
19 A table showing the error due to a particular measurement, a typical measured value and the ratio between the two. . . . . 204

# Chapter 1

# Introduction

"Robbie, you look so stressed!"

Zhu Diao, Chinese philosopher.

## 1.1 Spin electronics

The motivation behind this thesis is the investigation of materials that may be suitable for the emerging field of spin electronics. It seems fitting that the introduction should begin with a short discourse on spin electronics.

### 1.1.1 The Electron - Charge and Spin

The electron is a fundamental particle of physics - a *lepton*. It has a mass ($m_e = 9.11 \times 10^{-31}$ kg) and, significantly for the field of electronics, an electric charge of $q_e = -1.6022 \times 10^{-19}$ C $\equiv e$. To date, electronics has used the flow of the charge of electons (and holes) as a means for transporting and manipulating information. Initially, *analog* electronics used continuously variable physical properties, such as voltage - a property derived from the charge of electrons - to convey information. It is a fast but noisy method. This was superceded by *digitalization*, the encoding of information into 1's and 0's - a less noisy method of information transport that integrated well with the use of semiconductors. However, the basic physical processes remain the same - digital circuits are made from analog components which use the charge of the electron as the basis for information transport and manipulation, ignoring any other property.

The electron, however, is not limited to charge alone. The electron is a *fermion*, and posesses a half-integer *spin*. The spin of a particle is a property as intrinsic as mass or charge and refers to intrinsic angular momentum. The spin of the electron is $S = \pm\frac{\hbar}{2}$ and if this were thought of classically as the electron "spinning" on its own axis, the speed of rotation would exceed the speed of light, which is impossible. Thus, spin must be thought of as an intrinsic quantum phenonemon.

The spin of the electron implies an intrinsic magnetic moment, $\mu$, given by

$$\mu = g\frac{e}{2m_e}S$$

where $g$ is the gyromagnetic factor, and for an electron, $g = 2.0023193043768(86)$. The magnetic moments of unpaired electrons on atoms in a ferromagnetic material, such as alloys based on Fe, Ni, and Co, can couple and align themselves to each other. These materials thus produce a mesoscopic measureable field. These fields can be orientated, with applications such as magnetic storage devices, which encode 1's and 0's as magnetic fields of opposite orientation. The charge of the electron is irrelevant in this process.

### 1.1.2 Moore's Law

The use of electronics to perform calculations and data manipulation is now ubiquitous. However, despite "quantum leaps" with the advent of digital circuits, semiconductors and integrated circuits, the underlying physical principles behind the process have not changed

Moore's Law, an empirical observation due to Gordon E. Moore, the founder of Intel, is that the transistor density of integrated circuits, which is inversely correlated with component cost, doubles every 24 months[1]. This law has been remarkably accurate in predicting the development of transitor density from the early seventies to the present day (Fig. 1.1). However, this is more a reflection of an industry target rather than of any underlying physical process.

The discussion of Moore's Law in the present day is mostly about it's projected breakdown. For the law to hold, "trench size" - i.e., the smallest definable structure possible - must persistantly reduce. Currently, transitors are formed on the 65 nm level. IBM announced in 2006 that they have developed techniques that enable circuit print definition of just under 30 nm, ensuring the status of Moore's Law until 2013. However, as the trench size approaches atomic sizes, definition of structures becomes difficult and the complexities associated with size reduction, such as heating effects, parameter variation and leakage currents, will ensure that electronics-based computation will reach a fundamental limit. The progress required to further adhere to Moore's Law will consequently require a fundamental shift to different physical principles.

### 1.1.3 The Mechanisms Behind Spintronics

While electronics and magnetism have exploited different aspects of the electron,

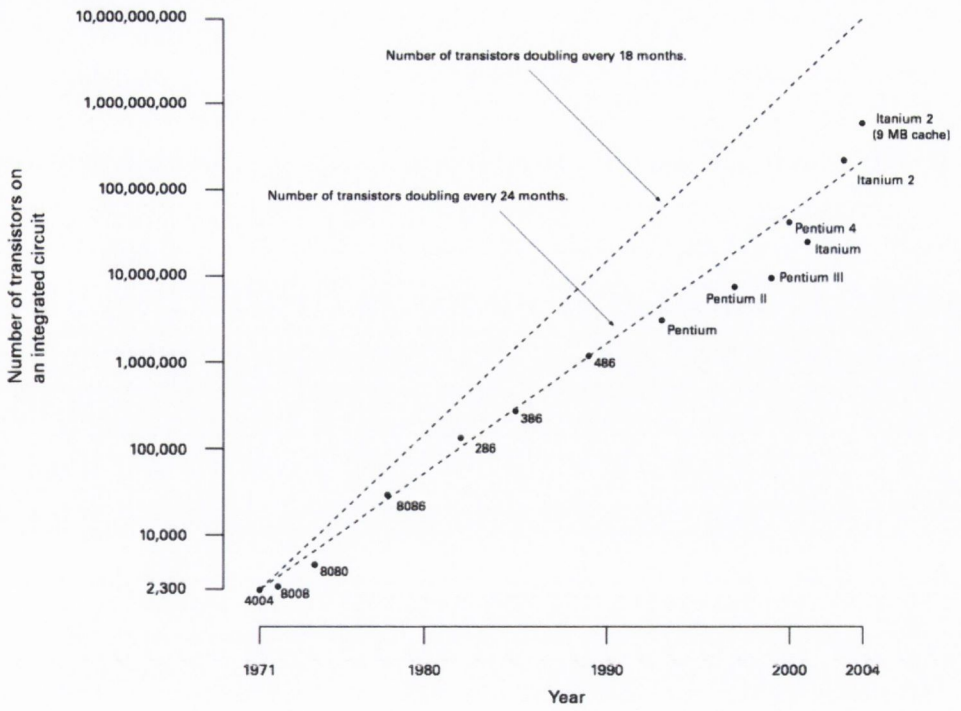



Figure 1.1. A graph of transitors per integrated circuit against year, illustrating Moore's Law

the field of "spintronics" is concerned with using spin and charge together.

The principles behind spintronics first appeared in 1936 when Mott suggested the two spin channel model [2], arguing that the spin-up and spin-down conduction electrons in a metallic ferromagnet could be considered two independent channels of conduction, i.e. spin-up charge carriers and spin-down charge carriers. Mott also suggested that both channels would have different transport properties, and this difference could explain some observations of anomolous transport in ferromagnetic conductors.

The two foundations of spin electrons can therefore be summarised as:

1. The two channels are independent and scattering probability from one channel to the other is small compared to the scattering probability within a channel.

2. The two channels have differing transport properties, be they due to different channel mobilities or different carrier concentration.

The splitting of the two conductions bands can be explained by the ferromagnetic exchange field lifting the degeneracy between the two spin states. This alters the electron densities of the two channels at the Fermi surface. As the conduction processes take place through electrons residing on this Fermi surface, an asymmetry in the den-

sities on this surface leads to an asymmetry in the transport of the channels. The mobility of the channels is split due to the fact that the asymmetric densities lead to asymmetric scattering probabilities.

### 1.1.4 Spin Accumulation, Spin Diffusion Lengths and Polarization

Having established spin asymmtery, we may consider a current flowing from a spin asymmetric material (SAM) to a spin symmetric material (SSM). When the spin asymmetric electrons enter the SSM, there cannot be a discontinuous jump in the polarization of the carriers. Instead, the spin-up surplus penetrates the SSM. However, in the SSM, the equilibrium state is equally populated spin-up and spin-down channels. Therefore, there is a large amount of unoccupied spin-down levels. Any spin flip scattering will preferentially scatter a spin-up to a spin-down until equilibrium has been restored (Fig 1.2a). The length the carrier travels before a spin flip occurs is dubbed the spin diffusion length, $\lambda_{sd}$, represented in Fig 1.2b, and is given by the equation

$$\lambda_{sd} = \sqrt{\frac{\lambda v_F \tau_{\uparrow\downarrow}}{3}} \tag{1}$$

where $\lambda$ is the mean free path (also indicated in Fig 1.2b), $v_F$ is the Fermi velocity and $\tau_{\uparrow\downarrow}$ is the spin-flip time. The spin diffusion length is dependent on the mean free path, so a large number of scattering sites - such as defects or impurites - tend to reduce $\lambda_{sd}$.

Another quantity we can derive from the mechanisms of spintronics is the *polarisation* - the extent to which the population of one channel exceeds the population of the other channel - and it is defined as the difference in carrier concentration at the Fermi surface divided by the sum of carriers:

$$P = \frac{n^{\uparrow} - n^{\downarrow}}{n^{\uparrow} + n^{\downarrow}} \tag{2}$$

where $n^{\uparrow}$, $n^{\downarrow}$ are the carrier concentrations for the up and down channels, respectively.

### 1.1.5 Devices

The spin valve was the first useful spintronic device [3]; it is a stack of two ferromagnetic (FM) layers with a non-magnetic (NM) layer sandwiched between them (Fig 1.3). The two spin channels experience different resistances as they pass through the magnetically orientated FM layers. When the two FM layers are aligned to each

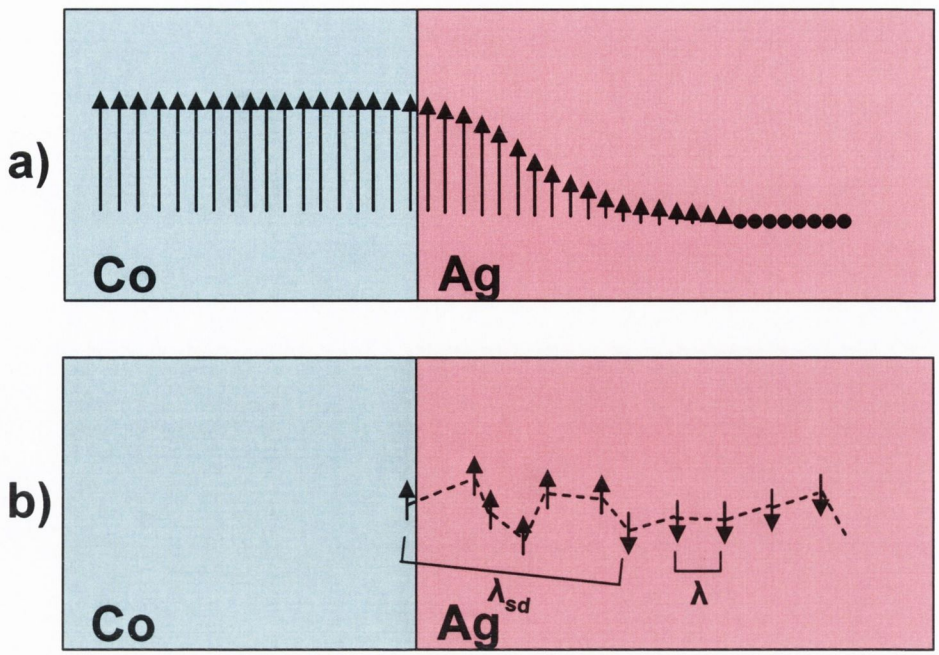



Figure 1.2. A schematic diagram representing a) spin accumulation extending into silver from a cobalt current injector, with the magnitude of the vector indicating magnitude of spin accumulation b) the scattering processes a spin encounters on entering the silver

other (Fig 1.3, top), the spin channel aligned to this orientation is effectively a "short circuit" through the stack, while anti-alignment of the two layers (Fig 1.3, bottom) leads to a higher resistance.

Usually, one of the ferromagnetic layers is "pinned", i.e. its orientation is held by an antiferromagnetic pinning layer. The other layer is then dubbed the "free layer", as its orientation may be switched using a magnetic field. Therefore, the resistance of the stack is dependent on the field applied. This is called a *magnetoresistive effect*, and the magnetoresistance (MR) is given by

$$MR = \frac{R^{\uparrow\downarrow} - R^{\uparrow\uparrow}}{R^{\uparrow\downarrow}}$$

where $R^{\uparrow\uparrow,\uparrow\downarrow}$ are the resistances of the aligned and anti-aligned states. The term GMR (giant magnetoresistance), used when referring to spin valves, is attributable to the large change in resistance observed in the spin valve. With this definition. $MR$ cannot exceed 100%.

The spin valve is in use as a magnetic field sensor which is used to read the bits of a magnetic hard disk. The stray field of the bit rotates the magnetization of the free layer, and a high and low measurement of resistance can be related to a 1 or a 0

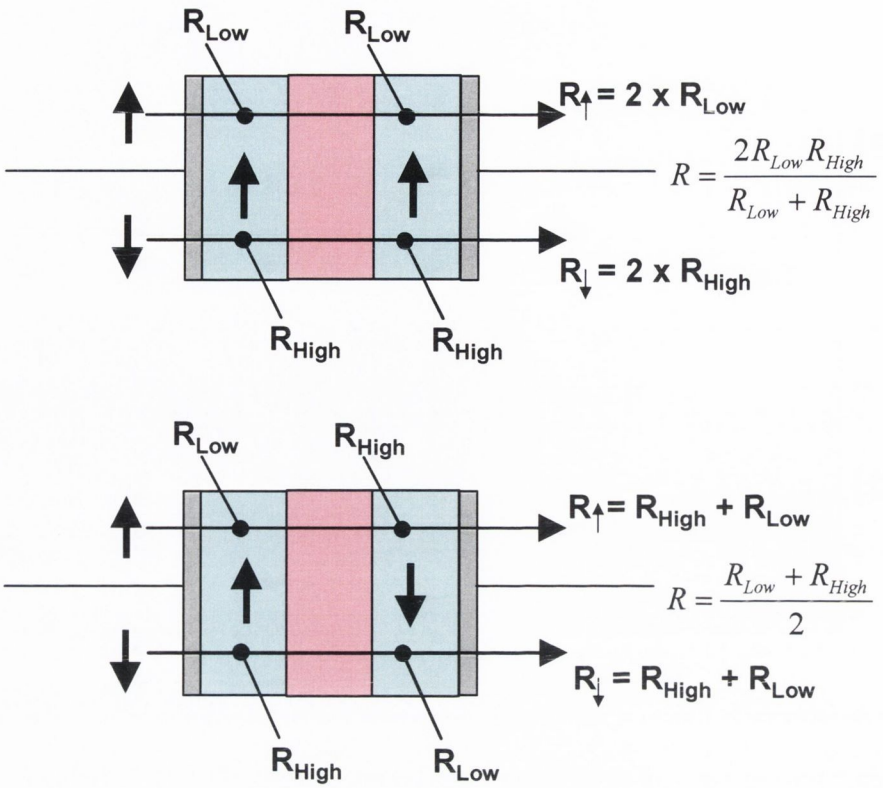



Figure 1.3. A schematic representation of a CPP (current perpendicular to plane) spin valve, with the resistances for both channels.

on that bit. The quality of the device is determined largely by the non-magnetic layer [4]. Indeed, if the layer is replaced by an insulating layer, it is called a *tunnel junction*, which is basically the same device, but as the monicker suggests, tunnelling currents flowing perpendicular to the plane are now used.

These are *two terminal* devices. The aim for future spintronic devices is the realisation of three-terminal devices, such as the spin transistor. An electronic transistor controls the flow of current in a circuit by the application of a voltage on a secondary circuit. Modulation of the voltage results in the modulation of the current in the primary circuit. A spin transistor would use a spin state to control the flow. The primary advantage is that once the spin state is set, there is no need to apply constant power to maintain it, unlike the electronic transistor. It is "non-volatile".

### 1.1.6 Materials

The conventional electronics industry has long ago identified the ideal materials for device manufacture as silicon, with galium arsenide for special applications.

These materials possess suitable physical properties without drawbacks in the areas of cost and stability. These materials are not suitable for use in spintronics due to lack of intrinsic ferromagnetism. Current spin valves use CoFe or NiFe layers with Cu, for example, as the spacer layer. Modern tunnel junctions [5] also use similar $3d$ ferromagnetic layers with $MgO_x$ or $AlO_x$ insulating layers.

More advanced devices will require a new class of material, and the following criteria will have to be satisfied:

1. Spin dependent transport. The independence of the two spin channels and their differing transport properties is fundamental for spintronics. Non-magnetic materials such as semiconductors do not possess this property.

2. High Curie temperature. Spintronic devices will need to operate at room temperature and well above if they are to be integrated into semiconductor electronics.

3. High mobilities and large spin diffusion lengths. The spin diffusion length needs to be long enough for spin orientation to survive an operation in a spintronic device.

4. $n$- and $p$-type behaviour with controlable carrier concentration. For device fabrication, both $n$- and $p$-type semiconductors are required. A main advantage of semiconductors for ordinary electronic applications is the ability to control carrier concentration. This would also be of use in spintronic devices.

Based on the above, what is required is a high $T_C$-ferromagnet which exhibits spin dependent transport and a high carrier mobility. The material would ideally be:

1. Inexpensive, so that fabrication is cost-effective.

2. Integrable with existing semiconductor technology.

3. Non-toxic and non-volatile, so that it is suitable for everyday public use.

Half-metals, metals which have only one spin orientation at their Fermi surface exhibit just-above room temperature $T_C$'s, while ferromagnetic semiconductors, such as EuO, and some dilute ferromagnetic semiconductors, such as GaMnAs, have $T_C$'s well below room temperatures. Furthermore, ferromagnets and half-metals have extremely poor mobilities. A ferromagnetic semiconductor with a $T_C$ above room temperature would satisfy all of the above critera.

In the next section we shall examine the eletrical properties of semiconductors.

## 1.2 Semiconductors

### 1.2.1 Conductivity

Electrical conduction is the movement of electrically charged particles through a medium. The movement can form an electric current in response to an electric field. The mechanism for transport of charge depends on the nature of the material.

The ease with which current density (current per area) $j$ appears in a material is measured by the conductivity $\sigma$, defined as:

$$j = \sigma \cdot E$$

where $E$ is the electric field applied. The current density can also be written as

$$j = e \cdot n_e \cdot \underline{v}_d$$

where $q_e$, $n_e$ and $\underline{v}_d$ are the charge, number density and drift velocity of the charged particle. Thus, we have that

$$\sigma = n \cdot e \cdot \mu$$

where $\mu = \underline{v}_d / E$ is the mobility of the charge carrier, a measure of how susceptible the charge carrier is movement under an electric field.

### 1.2.2 The Band Model

In the context of electrical conductivity, materials can generally be classified as one of the following three categories: conductors, semiconductors or insulators. Each category can be thought of as having a conduction band of electrons - a grouping of electrons involved in the conduction processes - and a valence band, whose electrons are involved in the binding of the material (Fig 1.4).

In insulating materials, the energy required to promote an electron is larger than the thermal energy of the electron and thus the conduction band is empty. Therefore, the material has no charge carriers available for conduction and the material is insulating. In a metal, however, the bands are overlapping so that any free electrons in the valence band are free to populate the conduction band and thus enable electrical conductivity in the material. Semiconductors sit in between these two definitions. The conduction band does not overlap the valence band, but the gap is narrow enough for

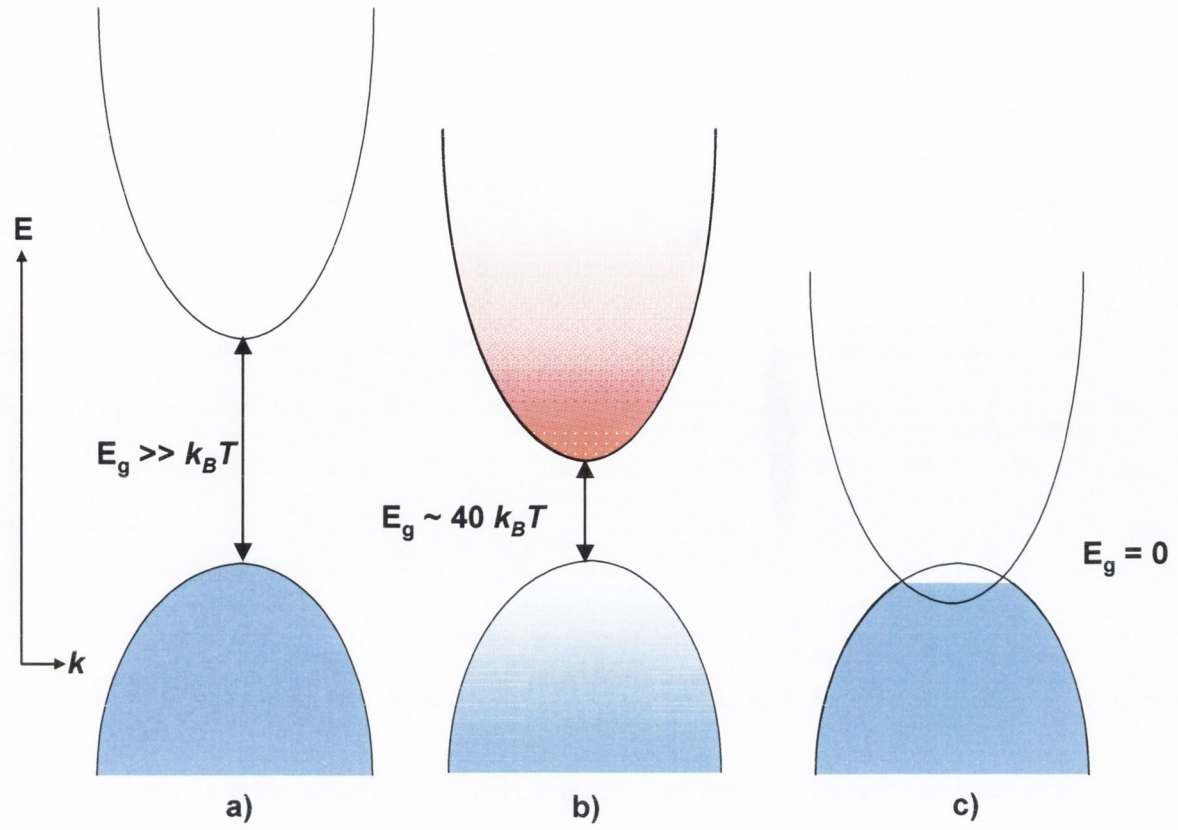



Figure 1.4. Band diagrams for a) an insulator b) a semiconductor and c) metal. The parabola at the top represents the conduction band (with shading as carrier population) and the parabola at the bottom is the valence band.

thermal or optical activation processes to enable carrier promotion to the conduction band. The gap, $E_g$, is of the order of 1 eV. While there is a definite criterion separating semiconductor from metal, the crossover between semiconductor and insulator is not so well definied.

### 1.2.3 Elemental and Compound Semiconductors

Semiconductors can exist as elemental semiconductors - such as Ge and Si - in which atoms of a single species are covalently bonded, each atom sharing electrons with its nearest neighbour, or as compound semiconductors, which are comprised of two or more elements, such as GaN or ZnS. While there is no disparity in electron affinity of the atoms in an elemental semiconductor, its presence in a compound semiconductor means that the bonding is no longer purely covalent, but slightly ionic in character. The classification of a compound semiconductor is determined by the periodic table group memberships of the constituent atoms. Thus, GaN is a III-V semiconductor,

Ga being in group III and N belonging to group V. Compound semiconductors are not only binary, but may be ternary and even quaternary. Varying the individual atomic concentrations allows tailoring of the physical properties, such as crystal lattice parameters and energy gap.

### 1.2.4 Semiconductor Doping and Carrier Concentrations

The semiconductors described so far have been intrinsic semconductors - i.e. semiconductors that contain no impurities. If the thermal energy of an electron promotes it to the conduction band, it leaves a "hole" - a positive charge - in the valence band. Both the electron and the hole are termed "charge carriers", and the semiconductor acquires a "carrier concentration", depending on the number of the carriers per volume of material. For an intrinsic semiconductor, the carrier concentration of negative carriers ($n$, electron) are equal to the number of positive carriers ($p$, holes) so that

$$n_i = n = p \tag{3}$$

where $n_i$ is termed in the intrinsic carrier concentration. At room temperature, silicon, for example would have an intrinsic carrier concentration of $n_i = 1 \times 10^{10}\,\mathrm{cm}^{-3}$. This number would obviously increase with temperature owing to the fact that more thermal energy would be available for electon-hole pair generation.

We can upset the balance of Eq. (3) by replacing a small number of host semiconductor atoms with atoms of a different valence - a process known as doping. Doping Si, a group IV semiconductor, with a group V element, such as As, inserts more electrons into the semiconductor than are needed for bonding purposes. This results in an $n$-type semiconductor, where the electron concentration, $n$, is now greater than the hole concentration, $p$. Doping Si with a group III element has the opposite effect, with there now being a larger hole concentration than electron concentration, resulting in a $p$-type semiconductor. These $p$- and $n$-type semiconductors are called extrinsic semiconductors. The doping creates energy levels just under the conduction band or above the valence band (Fig 1.5), which allows for much easier thermal activation of the $p$- or $n$-type charge carriers. The electrical conduction due to excitation from either the donor or acceptor level will then dominate the electrical conductivity of the material at lower temperatures.

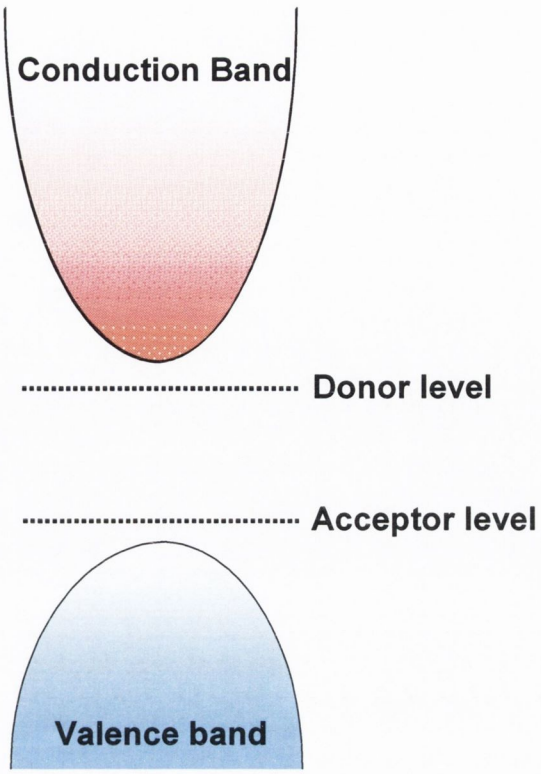



Figure 1.5. The $n$-type dopants, called donors, create donor levels just underneath the conduction band. $p$-type dopant create acceptor levels just above the valence band.

### 1.2.5 Doping Compound Semiconductors

While doping an elemental semiconductor results in a simple replacement of the semiconductor atom with the dopant atom, doping a compound semiconductor introduces complications. The effect of the dopant atom depends on the site occupied by the atom on the lattice. In a III-V semiconductor, a dopant atom from group IV may occupy the site of the group III atom or the group V atom, and its behaviour as a donor or acceptor would depend upon which site it occupied. This type of impurity is called an amphoteric impurity.

### 1.2.6 The Fermi Level

The Fermi level or Fermi energy, $E_F$, for electrons at absolute zero is the uppermost energy level occupied by an electron. The states below it are fully occupied and the states above it are empty, according to Fermi-Dirac statistics. Thus at 0 K, it is a sharp "edge" to the electron-occupied states. At finite temperature, this "edge" becomes blurred by, there now being a non-zero possibility that a state above the Fermi

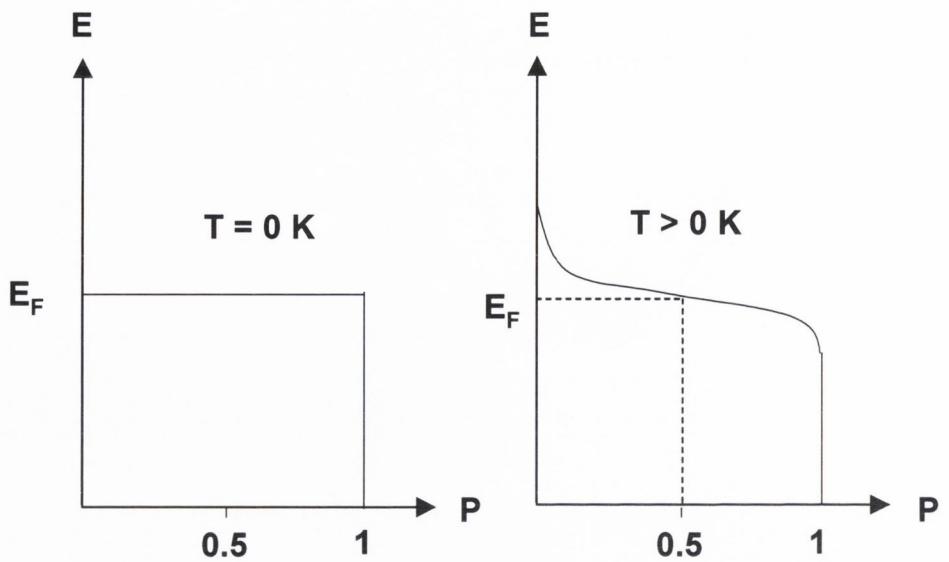



Figure 1.6. The probability of level occupation versus energy for absolute zero (left) and a non-zero temperature.

level is occupied and a state below unoccupied. The probability is given by

$$f(E) = \frac{1}{e^{\frac{E-E_F}{k_B T}} + 1}$$

where $k_B$ is the Boltzmann constant and $T$ is the temperature of the system. The Fermi energy is then redefined at the energy at which the probability of finding an electron is 0.5 (Fig 1.6).

### 1.2.6. Intrinsic Semiconductors

Given the density of states for the valence band in the free electron model is

$$D(E) = \frac{V}{2\pi^2\hbar^3}(2m_h)^{\frac{3}{2}}(-E)^{\frac{1}{2}} \tag{4}$$

and that of the conduction band is

$$D(E) = \frac{V}{2\pi^2\hbar^3}(2m_e)^{\frac{3}{2}}(E - E_g)^{\frac{1}{2}} \tag{5}$$

where $E$ is measured from the top of the valence band and $m_{e,h}$ is the effective electron and hole masses, respectively, we can calculate the electron density in the conduction band to be

$$n = 2\left(\frac{2\pi m_e k_B T}{\hbar^2}\right)^{\frac{3}{2}} e^{\frac{(E_F - E_g)}{k_B T}} \tag{6}$$

and the density of holes in the valence band to be

$$p = 2\left(\frac{2\pi m_h k_B T}{\hbar^2}\right)^{\frac{3}{2}} e^{-\frac{E_F}{k_B T}} \tag{7}$$

Multiplying $p$ and $n$ eliminates $E_F$ from the equations to give

$$np = n_i^2 = p_i^2 = N_c N_v e^{-\frac{E_g}{k_B T}} \tag{8}$$

where $N_{c,v}$ are the cumbersome prefactors in Eqns (6) and (7), with $n_i$ to indicate an intrinsic semiconductor. This equation is termed the *law of mass action.* Using this expression for $n$ and $p$ in Eqns. (6) and (7) and equating, we obtain

$$m_e^{\frac{3}{2}} e^{\frac{(E_F - E_g)}{k_B T}} = m_h^{\frac{3}{2}} e^{-\frac{E_F}{k_B T}} \tag{9}$$

yielding

$$E_F = \frac{E_g}{2} + \frac{3}{4} k_B T \ln\left(\frac{m_h}{m_e}\right) \tag{10}$$

This places the Fermi energy in the centre of the gap of the intrinsic semiconductor ($E$ is measured from the top of the valence band), with an additional temperature-dependent term which is also dependent on the effective mass ratio.

#### 1.2.6.2 Extrinsic Semiconductors

The introduction of donor and acceptor levels in the band gap alters the positioning of the Fermi level from that obtained in Eqn. (10). For a donor, say, the energy needed to excite an electron to the conduction band is the donor ionization energy, $E_d$. The donor ionization processes can be represented by

$$\begin{aligned} e^- + D^+ &= D \\ D^+ &= D - e^- \\ N_d^+ &= N_d - n \end{aligned} \tag{11}$$

for electrons and similarly for holes. Given that the donor-conduction band gap is $E_d$, we can use the Fermi function to obtain

$$N_d^+ = N_d\left[1 - f\left(E_g - E_d\right)\right] \tag{12}$$

where $N_d$ is the number of donor sites and $N_d^+$ is the number of ionized donor sites. A

similar argument can be constructed to show for holes that

$$N_a^- = N_a f(E_a)$$

Comparing and substituting with the law of mass action (Eqn. (8)), it can be shown that

$$E_F = E_g - k_B T \ln\left(\frac{N_c}{N_d - N_a}\right) \tag{13}$$

which places the Fermi level in between the donor level and the conduction band for an intrinsic $n$-type semiconductor. The stronger the compensation, the closer the Fermi energy is to the donor level.

## 1.3 Semiconducting Oxides

### 1.3.1 Defects in Oxides

Defects play an important rôle in the electrical properties of an oxide. A material such as $TiO_2$, when stoichiometric, is an insulator with a band gap of 3.1 eV. However, $TiO_2$ is extremely sensitive to reducing (even slightly reducing) conditions, and as such, readily becomes $TiO_{2-x}$. This reduced material has oxygen vacancies and is thus "doped" with electrons, making it a semiconductor. Unlike a covalent semiconductor, where the donors are easily ionized, the electrons introduced by doping may remain trapped near the oxygen vacancies. The oxygen vacancy is a common defect and explains why most oxide semiconductors are $n$-type. However, the oxygen vacancy is not the only defect to occur in an oxide. There are four basic types of point defect:

1) A vacancy, which is an atom missing from an atomic site, such as an oxygen vacancy in $TiO_{2-x}$. A vacancy is denoted as $\square'_{\mathrm{M}}$, $\square^{x}_{\mathrm{M}}$, or $\square^{\blacksquare}_{\mathrm{M}}$, for vacancies which result in negative change in charge, no change in charge and a positive change in charge, respectively where M is the atomic species which is vacated[1].

2) An interstitial, in which an extra atom occupies a position which is not on the lattice. This is denoted as $\mathrm{M}'_i$, $\mathrm{M}^{x}_i$, or $\mathrm{M}^{\blacksquare}_i$, for interstitials which result in negative change in charge, no change in charge and a positive change in charge, respectively where M is the atomic species which is inserted interstitially.

[1] The notation used for this defect and all others from this point in the thesis is called *Kröger-Vink* notation. The superscript $'$ denotes a 1− charge difference due to the defect, the $^{x}$ superscript denotes no charge difference and the $^{\blacksquare}$ superscript denotes a positive charge difference. The multiplicity of the superscript indicates the magnitude of the charge difference, e.g. $''$ denotes 2−.

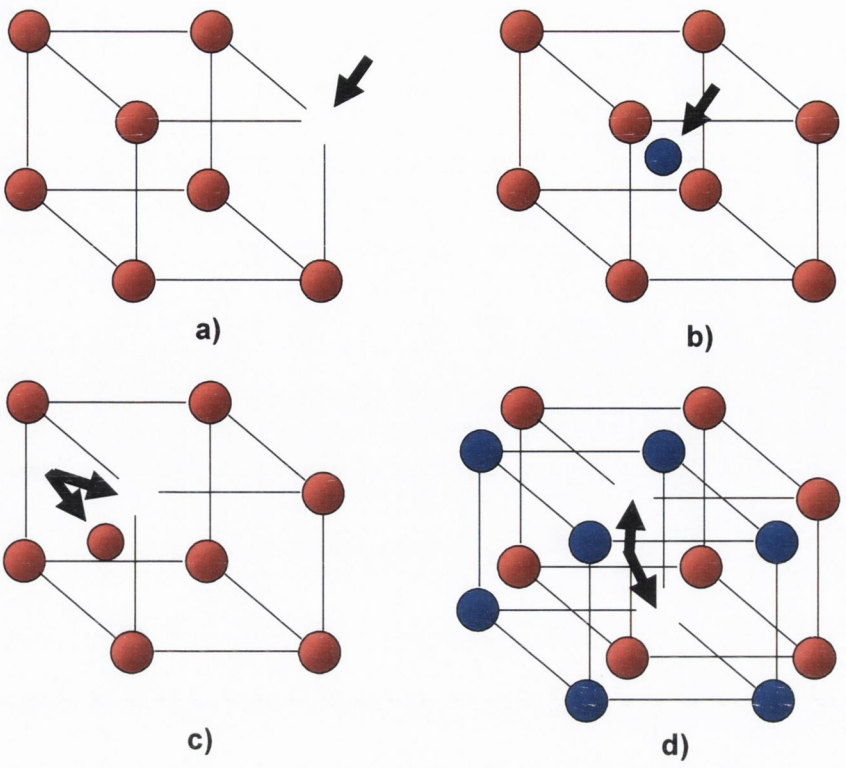



Figure 1.7. Simple diagrams depicting the four main point defect types a) a vacancy b) an interstitial c) a Frenkel defect and d) a Schottky defect. In all cases the black arrows point to the defect site

3) A Frenkel defect is a combination of a vacancy defect as mentioned above with a interstitial defect of the same ionic species. This would be denoted as $\square'_{\mathrm{M}} + \mathrm{M}_i^{\blacksquare}$ for a postive ion $\mathrm{M}^{+}$ and $\square_{\mathrm{M}}^{\blacksquare} + \mathrm{M}'_i$ for a negative ion $\mathrm{M}^{-}$. The combination of the two defects ensures charge neutrality. Unlike a Schottky defect (which will be defined next), this type of defect tends *not* to increase the lattice size, or only by a negligible amount.

4) A Schottky defect is a combination of two vacancies of two different ion species in a binary system, for instance. This combination can also allow for charge neutrality. Since the number of atoms has to stay constant, no matter how many Schottky defects are present, the surplus atoms must be thought of as sitting on the surface and therefore there is a measurable crystal expansion due to the formation of Schottky defects.

The four main types of point defect are represented schematically in Fig 1.7.

In addition to these four simple types, the lattice may contain a substitutional impurity - as in a doped semiconductor, e.g. $\mathrm{Mg}^{2+}$ for $\mathrm{Al}^{3+}$ in $\mathrm{Al_2O_3}$. This would be denoted by $\mathrm{Mg}'_{\mathrm{Al}}$.

In addition to point defects, the crystal may contain *dislocations*. A dislocation is a linear crystallographic defect, or irregularity, within a crystal structure. Usually

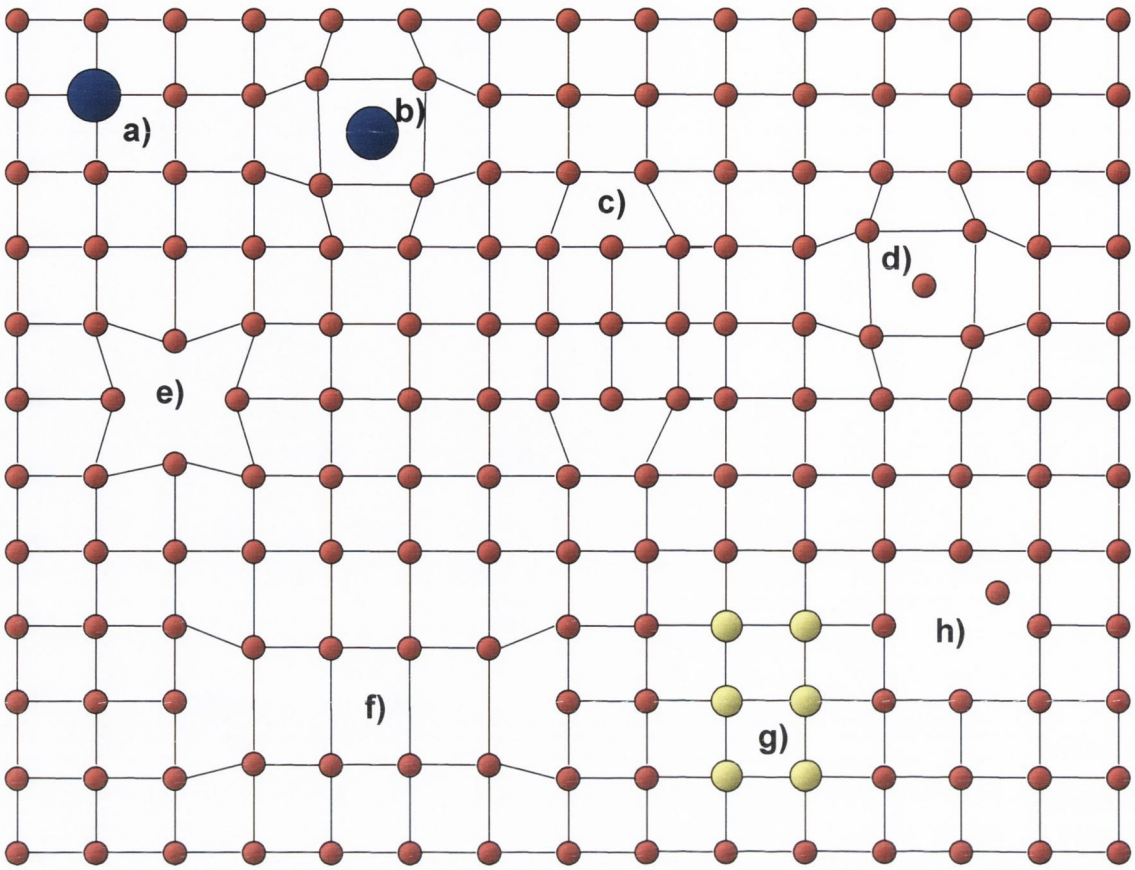



Figure 1.8. The several different classes of crystal defects. a) is a subtitutional impurity, b) is an interstitial impurity, c) is an interstitial dislocation, d) is a homo-interstitial, e) is a vacany, f) is a vacancy dislocation, g) is an impurity precipitation and h) is a Frenkel defect. As this is a unitary crystal, a Schottky defect cannot be represented.

this is caused and can be visualized as an atomic plane terminating *within* the crystal, rather than at the crystal edge.

The defects and dislocations combine to form general and more complicated defects. In general, an oxide will contain many different types of defects. A diagram detailing most 2-D crystal defects is shown in Fig 1.8.

The net effect of all these defects is the introduction of energy levels in the bandgap and also the introduction of charge carriers. Due to the highly complex structure of the oxides and their defects, the typical $n$-type doping is often highly compensated. While the defects primarily induce conductivity in the samples by introducing carriers, the defects may also directly provide conductivity by migrating through the lattice, a mechanism called ionic conductivity. The diffusivity of the defects is, however, much smaller than the mobility of electrons or holes. Transport will be dominated by mobile electrons or holes if they are present. A wide gap insulator will, however,

exhibit feeble ionic conductivity [6].

### 1.3.2 Semiconducting Behaviour in Oxides

The high number of defects naturally occuring in an oxide requires most oxide semiconductors to be extrinsic at room-temperature, with intrinsic behaviour only seen for highly pure, stoichiometric oxides in the high temperature limit. The defects present themselves as donor and acceptor levels in the bandgap. The general preponderance of oxygen vacancies implies that the conduction is generally $n$-type, and that the Fermi level generally is just above the donor level. Oxides tend to have wide bandgaps, in the range of $3 - 6\,\mathrm{eV}$, and large donor ionization energies, with $E_g \simeq E_d \simeq 0.1 - 0.5\,\mathrm{eV}$.

## 1.4 Dilute Magnetic Semiconductors

A class of materials that show promising properties for spin electronics is dilute magnetic semiconductors (DMS). A dilute magnetic semiconductor is a semiconductor that is doped with ions that have a net spin, usually a 3d atom such as Fe, Ni or Co, with the aim of inducing ferromagnetism in the host semiconductor. The host semiconductor would ensure that the carriers have the beneficial properties of semiconductors, but the induced ferromagnetism would in turn induce the spin dependent transport properties required for spintronics with the added advantage of being compatible with existing semiconductor technology.

### 1.4.1 III-V Materials

#### 1.4.1.1 GaMnAs

Mn-doped GaAs is a widely-researched magnetic semiconductor. It was reported to be ferromagnetic and to exhibit the anomolous Hall effect by Ohno et al. in 1996 [7]. The host semiconductor GaAs is already a widely-used material in the semiconductor industry. It's primary advantage over Si is its high electron mobility ($9200\,\mathrm{cm^2\,V^{-1}\,s^{-1}}$), making it suitable for high-speed electronics and the fact that it has a direct band gap, which allows it to be incorporated into optoelectronic devices.

A model for the mechanism of ferromagnetism in $p$-type III-V magnetic semiconductors was presented by Dietl [8], based on the Zener model of ferromagnetism in transition metals. These authors consider the effect of 5% Mn-doping on a range of

materials. The major disadvantage GaMnAs is its low $T_C$. As mentioned in the previous section, a $T_C$ well above room temperature, $> 500\,K$, is required. However, to date, the highest reported $T_C$ of GaMnAs is only $172\,K$ [9], well below the required temperature. Though there has been much effort to raise the $T_C$ of GaMnAs, it is unlikely that the material will find room temperature applications. Furthermore, mobility is greatly reduced by scattering from the Mn dopants. Its sister material Mn-doped InAs exhibits many of the same properties, but has an even lower Curie temperature of $\sim 61\,K$ [10].

#### 1.4.1.2 GaMnN

Dietl's paper mentioned above also contained a prediction of *above* room temperature ferromagnetism in other *p*-type Mn-doped III-V materials such as GaN and InN. Mn-doped GaN has been fabricated by MBE and for high Mn-doping, ferromagnetism was observed, with Curie temperatures well above room temperature ($> 900\,K$) [11]. However, the carriers were found to be *n*-type, unlike Dietl's prediction. Also contrary to the prediction are reports that Mn-doped InN displays paramagnetism, and not ferromagnetism [12].

### 1.4.2 IV Materials

In addition to the III-V materials described above, Dietl's paper extended to the elemental semiconductors of group IV, with $T_C$ predictions of $130\,K$, $475\,K$, $75\,K$ for 5% Mn-doped Si, C and Ge respectively. Near room-temperature ferromagnetism has been reported in Mn-doped Ge [13], displaying both *p*- and *n*-type conduction. No such reports exist for doped silicon or carbon.

Carbon, however, has given rise to many reports of ferromagnetism as an undoped material. This controversial subject will be discussed later in the chapter.

### 1.4.3 Oxide semiconductors

The field of ferromagnetic oxide semiconductors is somewhat of a "hot topic" at present, and ferromagnetic semiconducting oxides are widely promoted as strong contenders for a prototype material for use in spintronics [14].

#### 1.4.3.1 ZnO

ZnO is a II-VI semiconductor. It normally crystallizes in the würtzite structure, but can also take the zinc-blende structure if deposited on a ZnS buffer layer [15]. It was first reported to be ferromagnetic by doping with Mn [16] with a $T_C$ of 45 K. There is an extensive literature on magnetism in doped ZnO. For example, a study of doping ZnO with the complete range of transition metals has been carried out by Fitzgerald et al. [17].

#### 1.4.3.2 $TiO_2$

$TiO_2$ is a material that exists at room temperature in three different phases, rutile, anatase and brookite - with rutile being the most common of the three polymorphs. Matsumoto et al. [18] reported the occurrence of room temperature ferromagnetism in Co-doped $TiO_2$ in 2001. Since then, reports of ferromagnetism in Cr- [19], V- [20], Fe- [21] and Ni-doped $TiO_2$[22] have emerged. $TiO_2$, however, remains a material where there is much controversy over the origin of the ferromagnetic moment, as will be discussed later in the chapter.

#### 1.4.3.3 $SnO_2$

Tin (VI) oxide has a rutile crystal structure. It has been reported to be ferromagnetic when doped with Co [23], Mn [24] and Fe [*ibid.*]. A report of the systematic doping of $SnO_2$ with transition metals [25] confirmed these findings, while also reporting ferromagnetism in Cr- and Ni- doped $SnO_2$.

#### 1.4.3.4 $In_2O_3$

Indium oxide, a transparent conducting oxide which crystallizes in the cubic bixtyite structure, has been claimed to become a room temperature ferromagnet with Fe-doping [26]. Room temperature ferromagnetism has also been observed in Cr-doped [27], Ni-doped [28] and Mn and Fe co-doped $In_2O_3$ [29].

#### 1.4.3.5 ITO

Indium-tin oxide (ITO) is a mixture of tin (IV) oxide and Indium (III) oxide, which takes the same structure as indium oxide. Moodera et al. [30] have observed ferromagnetic behaviour at room temperature for Mn-doped ITO. Kim et al have re-

| Material | Curie Temperature (K) | Magnetization ($\mu_B$/dopant ion) | Carrier type | Reference |
|---|---|---|---|---|
| GaAs(Mn) | 172 | – | $p$ | [9] |
| InAs(Mn) | 61 | – | $p$ | [10] |
| GaN(Mn) | 930 | 0.54 | $p$ | [11] |
| InAs(Mn) | 0 | 0 | $p, n$ | [12] |
| Ge(Mn) | 280 | 0.03 | – | [13] |
| ZnO(Mn) | 45 | – | – | [16] |
| ZnO(Co) | > 300 | 2.7 | – | [17] |
| ZnO(Fe) | > 300 | 0.3 | – | [17] |
| $TiO_2$(Co) | > 300 | 0.32 | – | [18] |
| $TiO_2$(Fe) | > 300 | 2.4 | $p$ | [21] |
| $TiO_2$(Cr) | > 400 | 2.9 | $p$ | [19] |
| $TiO_2$(V) | > 400 | 4.23 | – | [20] |
| $TiO_2$(Ni) | > 400 | 2.7 | – | [22] |
| $SnO_2$(Mn) | > 300 | 0.6 | $n$ | [25] |
| $SnO_2$(Fe) | > 300 | 1.8 | $n$ | [25] |
| $SnO_2$(Co) | 650 | 7.5 | $n$ | [23] |
| $SnO_2$(Cr) | > 300 | 0.8 | $n$ | [25] |
| $SnO_2$(Ni) | > 300 | 0.6 | $n$ | [25] |
| $In_2O_3$(Fe) | 750 | 1.45 | $n$ | [26] |
| $In_2O_3$(Cr) | > 400 | 1.5 | $n$ | [27] |
| $In_2O_3$(Fe, Mn) | > 300 | 0.36 | – | [29] |
| $In_2O_3$(Sn, Mn) | > 300 | 0.8 | $n$ | [30] |
| $In_2O_3$(Sn, Cr) | > 300 | 1.6 | $n$ | [31] |

Table 1.A table detailing the properties of some dilute magnetic semiconductors. A dash indicates that no quantitive value was given in the reference.

ported ferromagnetism in thin films of chromium-doped ITO. The moment increase with Cr concentration, with a maximum value of $0.5\mu_B$/Cr reported for 15 mol% Cr doping [31].

Table 1 summarizes the properties of some dilute magnetic semiconductors.

## 1.5 Transparent Conducting Oxides

Transparent conducting oxides (TCOs) are a special group of materials that exhibit good electrical conductivity and optical transparency in the visible region. While the majority of conductors are opaque and the majority of solids which are optically transparent are electrically insulating, the unusual combination of optical transparency and electrical conductivity is observable in a small number of systems [32][33], and can therefore be labelled the rarest form of conductivity when compared to other electrical conduction phenomena such as semiconductivity and superconductivity. In common practice, a small group of materials form the basis for most TCOs - $SnO_2$, $In_2O_3$, ZnO (when doped with F, In or Al) and CdO. More complex materials are also being de-

| Material | Denisty ($kg\,m^{-3}$) | $T$ % | Resistivity ($\Omega\,cm$) | Carrier density ($cm^{-3}$) | Mobility ($cm^2\,V^{-1}\,s^{-1}$) | $E_g$ (eV) | Ref |
|---|---|---|---|---|---|---|---|
| $SnO_2$ | 6950 | 97 | $\sim 10^{-4}$ | $5 \times 10^{20}$ | 15 | 3.8 | [45] |
| $SnO_2$:F | 6950 | $> 92$ | $5 \times 10^{-4}$ | $10^{20}$ | $100^{(*)}$ | 4.24 | [46] |
| $SnO_2$:Sb | 6950 | 85 | $3 - 25 \times 10^{-3}$ | $10^{20}$ | $7^{(*)}$ | $> 4.0$ | [47][48] |
| ZnO:Al | 5610 | $> 85$ | $4 \times 10^{-3}$ | $> 2 \times 10^{20}$ | 11 | 4.1 | [49] |
| ZnO:In | 5610 | $> 85$ | $3 \times 10^{-3}$ | $10^{21}$ | 6 | 3.3 | [56] |
| ZnO:F | 5610 | $> 85$ | $1 \times 10^{-2}$ | $4 - 5 \times 10^{20}$ | $1 - 3$ | 3.35 | [57] |
| ZnO:In,Ga | 5610 | $> 85$ | $2 \times 10^{-3}$ | $1.2 \times 10^{20}$ | 24 | 3.5 | [59] |
| $Cd_2SnO_4$ | 7705 | $\sim 80$ | $2 \times 10^{-4}$ | $3.2 \times 10^{20}$ | 54 | $> 3.4$ | [50] |
| $In_2O_3$ | 7190 | $> 90$ | $\sim 10^{-3}$ | $10^{19}$ | $25 - 130$ | $> 3.2$ | [27] |
| $In_2O_3$:Sn | 7190 | $> 90$ | $\sim 10^{-5} - 10^{-4}$ | $10^{19} - 10^{21}$ | $12 - 90$ | 3.74 | [30] |
| $Zn_2SnO_4$ | 3900 | 90 | $2.3 \times 10^{-3}$ | $3.5 - 8 \times 10^{19}$ | $15 - 29$ | $> 3.1$ | [51] |
| $MgIn_2O_4$ | 6065 | 75 | $7 - 50 \times 10^{0}$ | – | – | 3.3 | [52] |
| $ZnSnO_3$ | 6417 | – | $\sim 10^{3}$ | $4 \times 10^{19}$ | 3 | – | [58] |
| CdO | 8240 | $> 90$ | $4 \times 10^{-4}$ | $1.5 \times 10^{20}$ | 150 | 2.9 | [60] |
| CdO:In | 8240 | $> 80$ | $5 \times 10^{-5}$ | $1.6 \times 10^{21}$ | 70 | 3.1 | [60] |
| $CdSb_2O_6$ | 6569 | $> 90$ | $2.5 \times 10^{-3(*)}$ | $1.3 \times 10^{20}$ | 1.9 | 4.0 | [53] |
| $GaInO_3$ | 6450 | $> 90$ | $2.5 \times 10^{-3}$ | $4 \times 10^{20}$ | 10 | 3.3 | [55] |
| $Zn_2In_2O_5$ | 6400 | $> 85$ | $2.9 \times 10^{-4}$ | $6.5 \times 10^{20}$ | 30 | $\sim 3$ | [61] |
| $In_4Sn_3O_{12}$ | $> 6000$ | $> 80$ | $2 \times 10^{-4}$ | $\sim 10^{21}$ | 20 | $> 3.1$ | [54] |

Table 2.The physical properties of some reported n-type transparent conducting oxides. T is transmission in the visible range. Entries marked by an asterisk have been calculated by the author

veloped, $Cd_2SnO_4$ being the most successful to date, however there are others such as $Zn_2SnO_4$ , $MgIn_2O_4$ , $CdSb_2O_6$:Y, $ZnSnO_3$, $GaInO_3$ , $Zn_2In2O5$ , $In_4Sn_3O_{12}$. The properties of these materials are listed in Table 2.

### 1.5.1 Uses of Transparent Conducting Oxides

Transparent conducting oxides are in widespread use in architecture as a coating on windows with the aim of increasing energy efficiency. The low emissivity of some TCO coatings prevent radiative heat loss from windows. The fact that TCOs reflect in the IR spectrum, while being optically transparent, adds to the energy efficiency.

In addition to this, the TCO coatings enable the production of "functional glasses", where properties of the glass, such as its temperature (anti-fogging) or its transparency (privacy windows) may be managed electronically using the conducting properties of the TCO.

The recent boom production of flat panel displays, whether for hand-held computer or high definition TV, has pushed the demand for transparent electrodes. The TCO in a flat panel display serves as a transparent conducting electrode for address-

ing individual pixels on the screen. Transparency coupled with conductivity is vital for the pixel to be addressed while remaining viewable by the user.

### 1.5.2 *p*-type Transparent Conducting Oxides

The TCOs reviewed so far have all been $n$-type conducting oxides. The delevopment of $p$-type transparent conducting oxides ($p$TCOs) would allow the creation of transparent $pn$ junctions when combined with the better known $n$TCOs. This would allow the development of transparent electronics, a field which would have a myriad of applications.

Creating a $p$TCO is not a trivial exercise. There are two main considerations which must be taken into account when choosing a suitable candidate material. An ionic compound will result in the strong localization of holes on the oxygen sites, due to the fact that the $2p$ levels on oxygen atoms are typically far lower than the valence orbitals of metallic atoms[34]. Since the $p$-type material will depend on the mobility of these holes, an ionic compound would require a huge hole concentration to be conductive. Therefore, it would be more appropriate to choose materials with a more covalent bonding of oxygen to minimize these localization effects

In order to ensure this chemical modulation of the valence band, an appropriate crystal structure and cation must be chosen. To preserve the transparency of the material, $d$-$d$ transitions must be avoided, as they absorb in the visible region. Thus, cations with closed $d$-shells (e.g. $Cu^+$, $Ag^+$) are required. The energy-level of the uppermost closed shell of the cation must match closely the energy-level of the $2p$ levels of the oxygen ions, as shown in Fig. 1.9. The resulting bond will be mostly covalent in nature, inhibiting localization around the oxygen ion, providing an antibonding level that will form a valence-band edge.

The energy levels of the $d^{10}$ electrons decrease with increasing atomic number (Fig. 1.9). The oxygen cation would usually sit at around 5 eV. Thus, only a few elements present themselves as possibilities for cations in a candidate material, with $Cu^+$ and $Ag^+$ being the two best ones.

Having selected the cation, a suitable crystal structure must be found. The most successful structure to date has been the delafossite structure, which can be represented by the formula $AMO_2$, where A is a monovalent cation and M is a trivalent cation.

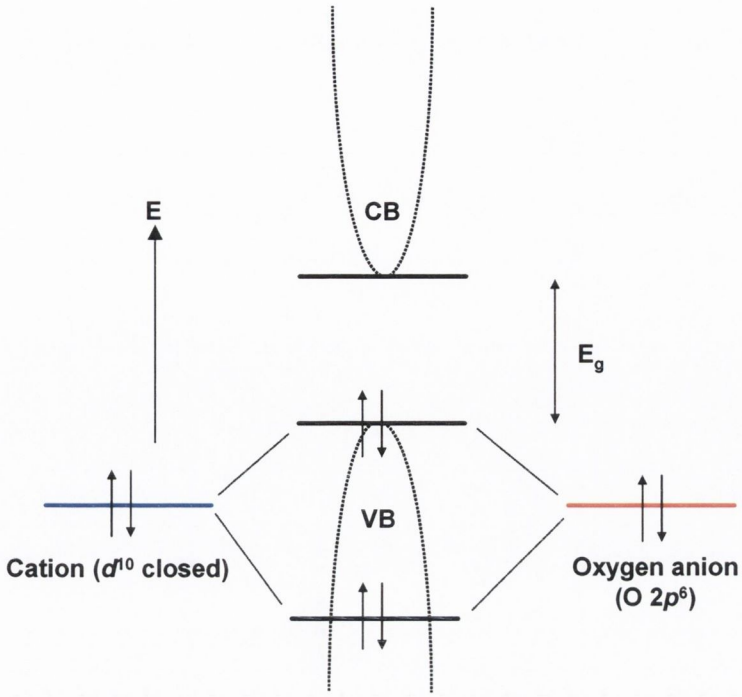



Figure 1.9. Schematic diagram of the energy levels of an ideal $p$TCO, showing the bond between the closed $d$-shell cation and the oxygen anion.

The structure maintains a large distance between the closed-shell A cation and the O anions, while forcing the oxygen ions to bond via $\sigma$ bonds with the coordinating cation. This reduces the localization of the valence band edge. $CuAlO_2$, $CuGaO_2$ and $AgIn(:Sn)O_2$ have been found to be $p$TCOs, all with the delafossite structure.

Other non-delafossite structures such as potassium-doped $SrCu_2O_2$ and nitrogen-doped ZnO have also been successfully demonstrated as $p$-type TCOs. A summary of the electrical properties of these materials is shown in Table 3.

| **Material** | **Resistivity** ($\Omega$ cm) | **Carrier density** ($cm^{-3}$) | **Mobility** ($cm^2 V^{-1} s^{-1}$) | **Bandgap** (eV) | **Ref** |
|---|---|---|---|---|---|
| $CuAlO_2$ | $1 \times 10^0$ | $1 \times 10^{17}$ | 10 | 3.5 | [63] |
| $CuGaO_2$ | $1.5 \times 10^1$ | $1.7 \times 10^{18}$ | 0.2 | 3.6 | [64] |
| $AgIn(:Sn)O_2$ | $1.7 \times 10^{-1}$ | $2.7 \times 10^{19}$ | 0.5 | 4.4 | [62] |
| $Sr(:K)Cu_2O_2$ | $2 \times 10^1$ | $6.1 \times 10^{17}$ | 0.5 | 3.3 | [65] |
| ZnO:N | $3 \times 10^0$ | $1.0 \times 10^{17}$ | 20.8 | 3.27 | [66] |

Table 3.The electrical properties of reported pTCOs

### 1.5.3 Transparent Conducting Oxides in Spin Electronics

Both spin electronics and transparent conducting oxides are growth industries. While spin electronics is pushing boundaries in the way information is processed and

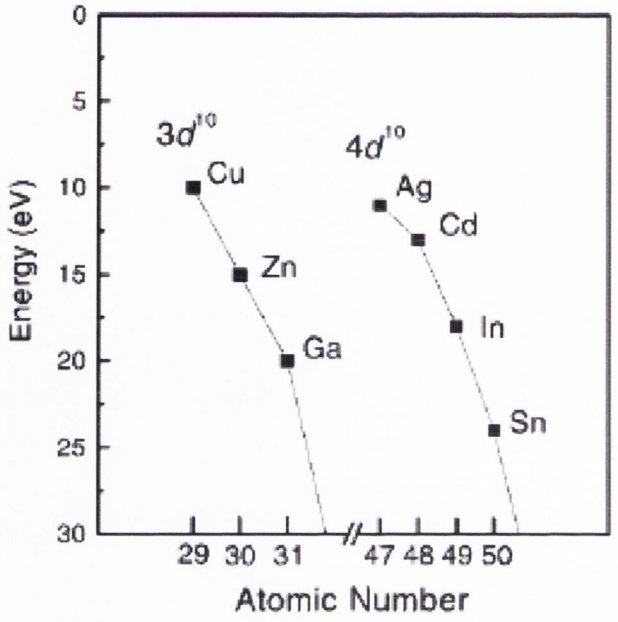



Figure 1.10. A graph showing the change in the energy levels of $d^{10}$ electrons with increasing atomic number. The energies obtained are for neutral atoms (from [62]).

stored, the field of transparent conducting oxides is leading to transparent electronics. Combination of the two fields is a goal for the future.

## 1.6 Intrinsic vs. Extrinsic

There is much debate on the origin of the moment in dilute magnetic semiconductors. The absence of any widely accepted mechanism of high temperature ferromagnetism, the lack of reproducibility and repeatability of the properties of many of these materials, together with the possibility of contamination and impurity phases casts doubt on the claims that the ferromagnetism is a truly intrinsic property of these materials.

### 1.6.1 The "syndrome"

In an effort to identify semiconductors (and insulators) which exhibit true ferromagnetism, Coey et al. [35] described a "syndrome" to distinguish the behaviour of these materials:

1. The oxides are n-type. They may be partially compensated.
2. They have high dielectric constants.
3. The ferromagnets may be degenerate semiconductors, or else exhibit activated

conduction.

4. The ferromagnetism is present at concentrations that lie far below the percolation threshold $x_p$ associated with nearest-neighbour cation coupling.

5. The average moment per transition-metal cation $m_c$ approaches (or even exceeds) the spin-only moment at low concentrations x of magnetic cations. It falls progressively as x increases towards $x_p$.

6. The moment is often anisotropic relative to the plane of the thin film; it does not scale with film thickness.

7. Properties vary greatly for samples of the same nominal composition prepared by different methods, or by different groups.

### 1.6.2 $d^0$ Ferromagnetism

The discovery of $d^0$ ferromagnetism [36] has lent its weight to the case for an intrinsic moment in room temperature magnetic semiconductors. Traditional ferromagnets have been based on elements with partially filled $d$ or $f$-shells or bands (besides a few exceptions, which are explainable by weak itinerant ferromagnetism [67]) - i.e. the presence of a "magnetic atom" is essential for the development of a ferromagnetic moment. A $d^0$ ferromagnet, conversely, exhibits ferromagnetism without the presence of a magnetic atom. Reported examples of this include carbon, $HfO_2$ [37], alkaline-earth hexaborides [38] and some dilute ferromagnetic oxides doped with non-magnetic cations. While dilute ferromagnetic oxides are often doped with magnetic $3d$ dopants, there have been reports of ferromagnetism in oxides doped with non-magnetic ($d^0$) atoms [17], and dilute oxide ferromagnets where the dopant seems to play no rôle in the coupling mechanism.

$d^0$-ferromagnetism is a phenomenon that is very much debated at present. While there are a growing number of reports of observation of $d^0$-ferromagnetism, whether or not it is termed so, there are also a number of contradicting reports which attribute the observed moments to impurity phases [39] and external contamination [40][41].

### 1.6.3 Impurity Phases

As the dopants involved in DMS materials are often magnetic cations with a net spin, it must be observed that these dopant ions may segregate into magnetic impurity

phases. These segregates may be metallic clusters of the dopant metal, such as Co clusters in Co-doped $TiO_2$ [42], a magnetic oxide of the dopant such as $Fe_3O_4$ in Fe-doped $TiO_2$ [39], inverse-doped oxide of the dopant [43] or a magnetic alloy of the dopant ion with atoms of the host matrix, such as $Mn_4N$ in GaMnN [44].

A significant observation of ferromagnetism should be qualified by the absence of ferromagnetic phases which can quantitatively explain the observed ferromagnetic moment.

### 1.6.4 Methods of Determination

Owing to the continued debate over the origins of ferromagnetism in the materials described above, it has become increasingly important to be able to determine when a ferromagnetic moment is due to the material itself, or an impurity phase.

What follows is a short summary of a few of these techniques which can, when used in combination, be used to identify a true dilute magnetic semiconductor/$d^0$ ferromagnet. The physics and mechanics of these experimental techniques will be discussed at length in Chapter 2 (with the exception of magneto-optical measurements).

#### 1.6.4.1 Magnetization measurements

The first experiment to perform is a magnetization measurement, in order to confirm that the material itself is ferromagnetic. However, owing to the fact that the ferromagnetic signals of all components of the sample, be they intrinsic or extrinsic, are all integrated in the measurement. Resonance and spectroscopic magnetic measurement can detect moments due to metallic precipitates, but are unable to differentiate magnetic signals due to impurity phases with similar chemical states [14].

Magnetic anisotropy, the difference in the ferromagnetic signal depending on sample orientation with respect to the applied field, is an indication of *intrinsic* ferromagnetism, insofar as it is not an expected property of clusters of a ferromagnetic impurity phase. However, such measurements must be performed with due consideration to the effect that sample size, position and shape may have on magnetic measurements [69].

The temperature dependence of the ferromagnetism is a possible way to identify the impurity content and its contribution to the ferromagnetism of the sample probed. Each ferromagnetic material has a Curie temperature, $T_C$, above which it no longer exhibits ferromagnetic behaviour. Reduction or extinction of ferromagnetic behaviour

at or around the $T_C$ of a well known magnetic phase in a sample may indicate that any moment in the sample may be explainable by that phase. If the host material is not stable at elevated temperatures, this method is of limited use.

Magnetization versus temperature M(T) measurements can also provide more information. Irreversibility between the zero-field-cooled (ZFC) and field-cooled (FC) processes may be an indication of the presence of a spin-glass or superparamagnetic phase.

#### 1.6.4.2 Magneto-transport measurements

The Hall resistivity of semiconductor may be expressed in the form

$$\rho_{xy} = R_0 B + R_S \mu_0 M$$

where $M$ is the magnetization of the sample. Thus a superimposed Hall resistivity co-ordinated to the ferromagnetic reponse of the material is an indication of spin polarization of the charge carrier, which is a strong indication of intrinsic ferromagnetism. However, the Hall effect is far from a conclusive test for intrinsic ferromagnetism. It has been shown [42] that the anomolous Hall effect may be observed in a material with impurity clusters, with the effect being due to current injection from the individual magnetic clusters under an electric field demanding that a Hall voltage be set up by the host matrix to preserve current continuity.

#### 1.6.4.3 Magneto-optical measurements

Another method of oberving spin-split charge carriers is by the observation of magneto-optical effects. Magnetically induced circular dichroism (MCD), is the differential absorption of left and right circularly polarized light in the presence of a magnetic field. The magnetic field breaks the degeneracy of the spin states and thus preferential observation is observed for spin-split charge carriers. The proportionality of the MCD signal to the derivative of the absorption with respect to the photon energy allows the identification of the origin of the spin-splitting. A disparity between the MCD and the absoption spectra may indicate that the source of the ferromagnetism may be extrinsic.

#### 1.6.4.4 Mössbauer measurements

Mössbauer spectroscopy enables the direct probing of (primarily) Fe- and Sn-atoms in a material. It allows measurement of oxidation state, electric field gradient and hyperfine field at the $^{57}$Fe- or $^{119}$Sn- atom itself. From these parameters many things may be inferred, but of primary interest for this study is the fact that the hyperfine parameter allows an iron phase to be identified and quantified.

A major drawback of the Mössbauer technique is that due to the limited number of Mössbaur transitions, it may only be applied to 14 transition group elements, and 9 main group elements. The relatively short lifetime of many of the parent sources mean that $^{57}$Fe and $^{119}$Sn are the two most successful and common resonances used, with Fe taking precedence due to its ubiquitousness. The expense of doping with isotope enriched material is also an inhibitive factor.

#### 1.6.4.5 X-ray diffraction

The presence of impurity phases may be also detected by the use of x-ray diffraction (XRD). This is the primary measurement on any sample. The lattice spacings of any impurity phases will produce peaks, and the area of these peaks will give a measure of the amount of material present. The width of the peaks also give an estimation of the average crystallite dimension of the impurity phase. Substitutional site doping may also be inferred from lattice expansion or contraction, which can be observed in systematic x-ray diffractograms.

This technique, however, does not provide any magnetic information. The background noise levels can also obscure peaks of the size that would be expected for impurity phases due to small doping levels ($< 5\%$). This problem can be further compounded by fact that the most commonly used radiation energy (Cu $K_{\alpha_1}$) causes elements in the middle of the transition block (Fe, Co, Ni) to fluoresce, adding to the background noise.

# References

[1] G. Moore, "Cramming more components onto integrated circuits", Electronics Magazine, 19 April (1965)

[2] N. F. Mott, Proc. R. Soc. 153, 699 (1936)

[3] P. Grünberg, R. Schreiber, Y. Pang, M. B. Brodsky and H. Sowers, Phys. Rev. Lett. 57, 2442 (1986)

[4] S. S. P. Parkin, N. More and J. Chazelas, Phys. Rev. Lett. 61, 2472 (1988)

[5] S. S. P. Parkin, C. Kaiser, A. Panchula, P. M. Rice, B. Hughes, M. Samant, and S. H. Yang, Nature Mater. 3, 862 (2004)

[6] J. D. Solier, I. Cachadiña, and A. Dominguez-Rodriguez, Phys. Rev. B 48, 3704–3712 (1993)

[7] H. Ohno, A. Shen, F. Matsukura, A. Oiwa, A. Endo, S. Katsumoto, and Y. Iye, Appl. Phys. Lett. 69, 363 (1996)

[8] T. Dietl, H. Ohno, F. Matsukura, J. Cibert, and D. Ferrand, Science 287, 1019 (2000)

[9] A. M. Nazmul and S. Sugahara, Phys. Rev. B 67, 241308 (2003)

[10] H. Ohno, J. Cryst. Growth 251, 285 (2003), H. Ohno, F. Matsukura and Y. Ohno, Jap. Soc. Appl. Phys. Int. 5, 4 (2002)

[11] S. Sonada, S. Shimizu, T. Sasaki, Y. Yamamoto, and H. Hori, J. Cryst. Growth 237-239, 1358 (2002)

[12] A. Ney, R. Rajaram, E. Arenholz, J.S. Harris, Jr., M. Samant, R.F.C. Farrow and S.S.P. Parkin, J. Magnetism Mag. Mat. 300, 7 (2006)

[13] Sunglae Cho, Sungyoul Choi, and Soon Cheol Hong, Yunki Kim and John B.

Ketterson, Bong-Jun Kim and Y. C. Kim, Jung-Hyun Jung, Phys. Rev. B 66, 033303 (2002)

[14] T . Fukumura, H. Toyosaki and Y. Yamada, Semicon. Sci. Technol. 20, S103-S111 (2005)

[15] A. A. Ashrafi, A. Ueta, H. Kumano and I. Suemune, J. Cryst. Growth 221, 435-439 (2000)

[16] T. Fukumura, Z. Jin, A. Ohtomo, H. Koinuma M. and Kawasaki, Appl. Phys. Lett. 75, 3366 (1999)

[17] M. Venkatesan, C.B. Fitzgerald, J.G. Lunney and J.M.D. Coey, Phys. Rev. Lett. 87, 026601 (2004)

[18] Y. Matsumoto, M. Murakami, T. Shono, T. Hasegawa, T. Fukumura, M. Kawasaki, P. Ahmet, T. Chikyow, S. Koshihara and H. Koinuma, Science 291, 854 (2001)

[19] J. Z. Wang, J. K. Tang , H. G. Zhang, V. Golub, L. Spinu and L. Tung, J. Appl. Phys. 95, 7381 (2004)

[20] N. Y. H. Hong, J. Sakai and A. Hassini, Appl. Phys. Lett. 84, 2602 (2004)

[21] Z. J. Wang, J. K. Tang, L. D. Tung, W. L. Zhou, L. Spinu, J. Appl. Phys. 93, 7870 (2003)

[22] N. H. Hong, W. Prellier, J. Sakai and A. Hassini, Appl. Phys. Lett. 84, 285 (2004)

[23] S. B. Ogale, R. J. Choudhary, J. P. Buban, S. E. Lofland, S. R. Shinde, S. N. Kale, V. N. Kulkarni, J. Higgins, C. Lanci, J. R. Simpson, N. D. Browning, S. Das Sarma, H. D. Drew, R. L. Greene and T Venkatesan, Phys. Rev. Lett. 91, 077205 (2003)

[24] C. B. Fitzgerald, M. Venkatesan, A. P. Douvalis, S. Huber, J. M. D. Coey and T. Bakas, J. Appl. Phys. 95, 7390 (2004)

[25] C. B. Fitzgerald, M. Venkatesan, L. S. Dorneles, R. Gunning, P. Stamenov, J. M. D. Coey, P. A. Stampe, R. J. Kennedy, E. C. Moreira, U. S. Sias, Phys. Rev. B 74, 115307 (2006)

[26] J. He, S. Xu, Y. K. Yoo, Q. Xue, H.-C. Lee, S. Cheng, X.-D. Xiang, G. F. Dionne, and I. Takeuchi, Appl. Phys. Lett. 86, 052503 (2005)

[27] J. Philip, A. Punnoose, B.I. Kim, K.M. Reddy, S. Layne, J.O. Holmes, B. Satpati, P.R. Leclair, T.S. Santos, J.S. Moodera, Nature Materials 4, 298-304 (2006)

[28] G. Peleckis, X. Wang, and S. X. Dou, Appl. Phys. Lett. 89, 022501 (2006)

[29] G. Peleckis, X. Wang, and S. X. Dou, Appl. Phys. Lett. 88, 132507 (2006)

[30] J. Philip, N. Theodoropoulou, G. Berera, J. S. Moodera, and B. Satpati, J, Appl. Phys. Lett. 85, 777 (2004)

[31] H. S. Kim, S. H. Ji, H. Kim, S.-K. Hong, D. Kim, Y.E. Ihm and W. K. Choo, Solid State Communications 137, 41 (2006)

[32] K. L. Chopra, S. Mayor and D. K. Pandya, Thin Solid Films 102, 1 (1983)

[33] J. L. Vossen, Phys. Thin Films 9, 1 (1977)

[34] S. Fraga, J. Karwowski, and K.M.S. Saxena, Handbook of Atomic Data (Elsevier, Amsterdam, 1976) p. 259

[35] J. M. D. Coey, M. Venkatesan and C. B. Fitzgerald, Nature Materials 4, 173 (2005)

[36] J.M.D. Coey, Solid State Sciences 7, 660-667 (2005)

[37] M. Venkatesan, C.B. Fitzgerald and J.M.D. Coey, Nature 430, 630 (2004)

[38] D. P Young, D. Hall, M.E. Torelli, Z. Fisk, J.L. Sarrao, J.D. Thompson, H.R. Ott, S.B. Oseroff, R.G. Goodrich and R. Zysler, Nature 397, 412 (1999)

[39] Y.J. Kim, S. Thevuthasan, T. Droubay, A.S. Lea, C.M. Wang, V. Shutthanandan, S.A. Chambers, R.P. Sears, B. Taylor and B. Sinkovic, Appl. Phys. Lett. 84, 3531 (2004)

[40] Y. Belghazi, G. Schmerber, S. Colis, J. L. Rehspringer, A. Dinia, and A. Berrada, Appl. Phys. Lett. 89, 122504 (2006)

[41] D.W. Abraham, M.M. Frank and S. Guha, Appl. Phys. Lett., 87, 252502 (2005)

[42] S. R. Shinde, S. B. Ogale, J. S. Higgins, H. Zheng, A. J. Millis, V. N. Kulkarni, R. Ramesh, R. L. Greene, and T. Venkatesan, Phys. Rev. Lett. 92, 166601 (2004)

[43] D. C. Kundaliya, S. B. Ogale, S. E. Lofland, S. Dhar, C. J. Metting, S. R. Shinde, Z. Ma, B. Varughese, K. V. Ramanujachary, L. Salamanca-Riba, and T. Venkatesan, Nat. Mater. 3, 709 (2004)

[44] S. J. Pearton, C. R. Abernathy, D. P. Norton, A. F. Hebard , Y. D. Park , L. A. Boatner and J D Budai Mater.Sci.Eng. R 40 137 (2003)

[45] Ç. Kiliç and A. Zunger, Phys. Rev. Lett. 88, 095501 (2002)

[46] A. Bhardwaj, B. K. Gupta, A. Raza, A. K. Sharma, O. P. Agnihotri, Solar Cells 5, 39-49 (1981)

[47] C. Terrier, J. P. Chatelon, R. Berjoan and J. A. Roger, Thin Solid Films 263, 37-41 (1995 )

[48] D. Burgard, C. Goebbert and R. Nass, Jour. Sol-Gel Sci. Tech. 13, 789-792 (1998)

[49] D. S. Ginley and C. Bright, MRS Bull. 25, 15 (2000)

[50] X. Wu, P. Sheldon, T.J. Coutts, D.H. Rose, H.R. Moutinho, Proc. $26^{th}$ IEEE

Photovoltaic Spec. Conf., 347-350 (1997)

[51] O. Kluth, C. Agashe, J. Hüpkes, J. Müller and B. Rech, Proc. $3^{rd}$ World Conf. Photovoltaic Energy Conv., 1800 (2003)

[52] S. E. Dali, M. Jayachandran and M. J. Chockalingam, Journal of Materials Science Letters 18, 915-917 (1999)

[53] K. Yanagawa, Y. Ohki, T. Omata, H. Hosono, N. Ueda and H. Kawazoe, Appl. Phys. Lett. 65, 406 (1994)

[54] T. Minami, Y. Takeda, S. Takata and T. Kakumu, Thin Solid Films 308-309, 13-18 (1997)

[55] J. M. Phillips, J. Kwo, G. A. Thomas, S. A. Carter, R. J. Cava, S. Y. Hou, J. J. Krajewski, J. H. Marshall, W. F. Peck, D. H. Rapkine and R. B. van Dover, Appl. Phys. Lett. 65, 115 (1994)

[56] A. Maldonado, M. Olvera, S. Tirado Guerra, R. Asomoza, Sol. energy mater. sol. cells 82, 75-84 (2004)

[57] A. Guillén-Santiago, M. de la L. Olvera, A. Maldonado, A. Reyes, R. Asomoza, phys. stat. sol. a 191, 499 (2002)

[58] J.D. Perkins, J.A. del Cueto, J.L. Alleman, C. Warmsingh'. B.M. Keyes. L.M. Gedvilas, P.A. Parilla. X. Li, E. To, D.W. Readey', M. Van He&, and D.S. Ginley, Proc. $29^{th}$ IEEE Photovoltaic Spec. Conf., 1126 (2002)

[59] M. Orita, H. Tanji, M. Mizuno, H. Adachi, I. Tanaka, Phys. Rev. B 61, 1811–1816 (2000)

[60] A. Wang, J. R. Babcock, N. L. Edleman, A. W. Metz, M. A. Lane, R. Asahi, V. P. Dravid, C. R. Kannewurf, A. J. Freeman, and T. J. Marks, Proc. Nat. Acad. Sci.

98, 7113-7116 (2001)

[61] T. Minami, T. Kakumu, Y. Takeda and S. Takata, Thin Solid Films 317, 326-329 (1998)

[62] H. Kawazoe, H. Yanagi, K. Ueda, and H. Hosono, MRS Bull. Aug 2000, 28 (2000)

[63] H. Kawazoe, M. Yasukawa, H. Hyodo, M. Kurita, H. Yanagi, and H. Hosono, Nature 389, 939 (1997)

[64] H. Yanagi, H. Kawazoe, A. Kudo, M. Yasukawa, and H. Hosono, J. Electroceram. 4, 427 (2000)

[65] A. Kudo, H. Yanagi, H. Hosono, and H. Kawazoe, Appl. Phys. Lett. 73, 220 (1998)

[66] M.-L. Tu, Y.-K. Su, and C.-Y. Ma, J. Appl. Phys. 100, 053705 (2006)

[67] P. Fulde, Electron Correlations in Molecules and Solids, Springer-Verlag, Berlin (1995)

[68] T.L. Makarova, Semiconductors 38, 615 (2004)

[69] P. Stamenov, J. M. D. Coey, Rev. Sci. Instrum. 77, 015106 (2006)

# Chapter 2

# Experimental Procedures

"Experience does not ever err; it is only your judgement that errs in promising itself results which are not caused by your experiments"

Leonardo da Vinci

## 2.1 Sample Preparation

### 2.1.1 Ceramic Target Production

The ceramic targets were made by sintering pellets of mechanically mixed high-purity oxide powders. The purity of the starter materials, and their sources, are detailed in Table 4. The mixing process was carried out by hand in an agate mortar and pestle which was cleaned thoroughly before and after use with aqua regia, then an acid that any material used in the previous mixing is known to be soluble in, acetone and finally isopropanol. The pellets were sintered in air for 12 hours at a temperature of 1250 K. To avoid contamination, the pellets were handled using plastic tweezers.

| Material | Use | Source | Purity | Catalogue Number |
|---|---|---|---|---|
| $TiO_2$ | Host | Aldrich | 99.999% | 204730-25G |
| ZnO | Host | AlfaAesar | 99.9995% | 012855 |
| $In_2O_3$ | Host, dopant | Aldrich | 99.999% | 203424-25G |
| C (graphite) | Host | Aldrich | 99+% | 28,286-3 |
| C (graphite) | Host | AlfaAesar | 99.9999% | 014734 |
| $SnO_2$ | Dopant | Aldrich | 99.99+% | 204714-5G |
| $Fe_2O_3$ | Dopant | Aldrich | 99.999% | 529311-5G |
| $V_2O_5$ | Dopant | Sigma-Aldrich | 99.99% | 204854-5G |
| $Cr_2O_3$ | Dopant, host | Aldrich | 99.995% | 20,306-8 |
| $^{57}Fe_2O_3$ | Dopant | AMT, Israel | 99.97% | n/a |
| $MnO_2$ | Dopant | Aldrich | 99.99% | 20,375-0 |
| NiO | Dopant | Sigma-Aldrich | 99.999% | 481793-25G |
| $Al_2O_3$ | Dopant | Aldrich | 99.998% | 202606-5G |

Table 4.A list of materials used for ceramic target preparation, quoting their sources and purity

### 2.1.2 Pulsed Laser Deposition

The thin films were produced using PLD (Pulsed Laser Deposition). The process was first used in 1987 to grow high-$T_C$ superconductors. In this process, the ceramic

targets are ablated by a laser [1]. The photon interaction with the ceramic target ejects a plasma plume. A subtrate is placed a short distance (3.5 cm for all the films produced in this thesis) from the target. The plume deposits on to this substrate and a thin film is formed on the surface of the substrate. The plume is stoichometrically similar to the target, and so thin films of roughly the same composition of the target can be easily produced.

The main components of a PLD system are the laser, the chamber and the optics. The laser used in this thesis is a KrF excimer laser (Lamda Physik Compex PRO 102), with a wavelength of $\lambda = 248\,\text{nm}$. The energy of the beam can range from $100 - 450\,\text{mJ}$ per pulse. The vacuum chamber has a base pressure of $5 \times 10^{-6}\,\text{mbar}$ and can be partially filled with oxygen or nitrogen to allow deposition at higher pressures. The optics focus the beam to a spot $4\,\text{mm}^2$ in area inside the chamber (from an initial beam spot size of $240\,\text{mm}^2$ outside the chamber), losing 40-60% of the beam energy in the process. As a result, fluences of typically $1 - 5\,\text{J}\,\text{cm}^{-2}$ are incident upon the target. The repetition rate varied between 1 and 20 Hz. The nominal FWHM of the pulse duration for this laser is 25 nm. A photo of the plume generated is shown in Fig. 2.11.

In-situ measurement of the thicknesses of the thin films is achieved by optical reflectometry [1], using a laser of wavelength $\lambda = 645\,\text{nm}$. Using the interference pattern between the beam reflected the film surface and that reflected from the film/substrate interface, the thickness of the film can be monitored. The thicknesses are calibrated by measuring the thickness of a film less than 100 nm using x-ray reflectometry, which will be mentioned later in the chapter.

## 2.2 Structural Characterization

### 2.2.1 X-ray Diffraction (XRD)

Both a Philips X'Pert Pro and a Siemens D500 powder diffractometer were used to characterise the structure of the materials by X-ray diffraction. This technique uses the diffraction of x-ray to determine the spacing between parallel planes of atoms in a crystal. From these inter-planar distances the crystal structure can be deduced.

The radiation used has a wavelength of the order of an angstrom, which is also the order of magnitude of the separation of atoms, which allows all spacings to be

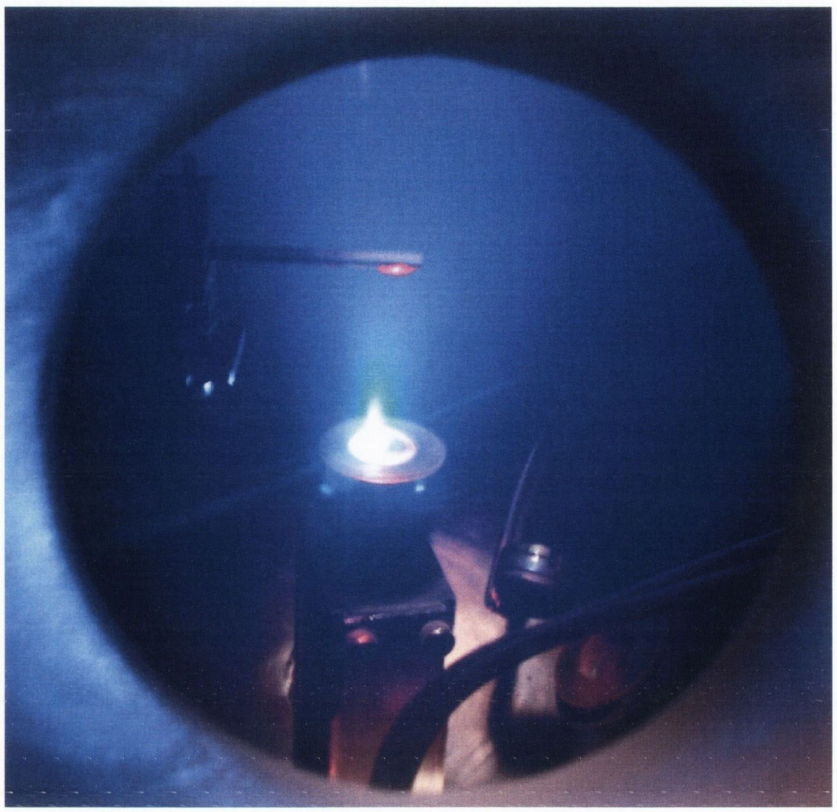


Figure 2.11. A photograph showing the laser ablating the ceramic target, producing a plasma plume. The substrate is 3.5 cm above the target

probed. Both diffractometers use Cu $K_{\alpha 1}$ which has a wavelength $\lambda = 1.54056\,\text{Å}$.

X-rays irradiate the sample at an angle $\theta$ to the surface plane of the sample. A detector is rotated to $\pi - \theta$ and collects the intensity of the diffracted x-rays. The x-rays are diffracted when the Bragg condition, $n\lambda = 2d\sin\theta$, is satisfied as shown in fig.2.12.

Hence, a peak in intensity represents a $d$-spacing. Since the powder of the sample is randomly orientated, statistics dictate that each crystal plane will have some fraction parallel to the sample surface. The Bragg condition will only be satisfied for one incident angle for each inter-planar distance.

In addition to crystal structure and preferential orientation, XRD can be used to estimate the crystallite size of the sample probed using the Scherrer forumla:

$$D_v = \frac{K \cdot \lambda}{\beta \cdot \cos\theta} \tag{14}$$

where $D_v$ is the dimension of the crystal (i.e. the crystal size), $K$ is a shape factor, ranging from 0.7 to 1.2 - usually taken as 0.9, and $\beta$ is the full width at half maximum

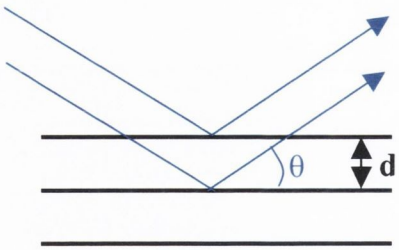



Figure 2.12. Schematic drawing of Bragg reflection.

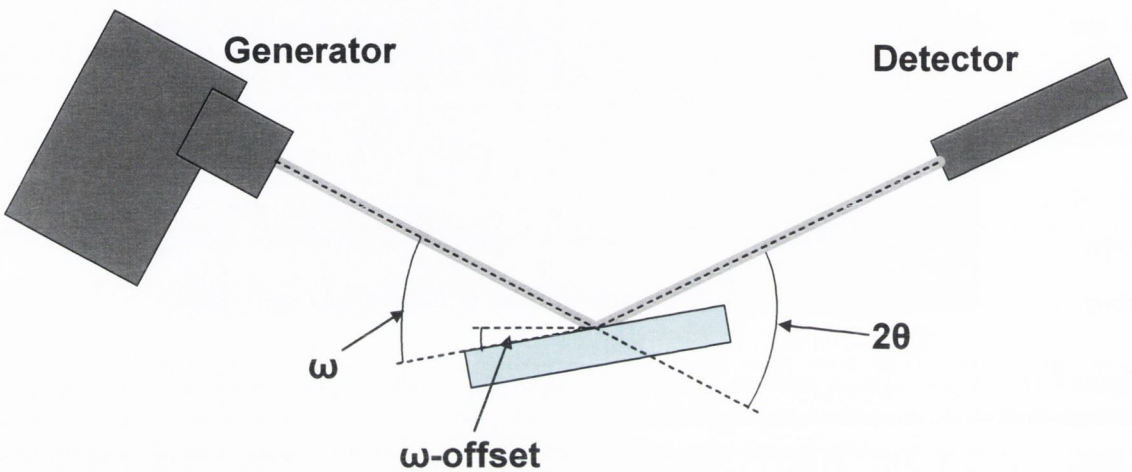



Figure 2.13. The $\omega$-scan. The angle $2\theta$ is kept fixed and the angle $\omega$ is scanned. Fixing $2\theta$ allows only one value of lattice spacing $d$ to cause Bragg refraction, therefore the orientation of a selected lattice plane is measured.

of the peak(s) due to the phase being investigated.

To investigate how orientated the crystallites in a sample are, *omega* scans are used. An omega scan keeps the angle $2\theta$ fixed, thereby satisfying the Bragg condition for only one $d$-spacing - locking the scan to only one lattice plane. The angle between the sample and the generator is then rotated. The FWHM of the subsequent curve gives a measure of orientation of the crystal.

### 2.2.2 X-ray Reflectivity (XRR)

While thickness is monitored during deposition using optical reflectivity, x-ray reflectivity, performed in a Philips X'Pert Pro, is also used for absolute thickness measurements on samples thinner than 150 nm. XRR also has the advantage of being able to indirectly measure the surface and interface roughnesses of the films. The ac-

curacy of these roughness measurements has been verified using AFM (atomic force microscopy) measurements.

XRR depends on the fact that for x-rays, the index of refraction, $n$, is less than one. Thus at a critical angle, total internal refraction occurs for the x-ray beam passing from the ambient medium (air) into the thin film, giving the illusion of reflection (*refraction* from the surface, not reflection is observed). The complex index of refraction, $n$, is given by:

$$n = 1 - \delta + i\beta \tag{15}$$

where $\delta$, the dispersion, is given by

$$\delta = \frac{r_e \lambda^2}{2\pi} n_e \tag{16}$$

where $r_e$ is the classical electron radius, $n_e$ is the electron density and $\lambda$ is the wavelength of radiation. The electron density, $n_e$ can be written as

$$n_e = N_A \frac{Z - f'}{A} \rho \tag{17}$$

where $N_A$ is Avogadros number, $A$ is the atomic weight, $Z$ is the number of electrons per atom and $f'$ is a correction term due to the x-ray absorption edge. The dispersion, $\delta$, is a positive number of the order $10^{-5} - 10^{-6}$, while the absorption is usually smaller by one or two orders of magnitude. The dispersion can be related to the mass density of the material. This allows us to then relate the critcal angle, $\theta_c$, where the beam first begins to penetrate the film, to the mass density, $\rho$, of the film since, neglecting $\beta$,

$$\begin{aligned} 1 - \delta &\approx n_1 \\ \cos\theta_c &= n_1 / n_{air} \\ 1 - \frac{\theta_c^2}{2} &\approx 1 - \delta_{TIT} \end{aligned} \tag{18}$$

The dispersion at the critical angle, $\delta_{TIT}$, is given by

$$\delta_{TIT} = \frac{\theta_c^2}{2} = \left( \frac{r_e}{2\pi} N_A \frac{Z - f'}{A} \right) \rho \lambda^2 \tag{19}$$

Thus, we can determine the mass density of the material. The Kiessig fringes that result from interference after the beam has penetrated the sample can be used to determine the thickness, using the equation:

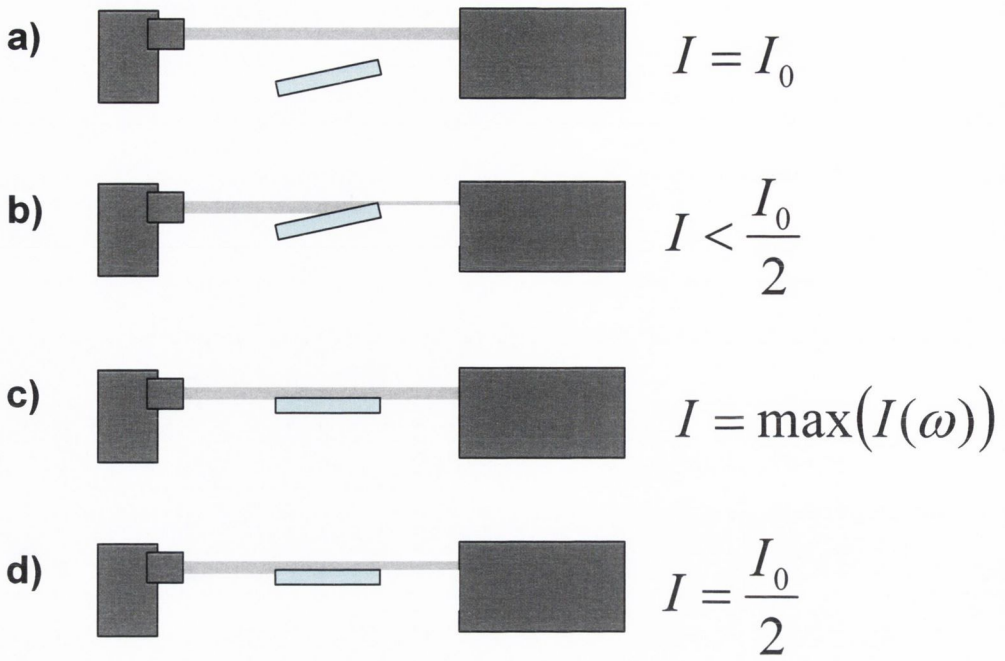



Figure 2.14. The method for alignment for an XRR measurement. The grey box on the left is the x-ray generator, the box on the right represents the detector, with the grey strip representing the x-ray beam. The sample is the rectangle in the centre.

$$\alpha_m^2 = \alpha_c^2 + m^2 \frac{\lambda^2}{4t^2} \tag{20}$$

where $t$ is the thickness of the film and $m$ is the order of the fringe and $\alpha_m$ is position of the fringe in radians. Surface roughness of the films can also be determined by modelling the extinction of the reflected intensity and the attenuation of the Kiessig fringes.

In practice, the x-ray generator and the detector are positioned into a straight through position (i.e. $2\theta = 0$) and the intensity measured (Fig. 2.14a). The sample is raised until the beam's intensity is reduced to less than half its initial value (Fig. 2.14b). The sample is rotated through $\omega$, the angle the surface makes with the beam, until the intensity is at a maximum (Fig. 2.14c). The sample surface is then parallel to the beam. The sample is raised again until the intensity is half the initial intensity (Fig. 2.14d). The beam is thus aligned to the beam and bisecting it. A $\theta - 2\theta$ measurement is then performed from $0 - 3\,^\circ$. The intensity curves are modelled using IMD[2], a freeware program available on the internet that calculates optical properties of a multilayer structure and fits using a least squares method.

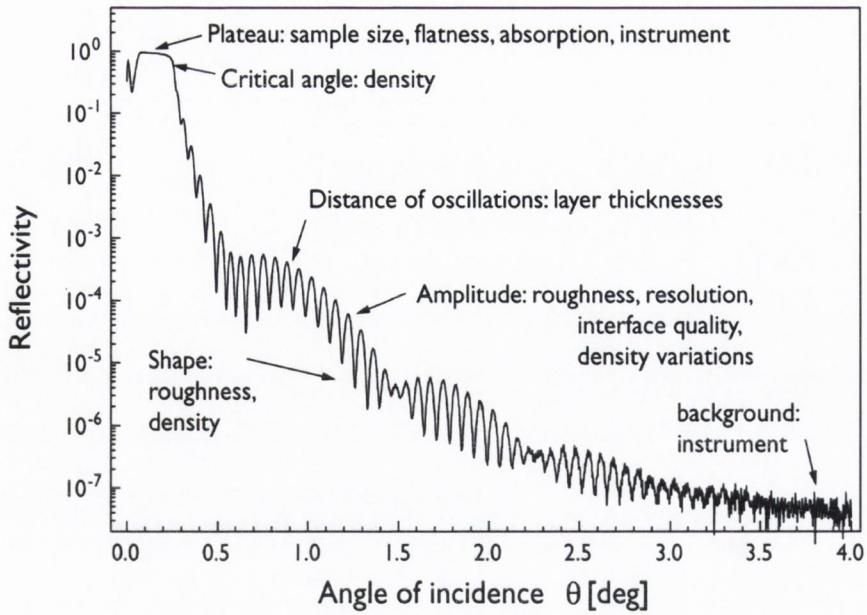



Figure 2.15. A sample x-ray reflectivity curve with its features highlighted and their sources explained (from Philips/Panalytical).

### 2.2.3 Morphology

Morphology of the samples was studied using an optical microscope adapted for use with a digital camera or a scanning electron microscope. The scanning electron microscope accelerates electrons that have been generated by heating a tungsten filament through a many kilovolt potential. The electrons are focused to a beam by magnetic lenses and irradiated onto the sample. The electrons interact with the sample under investigation and backscattered and secondary electrons are emitted. These electrons can be used to image the surface in question. The SEM used in this study was the Hitachi S-3500N Variable Pressure SEM in the Centre for Microscopic Analysis in Trinity College Dublin.

A variable pressure SEM was used for this study to avoid charging of the sample surfaces since many of the sample are insulators. When gas molecules in the sample chamber are struck by the electron beam, the gas is ionized. These positive ions are attracted to and neutralize the negative charge building up on a nonconductive specimen. By controlling the pressure in the sample chamber, the number of gas molecules intercepting the electron beam is maintained at a level that is sufficient to prevent charging, but does not deflect the beam sufficiently to prevent imaging and

microanalysis.

### 2.2.4 FTIR spectroscopy

Fourier Transform Infra-Red spectroscopy can be used to identify the bond type that exists between atoms in a sample. It uses a heated ceramic (at around 1300 K) as a source of radiation. It is important to note the radiation is not monochromatic. The radiation is passed through an interferometer. The interferometer splits the light into two beampaths - one slightly longer than the other - and recombines them afterwards. The path difference is modulated with time. The path difference means that light of different wavelength arrives at a different phase of its wave an so a frequency-dependent interferogram is created. This beam is passed through the sample, and the sample absorbs wavelengths that correspond to bond energies in the sample. After the beam has passed through the sample, it is analysed by a detector, which records the post absorption energy versus time. The interferogram is passed through a fast fourier transform

$$A(r) = \sum X(k) \exp\left(-2\pi \frac{irk}{N}\right) \tag{21}$$

to reconstitute the beam in terms of energy absorption against frequency. Certain bond types between atoms have characteristic spectra that can be overlapped with varied intensities and compared to the spectrum produced. From this the bond types and their relative abundances can be estimated.

The measurements in this thesis were carried out using a Nicolet Nexus FTIR in the Materials Ireland Polymer Research Centre in Trinity College Dublin with the assistance of Dr. Manuel Rüther.

### 2.2.5 Optical Spectroscopy

Optical spectrometry measurements were performed using a dual-beam PerkinElmer Lambda 900 spectrophotometer, which measures transmission for wavelengths ranging from $180 - 3300$ nm. The signal difference between the two arms is first balanced by measuring the transmission with the sample holders in place, but without any sample. The transmission detected at both arms is then set to be equal. To obtain a background reading for the effect the subtrate has on the transmittance, a blank substrate is loaded in the sample and blank sample beam paths and the transmittance measured.

Then, a blank substrate is then loaded in one beampath as a reference sample, with the film and substrate in the second beampath. In this way the transmission of the film is obtained, although a correction needs to be made for reflections from the additional interface. Measurements were typically range from 200 nm to 1500 nm ($\approx 5 - 0.8$ eV).

## 2.3 Magnetic Measurements

### 2.3.1 Vibrating Sample Magnetometry (VSM)

Room temperature magnetisation measurements were taken by vibrating sample magnetometry. The applied field (of up to 1.1 T) was created in the bore of two concentric Hallbach cylinders, which could be varied by rotating the cylinders with respect to each other.

The magnetisation of the sample when vibrated at a frequency of 29.4 Hz induces a voltage in a set of pick-up coils, which are also located inside the bore. The voltage is given by Faraday's Law.

$$V = -\frac{d\Phi}{dt}$$

The voltage obtained is referenced against that of a known calibration sample (Ni sphere) and the magnetisation deduced. The saturation magnetization of the nickel sphere is 55.86 A m$^2$ kg$^{-1}$.

### 2.3.2 Superconducting Quantum Interference Device Magnetometry (SQUID Magnetometry)

The SQUID performs a similar function to the VSM, but with the added advantages that it is more sensitive than the VSM and the measurements can be performed at temperatures of $2 - 300$ K.

For the majority of the magnetization measurements, the SQUID was used in Reciprocating Sample Option (RSO) mode. In an RSO measurement, the sample is moved rapidly and sinusoidally throught the SQUID pickup coils by a high-quality servo motor. The sample position is recorded in synchronicity to the SQUID signal acquisition and the data is then analysed and fitted to the response of an ideal dipole by a least-squares fitting routine. The physical principle is the same as the vibrating sample method previously mentioned, but the coils are superconducting and are attached to the SQUID (a superconducting loop interrupted by Josephson Junctions).

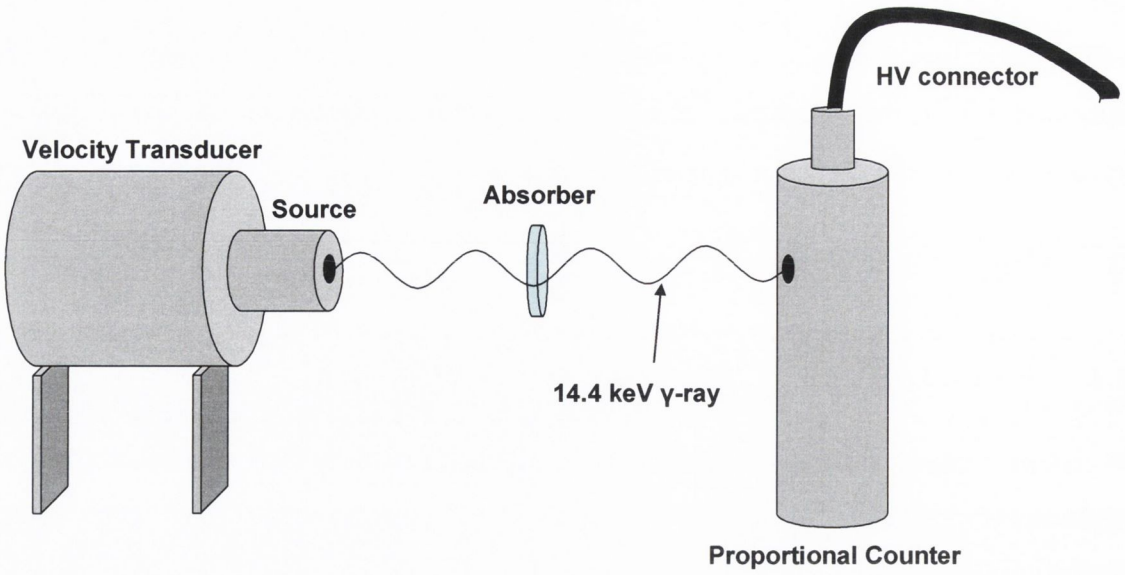



Figure 2.16. Diagramatical representation of a transmission Mössbauer set-up, including the drive unit (left), a thin absorber (middle) and a proportional counter (right).

The output voltage of the SQUID is proportional to the moment.

The SQUID used to perform most of the magnometric measurements in this thesis was a Quantum Design MPMS *XL*. Fields of up to 5 T can be reached.

### 2.3.3 MFM

MFM is a process in which a tapping cantilever with a ferromagnetic tip scans the surface of the sample in question. This provides a map of the topology of the sample. The cantilever is then lifted a certain distance from the surface. The scan is repeated without the "tapping", keeping a fixed height using the topology recorded in the first scan. Any deflection of the tip during this scan will be due to a magnetic interaction between the surface and the ferromagnetic cantilever tip. This deflection is measured using a laser and mapped to an image.

### 2.3.4 $^{57}$Fe Mössbauer Spectrometry

#### 2.3.4.1 Transmission measurements

The presence of Fe and its properties were investigated in some samples using Mössbauer spectroscopy. The Mössbauer effect utilizes the fact that $^{57}$Fe nuclei in a lattice has a finite probability of absorbing gamma rays without recoil. This is due to

the fact that the atom is bound in the crystal lattice, and the lattice vibrations are quantized, opening the possibility of zero-phonon processes with no recoil motion of the absorbing atom. The emitted gamma ray's energy is not affected. Any Fe nuclei can thus resonantly absorb the recoil-free radiation. In practice, to obtain a spectrum, the radiation is Doppler-shifted through a range of energies by movement of the source relative to the sample. The sample must be thin enough so as not to absorb the radiation completely in a non-resonant fashion and to avoid the chance of re-emitted radiation to be re-absorbed.

The spectrum of $\gamma$-ray absorption against energy will produce a series of absorption peaks at resonant energies (Fig. 2.17). The strength of the hyperfine interactions determine the position of the peaks. The magnetic and electric quadrupole interactions can only be combined when the electric quadrupole interaction is weak. The area subtended by these peaks is proportional to the number of nuclei present in the sample and the recoil-free fraction, $f$. This can be used to estimate the relative abundance of two phases in a sample.

The probability that a recoil-free event (zero-phonon) will occur depends on three things:

1) The properties of the solid lattice in which the $^{57}$Fe nucleus undergoing the recoil-free event is embedded

2) The free atom recoil energy

3) The ambient temperature for the measurement

Therefore, the recoil-free fraction may not be the same for two different phases in a sample, leading to inaccuracy in phase analysis. According to the Debye model, $f$ is given by

$$f = \exp\left[\frac{-6E_R}{k\theta_D}\left\{\frac{1}{4} + \left(\frac{T}{\theta_D}\right)^2 \int_0^{\theta_D/T} \frac{x\,dx}{e^x - 1}\right\}\right]$$

where $\theta_D$ is the Debye temperature for the phase and $E_R$ is the recoil energy. In the high temperature limit ($T \geq \frac{1}{2}\theta_D$), this simplifies to

$$f = \exp\left[\frac{-6E_R T}{k\theta_D^2}\right]$$

Thus, the ratio between recoil-free fractions for different phases can be found be varying the ambient temperature.

In this study, we have assumed for all cases that the recoil-free fraction are equal

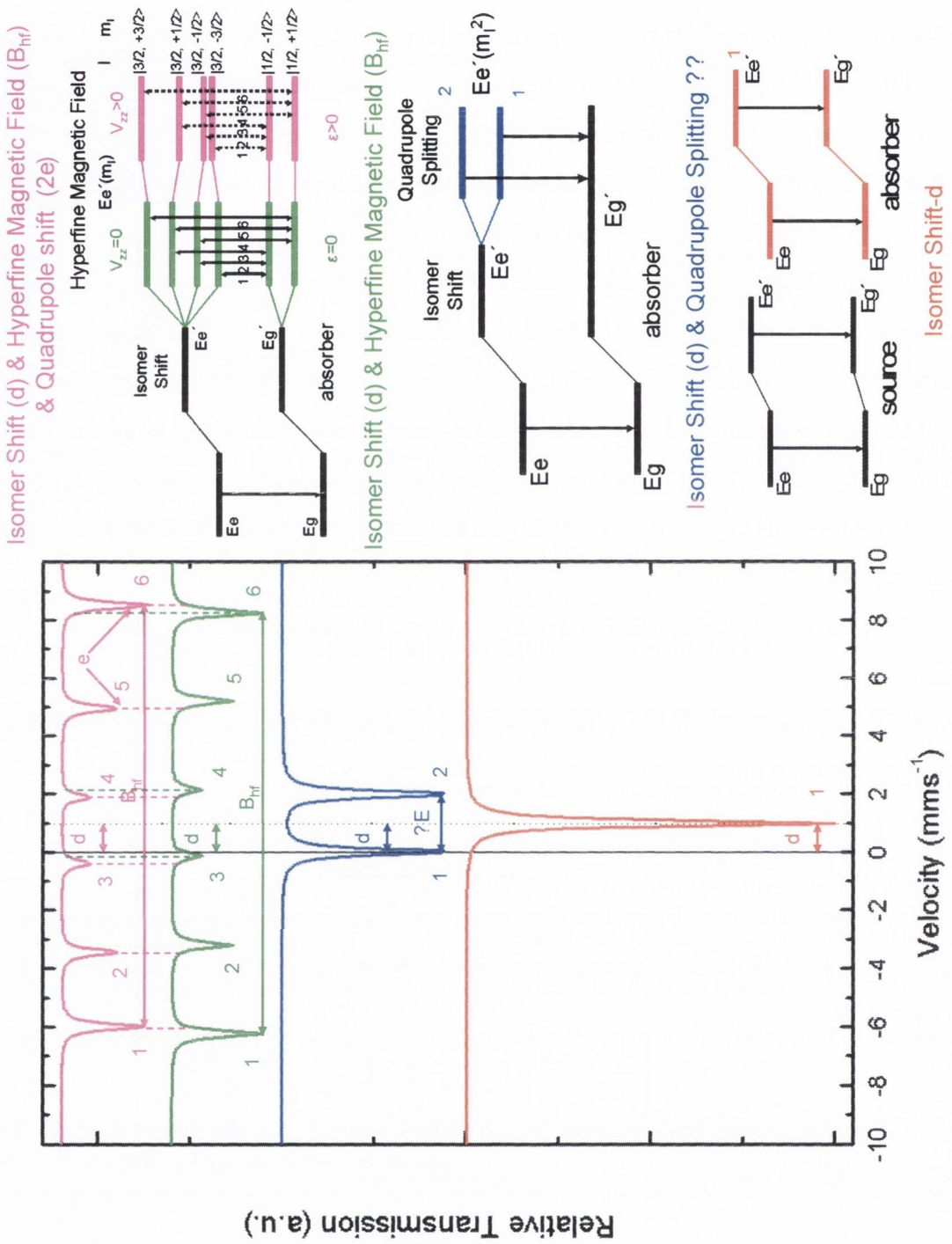



Figure 2.17. Schematic representations of Mössbauer spectra altered due to hyperfine interactions.

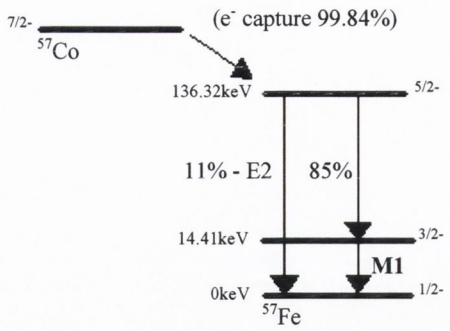



Figure 2.18. The $^{57}$Co Mössbauer decay scheme.

for all phases present, due to the fact that we are mainly dealing with oxides and have no reason to suspect large changes in $f$.

The source used is $^{57}$Co, which has a conveniently long half-life of 270 days. The $^{57}$Fe 14.41k eV level is efficiently populated by electron capture of $^{57}$Co and subsequent $\gamma$-ray emission. The 14.41k eV state transition to ground state produces a $\gamma$-ray (fig.2.18) and the transition type is primarily M1 (with a tiny fraction of E2). The lifetime of this state gives a Heisenberg linewidth $\Gamma_H$ of $0.192\,\mathrm{mm\,s^{-1}}$.

Since the resonant absorption only occurs with the $^{57}$Fe isotope and its natural abundance is relatively low (2.17%), it may be necessary to prepare samples using $^{57}$Fe for maximum signal. The usual form of the samples is a fine powder, but foils and thin films can also be measured.

#### 2.3.4.2 Conversion Electron Mössbauer Spectroscopy (CEMS)

Conversion Electron Mössbauer Spectroscopy (CEMS) is a convenient technique to study the properties of Fe atoms in thin films. The transmission geometry demands the $\gamma$-ray pass through the substrate. This forces the 14.4 keV $\gamma$-rays to undergo further scattering processes which lead to a massive reduction in the signal-to-noise ratio. However, CEMS uses electrons emitted from the surface of the sample, creating a *reflective* geometry and thus avoiding the subtrate.

CEMS makes use of a phenonemon known as *internal conversion.* When a resonant $\gamma$-ray is incident upon an $^{57}$Fe nucleus, it is absorbed by the nucleus to create an

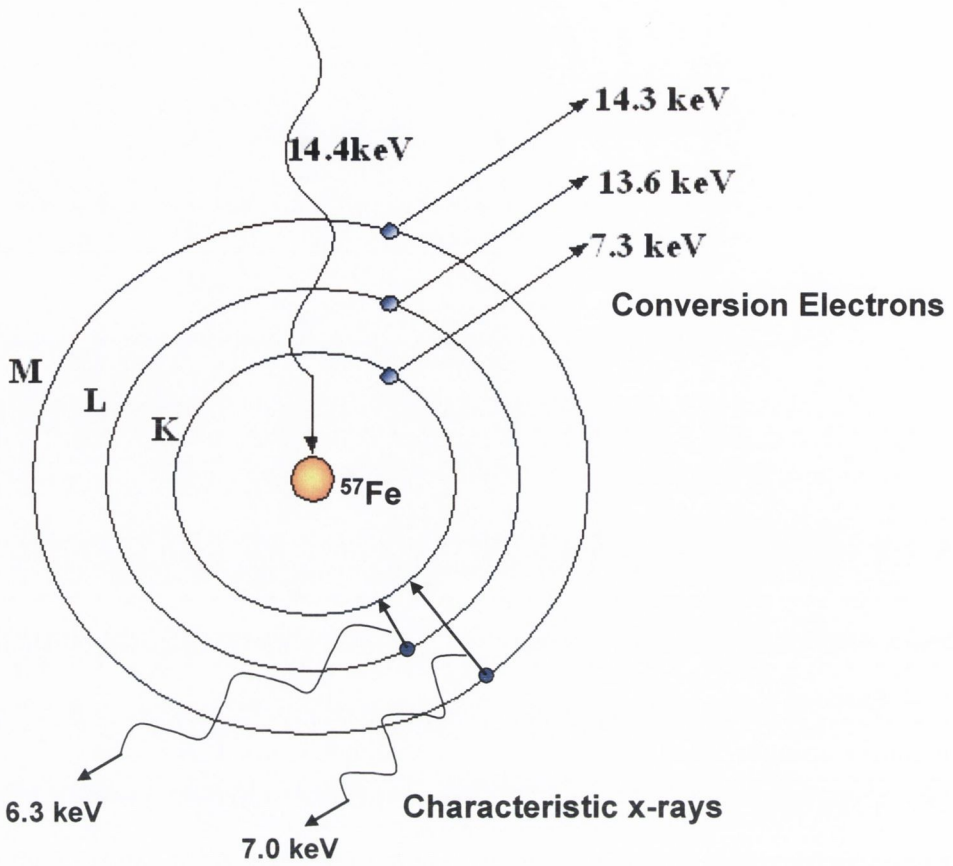



Figure 2.19. Absorption of a 14.4 keV $\gamma$-ray by the $^{57}$Fe nucleus and subsequent de-excitation by emission of a conversion electron.

excited state. This metastable nucleus can transfer its energy to an $s$ electron that has a certain probability of being in the nucleus. The electron will be ejected as a *conversion electron* with a kinetic energy equal to the energy of the excited state minus the binding energy of the electron. This will create a hole in the electron shell where the electron came from (most likely the K shell), which is then filled by an electron from a higher shell thus emitting the characteristic 6.3 keV iron K X-ray. The x-ray may then reproduce the effect and cause the emission of an *Auger electron.* The K shell produces conversion electrons with an energy of 7.3 keV, the energy of the conversion electron, $E_{ec}$ being given by

$$E_{ce} = E_{\gamma} - E_{edge}$$

where $E_{\gamma}$ is the energy of the excited state and $E_{edge}$ is the x-ray absorption edge. For the K-shell, $E_{edge}$ takes a value of 7.112 keV (Fig. 2.20). A discriminator can be used to isolate the energy of the conversion electrons over other energetic electrons which can add to the background noise. A pulse height analysis (PHA) - an energy

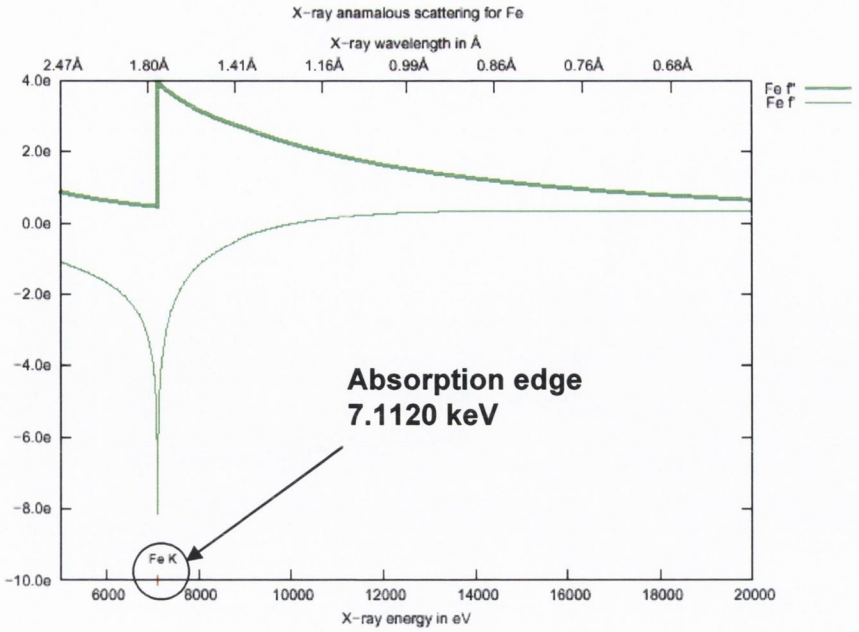



Figure 2.20. Plot of a calculation of the anomolous scattering coefficients of x-rays for the Fe K-shell. The absorption edge is cirled.

spectrum of the detected electrons - is taken for resonant and non-resonant $\gamma$-quanta 2.21. The difference between the two spectra leaves an energy window where the conversion electrons can be detected. The detector is then set to discriminate against pulses received outside this window.

The Doppler effect is used to shift the incident $\gamma$-ray energy to produce an energy spectrum in exactly the same fashion as the transmission geometry. The electrons are detected by an Wissel Rikon-5 electron detector with a Pt-coated tungsten wire (Fig. 2.22), which is kept at a voltage of 1300 V in a flowing atmosphere of 95% He: 5% $CH_4$. The flow rate is kept at $6\,\mathrm{ml\,min^{-1}}$.

The reduced mean escape depth, $x_m$, of the electrons is the given by

$$x_m = \frac{d_{escape}}{\rho} \tag{22}$$

where $d_{escape}$ is the escape depth and $\rho$ is the density of the material probed. It depends on the average atomic mass of the atoms which constitute the material probed, the energy of the electron and the density of the material [3]. The depth is given by:

$$x_m = (\frac{R}{2}) \cdot (\sqrt{\gamma^4 + 4\gamma^2} - \gamma^2) \tag{23}$$

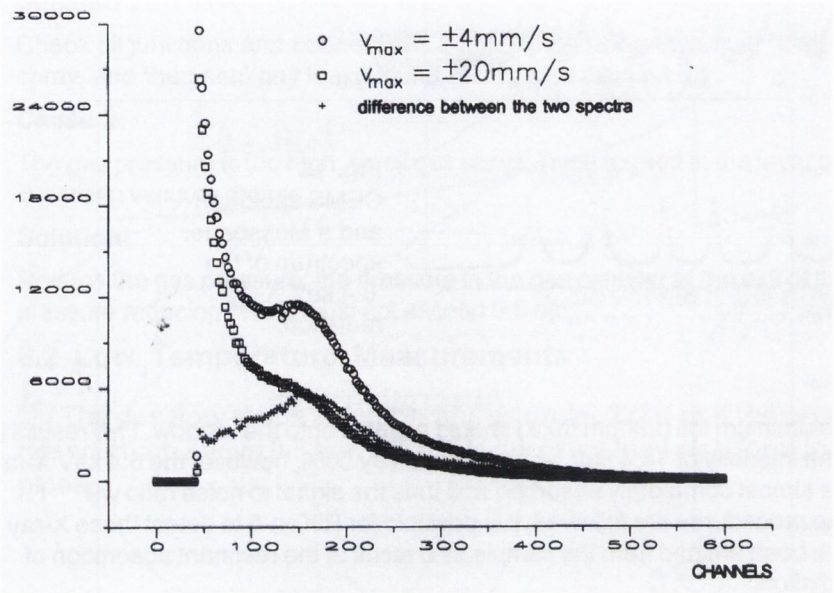



Figure 2.21. Two pulse height analyses, and their absolute difference of a stainless steel absorber.

The constant $\gamma$ is a parameter which takes a value of 1.92 [3], giving

$$x_m \approx 0.82R \tag{24}$$

and

$$\ln R = \ln a + b \ln E + c(\ln E)^2$$

where $E$ is the energy of the electron,and $a$, $b$ and $c$ are electron-electron and electron-neutron interaction co-efficients which are second-order polynomials of $Z$, the average atomic number of the material. $R$ has been calculated by fitting the equation for the escape probability, $T(x)$ to simulated data, where $T(x)$ is given by

$$T(x) = A \exp\left(-\frac{x}{R}\right) \exp\left(-\left(\frac{x}{\gamma R}\right)^2\right)$$

which has been derived from qualitative analysis of data [3].For the average atomic number of most of our samples and the 7.3 k eV energy of the electrons involved, $R$ takes a value of approximately 75 . Using (24) and these values, we get

$$x_m \approx 61.5\,\mu\mathrm{g\,cm^{-2}} \tag{25}$$

Using this equation and Eqn. (22), the densities of the oxides ($4 - 8\,\mathrm{g\,cm^{-3}}$) probed in this thesis imply a mean escape depth, $d_{escape}$, of

$$70\,\mathrm{nm} \lesssim d_{escape} \lesssim 140\,\mathrm{nm}$$

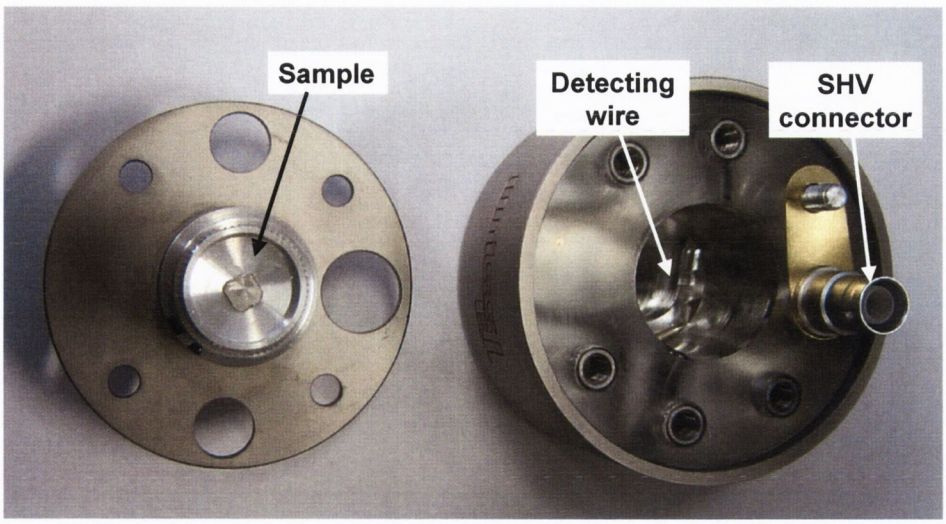



Figure 2.22. The opened CEMS detector, with the sample on the left and the chamber with detecting wire on the right.

When applied to Fe foil, this agrees with accepted values in Fe foil of up to 400 nm of maximum escape depth, and $< 200$ nm for mean escape depth.[4].

### 2.3.5 Electronic Paramagnetic Resonance (EPR)

Electron paramagnetic resonance is a useful tool that can reveal much about electronic, magnetic and structure properties of a material. Magnetic energy level transitions are induced in the sample using a range of microwave frequencies. The derivative of the absorption is plotted revealing characteristic energies of transitions, which can be fitted and analysed to provide information about the electrons in the system. The system used in these studies was a Bruker EMX EPR spectrometer.

The principle of EPR is that electromagnetic radiation will be absorbed if the energy of the radiation is exactly the energy required to instigate a transition from one discrete atomic or molecular energy level to another

$$\Delta E = hv \tag{26}$$

where $\Delta E$ is the difference in energy of the two states, $v$ is the radiation frequency and $h$ is Planck's constant. In EPR, a magnetic field is applied to the sample, which causes *Zeeman splitting*. Zeeman splitting occurs because the unpaired electrons in a sample have spin, with a value of $\pm\frac{1}{2}$, and upon application of a magnetic field the energy of

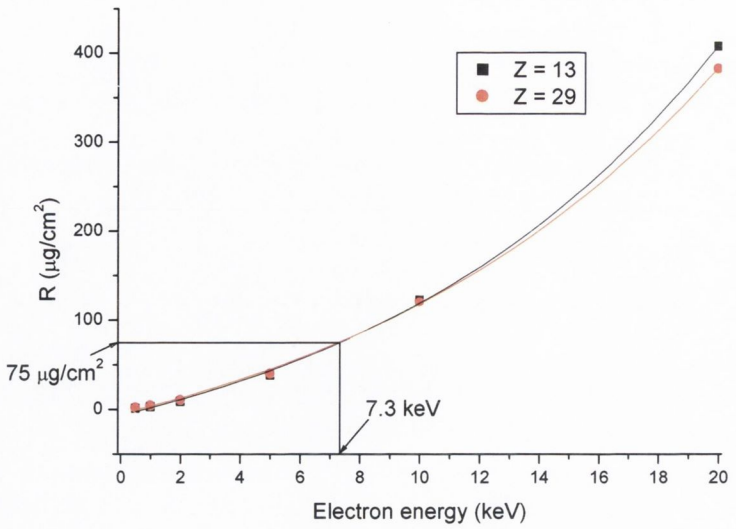



Figure 2.23. The $R$ versus $E$ plot for average atomic numbers $Z = 13$ and $Z = 29$. The 7.3 keV energy (i.e. that of the conversion electrons used in CEMS) is marked with its corresponding $R$ value. The values for the plot were taken from Liljequist's paper [3].

the system is split with

$$\begin{aligned} E &= \pm\frac{1}{2}g\mu_B B_0 \\ \Rightarrow \Delta E &= g\mu_B B_0 \end{aligned} \tag{27}$$

Combining Eqn (26) with Eqn (27), we get

$$g = \frac{h\upsilon}{\mu_B B_0} \tag{28}$$

Sweeping the magnetic field for a specified microwave radiation allows a g-value spectrum to be recorded. Spins with differing g-values will appear as absorptions at different magnetic fields. The integrated absorption intensities are proportional to the spin concentrations. The fields at which absorption takes place can be further altered by interaction between the electron and the magnetic moment of any nucleus close to its orbit. The signal is split into $2^N$ absorptions for each spin $\frac{1}{2}$ nucleus, with the splitting proportional to the magnetic field of the nucleus. The signals may overlap so that only a broad signal is observed.

In practice, the components of the spectrometer (Fig. 2.24) are the magnet, the sample cavity (a metal box that helps amplify the signals from the sample) and "bridge" which houses the electromagnetic source and detector. The bridge allows the

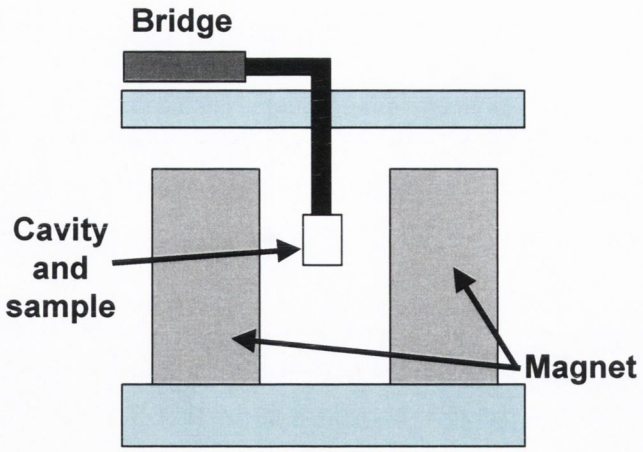



Figure 2.24. A schematic representation of an EPR set-up, showing the sample cavity placed in a magnetic field.

cavity to be irradiated with electromagnetic radiation, and to measure the absorption from the sample in the cavity. The magnetic field is swept and the derivative of the absorption is measured with respect to the field applied.

The EPR measurements in this thesis were carried out with the assistance of Dr. Ben Jones of the Physics Department in Trinity College Dublin.

## 2.4 Composition Determination

### 2.4.1 Residual Gas Analysis (Mass Spectrometry)

The composition of the residual gas in the tubes used to synthesize graphite by pyrolysis was determined using an MKS/Spectra Products Vacscan Residual Gas Analyser. A Faraday detector was mostly used, but in better vacuum conditions an electron multiplier was used. The analysis was carried out in a two-chamber arrangement (fig.2.25), which was evacuated to a maximum pressure of $2 \times 10^{-5}$ mbar, using a Alcatel Drytel 31 turbopump. The tube was stored in the left chamber (Chamber B), which was sealed off from the main chamber (Chamber A) using a needle valve. The detector was mounted on Chamber A. The tube was broken in the vacuum of Chamber B using a mechanical arrangement and gas was bled into Chamber A through the needle valve, for analysis. The pressure in Chamber B was kept below $1.33 \times 10^{-4}$ mbar at all times.

The Vacscan was connected to a PC via a RS-232 cable, onto which the mass

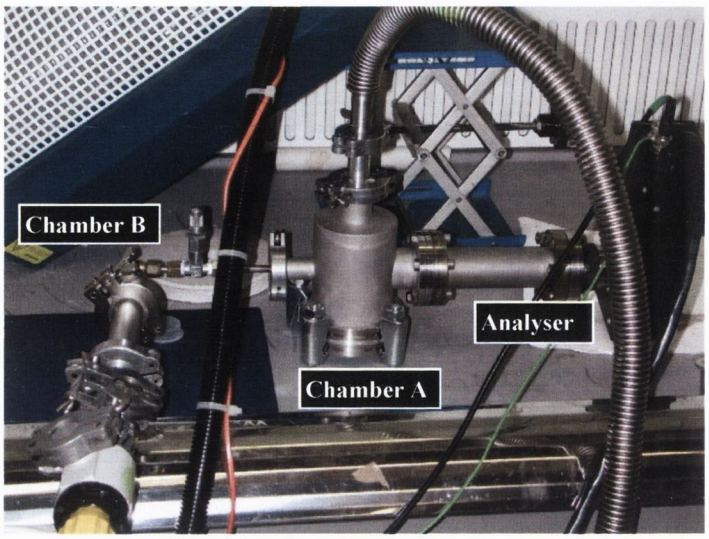



Figure 2.25. RGA/Mass Spectrometer

spectra were recorded. A BASIC-language program was written to acquire the spectra on to PC from the Vacscan controller. The code is reproduced in Appendix A.

### 2.4.2 Combustion Analysis

Combustion analysis was carried out in the Chemical Services Unit of the Chemistry Department, University College Dublin. The elemental analysis of C, H and N was carried out using an Exeter Analytical CE-440 elemental analyser.

### 2.4.3 EDAX

The SEM used for morphology studies was also equipped with an EDAX (energy dispersive analysis of X-rays) elemental analyser. The bombardment of electrons from the collimated beam produces characteristic x-rays as well as the backscattered and secondary electrons. The energy spectrum of these x-rays contains characteristic peaks of elements present in the sample. From the peak positions and their intensities, the elements and their relative abundances in the samples can be found.

Powders of elements of known stoichiometric ratio were first measured to calibrate the values returned from the spectra fitting procedure. Multiple measurements (approx. 10) were taken for each sample and the error in measurement was determined from the standard deviation of these measurements.

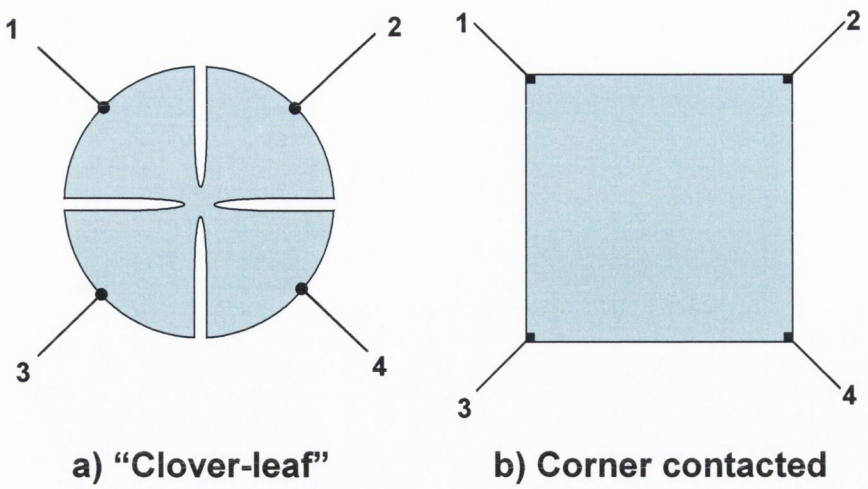



Figure 2.26. The acceptible methods of applying contact for a van der Pauw measurement. In case b), it is important that the contacts are at the corners an not inside the perimeters.

## 2.5 Electronic Measurements

### 2.5.1 Transport Measurements

The definition of resistivity, $\rho$, is given by equation (29) where R is resistance, A is the area of the sample cross section and L is the distance between contacts.

$$\rho = \frac{RA}{L} \tag{29}$$

#### 2.5.1.1 Thin Films

The resistivity of the thin films was measured using the van der Pauw method [5]. Silver wires are contacted to the corners of the sample by indium soldering or attachment with silver paste, as per figure 2.26b). For the description of the method, the following conventions are kept: $V_{xy}$ is the voltage measured between contacts $x$ and $y$ (i.e. $V_x - V_y$), $I_{xy}$ is the current passed from contact $x$ to contact $y$. The resistance, $R_A$ (defined as $\frac{V_{43}}{I_{12}}$) and $R_B$ (defined as $\frac{V_{14}}{I_{23}}$) are then measured by measuring the voltages for the currents passed.

The resistivity can then be derived from the relation

$$\exp\left(-\frac{\pi t}{\rho}R_A\right) + \exp\left(-\frac{\pi t}{\rho}R_B\right) = 1 \tag{30}$$

When resistivity of thin films is measured by the van der Pauw method with the

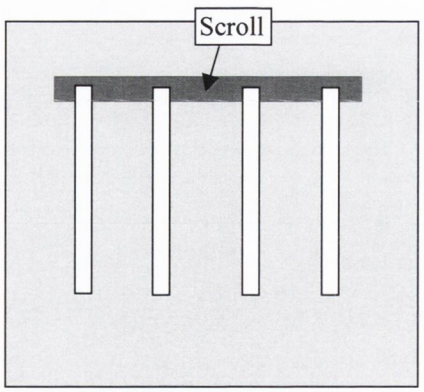



Figure 2.27. Schematic drawing of contacts made to a whisker.

contacts made as per Fig. 2.26b), the geometry of the sample demands that

$$R_A \approx R_B \equiv R$$

It follows that

$$\begin{aligned} 2\exp\left(-\frac{\pi t}{\rho}R\right) &= 1 \\ \Rightarrow \rho &= \frac{\pi t}{\ln 2}R \end{aligned} \tag{31}$$

Here $t$ is the sample thickness in cm. The resistivities of the thin film samples were measured by soldering four indium contacts to the thin films, one on each corner. The resistivities of the films were then determined by passing a current from one corner to an adjacent corner and measuring the voltage between the other two corners.

#### 2.5.1.2 Other samples

The resistivities of other linear samples, e.g. the scroll samples, were measured using a 4-point geometry (fig.7.94). The contacts were made using either indium solder or Agar Scientific quick drying silver paint. The measurements were carried out in a cryostat to which a magnetic field could be applied, which allowed the temperature dependence of the resistivity or the effect of magnetic field on resistance to be measured.

### 2.5.2 The Hall effect

The density of carriers in samples was measured using the Hall effect. The Hall

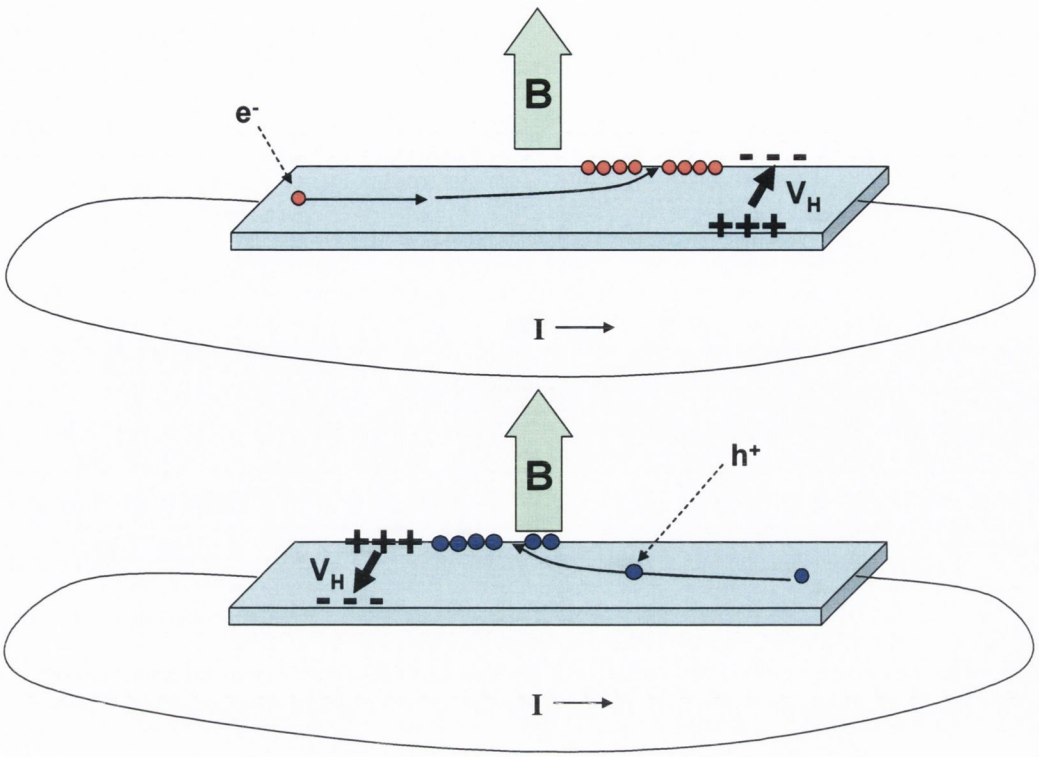



Figure 2.28. A diagram describing the Hall Effect for negative charge carriers (top) and positive charge carriers (bottom). The magnetic field is applied in the direction of the green arrow.

Effect uses the principle of the Lorentz force produced by a magnetic field on a moving charge carrier. The Lorentz force is given by

$$F = q(E + v \times B)$$

where $v$ is the velocity of the charge carrier and $q$ is its charge. The field will deflect charge carriers perpendicular to the field and the direction of current (Fig. 2.28). A measurable voltage will build up, and the density of the charge carriers, $n$, can be calculated from the normal Hall coefficient

$$R_0 = \frac{1}{nq}$$

assuming a one-band model.

The Hall resistivy, $\rho_H$ can be represented by

$$\rho_H = R_0 B + \mu_0 R_S M$$

where $R_0$ and $R_S$ are the normal and anomalous Hall coeffecients respectively, $B$ is the applied field and $M$ is the magnetization of the sample investigated. All Hall

measurements were performed in a the 5 T Cryomag.

Thin film samples were measured by soldering contacts to the corners and measuring the Hall effect in a van der Pauw configuration. The van der Pauw method of determining the Hall voltage is similar to the van der Pauw method for measuring resistivity previously mentioned. This time, a current is passed from opposite corners, $I_{13}$, and voltage $V_{24}$ is measured. The Hall resistance is then $\frac{V_{24}}{I_{13}}$. The sign of the charge carriers can be related to the sign of the voltage by careful analogy with Fig. 2.28.

#### 2.5.2.1 Other samples

Carbon whisker samples were broken mechanically and a flake from the scroll was patterned with contacts using a dual FEI Strata FIB/E-beam system. Patterning was performed with the assistance of Dr. Richard Langford. The measurements were then taken in the 5 T Janis cryostat and the measurements were performed using the van der Pauw method.

# References

[1] C. B. Fitzgerald, "Novel magnetic materials for spin electronic applications", PhD. Thesis, University of Dublin (2004)

[2] D. L. Windt, http://cletus.phys.columbia.edu/~windt/idl/

[3] D. Liljequist, Nucl. Inst. and Meth. for Phys. Res. B, **142** 295 (1998)

[4] U. Gonser (ed.), Topics in Current Physics: Mössbauer Spectroscopy II (Springer-Verlag, Berlin), p146 (1981)

[5] L. J. van der Pauw, Philips Technical Rev. 20, 224 (1958)

# Chapter 3

# $TiO_2$

"The only day you really can't be in the lab is the December 25th, and if you want to get in then, you can make up some excuse for security"

Mike getting into the Christmas spirit

## 3.1 Introduction

Titanium dioxide is a wide bandgap ($E_g \sim 3.1\,\text{eV}$) n-type semiconductor. It exists as three structural polymorphs - rutile, anatase and brookit., rutile being the most stable and abundant in nature. The $TiO_2$ fabricated for the work in this thesis was in the form of rutile. The rutile structure has space group $P4_2/mnm$ (Fig. 3.29). The lattice parameters $a$ and $c$ are 4.593 Å and 2.959 Å respectively, with the $Ti^{4+}$ radius being 0.60 Å and the $O^{2-}$ radius being 1.46 Å. It has a formula weight of $79.865\,\text{g mol}^{-1}$ and a density of $4,250\,\text{kg m}^{-3}$. The melting point of rutile is 2190 K [1], while its boiling point is approximately 3000 K [2].

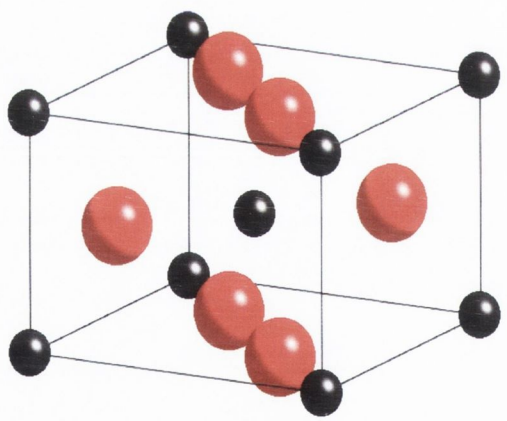


Figure 3.29. The rutile $TiO_2$ crystal structure with Ti atoms in black and oxygen atoms in red

The magnetism of thin films of titanium oxide doped with a few percent of $3d$ ions has been a subject of intense controversy ever since the first report of high temperature ferromagnetism in thin films of anatase doped with 8% of Co by Matsumoto in 2001[3]. The $TiO_2$:Fe system has been shown to be magnetic in several previous investi-

gations[4][5][6], although in one case the magnetism was shown to be due to a secondary $Fe_3O_4$ phase[7].Almost anhysteretic and largely temperature independent magnetization curves have been reported for many other films such as ZnO:Co[8], $SnO_2$:Fe[9], $Cu_2O$:Co[10] and $In_2O_3$:Cr[11].

Long-range magnetic order in dilute magnetic oxides is puzzling, because the concentration of magnetic dopant cations lies far below the percolation threshold and the normal superexchange and double-exchange interactions couple nearest-neighbour cations only. Some of the films are insulating[12][13], so carrier-induced exchange cannot be a general explanation. Furthermore the exchange energy density at a few percent doping is far too small to produce uniform room-temperature ferromagnetism[14], even if the exchange were as strong as it is in cobalt, the ferromagnet with the highest known Curie temperature.

Bulk samples[15] and well-crystallised thin films[16] of the dilute magnetic oxides behave as expected; they are paramagnetic down to the helium temperature range. Hence, there is a widespread presumption that the ferromagnetic behaviour of thin film samples is due to ferromagnetic impurity phases present as inclusions in the films[7][17] or as uncontrolled contamination, introduced, for example, by handling samples with the wrong sort of tweezers[18]. The magnetic moment of a typical sample, $10^{-8}\,\mathrm{A\,m^2}$, is only that of a speck of iron or magnetite a few tens of microns in size.

### 3.1.1 Applications

There are few applications for sintered titania because of it's poor mechanical properties. Its main application is as a white pigment, where it is used in powder form. It provides whiteness and opacity to products such as paints and coatings (including glazes and enamels), plastics, paper, inks, fibres and food and cosmetics. Owing to its high refractive index, surpassed only by that of diamond, relatively low levels of titania pigment are required to achieve an opaque coating. Titania-based paint is also a good reflector of infrared, and thus finds use in solar observatories where heat can cause poor visibility. Titania's opacity and resistance to discolouration under UV light makes it an excellent material to base sunscreen and cosmetics on.

Titania also has a number of electrical uses, and has found applications in sensors and as a electrocatalysist. It acts as a photosensitiser for photovoltaic cells, and

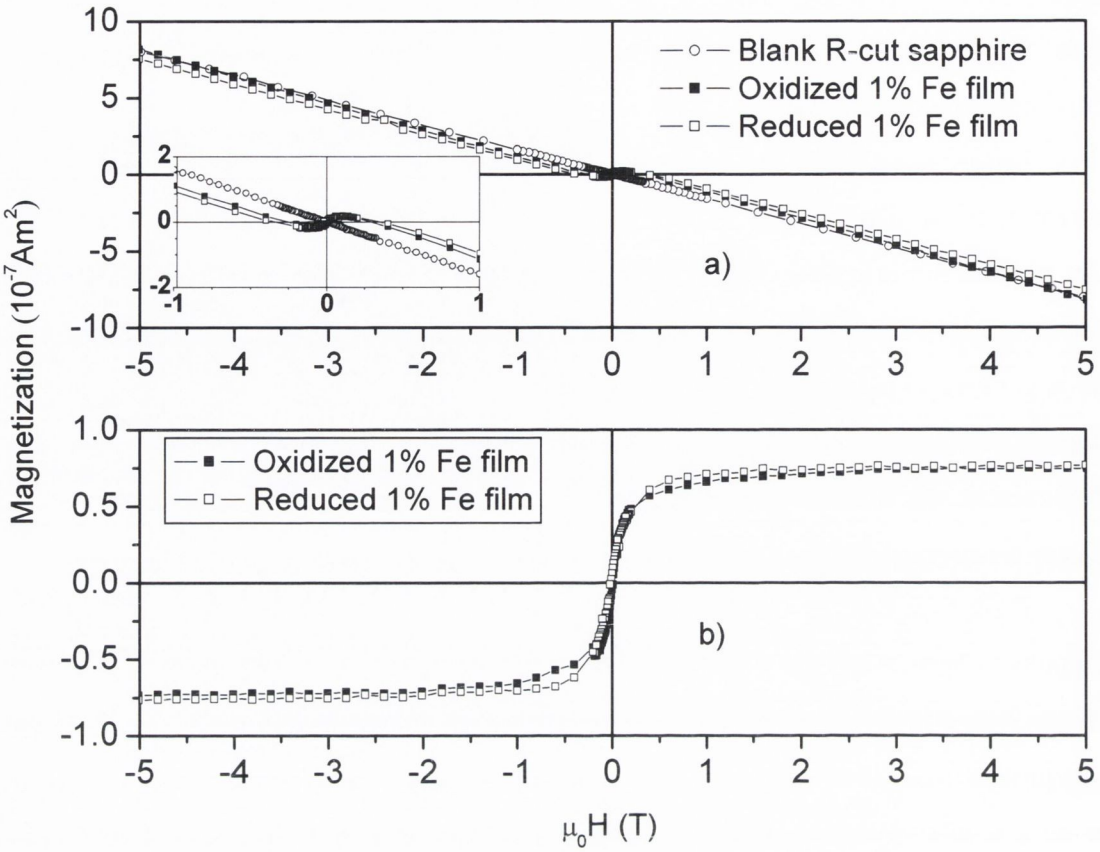



Figure 3.30. Room temperature magnetization curves oxidized (•) and reduced (o) films of a) a blank sapphire substrate and $Ti_{0.99}Fe_{0.01}O_2$ film on sapphire and b) data for $Ti_{0.99}Fe_{0.01}O_2$ film after subtracting the diamagnetic contribution from the substrate.

when used as an electrode coating in photoelectrolysis cells can enhance the efficiency of electrolytic splitting of water into hydrogen and oxygen. Even mildly reducing atmospheres tend to create oxygen vacancies in titania. In this form the material becomes a semiconductor and the electrical resistivity of the material can be correlated to the oxygen content of the atmosphere to which it is exposed. Hence titania can be used to sense the amount of oxygen (or reducing species) present in an atmosphere.

The photocatalytic activity of titania results in thin coatings of the material exhibiting self cleaning and disinfecting properties under exposure to UV radiation. These properties make the material a candidate for applications such as medical devices, food preparation surfaces, air conditioning filters, and sanitaryware surfaces.

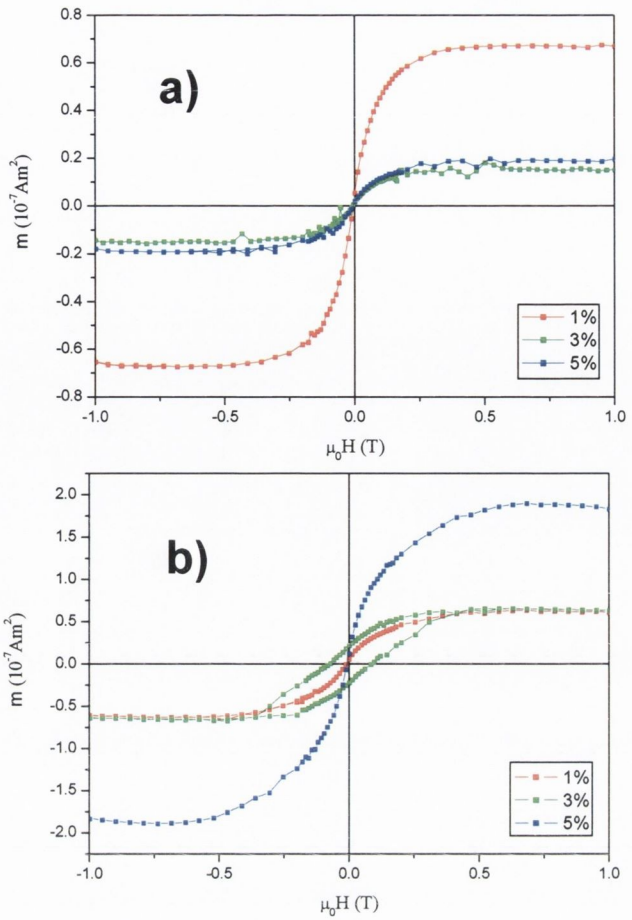



Figure 3.31. M-H loop of a) the oxidized and b) the reduced $Ti_{1-x}Fe_xO_2$ thin films. The diamagnetic susceptibility due to the substrate has been removed.

## 3.2 Sample Preparation

Two series of films were prepared by pulsed-laser deposition from sintered targets made from 99.999 % pure $TiO_2$ and 95% enriched $^{57}Fe_2O_3$. The targets had an Fe/(Fe+Ti) atomic ratio in the range 0 – 5 at%. Substrates were $5 \times 5 \times 0.5\,mm^3$ squares of R-cut sapphire, polished on both sides. They were maintained at 750 °C during deposition, in an ambient oxygen pressure of $10^{-3}$ Pa (Series A, reducing conditions) or $10^2$ Pa (Series B, oxidizing conditions). The thin films were deposited on R-cut $(1\bar{1}02)$ sapphire substrates using the Lambda Physik KrF excimer laser operating at 248 nm and 10 Hz. Laser fluence on the target was $2\,J\,cm^{-2}$. Films were typically 140 nm thick, with an rms roughness of 2.5 nm, but some 70 nm films were also grown.

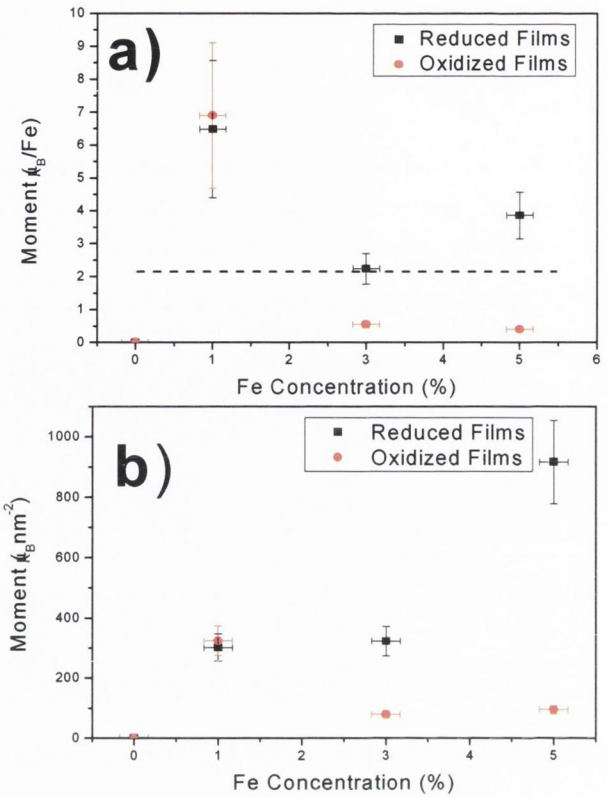



Figure 3.32. Magnetic moments of oxidized (red circles) and reduced (black squares) films plotted as a) $\mu_B$ per Fe and b) $\mu_B$ nm$^{-2}$ of substrate area. The dashed line shows the moment for metallic iron.

## 3.3 Sample Characterization

### 3.3.1 SQUID Magnetometery

Magnetization measurements were made in the 5 T SQUID magnetometer, mounting the samples in a drinking straw. Undoped samples exhibited a linear diamagnetic susceptibility (Fig 3.30a), dominated by the substrate. No trace was found of the ferromagnetic component that has recently been reported for undoped anatase films on LAO substrates [19][20], whereas many of the 140 nm iron-doped films showed a superposed ferromagnetic signal. Data shown for a few samples in Fig. 3.30b have been corrected for the high-field diamagnetism of the substrate. The susceptibility of sapphire is $-4.6 \times 10^{-9}\,\mathrm{m^3\,kg^{-1}}$. Saturation moments are in the range $2 - 20 \times 10^{-8}\,\mathrm{A\,m^2}$ or 90-900 $\mu_B$ nm$^{-2}$ of substrate area. The moment is plotted in Fig 3.32 in Bohr magnetons per film area and per iron atom. The latter is obviously not a sensible way to

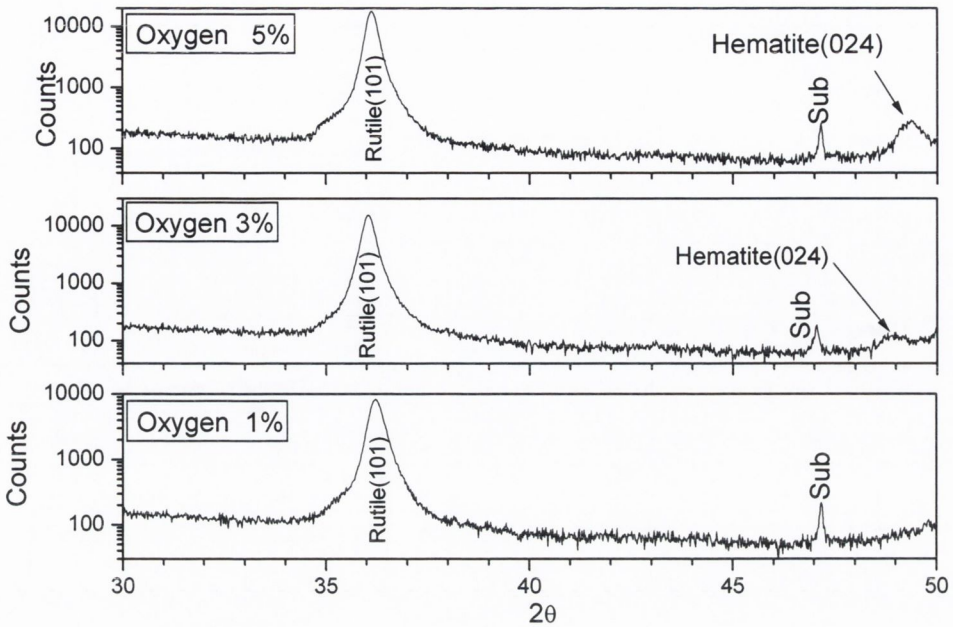



Figure 3.33. X-ray diffractograms of 1%, 3%, and 5% oxidized thin films in the area of the rutile (101) and the hematite (024) reflections.

plot the data, as the moments sometimes exceed that of any known form of iron. The moment for iron metal is shown by the dotted line.

### 3.3.2 X-Ray Diffraction

X-ray diffraction was carried out using both the Philips X'Pert Pro for the thin films and a Siemens D500 for the ceramic targets. For the oxygen-deposited thin films, the $TiO_2$ forms the rutile phase, orientated in the (101) direction. The (024) peak of hematite is also observed, and the intensity of this peak increases with Fe concentration (Fig.3.33). Rietveld analysis of the peaks permit a rough estimation of the percentage of hematite as 2 at%, 0.9 at% and $< 0.25\%$ of the sample for the nominal 5%, 3%, and 1% films respectively. The 1% film is quoted as $< 0.25$ at% as this is the minimum detection level set by the background noise for the measurements performed. These values are in rough agreement with the amounts determined by a combination of EDAX elemental analysis and Mössbauer iron phase determination..

The reduced films showed only one peak, at $2\theta = 26.5\,^{\circ}$, characteristic of the

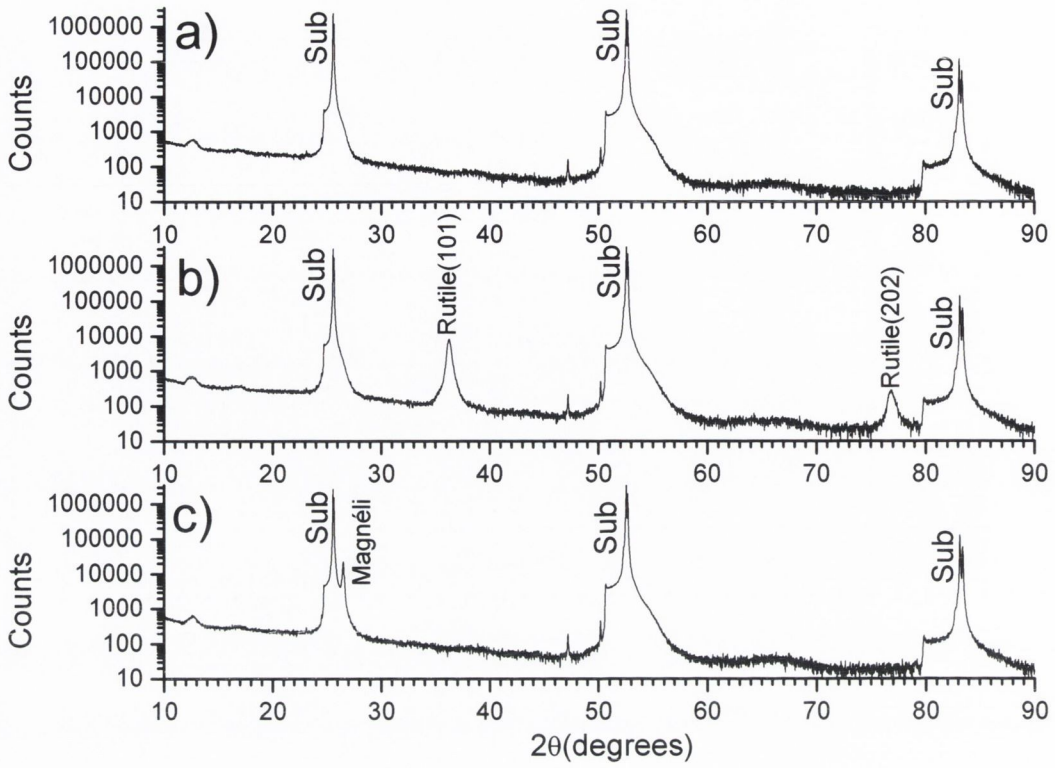



Figure 3.34. X-ray diffraction pattern of a thin film of $TiO_2$ on R-cut sapphire substrate. a) blank R-cut sapphire substrate. b) 1% Fe doped $TiO_2$ film grown in oxygen pressure of $10^2$ Pa (oxidized) c) 1% Fe doped $TiO_2$ film grown in oxygen pressure of $10^{-3}$ Pa (reduced)

$Ti_nO_{2n-1}$ series of Magnéli phases with ordered planes of oxygen vacancies. No metallic Fe or hematite peaks were observed. The undoped vacuum deposited films (pure $TiO_2$) show rutile (101).

The rutile (101) peak was fitted using a Pseudo-Voigt function for both 70 nm and 140 nm thick films (Fig.3.35). While we can accurately fit the rutile (101) peak for the 70 nm film using one peak at 36.2 °, the same peak for the 140 nm film must be fitted with two peaks in order to obtain an accurate fit. These peaks have $2\theta$ positions 36.25 ° and 36.53 °, and relative areas in the ratio of 2:1 (respectively). The (101) peaks on both films deviate from the expected peak positions for bulk $TiO_2$, indicating a slight reduction in the lattice parameter. This may be due to lattice strain due to the growth of the material on sapphire substrates or a lattice contraction due to a substoichiometric amount of oxygen in the material.

The optical reflectivity of these two films shows that there are two different growth

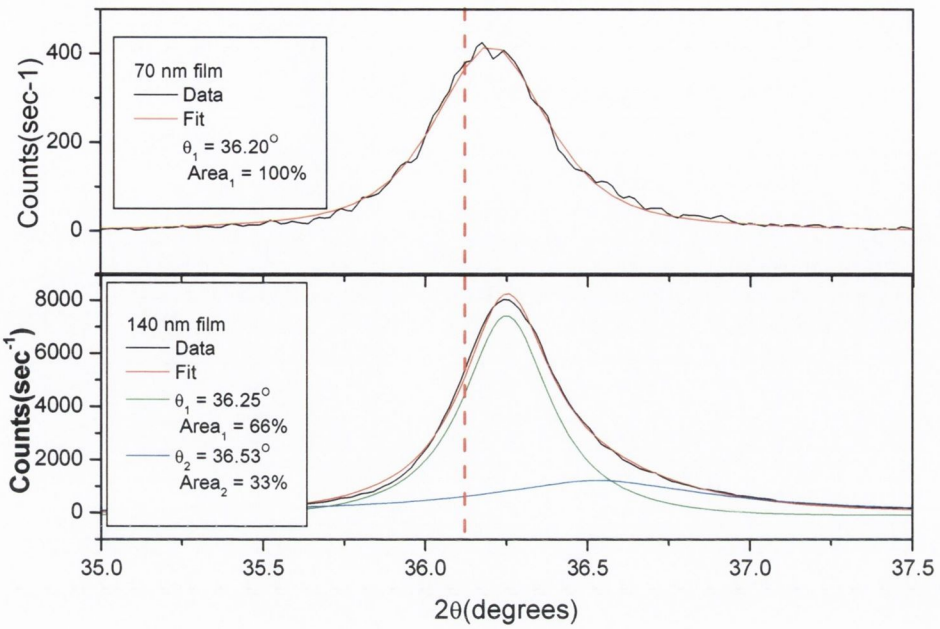



Figure 3.35. (101) rutile peaks of a 70 nm (top) and 140 nm (bottom) thin film fit using a Pseudo-Voigt function. The red dotted line indicates the $2\theta$ position of the (101) peak for bulk rutile $TiO_2$.

rates. After ~70 nm (or the first crest in Fig.3.36), the depostion rate slows by approximately 50%. From this, we can assume that there are two different growth régimes in the deposition of the $TiO_2$ films, and that there is a slight change in the lattice parameter, toward a smaller size. Given the large size of the oxygen anion, we can deduce that the second growth régime involves slightly less oxygen-rich $TiO_2$.

### 3.3.3 X-Ray Reflectometry

X-ray reflectometry was used to verify the thickness measured during the in-situ deposition. For this purpose, a film was grown to half the thickness (70 nm) of the standard thickness of the films deposited. The measurement verified the optical reflectometry method used, to within 1 nm. Using the IMD fitting program, the surface roughness could also be estimated to be 2.5 nm, using an error function to fit the roughness.

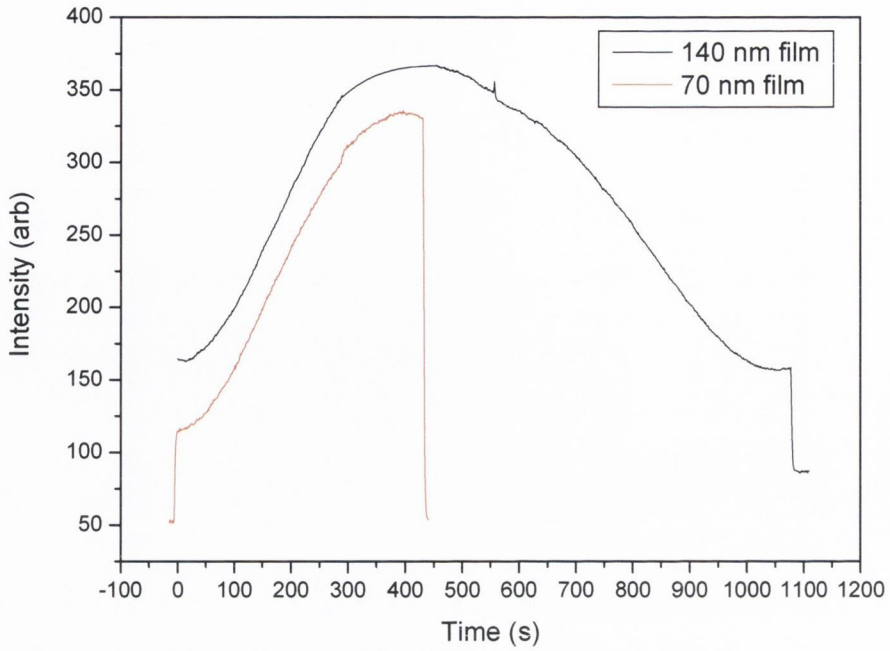



Figure 3.36. Thickness monitoring using optical reflectivity of a 70 nm film and a 140 nm film deposited from the same target under the same conditions.

### 3.3.4 AFM

The surface roughness of the films was also measured using atomic force microsopy (AFM), to check the values given by XRR. A typical scan is shown in Fig.3.38. The surface roughness is found to be between 1.7 nm and 3.5 nm, confirming the values given by XRR.

### 3.3.5 EDAX Elemental analysis

EDAX (Energy Dispersive X-Ray Microanalysis) was used to determine the ratio of Fe to Ti in the thin films. Firstly, to calibrate the EDAX, we used the three ceramic targets and some $Fe_{60}Ti_{40}$ powder as standards (Fig.3.39a). In both the vacuum and oxygen-deposited films, it was found that the value of Fe concentration in the thin films is approximately 81% of the nominal concentration (i.e. that of the targets), using a linear fit of the results (Fig.3.39b).

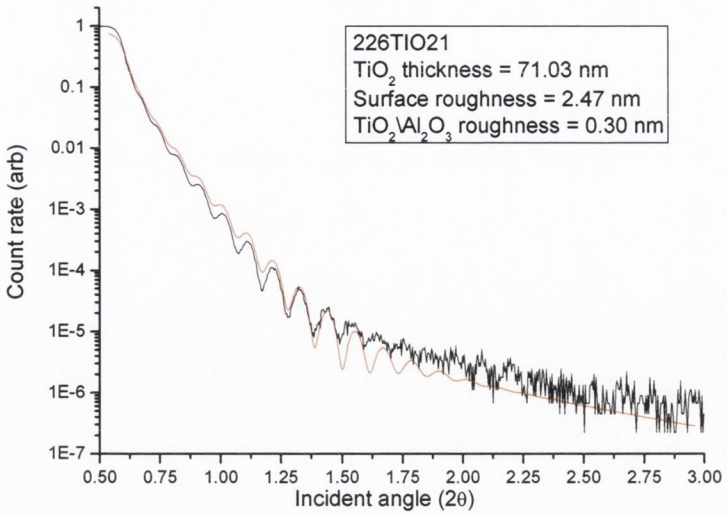



Figure 3.37. An XRR measurement of an undoped $TiO_2$ thin film with a fitting simulation. The measured data is in black, while the simulation is in red.

### 3.3.6 Mössbauer Spectrometry

Transmission Mössbauer spectrometry of the ceramic targets was performed at room temperature (Fig. 3.40). From the ceramic spectra, we can see that approximately 5% of the iron orders as hematite for the 1% doped target. The rest has an isomer shift that indicates $Fe^{3+}$, and may substitute into the octahedral Ti site.

| Fe (at%) | Isomer shift ($mm\,s^{-1}$) | Quadr. Splitting ($mm\,s^{-1}$) | $B_{eff}$ ($T \pm 0.1$) | Area ($\% \pm 3\%$) |
|---|---|---|---|---|
| 0.3 | $0.35 \pm 0.01$ | $-0.04 \pm 0.06$ | 51.2 | 27 |
| | $0.33 \pm 0.01$ | $0.641 \pm 0.06$ | 0 | 73 |
| 1 | $0.37 \pm 0.02$ | $-0.07 \pm 0.08$ | 51.6 | 6 |
| | $0.33 \pm 0.01$ | $0.71 \pm 0.06$ | 0 | 94 |
| 3 | $0.35 \pm 0.02$ | $-0.04 \pm 0.08$ | 51.0 | 3.5 |
| | $0.35 \pm 0.01$ | $0.76 \pm 0.06$ | 0 | 96.5 |

Table 5.Fit parameters for Transmission Mössbauer spectra of ceramic targets of Fe-doped $TiO_2$. Isomer shifts relative to an $\alpha$-Fe absorber.

Mössbauer spectra of the doped thin films were obtained using conversion electron Mössbauer spectroscopy. The spectra for 1%, 3% and 5% doped films, both oxidized and reduced, are shown in Fig.3.41. The mean escape depth of the 7.3 k eV conversion electrons in $TiO_2$ is calculated to be about 140 nm [21], so they effectively probe the depth of our films. The data and least-squares fits to the hyperfine parameters are shown in Fig 3.41, and the fit parameters are listed in Table 6. It is clear from the data

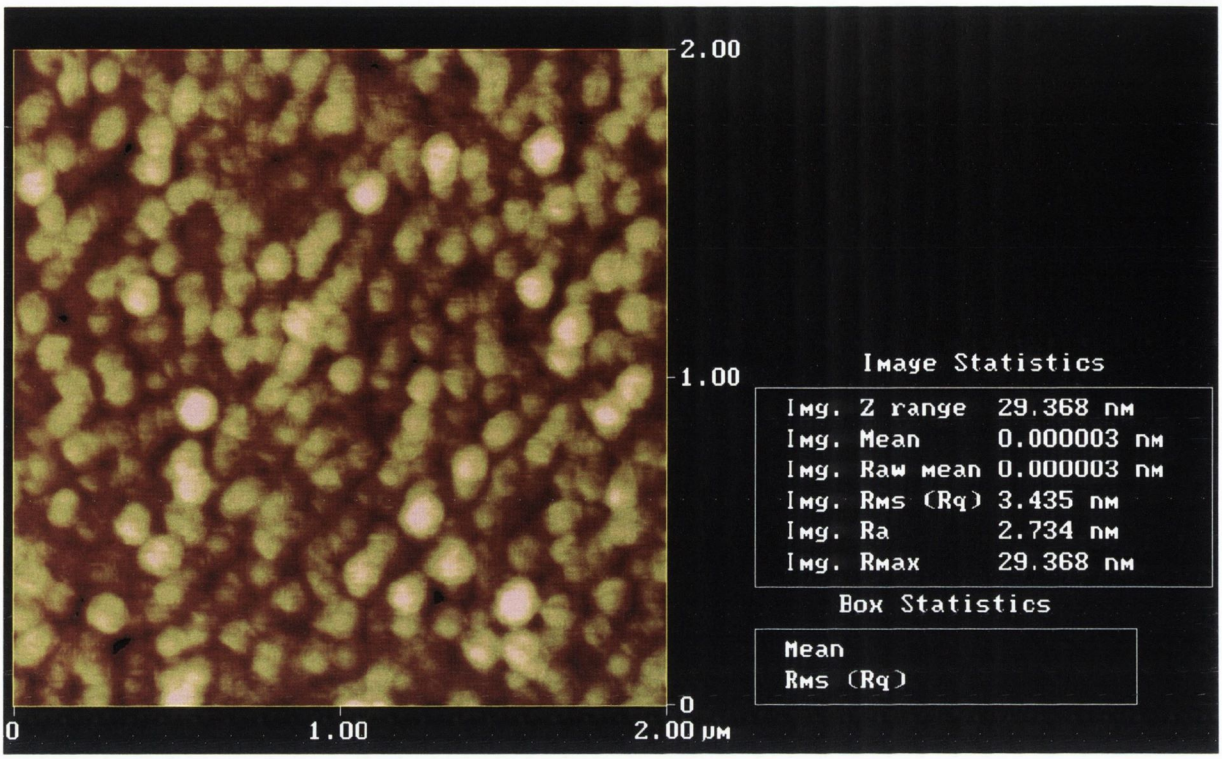



Figure 3.38. An AFM scan of an undoped 140 nm $TiO_2$ thin film.

that most of the iron in the reduced films is present as inclusions of well-crystallised iron metal, whereas in the 3 % and 5% oxidized films much of the iron is present as well-crystallised hematite with some paramagnetic $Fe^{3+}$ also present. However, in the magnetic 1 % oxidized film, all the iron is paramagnetic and most of it is in the $Fe^{2+}$ state.

The 5% oxygen-deposited films show a spectrum which indicate the presences of a hyperfine field at the iron nucleus of 49.0 T. We see that 60% of the iron is in this antiferromagnetic hematite phase. Since the x-ray diffractograms 3.33 indicate the presence of hematite, the phase present may be hematite with a reduced internal field. We would expect to see a $B_{eff} = 51.7$ T for pure hematite, but the reduced field may be due to Ti substitution, as has previously been observed [22]. Given that the moment of pure $\alpha$-$Fe_2O_3$ is 0.006 $\mu_B$/Fe for hematite, we expect 0.003 $\mu_B$/Fe for the sample if the moment is due to hematite alone. However, a moment of 1.17 $\mu_B$/Fe is observed for this particular sample. It cannot be associated with the hematite.

### 3.3.7 Optical Transmission

The optical transmission spectra for the oxygen-deposited films (Fig.3.42a) show

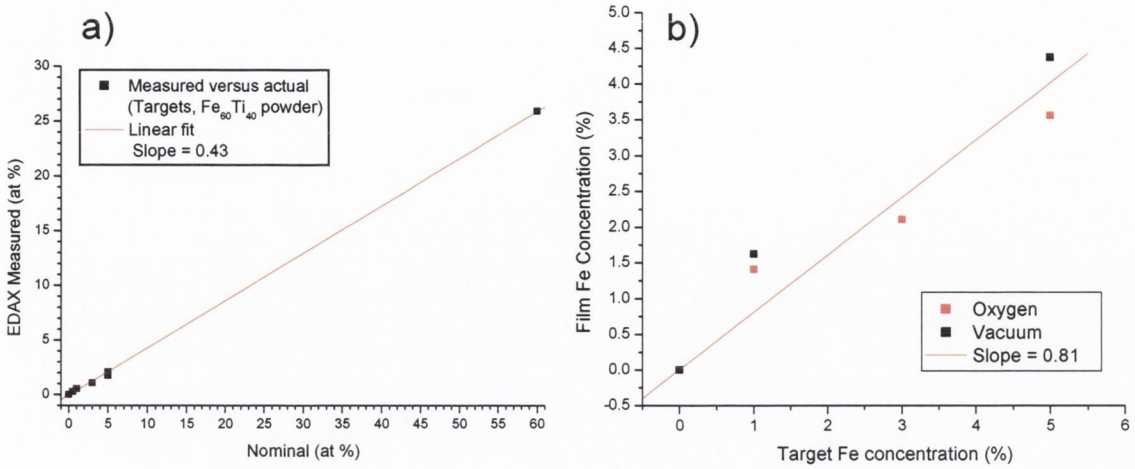



Figure 3.39. a) EDAX calibration using targets and $Fe_{60}Ti_{40}$ powder as standard and b) calibrated measurements of the thin film samples

large near-edge absorption for the 1% doped sample. This sample shows the largest moment of the four films.

For the vacuum deposited films (Fig.3.42b), we see an increase in transmission with doping. The largest transmission is seen in the 3%-doped sample, which is the only sample to show coercivity in its magnetization loop. There is also a large shift in the band gap of the vacuum deposited films. To find the bandgap of the films, the square of the absorption coefficent, $\alpha^2$, was plotted against photon energy for both oxidized (Fig3.43.a) and reduced (Fig3.43.b) films, where $\alpha$ is given by

$$\alpha = \frac{\ln(\frac{T}{T_0})}{d}$$

where $T$ is the transmission, $T_0$ is the average transmission in the visible range and $d$ is the thickness of the thin film. Since the thickness was the same for all the films, $d$ was given the value 1, making the coefficent unitless. From plots, we can see that the optical bandgap for the oxidized films was $3.5 - 3.7\,\text{eV}$, higher than the expected $3.1\,\text{eV}$ for rutile $TiO_2$ [23], whereas the bandgap of the reduced films was $3.9 - 4.2\,\text{eV}$. All the thin films show an appreciably greater band gap than pure $TiO_2$. This is understandable for the reduced films, which have a different crystal structure, $Ti_nO_{2n-1}$. The blue shift

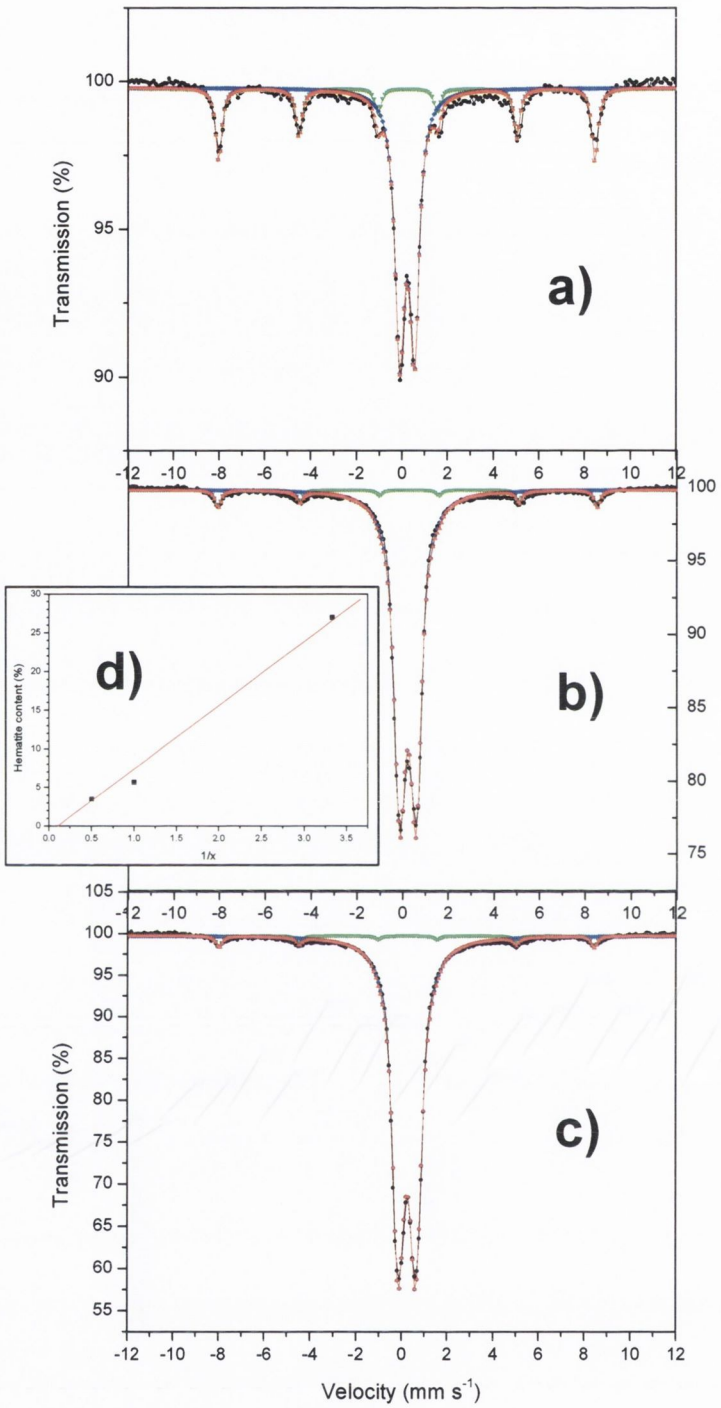



Figure 3.40. Transition Mössbauer spectra of a) $Ti_{0.997}Fe_{0.003}O_2$ target, b) $Ti_{0.99}Fe_{0.01}O_2$ target and c) $Ti_{0.97}Fe_{0.03}O_2$ target. d) A plot of hematite content versus the reciprocal of the Fe content. The fit values are given in Table 5.

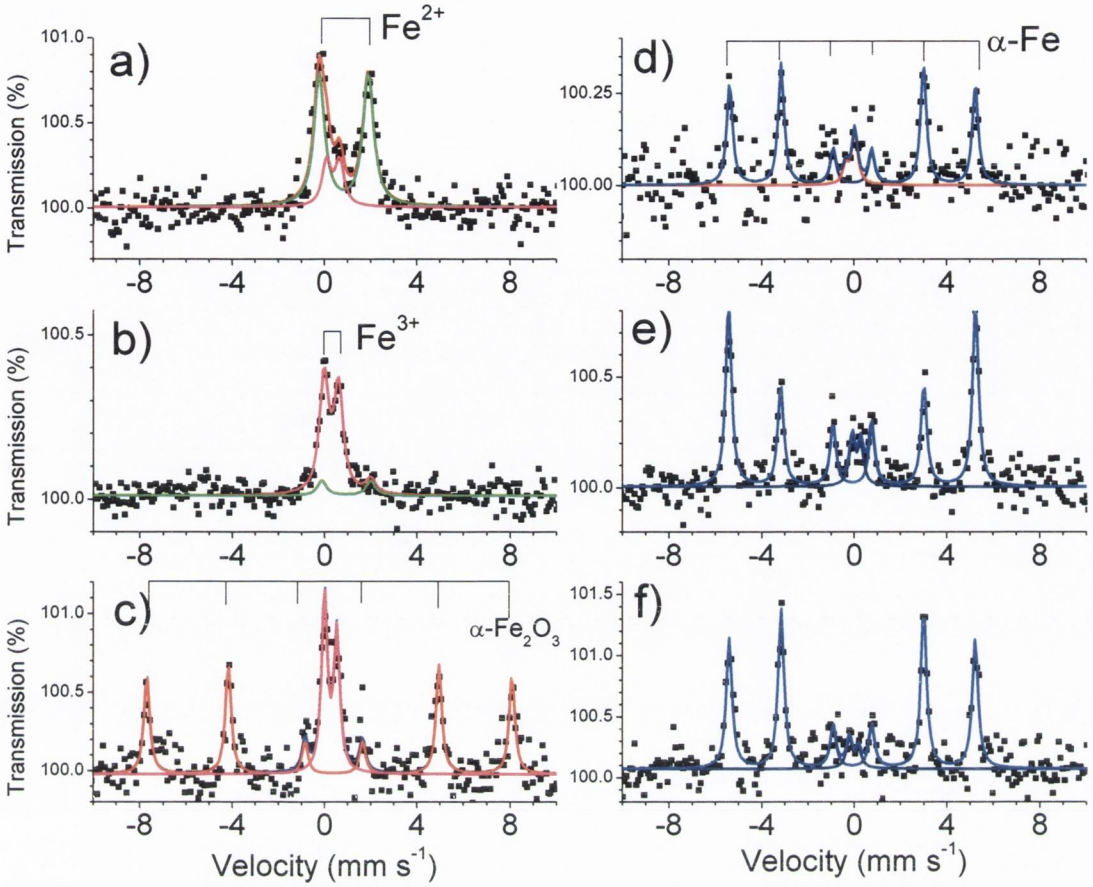



Figure 3.41. Conversion electron Mössbauer spectra a) 1%, b) 3%, c) 5% oxidized and d) 1%, e) 3%, f) 5% reduced films

in the films produced in higher oxygen pressure may reflect the film strain.

## 3.4 Discussion

We are now able to discuss of the origin the magnetism in the films. Contamination is ruled out because undoped films which are prepared in the same chamber and handled in the same way as the doped films exhibit no moment. The moment of the reduced films can be partly, but not entirely explained, by metallic iron inclusions, whose presence is clear from the Mössbauer data although metallic iron was not detected by X-ray diffraction. Judging from the form of the spectra, these iron inclusions are blocked on the Mössbauer timescale of $\sim 10^{-9}$ s, so they are at least 15 nm in size. However, the moment per iron atom for 1% and 5% films in Fig 3.32 significantly ex-

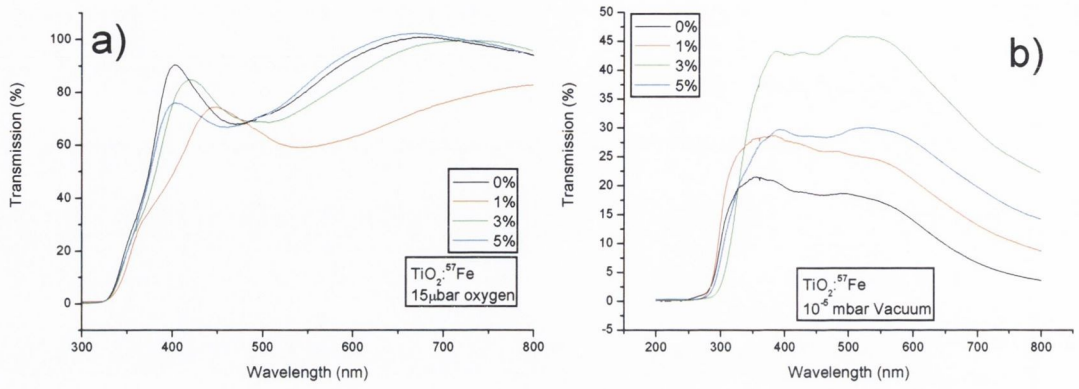



Figure 3.42. Optical transmission plotted against photon wavelentgh for a) the oxidized films and b) the reduced films.

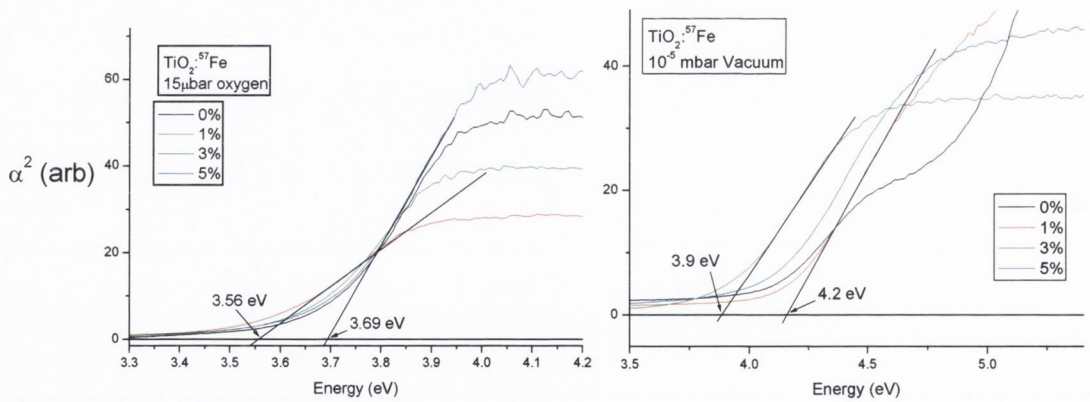



Figure 3.43. Optical absorption coefficient squared ($\alpha^2$) plotted against photon energy for the oxidized films (left) and the reduced films (right).

| | Fe (at%) | Isomer shift ($mm\,s^{-1}$) | Quadr. Splitting ($mm\,s^{-1}$) | $B_{eff}$ ($T \pm 0.1\,T$) | Area ($\% \pm 3\%$) |
|---|---|---|---|---|---|
| Oxidized | 1 | $0.96 \pm 0.02$ | $2.11 \pm 0.06$ | 0.0 | 78 |
| | | $0.40 \pm 0.03$ | $0.56 \pm 0.06$ | 0.0 | 22 |
| | 3 | $0.96 \pm 0.05$ | $2.11 \pm 0.07$ | 0.0 | 13 |
| | | $0.41 \pm 0.02$ | $0.60 \pm 0.06$ | 0.0 | 87 |
| | 5 | $0.42 \pm 0.03$ | $-0.20 \pm 0.05$ | 49.0 | 60 |
| | | $0.39 \pm 0.03$ | $0.53 \pm 0.06$ | 0.0 | 40 |
| Reduced | 1 | $0.05 \pm 0.03$ | $0.01 \pm 0.06$ | 33.0 | 88 |
| | | $-0.04 \pm 0.05$ | $0.40 \pm 0.06$ | 0.0 | 12 |
| | 3 | $0.03 \pm 0.03$ | $-0.01 \pm 0.06$ | 33.2 | 89 |
| | | $0.22 \pm 0.06$ | $0.37 \pm 0.07$ | 0.0 | 11 |
| | 5 | $0.03 \pm 0.05$ | $-0.01 \pm 0.06$ | 33.0 | 93 |
| | | $0.11 \pm 0.06$ | $0.40 \pm 0.08$ | 0.0 | 7 |

Table 6.Fit parameters for CEMS spectra of thin films of Fe-doped rutile. Isomer shifts relative to an $\alpha$-Fe absorber.

ceeds the value of 2.2 Bohr magnetons for iron metal. Nor can the moment of the 5% oxidized film be explained by the hematite impurity, which is antiferromagnetic. The iron in the 1% and 3% oxidized films is in an $Fe^{3+}$ or $Fe^{2+}$ state, but is not magnetically ordered and cannot therefore contribute to the observed moments. Of 18 films which showed ferromagnetism, in only one could the moment be explained by the $\alpha$-Fe content. That was the only film with appreciable coercivity (Fig. 3.31b). In every other case, the moment exceeded that due to magnetically-ordered iron impurity phases.

We have to conclude that the magnetism of the iron-doped rutile films cannot be explained either by contamination or by iron-rich impurity phases. The magnetic moments of the dopant iron ions are not the cause of the ferromagnetism. The key, highlighted by the 1% oxidised film, seems to be the iron valence state. No reduction of $Ti^{4+}$ is expected for substitutional iron. The effect of $Fe^{2+}$ replacing $Ti^{4+}$ is the creation of interstitial atoms or electronic defects:

$$Ti^{4+} + 2O^{2-} \rightarrow Fe^{2+} + 2O^{-}$$

Two holes are created in the p-shells of oxygen anions coordinating the iron cation. These holes are expected to be strongly correlated, and delocalized over the first or more distant coordination spheres. Their spins will couple ferromagnetically. Orbital moments on each $O^{-}$ anion should couple parallel to the spin, according to Hund's third rule, although the spin-orbit coupling for oxygen is very weak. If the orbital moment is unquenched, the greatest moment achievable for the $^2P_{3/2}$ state

with $g = 4/3$ is 2 $\mu_B$. In fact we observe larger moments than this, which suggests the presence of extra oxygen holes or Ti vacancies[24]. A suggestion by Gallego et al[25] that magnetism in oxide films is due to oxygen holes associated with the surface atoms leads to a moment of 18 $\mu_B\,nm^{-2}$ in $TiO_2$, assuming 1 $\mu_B$ per oxygen and taking both surface and interface oxygen into account, an insufficient explanation of the observed moment. An alternative suggestion is a giant orbital moment associated with orbital surface currents[26][27].

# References

[1] M. W. Chase, Jr., J. Phys. Chem. Ref. Data Monogr. 9, 1759 (1998)

[2] According to Strem Chemicals' product catalog printed version or online catalog at http://www.strem.com/ , the boiling temperature of titanium dioxide is 2773–3273 K.

[3] Y. Matsumoto, M. Murakami, T. Shono, T. Hasegawa et al, Science 292 854 (2001).

[4] Z. Wang, W. Wang, J. Tang, L.D. Tung, L. Spinu and W. Zhou, Appl. Phys. Lett., 83, 518 (2003).

[5] R. Suryanarayanan, V.M. Naik, P. Kharel, P. Talagala and R. Naik, J. Phys. Condens. Matter. 17, 755 (2005).

[6] N.H. Hong, J. Sakai, W. Prellier, A. Hassini, A. Ruyter and F. Gervais, Phys. Rev. B, 70 195204 (2004).

[7] Y.J. Kim, S. Thevuthasan, T. Droubay, A.S. Lea, C.M. Wang, V. Shutthanandan, S.A. Chambers, R.P. Sears, B. Taylor and B. Sinkovic, Appl. Phys. Lett., 84 3531 (2004).

[8] K. Ueda, H. Tabata and T Kawai, Appl. Phys Lett. 79, 988 (2001).

[9] J. M. D. Coey, A. P. Douvalis, C. B. Fitzgerald and M. Venkatesan, Appl. Phys. Lett. 84 1332 (2004).

[10] S.N. Kale, S.B. Ogale, S.R. Shinde, M. Sahasrabuddhe, V.N. Kulkarni, R.L. Greene, T. and T. Venkatesan, Appl. Phys. Lett., 82, 2100 (2003).

[11] J. Philip, A. Punnoose, B.I. Kim, K.M. Reddy, S. Layne, J.O. Holmes, B. Satpati, P.R. Leclair, T.S. Santos and J.S. Moodera, Nature Materials 5, 298 (2006 ).

[12] K.A. Griffin, A.B. Pakhomov, C.M. Wang, S.M. Heald, and K.M. Krishnan, Phys. Rev. Lett., 94, 157204 (2005).

[13] T. Zhao, S.R. Shinde, S.B. Ogale, H. Zheng, T. Venkatesan, R. Ramesh and S. Das Sarma, Phys. Rev. Lett., 94, 126601 (2005).

[14] J.M.D. Coey, M. Venkatesan and C.B. Fitzgerald, Nature Materials 4, 173 (2005).

[15] C.N.R. Rao and F.L. Deepak, J. Mat. Chem., 15, 573 (2005).

[16] T.C. Kaspar, S.M. Heald, C.M. Wang, J.D. Bryan, T. Droubay, V. Shutthanandan, S. Thevuthasan, D.E. McCready, A.J. Kellock, D.R. Gamelin and S.A. Chambers, Phys. Rev. Lett., 95, 217203 (2005)

[17] S.A. Chambers., T. Droubay, C.M. Wang, A.S. Lea, R.F.C. Farrow, L. Folks, V. Deline and S. Anders, Appl. Phys. Lett., 82, 1257 (2003).

[18] D.W. Abraham, M.M. Frank and S. Guha, Appl. Phys. Lett., 87, 252502 (2005)

[19] N. Hoa H., J. Sakai, N. Poirot, and V. Brize, Phys. Rev. B 73, 132404 (2006)

[20] S. D. Yoon, Y. Chen, A. Yang, T. L. Goodrich, X. Zuo, D. A. Arena, K. Ziemer, C. Vittoria and V. G. Harris 2006 J. Phys.: Condens. Matter, 18, L355-L361 (2006)

[21] D. Liljequist, Nucl. Inst. Meth. Phys. Res. B, 142, 295 (1998)

[22] H. M. Widatallah, A. M. Gismelseed, K. Bouziane, F. J. Berry, A. D. Al Rawas, I. A. Al-Omari, A. A. Yousif and M. E. Elzain, Hyperfine Interactions 156-7, 223 (2006)

[23] J. Pascual, J. Camassel, and H. Mathieu, Phys. Rev. B 18, 5606 (1978)

[24] C.D. Pemmaraju and S. Sanvito, Phys. Rev. Lett., 94, 217205 (2005).

[25] S. Gallego, J. I. Beltrán, J. Cerdá and M. C. Muñoz, J. Phys.: Condens. Matter, 17, L451 (2005)

[26] Z. Vager, R. Naaman, Phys. Rev. Lett., 92, 087205 (2004)

[27] A. Hernando, P. Crespo, M.A. Garcia, Phys. Rev. Lett., 96, 057206 (2006)

# Chapter 4

# $In_2O_3$

"Delay after delay after delay - I mean, Robbie, how do you live your *life* like this?"

Inspirational words from Mike.

## 4.1 Introduction

Indium (III) oxide ($In_2O_3$) is a transparent conducting oxide, with a band gap of 3.6 eV and a transparency in the visible range typically above 90%. The crystal structure is cubic bixbyite ($Ia3$) (Fig. 4.44), with 80 atoms per unit cell and two different In sites. The lattice parameter for bulk $In_2O_3$ has been determined to be $10.117 \pm 0.001$ Å [1], with interatomic bond length distances given in Table 7.

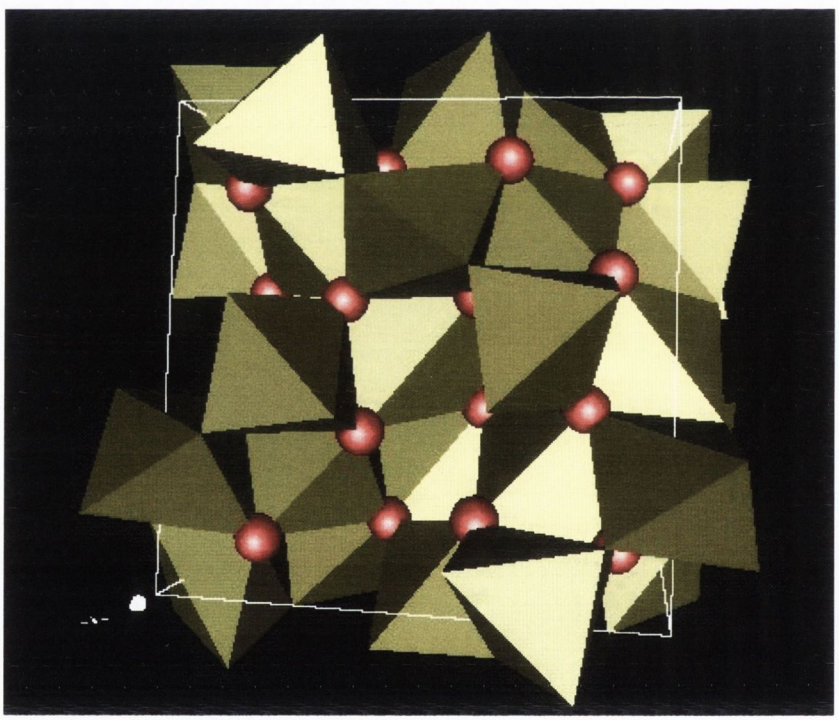


Figure 4.44. The cubic bixbyite structure of $In_2O_3$.

Indium oxide has a density of $\rho = 7120\,\mathrm{kg\,m^{-3}}$ and a formula weight of $277.64\,\mathrm{g\,mol^{-1}}$. It has a melting point of 1913 °C. It is an amphoteric oxide, is insoluble in water and its powder is green/yellow in colour.

| Bond | Distance (Å) | Multiplicity |
|---|---|---|
| In(1)-O | 2.18 | 6 |
| In(2)-O | 2.13 | 2 |
| In(2)-O | 2.19 | 2 |
| In(2)-O | 2.23 | 2 |

Table 7.Bond lengths for bulk indium oxide

Pure stoichiometrical $In_2O_3$ is an insulator, but like most oxides, rarely exists in a perfectly stoichiometric form. $In_2O_3$ is usually substoichiometric with an In/O ratio large than 2/3 [1]. The oxygen vacancies induce donor levels just below the conduction band, and contributing electrons to the conduction band. In Kröger-Vink notation[2], the generation of an oxygen vacancy can be represented as

$$2In_{In} + 3O_O \rightarrow 2In_{In} + 3\square_O^{\blacksquare\blacksquare} + 6e' + \frac{3}{2}O_2$$

Interstitial In from the reduction of an $In_2O_3$ molecule can also donate conduction electrons, with

$$2In_{In} + 3O_O \rightarrow 2In_i^{+C} + 3\square_O + 2Ce' + \frac{3}{2}O_2$$

where C is the magnitude of the positive charge on the interstitial In. Combining these two relations, and given that the $C = 1$ [3], we get

$$2In_{In} + 3O_O \rightarrow 2(1-z)In_{In} + 3\square_O + 2zIn_i^{\blacksquare} + 2ze' + \frac{3}{2}O_2$$

where $z$ is a parameter such that $(0 < z < 1)$. Applying the mass action law, we can derive an equilibrium constant, $K$, relating the carrier concentration, $n$, and the oxygen partial pressure, $p_{O_2}$

$$K = [\square_O]^3 \cdot \left[In_i^{\blacksquare}\right]^{2z} \cdot n^{2z} \cdot p_{O_2}^{\frac{3}{2}}$$

giving us

$$n \propto p_{O_2}^{-\frac{3}{8z}}$$

The conductivity of $In_2O_3$ is therefore highly dependent on the oxygen partial pressure during deposition. The energy of the donor levels produced by stoichiometrical defects, $E_d$, are typically $0.008 - 0.03\,\text{eV}$, though dependent on donor concentration. A donor level of $1.48 \times 10^{-18}\,\text{cm}^{-3}$ is sufficient for the donor level to overlap the bottom of the conduction band. When this occurs, the $In_2O_3$ becomes degenerate [1].

Thin films of $In_2O_3$ have been produced by several different methods: chemi-

[2] See the introduction for an explantation of the use of Kröger-Vink notation.

cal vapour deposition (CVD), evaporation, reactive evaporation, e-beam evaporation, sputtering and ion-beam sputtering - with e-beam evaporation in $0.7 - 2.8 \times 10^{-4}$ mbar providing the films with the highest conductivity [1].

### 4.1.1 Uses of Indium Oxide

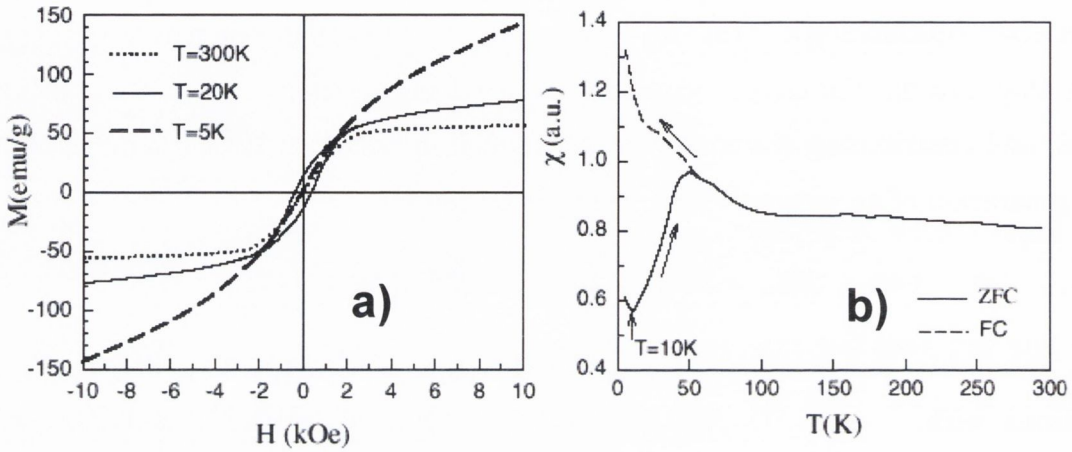



Figure 4.45. Plots showing (a) magnetization loops at different temperatures and (b) the susceptibility behaviour versus temperature for granular $(In_{0.65}Fe_{0.35})_2O_3$ films. From [6].

Indium oxide, while being a transparent conducting oxide, is generally superseded in its use as such by the closely related Sn-doped indium oxide (ITO). As ITO is cheaper and performs better as a TCO, it generally is used instead. ITO is discussed in the next chapter.

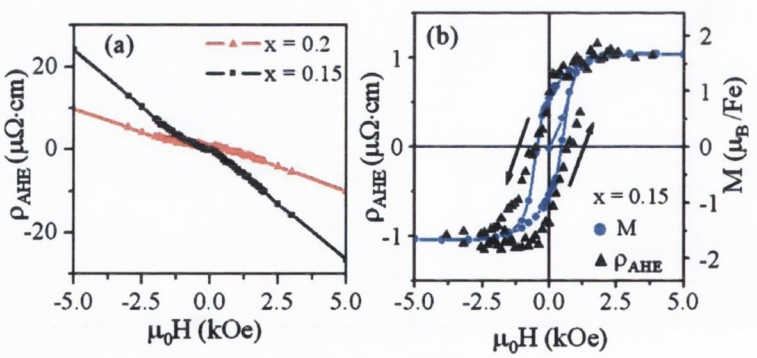



Figure 4.46. Magnetization and Hall effect data for Fe- and Cu- codoped $In_2O_3$. From [8].

In the semiconductor industry, the ease of deposition of indium oxide and its inertness have led to its use as a diffusion barrier - a material that prevents inter-diffusion of metal atoms from two layers into eachother and thus spoiling their properties. As it

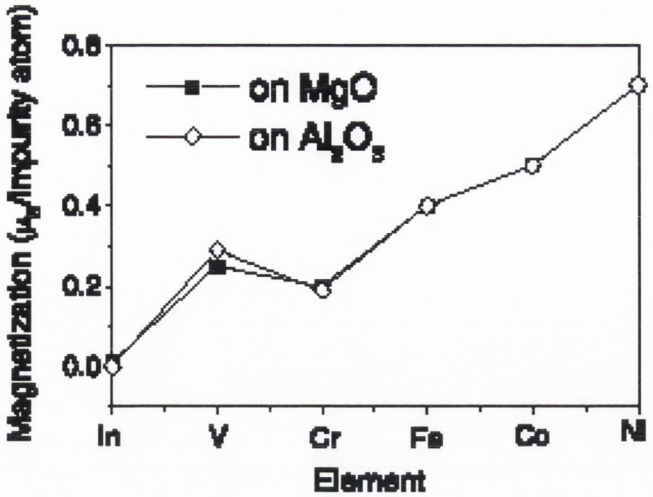



Figure 4.47. A graph of magnetization in $\mu_B$/dopant ion against dopant for $In_2O_3$ thin films. From [12].

is an $n$-type semiconductor, it can be used as a resistive element in integrated circuits. Field effect transistors have been successfully formed from nanowires of indium oxide [4].

It also has uses in histology as an ingredient in staining formulations.

### 4.1.2 Ferromagnetism in Indium Oxide

Magnetism was first reported in thin films of $In_2O_3$ in 1999 by Zhang et al. [5] for granular films of iron clusters in an $In_2O_3$ matrix. The Fe formed clusters in the material which were superparamagnetic at room temperature and ferromagnetic below 50 K, the blocking temperature of the ferromagnetic particles. Follow-up work by the same group [6] also revealed an antiferromagnetic state below 10 K and MR of 5% at room temperature and 500% at 2.2 K.

In 2005, Yoo et al [7] presented evidence of room temperature ferromagnetism in bulk $(In_{1-x}Fe_x)_2O_{3-\delta}$ with Cu co-doping. Moments of up to 6 $\mu_B$/Fe were reported for $x = 0.3$. The presence of impurity phases was investigated by synchotron XRD, transmission electron microscopy (TEM) and Curie temperature analysis. While 1% of the sample was found to be $Fe_3O_4$ in a $x = 0.1$ sample, the authors claim that impurity phases such as ferromagnetic $Fe_3O_4$ and $CuFe_2O_4$ are not responsible for the observed moment, as $T_C$ differs slightly from the two possible impurity phases ($T_C = 750$ K).

This report was soon followed by claims of ferromagnetism in thin films of $(In_{1-x}Fe_x)_2O_{3-\delta}$

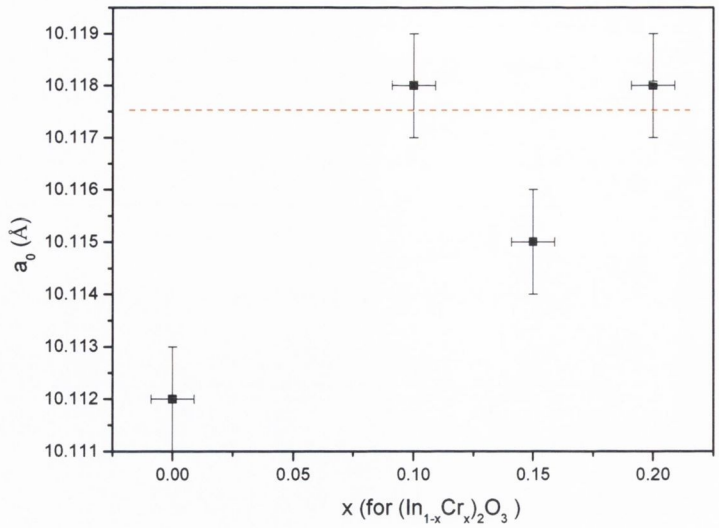



Figure 4.48. A graph of lattice parameter, $a_0$, versus dopant concentration for Cr.

with 2% Cu co-doping for $x = 0.2$ and $x = 0.15$ [8]. The films also had a $T_C = 750\,\mathrm{K}$ and exhibited the anomalous Hall effect (AHE). The films showed a resistivity of $\rho \approx 6 \times 10^{-3}\,\Omega\,\mathrm{cm}$ and a carrier concentration of $n \approx 5 \times 10^{-19}\,\mathrm{cm}^{-3}$.

Peleckis et al have observed room temperature ferromagnetic behaviour in Mn and Fe co-doped $In_2O_3$ [9] and also in Ni-doped $In_2O_3$ [28]. The (Mn,Fe) exhibited a moment of 0.98 $\mu_B$/(Fe+Mn) and the Ni-doped films exhibited a moment of up to 0.7 $\mu_B$/Ni. Peleckis also reported that Fe-doped $In_2O_3$ is paramagnetic [9]. Room temperature ferromagnetism has also been reported in Cr-doped $In_2O_3$ [11], with moments of 1.5 $\mu_B$/Cr for 2% Cr reported and the anomalous Hall effect observed in these samples. Hong et al. [12] have doped $In_2O_3$ thin films with a range of transition metals and found them all to be ferromagnetic at room temperature (Fig. 4.47).

Undoped $In_2O_3$ has also been reported as ferromagnetic at room temperature when deposited on MgO substrates [13].

## 4.2 Sample Preparation

Ceramic target pellets of differing transition-metal dopant and concentration were prepared by the mechanical alloying of $In_2O_3$ and an oxide of the relevant metal dopant(s) (Table 8). The targets were then sintered at 1323 K for 12 hours. PLD films were prepared from these targets using a Lambda Physik KrF Excimer laser op-

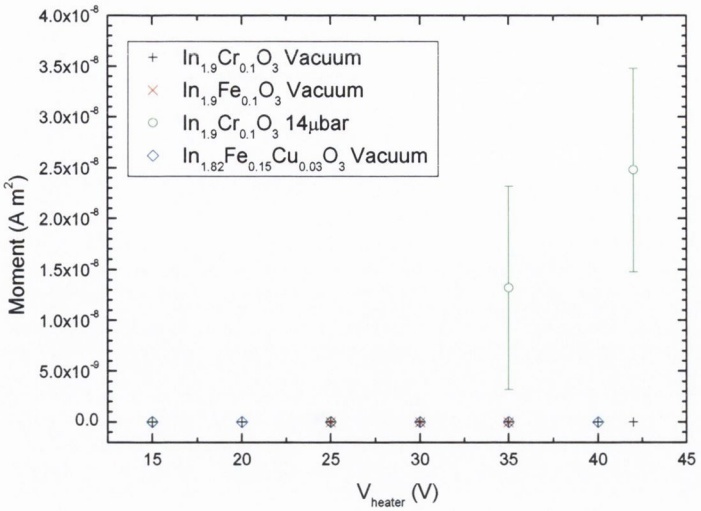



Figure 4.49. A plot of magnetic moment at 300 K versus substrate heater voltage for different dopings of $In_2O_3$ thin films.

| | Cr | Fe | Fe,Cu |
|---|---|---|---|
| 2.5% | √ | × | × |
| 5% | √ | √ | × |
| 7.5% | √ | × | √ |
| 10% | √ | √ | × |

Table 8.A table of $In_2O_3$ targets prepared.

erating at $\lambda = 248\,\text{nm}$. The fluence of the beam was $2\,\text{J}\,\text{cm}^{-2}$, with a pulse frequency of 3, 5 and 10 Hz. The films were deposited onto single crystal $Al_2O_3$ (001) and (102) substrates at temperatures ranging between 200 °C and 800 °C[3]. The base pressure of the chamber was $1 \times 10^{-5}$ mbar prior to deposition and the chamber was flushed with 300 $\mu$bar of $O_2$ three times before acquiring a probe signal to characterize the plume and once again before deposition. The films were deposited in $O_2$ partial pressure 14 $\mu$bar and $8 \times 10^{-5}$ mbar.

To investigate the properties of $Cr_2O_3$ when doped with indium, thin films of In-doped $Cr_2O_3$ were produced in exactly the same manner as the Cr-doped $In_2O_3$ thin films, with separate ceramic targets made for this purpose.

A list of a representative set of samples produced is given in Table 9.

## 4.3 Sample Characterization

[3] Refer to Appendix 2 for the relationship between heater voltage, $V_{heater}$, and substrate temperature.

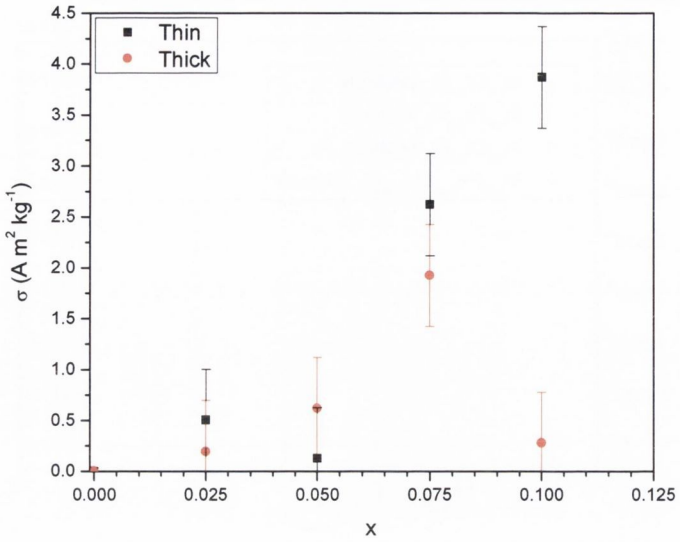



Figure 4.50. A plot of magnetization versus dopant concentration, $x$, for $(In_{1-x}Cr_x)_2O_3$ thin films deposited in 14 $\mu$ bar of $O_2$.

### 4.3.1 Structure

Analysis of films grown on r-cut sapphire show that the films also grow with a (111) and (110) orientation (Fig. 4.51a). Careful measurement of $2\theta$ regions where $Cr_2O_3$ lattice reflection can appear show the presence of a tiny amount ($< 0.1\%$) of $Cr_2O_3$ present in the $(In_{0.9}Cr_{0.1})_2O_3$ thin film. $Cr_2O_3$ peaks were not observed in films with small doping concentrations.

The (222) reflection peak was fitted using a Pseudo-Voigt function and the lattice parameter derived from its position using the

$$\frac{1}{d^2} = \frac{h^2 + k^2 + l^2}{a^2}$$

The lattice constant for $In_2O_3$ is given as $a_0 = 10.117 - 10.118$ Å. For the undoped films, the values obtained were lower, with $a_0 = 10.112$ Å. The lattice expanded with addition of Cr (Fig. 4.48) to the accepted value for $In_2O_3$.

The thin films of In-doped $Cr_2O_3$ were measured and were found to grow highly orientated in the (012) direction (Fig. 4.52). The Scherrer formula estimated the size of the crystallites to be $D_v \approx 20$ nm.

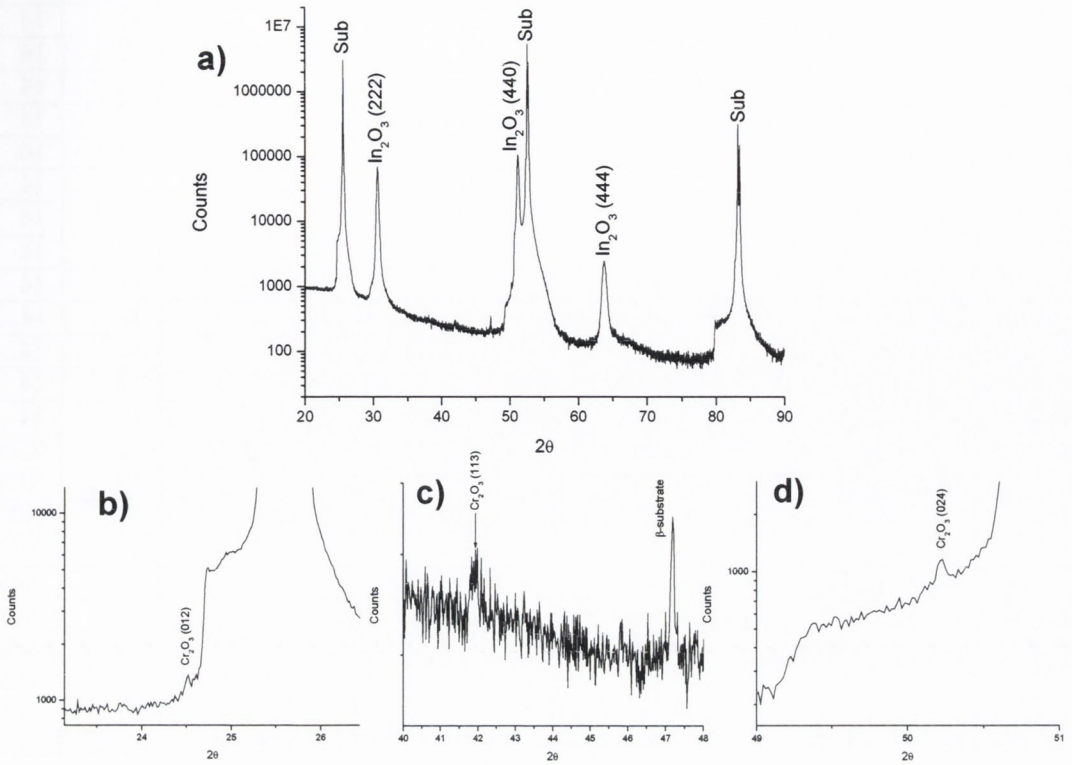



Figure 4.51. a) An x-ray diffractogram of an $(In_{0.95}Cr_{0.05})_2O_3$ thin film with b), c) and d) as close-ups of $Cr_2O_3$ peaks positions.

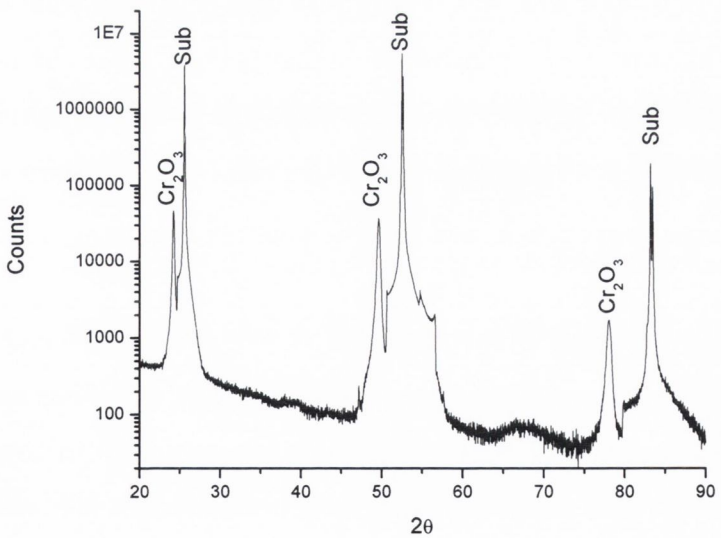



Figure 4.52. A x-ray diffractogram of a $(Cr_{0.95}In_{0.05})_2O_3$ thin film. The $Cr_2O_3$ peaks are (012), (024) and (036).

| Sample Code | Composition | Substr. $Al_2O_3$ | Moment ($10^{-8}$ A m$^2$) | t (nm) | $\rho_{RT}$ ($\Omega$ cm) | $V_{heat}$ (V) | $p_{dep}$ ($\mu$ bar) |
|---|---|---|---|---|---|---|---|
| 44ICR201 | $In_{1.8}Cr_{0.2}O_3$ | r-cut | $4.48 \pm 1$ | 70 | - | 42 | 14 |
| 54ICR201 | $In_{1.8}Cr_{0.2}O_3$ | r-cut | $1.10 \pm 1$ | 240 | 0.0131(3) | 42 | 14 |
| 54IC1501 | $In_{1.85}Cr_{0.15}O_3$ | r-cut | $3.03 \pm 1$ | 70 | - | 42 | 14 |
| 64ICR201 | $In_{1.85}Cr_{0.15}O_3$ | r-cut | $7.79 \pm 1$ | 240 | 0.00122(4) | 42 | 14 |
| 64ICR101 | $In_{1.9}Cr_{0.1}O_3$ | r-cut | $0.15 \pm 1$ | 70 | - | 42 | 14 |
| 64ICR102 | $In_{1.9}Cr_{0.1}O_3$ | r-cut | $2.48 \pm 1$ | 240 | 0.00922(1) | 42 | 14 |
| 74ICR501 | $In_{1.95}Cr_{0.05}O_3$ | r-cut | $0.58 \pm 1$ | 70 | - | 42 | 14 |
| 74ICR502 | $In_{1.95}Cr_{0.05}O_3$ | r-cut | $0.73 \pm 1$ | 240 | 0.01371(3) | 42 | 14 |
| 45IN2O31 | $In_2O_3$ | r-cut | 0 | 240 | 0.0083(2) | 42 | 14 |
| 45IN2O32 | $In_2O_3$ | r-cut | 0 | 70 | - | 42 | 14 |
| 104IC201 | $In_{1.8}Cr_{0.2}O_3$ | r-cut | 4.00 | 140 | - | 42 | 14 |
| 104IC202 | $In_{1.8}Cr_{0.2}O_3$ | r-cut | 0.06 | 35 | - | 42 | 14 |
| 124IC201 | $In_{1.8}Cr_{0.2}O_3$ | r-cut | 6.79 | 175 | - | 42 | 14 |
| 128IFCu1 | $In_{1.82}Fe_{0.15}Cu_{0.03}O_3$ | c-cut | 0 | 280 | 0.041(1) | 42 | 0.08 |
| 99ICr1O1 | $In_{1.9}Cr_{0.1}O_3$ | r-cut | 0 | 280 | - | 40 | 0.08 |
| 129ICr11 | $In_{1.9}Cr_{0.1}O_3$ | r-cut | 0 | 280 | - | 35 | 0.08 |
| 129ICr12 | $In_{1.9}Cr_{0.1}O_3$ | r-cut | 0 | 280 | - | 30 | 0.08 |
| 139ICr11 | $In_{1.9}Cr_{0.1}O_3$ | r-cut | 0 | 280 | - | 25 | 0.08 |
| 149ICr11 | $In_{1.9}Cr_{0.1}O_3$ | r-cut | 0 | 280 | - | 20 | 0.08 |
| 149ICr12 | $In_{1.9}Cr_{0.1}O_3$ | r-cut | 0 | 280 | - | 15 | 0.08 |
| 199IF1O1 | $In_{1.9}Fe_{0.1}O_3$ | r-cut | 0 | 280 | $1.3 \times 10^{-2}$ | 30.4 | 0.08 |
| 219IF1O1 | $In_{1.9}Fe_{0.1}O_3$ | r-cut | 0 | 280 | $1.3 \times 10^{-1}$ | 25.3 | 0.08 |
| 219IF1O2 | $In_{1.9}Fe_{0.1}O_3$ | r-cut | 0 | 280 | $2.5 \times 10^{-2}$ | 35.2 | 0.08 |

Table 9.A table summarising the properties of doped indium oxide films

### 4.3.2 Film Thickness

Film thicknesses for films thinner than 100 nm were measured using x-ray reflectivity. The film deposition rate was calibrated against the thicknesses measured by XRR. The time taken to deposit the thicker films (140 nm) was extrapolated from the time taken to deposit the thinner films and cross-checked with optical reflectometry. The films were deposited at thicknesses of 18 nm and 140 nm. There was no significant change in deposition rate for differing transition-metal doping.

### 4.3.3 Magnetization

Room temperature moments were only observed in thin films of Cr-doped $In_2O_3$ deposited on r-cut sapphire at substrate heater temperatures in the range of $T_{dep} = 700 - 750\,^{\circ}C$. In addition, ferromagnetism and high conductivity were only observed in films deposited in a 14 $\mu$ bar partial pressure of $O_2$ (Fig. 4.49).

The magnetization of thin films scaled with the concentration $x$ (where $x$ is derived from the composition $(In_{1-x}Cr_x)_2O_3$). No moment was observed for undoped

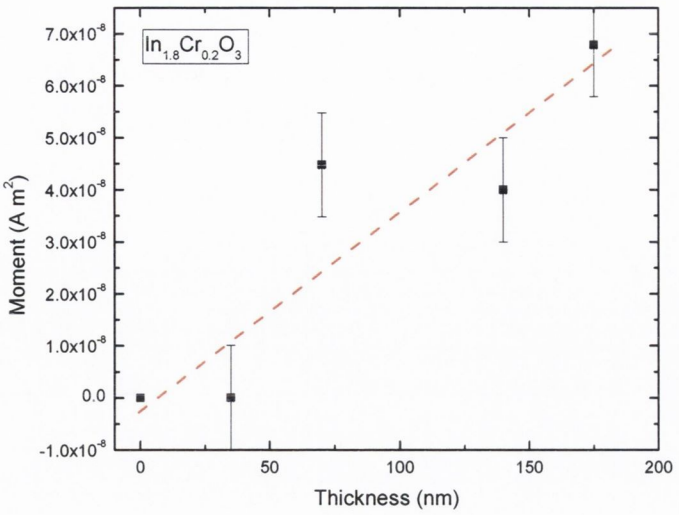



Figure 4.53. A plot of magnetic moment of $(In_{0.9}Cr_{0.1})_2O_3$ thin films versus their thickness in nanometers.

$In_2O_3$, nor was any moment observed for a substrated that had been heated to 725 °C in the deposition chamber at a oxygen partial pressure of 14 $\mu$ bar.

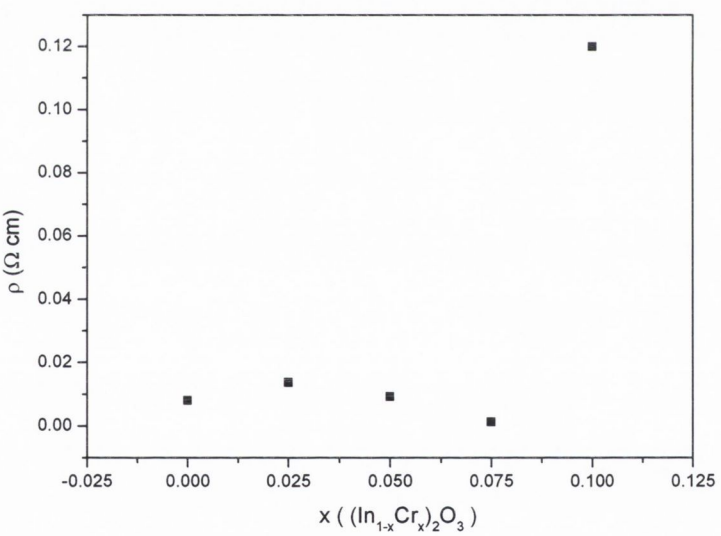



Figure 4.56. A plot of resistivity versus Cr doping concentration. The error bars are too small to be seen.

The magnetization of the thin films was measured as a function of thickness of the thin films as measured by x-ray and optical reflectometery. The moment was found

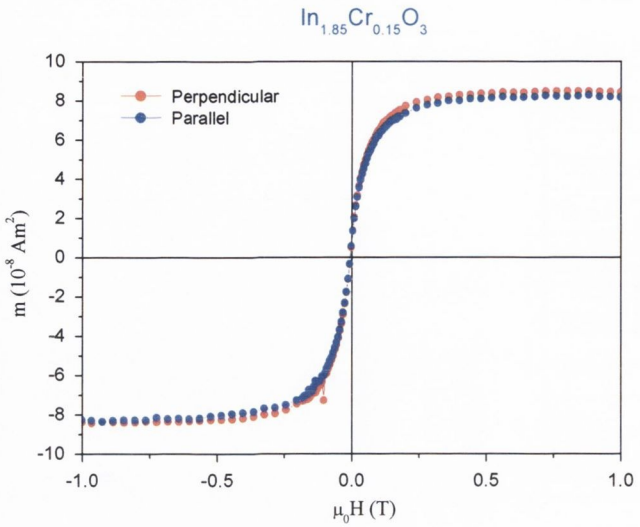



Figure 4.54. Magnetization measurements of an $(In_{0.925}Cr_{0.075})_2O_3$ thin film with the field applied parallel and perpendicular to the sample. The diamagnetic background due to the substrate has been subtracted.

to increase with thickness.

Measurements of the moment of the films with the field perpendicular and parallel to the thin film revealed no evidence of anisotropy of the moment in the sample (Fig. 4.54).

The thin films of In-doped $Cr_2O_3$ showed no ferromagnetic moment at room temperature (Fig. 4.55). This excludes the possibility that the moment is due to uncompensated antiferromagnetic $Cr_2O_3$ clusters.

### 4.3.4 Electrical Conductivity

Resistance versus temperature measurement for the Cr-doped $In_2O_3$ measurements showed no dependence on doping levels for lower concentrations. For the largest doping concentration examined, $(In_{0.9}Cr_{0.1})_2O_3$, a much larger resistivity was observed.

The undoped films show a minimum in resistivity at around 175 °C. Above this temperature, the films exhibit metallic behaviour and below it, they display a semiconducting behaviour (Fig. 4.57a). For small and medium doping concentrations, the films show no change in slope of the thermal coefficient of resistivity from $4-300$ K, showing only a semiconductor-like temperature dependence (Fig. 4.57b). The heavily doped films show a large increase in resistivity at low temperatures (Fig. 4.57c).

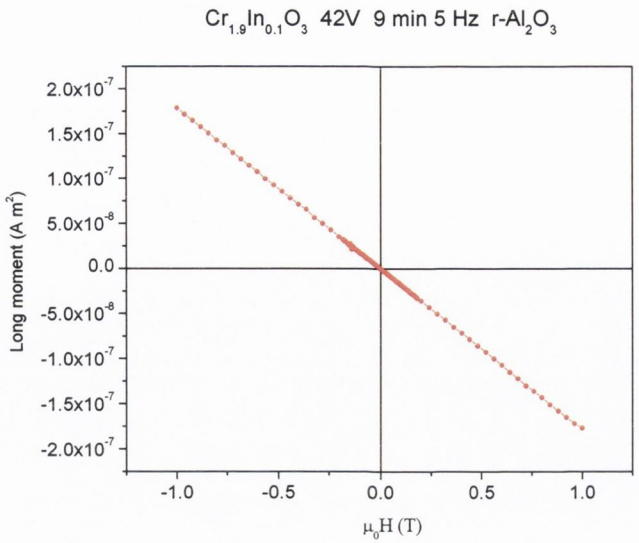



Figure 4.55. A M-H loop of a $(Cr_{0.95}In_{0.05})_2O_3$ thin film.

### 4.3.5 MR measurements

MR measurements of the undoped $In_2O_3$ thin film show a positive MR at room temperature. At temperatures below 100 K, a negative MR is observed in fields of less than 2.5 T, but a positive MR is present for applied fields greater than 2.5 T (Fig. 4.58a).

For the $(In_{0.9}Cr_{0.1})_2O_3$ and $(In_{1.975}Cr_{0.025})_2O_3$ thin films, there is no observable MR at room temperature. At 2 K, there is a large positive MR of $30 - 60\%$. A small negative MR is present in intermediate temperatures (Fig. 4.58b and d).

The $(In_{0.925}Cr_{0.075})_2O_3$ thin films showed only a small negative MR at low temperatures.

### 4.3.6 Magneto-Optical Kerr Effect (MOKE)

Magnetic Cr-doped thin films of $In_2O_3$ were examined by magneto-optical Kerr effect. There was no measureable Kerr effect in any of the magnetic samples in fields of up to 100 mT.

## 4.4 Discussion

From the magnetometry measurements, we see that only the Cr-doping clearly

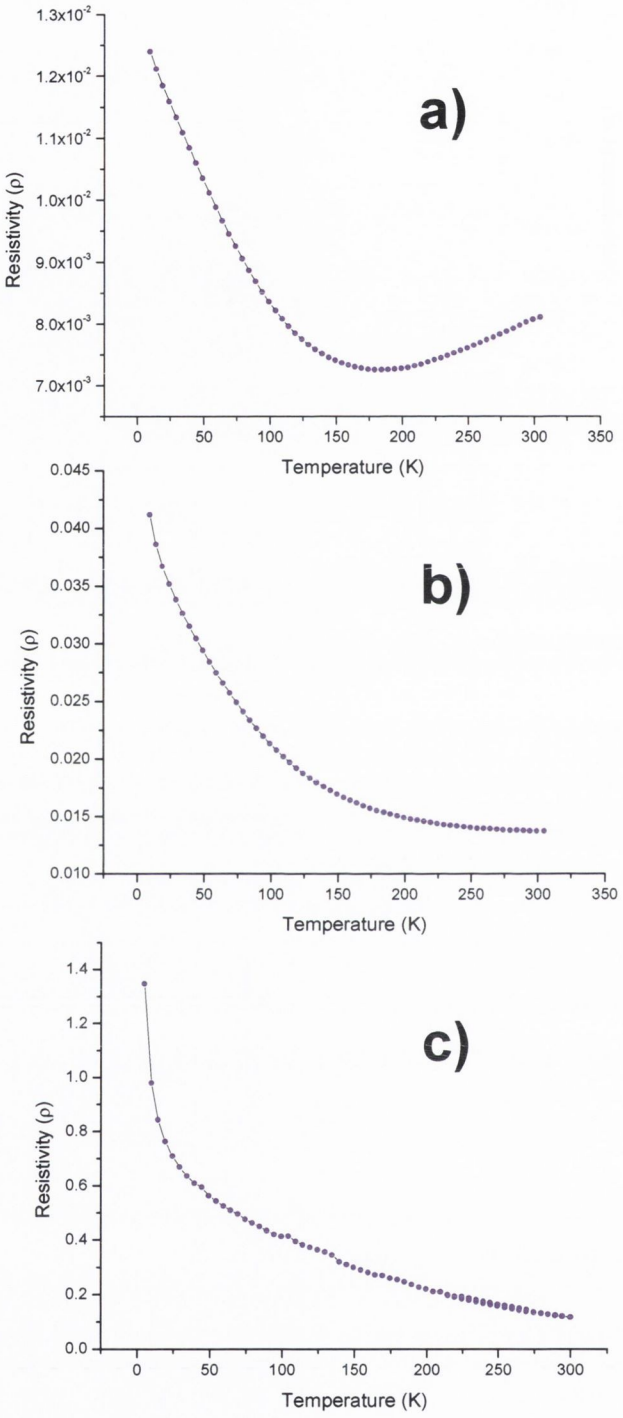



Figure 4.57. Resistivity versus temperature measurements for a) an $In_2O_3$ thin film b) an $(In_{0.925}Cr_{0.025})_2O_3$ thin film and c) an $(In_{0.9}Cr_{0.1})O_3$ thin film

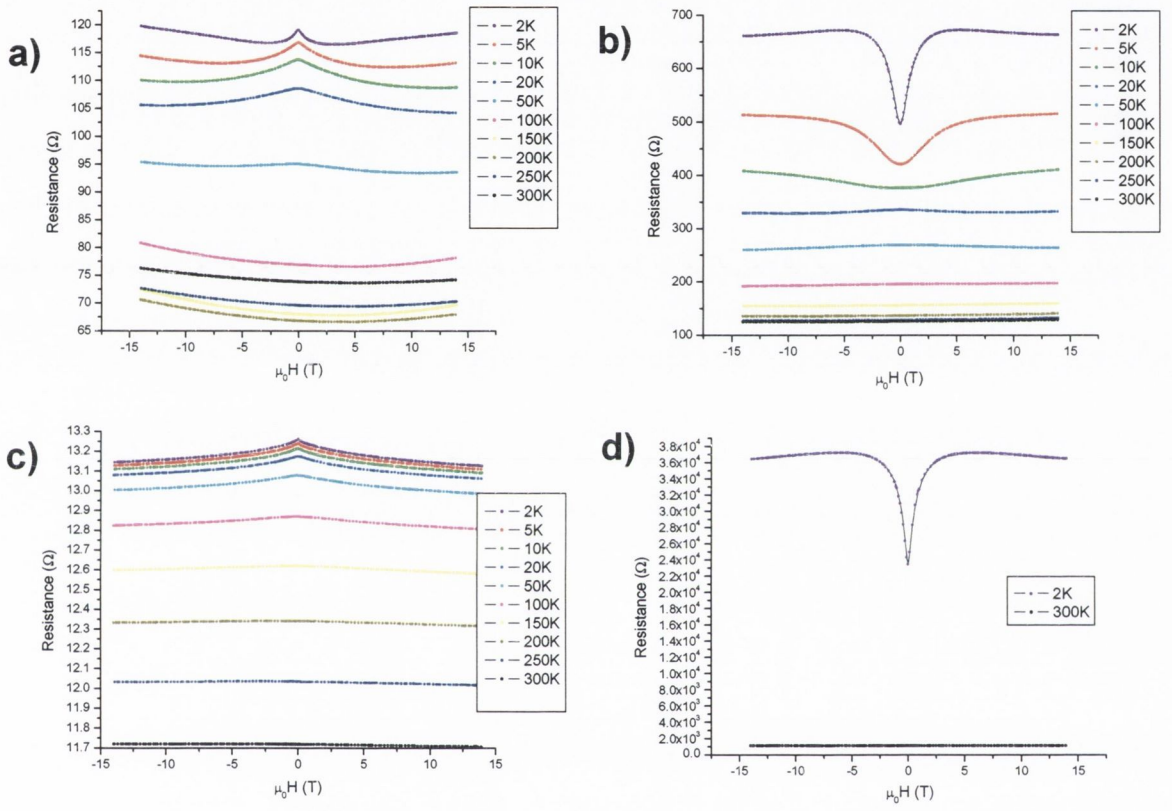



Figure 4.58. Magnetoresistance measurements at temperature from $2 - 300\,K$ for thin films of a) $In_2O_3$,b) $(In_{0.975}Cr_{0.025})O_3$, c) $(In_{0.925}Cr_{0.075})_2O_3$, and d) $(In_{0.9}Cr_{0.1})_2O_3$.

induces ferromagnetism in the thin films at higher deposition temperatures. This is in agreement with previous reports [11]. The results here, however, directly show the presence of Cr2O3 segregation while this has only been speculated upon. While phase segregation is undesirable, the fact that Cr2O3 is antiferromagnetic implies that it cannot contribute to the moment observed. Moreover, there was no observation of phase segregation of the dopant Cr into ferromagnetic CrO2, which was previously dismissed as unlikely and not disproved [11].

The magnetization increases with increasing dopant concentration, reaching values of up to 4 Am2/kg, approximately 4% that of magnetite.

Comparing the magnetoresistance data to the magnetization results, we see little or no correlation. The MR maybe related to the inclusions of Cr2O3, which is known to increase magnetoresistance and lower the conductivity [16], as was observed in these films. If the Cr2O3 does not contribute to the measured ferromagnetic moment and is responsible for the magnetoresistance, we would not expect to see any correlation between the two properties.

# References

[1] M. Marezio, Acta Cryst. 20, 723 (1966)

[2] H. L. Hartnagel, A. L. Dawar, A. K. Jain and C. Jagadish, "Semiconducting transparent thin films" (London, 1995)

[3] T. Tomita, K. Yamashita, Y. Hayafuji and H. Adachi, Appl. Phys. Lett. 87, 051911 (2005)

[4] C. Li, D. Zhang, S. Han, X. Liu, T. Tang, B. Lei, Z. Liu, C. Zhou, Ann. N.Y. Acad. Sci. 1006, 104 (2003)

[5] L. Zhang, L. S. Zhang, R. Z. Zhang, Y. H. Liu, W. X Zhang, B. X. Huang, L. M. Mei, Prog. in Natural Sci. 9, 353 (1999)

[6] B. Huang, Y. Liu, J. Wang, R. Zhang, L. Zhang, L. Zhang and L. Mei, J. Phys.: Condens. Matter 15, 47 (2003)

[7] Y. K. Yoo, Q. Xue, H.-C. Lee, S. Cheng, X.-D. Xiang, G. F. Dionne, S. Xu, J. He, Y. S. Chu, S. D. Preite, S. E. Lofland and I. Takeuchi, Appl. Phys. Lett. 86, 042506 (2005)

[8] J. He, S. Xu, Y. K. Yoo, Q. Xue, H.-C. Lee, S. Cheng, X.-D. Xiang, G. F. Dionne,and I. Takeuchi, Appl. Phys. Lett. 86, 052503 (2005)

[9] G. Peleckis, X. Wang, and S. X. Dou, Appl. Phys. Lett. 88, 132507 (2006)

[10] G. Peleckis, X. Wang, and S. X. Dou, Appl. Phys. Lett. 89, 022501 (2006)

[11] J. Philip, A. Punnoose, B.I. Kim, K.M. Reddy, S. Layne, J.O. Holmes, B. Satpati, P.R. Leclair, T.S. Santos, J.S. Moodera, Nature Materials 4, 298-304 (2006)

[12] N. H. Hong, J. Sakai, N. T. Huong, A. Ruyter and V. Brizé, J. Phys.: Condens. Matter 18, 6897 (2006)

[13] N. H. Hong, J. Sakai, N. Poirot, V. Brizé, Phys. Rev. B 73, 132404 (2006)

[14] S. Kohiki, Y. Murakawa, K. Hori, H. Shimooka, T. Tajiri, H. Deguchi, M. Oku, M. Arai, M. Mitome, Y. Bando, Jpn. J. Appl. Phys. 44, L979 (2005)

[15] N. H. Hong, J. Sakai, N. T. Huong, V. Brizé, Appl. Phys. Lett. 87, 102505 (2005)

[16] J. M. D. Coey, A. E. Berkowitz, Ll. Balcells, and F. F. Putris, Phys. Rev. Lett. 80, 3815 - 3818 (1998)

# Chapter 5

# Indium-Tin Oxide

"Basic research is like shooting an arrow into the air and, where it lands, painting a target."

Homer Burton Adkins

## 5.1 Introduction

Indium tin oxide (ITO) is a mixture of indium oxide ($In_2O_3$) and tin oxide ($SnO_2$), typically 90% $In_2O_3$, 10% $SnO_2$ by weight. It crystallizes in the cubic bixbyite lattice, space group Ia3 [1] (Fig. 5.59). ITO has a density of $\rho \approx 7160\,\mathrm{kg\,m^{-3}}$ (depending on the tin content) and is greenish-yellow in its powder form. The thin films are transparent, even when grown in low oxygen pressures. It has a melting point of approximately 1700 °C. Its formula weight is around $264.94\,\mathrm{g\,mol^{-1}}$, depending on the tin content.

The lattice constant values have commonly been reported larger for ITO than for $In_2O_3$ [2],[3] (Fig. 5.60a), and this increase in lattice parameter is highly dependent on the deposition conditions [3], with values for $a_0$ ranging between 10.15 Å and 10.31 Å. Lower values of oxygen partial pressure result in smaller lattice parameters [4], while larger lattice parameters can be achieved with higher deposition temperature [5]. The lattice expansion is attributed to both substitutional $Sn^{4+}$ ions replacing the $In^{3+}$ and interstitial Sn [3], however the fact that the ionic radius of $In^{3+}$ is typically larger (81 pm) than that of $Sn^{4+}$ (71 pm) implies the lattice expansion is primarily due to interstitials. The valence state of the Sn atoms (Fig. 5.61) has been determined to be 4+ by $^{119}$Sn Mössbauer studies [6]. The lattice constant is reported to reduce with increased tin doping when the valence of the tin has been confimed as 4+ (Fig. 5.60b). The contradiction between Fig. 5.60a) and Fig. 5.60b) can be explained by the fact that the lattice contracts when the Sn dopes into the In site, but expands when it assumes interstitial positions. ITO exhibits a strong preference of orientation in the (111) or (001) directions, depending on the deposition conditions [3].

ITO is a transparent conducting oxide, with a direct bandgap of 3.75 eV [7] and metallic resistivities as low as $10^{-5} - 10^{-4}\,\Omega\,\mathrm{cm}$. $In_2O_3$ is usually oxygen-deficient and

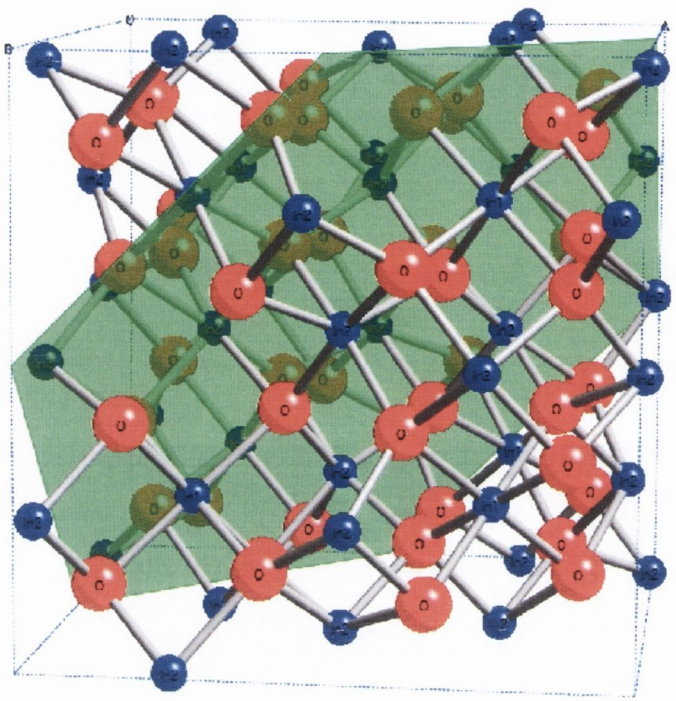


Figure 5.59. The cubic bixbyite crystal structue of $In_2O_3$, and hence ITO, with the (222) plane in shaded green. The O atoms are represented by red spheres and the In/Sn atoms are represented by blue spheres.

these oxygen vacancies form a shallow donor level close to the conduction band, as is characteristic of an oxygen-deficient semiconductor. However, this level is extremely shallow, lying just 0.03 eV below $E_c$, much less than the usual values for semiconducting oxides ($0.1 - 0.5$ eV) [3]. The tin-doping introduces an impurity $5s$ band just below the $\square_o^x$ level[4]. If the $Sn^{4+}$ substitutes the $In^{3+}$, it forms a $Sn^{3+}$:($4d^{10}5s^1$) one electron level which is easily ionized to contribute its extra conduction electron to the In $5s$ conduction band, leaving an $Sn^{4+}$ core. The Sn is thus an $n$-type donor (Fig. 5.62). The oxygen vacancy level also contributes electrons to the conduction band.

This holds for low (< 10 mol%) doping, with higher doping levels producing compensation of the $n$-type doping. The low resistivity is due then to the large electron concentration resulting from the introduction of electrons from the $Sn^{4+}$ and the presence of oxygen vacancies. The carrier density is typically $10^{20} - 10^{22}\,cm^{-3}$, and the carrier mobility is $12 - 92\,cm^2\,V^{-1}\,s^{-1}$, depending on the Sn concentration and the

[4] Using Kröger-Vink notation, from Chapter 1.

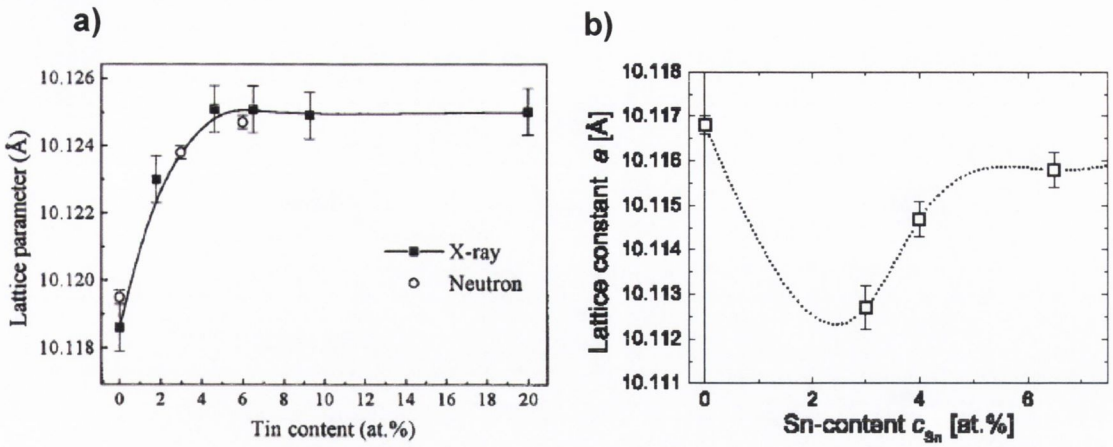



Figure 5.60. The effect of Sn-doping on the lattice parameter of $In_2O_3$ a) from [2] and b) from a study confirming the presence of the $Sn^{4+}$ ion [6].

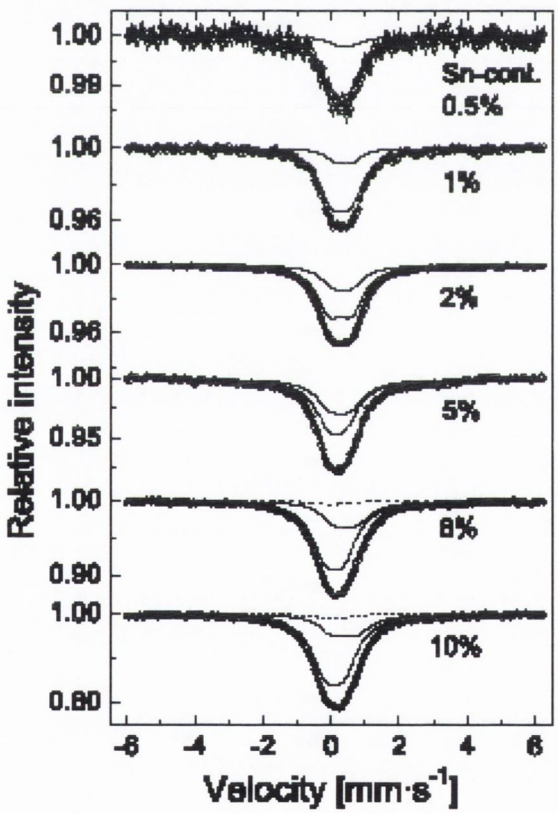



Figure 5.61. Mössbauer spectra of ITO samples with various Sn content (Sn content indicated in the figure [at%]). From [6].

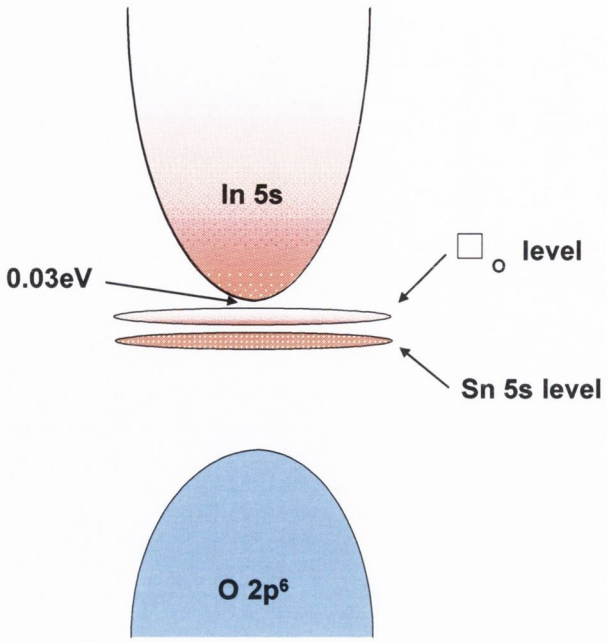



Figure 5.62. Schematic energy band model of indium-tin oxide for light (< 10 mol%) tin doping.

crystal quality.

Many different techniques have been used for deposition of ITO such as reactive thermal evaporation [8], RF and DC sputtering [9], [10], spray pyrolysis [11], magnetron sputtering [12] and ion beam sputtering [13].

### 5.1.1 Uses of ITO

As indium is a relatively scarce metal, uses for indium-tin oxide tend to focus on its property of being an excellent transparent conducting oxide. Even for these purposes, the fact that tin, which also forms a conducting transparent oxide of its own, is 1,000 times more abundent in nature means that ITO is only used when a very high conductivity is needed in a transparent solid. As a result, ITO is used as a transparent contact in high-performance optoelectronic devices such as LEDs, solar cells, lasers and phototransistors.

It has also been used in heating elements for windows, anti-reflection coatings and for thermally insulating coatings on glass.

### 5.1.2 Ferromagnetism in ITO

The first report of a ferromagnetic moment in ITO thin films came in 2004 when Moodera et al [8] reported high-temperature ferromagnetism in Mn-doped ITO grown

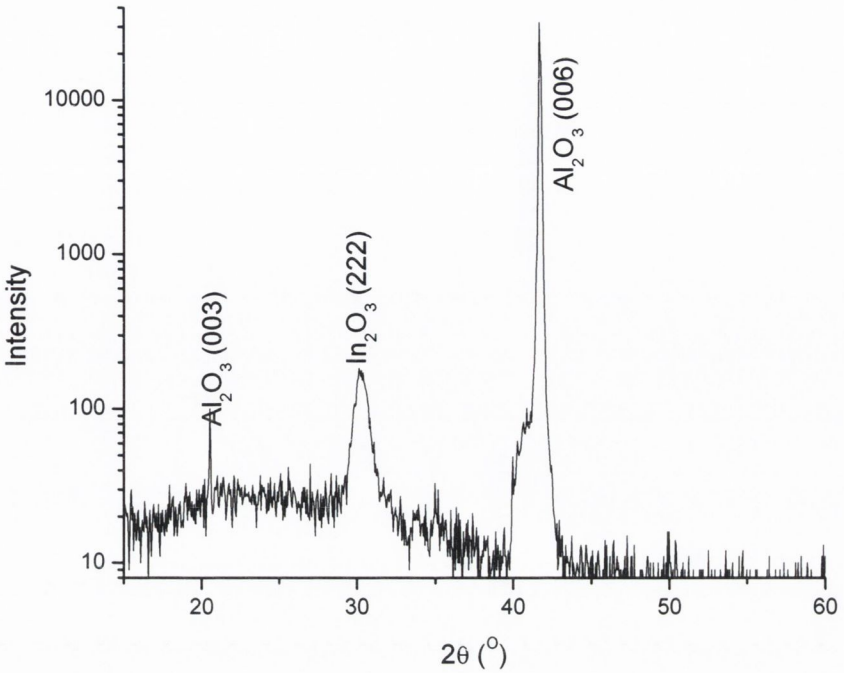



Figure 5.63. An XRD of undoped ITO thin film deposited on c-cut sapphire, exhibiting a (111) orientation.

on $Si/SiO_2$ substrates. The films were grown by reactive thermal evaporation, and the films had a lattice constant of 10.110 Å, suggesting that the Sn doped substitutionally in the In site. The room temperature magnetic moment is 0.8 $\mu_B$/Mn in 5% Mn-doped films with $n$-type electrical conduction, with a carrier concentration of $n \approx 10^{-19}\,\mathrm{cm}^{-3}$ for the ferromagnetic samples. Larger concentrations of Mn resulted in a smaller moment. In addition, an anomalous Hall effect is observed, showing that the charge carriers are spin polarized. TEM analysis revealed no clustering.

In 2005, Peng et al [14] reported ferromagnetism in ITO-Fe-cluster composite films. The Fe clusters, of dimension $d = 15\,\mathrm{nm}$, are visible in the x-ray diffractograms, and the amount present is sufficient to explain the magnetization ($3 \times 10^{-7}\,\mathrm{A\,m^2}$) observed. The amount of iron deposited corresponds to roughly a 5% by mass doping, assuming the iron clusters have the same density as bulk iron. The Fe-cluster doped films exhibited a lower resistivity than the undoped ITO films, possibly due to the iron reducing the ITO and introducing oxygen defects into the lattice.

In January 2006, Kim et al [15] reported ferromagnetism in thin films of chromium-doped ITO. The moment increases with Cr concentration, with a maximum value

of $0.5\mu_B$/Cr reported for 15 mol% Cr. Analyses by TEM and SIMS did not reveal secondary phase clustering and showed homogenous distribution of the Cr ions. The films also exhibited the anomalous Hall effect, and carrier concentrations of up to $1.23 \times 10^{21}\,\mathrm{cm}^{-3}$ were recorded for magnetic films.

Most recently, Peleckis et al [16] have reported room temperature moments of $0.03 - 0.06\mu_B$/Ni for bulk 5-15% Ni-doped ITO. The material exhibits a resistivity of $\rho = 2 \times 10^{-2}\,\Omega\,\mathrm{cm}$. Carrier mediated magnetism is mooted as a mechanism for the observed ferromagnetism, but as no effort was made to investigate the possible clustering of nickel in the sample, it can not be ruled out as a possibility

## 5.2 Sample Preparation

Ceramic target pellets of differing transition-metal dopant and concentration were prepared by the mechanical alloying of $In_2O_3$, $SnO_2$ and an oxide of the relevant metal dopant. A list of targets manufactured is given in Table 10. The targets were then sintered at 1323 K for 12 hours. PLD films were then prepared from these targets using a Lambda Physik KrF Excimer laser operating at $\lambda = 248\,\mathrm{nm}$. The fluence of the beam was $2\,\mathrm{J\,cm}^{-2}$, with a pulse frequency of 5 Hz and 10 Hz. The films were deposited onto single crystal c-cut $Al_2O_3$ (001) and r-cut $Al_2O_3$ (102) substrates at temperatures ranging between 0 °C and 800 °C. The base pressure of the chamber was $1 \times 10^{-5}$ mbar prior to deposition and the chamber was flushed with 300 $\mu$bar of $O_2$ three times before acquiring a probe signal to characterize the plume and once again before deposition. The films were deposited in 14 $\mu$bar of $O_2$.

| | Mn | Fe | $^{57}$Fe | Co | Cr | Ni |
|---|---|---|---|---|---|---|
| 2.5% | ✓ | ✓ | ✓ | ✓ | ✓ | ✓ |
| 5% | ✓ | ✓ | × | ✓ | ✓ | ✓ |
| 7.5% | ✓ | ✓ | ✓ | ✓ | × | × |

Table 10.A table showing the ceramic targets made, with the 2.5 percent indicating x = 0.025, etc.

The formula for the films can be written as $(In_{1-x}Sn_{0.1}M_x)_2O_3$, where M is the dopant cation. Thin films of $Sn_{0.97}Fe_{0.03}O_2$ (with $^{57}$Fe) were also produced for comparison.

## 5.3 Sample Characterization

### 5.3.1 Structure

The x-ray diffraction patterns of the targets show the polycrystalline cubic bixbyite phase of ITO. No secondary phases are seen. The diffractograms of the thin films reveal that they are oriented in the (222) direction (Fig.5.63) for deposition on c-cut sapphire.

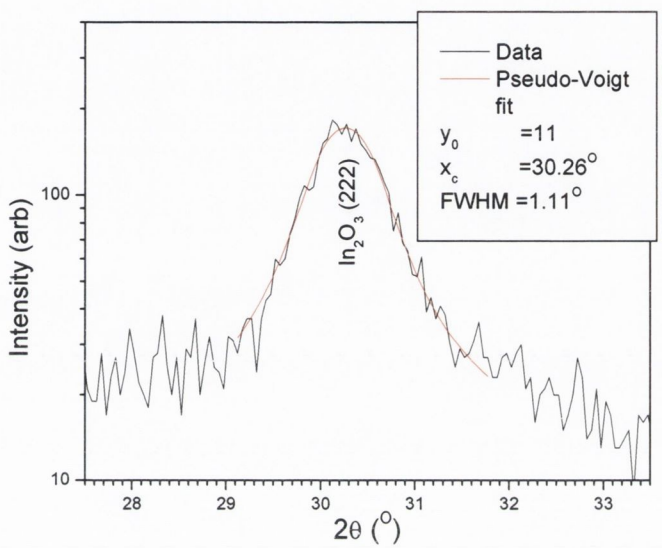



Figure 5.64. Pseudo-Voigt fit of a (222) $In_2O_3$ reflection grown on c-cut sapphire with fitting parameter in the inset

Analysis of films grown on r-cut sapphire show that the films also grow with a (111) orientation. There is a second orientation present - the (211) orientation. The structure factor for the (211) reflection is much weaker than the (222) reflection, with the intensity of the (222) reflection being 50 times that of (211) due to a difference in structure factors for the two reflections. Using this, it can be determined that 33% of the crystal is orientated in the (211) direction while the remaining 66% is orientated in the (111) direction.

The (222) reflection peak was fitted using a Pseudo-Voigt function given by

$$y = y_0 + A\left[m_u \frac{2}{\pi}\frac{w_L}{4(x-x_c)^2 + w_L^2} + (1-m_u)\frac{\sqrt{4\ln 2}}{\sqrt{\pi}w_G} e^{-\frac{4\ln 2}{w_G^2}(x-x_c)^2}\right] \tag{32}$$

where $y_0$ is the baseline, $x_c$ is the peak position and $m_u$ is the FWHM (Fig.5.64). The

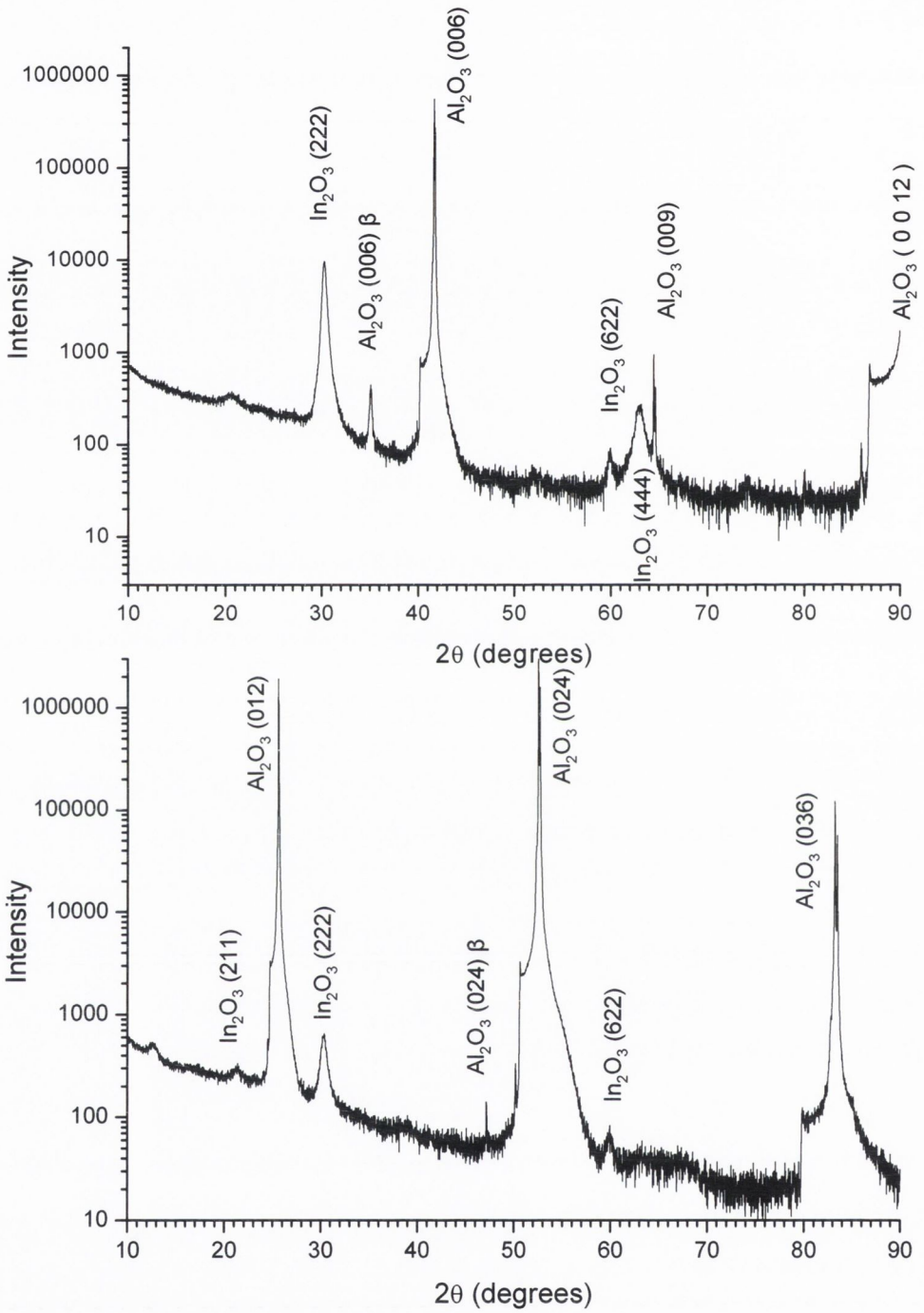



Figure 5.65. X-ray diffractograms of $(In_{0.875}Sn_{0.1}Mn_{0.025})_2O_3$ deposited on c-cut sapphire (top) and r-cut sapphire (bottom).

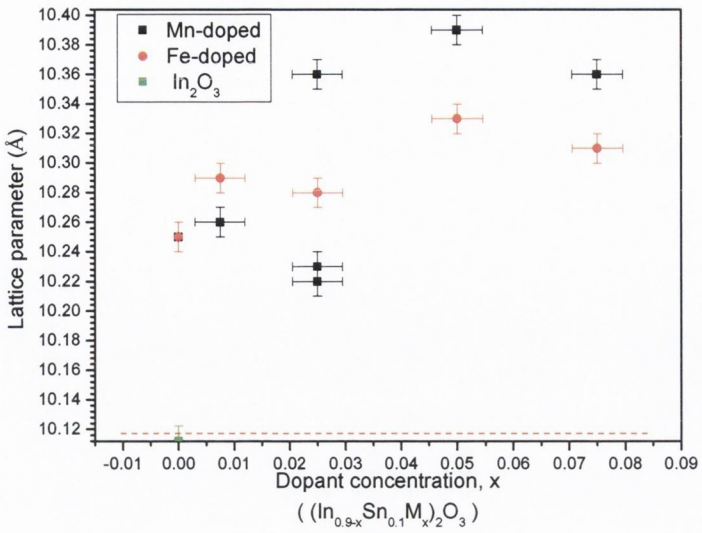



Figure 5.66. A plot of dopant concentration versus lattice constant x, for $(In_{1-x}Sn_{0.1}M_x)_2O_3$, calculated from the $d_{222}$ peak position. The value for the lattice constant for $In_2O_3$ is marked by a dotted red line. An undoped $In_2O_3$ is also shown.

position of the (222) peak was determined using this fitting method. As we have cubic symmetry, the $d$-spacing of the (222) reflection can be related to the lattice parameter using the formula

$$\begin{aligned} d_{hkl} &= \frac{a_0}{\sqrt{h^2+k^2+l^2}} \\ a_0 &= \sqrt{12}d_{222} \end{aligned}$$

where $a_0$ is the lattice constant. The lattice constant for $In_2O_3$ is approximately 10.117 Å. The values obtained ranged between 10.38 Å and 10.22 Å. Both the Fe- and Mn-doped films show a maximum lattice parameter at $x = 0.05$.

Using the Scherrer formula, the crystallite dimension in the films was estimated to be 9 nm.

### 5.3.2 Film Thickness

Film thicknesses for films thinner than 100 nm were measured using x-ray reflectivity. The film deposition rate was calibrated against the thicknesses measured by XRR. The time taken to deposit the thicker films (140 – 180 nm) was extrapolated from the time taken to deposit the thinner films and cross-checked with optical reflectometry. The films were deposited at thicknesses of 18 nm, 140 nm and 180 nm. There

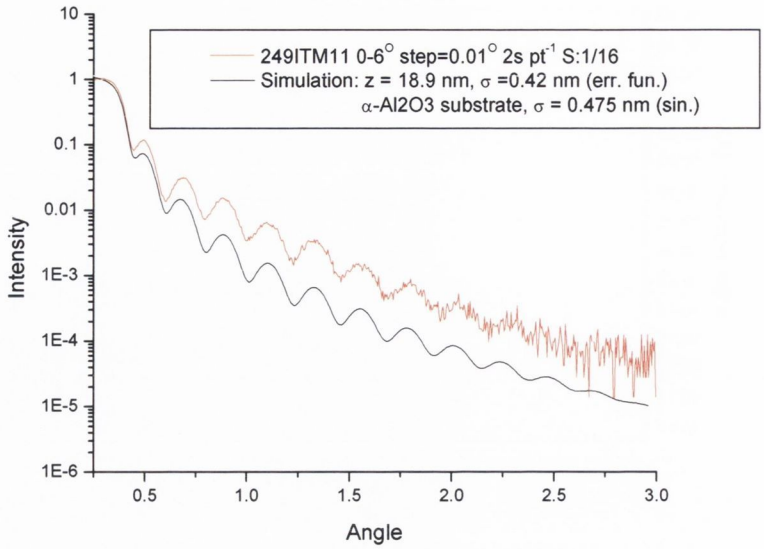



Figure 5.67. XRR measurement and simulation of nominal 18 nm thin film. The simulation returns a thickness of 18.9 nm.

was no significant change in deposition rate for differing transition-metal doping.

### 5.3.3 Magnetization

Magnetization measurements of films deposited at different temperatures indicated ferromagnetism only appears for deposition temperatures, $T_{dep} > 600\,^{\circ}\mathrm{C}$, with the highest moment for films deposited at $T_{dep} = 700 - 750\,^{\circ}\mathrm{C}$. $725\,^{\circ}\mathrm{C}$ was chosen as the optimum deposition temperature for the films. The correlation between heater voltage and temperature is given in Appendix B.

Many careful background measurements of the sample holder and blank substrate were made to ensure any ferromagnetic signals observed came only from the transition metal-doped ITO thin film. Blank substrates were heated treated on the substrate heater and subjected to "mock" deposition conditions - identical conditions to a deposition without the procution of a plume. No magnetic signal was observed in these samples, or in undoped ITO samples deposited in the same conditions.

Fig. 5.69 shows typical M-H loops for Mn-doped and Fe-doped thin films. The Mn-doped films are anhysteretic, while the Fe-doped films exhibit a hysteresis with a coercivity, $H_c \sim 30$ m T.

A plot of moment versus concentration for Fe- and Mn-doped thin films is shown

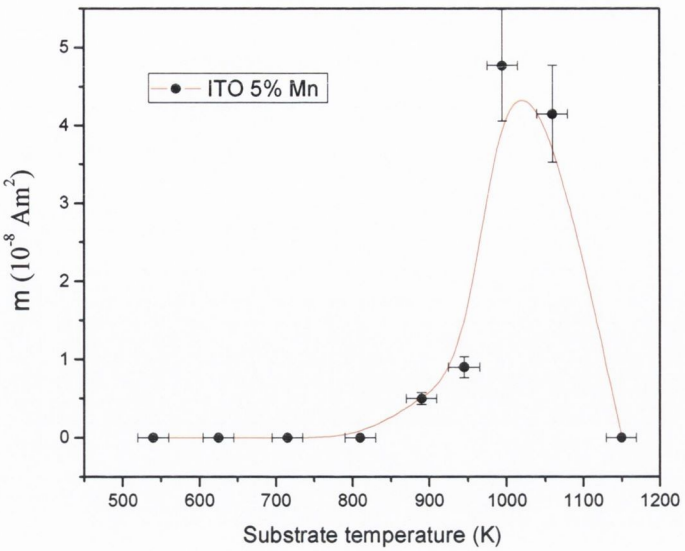



Figure 5.68. Measured magnetic moment versus heater voltage, $V_{dep}$, for 5 mol% doped Mn films.

in Fig. 5.71. In the Fe-doped films, the moment increases with concentration. However, in the Mn-doped samples, we see a higher moment for the lower concentrations. The moment disappears at higher concentrations. The remanent magnetization, $M_r$, is plotted against temperature in Fig. 5.70, and the remanent magnetization appears to be temperature independent. Mn-doped films are only found to be magnetic when deposited on c-cut sapphire, while Fe-doped films are magnetic when deposited on c- and r-cut sapphire. One out of ten 5 at% Cr-doped ITO on c-cut sapphire show a ferromagnetic moment of $2 \times 10^{-8}\,\mathrm{A\,m^2}$ for a 140 nm thick film. None of Co- and Ni-doped ITO were found to be magnetic (Fig. 5.71).

Magnetization curves of an Mn-doped film were recorded at different temperatures ranging from 300 K to 4 K (Fig. 5.72). The magnetization at 1 T was also recorded continuously as a function of temperature from 300 K to 4 K, with a blank substrate and an undoped ITO film to ensure any susceptibility increase seen was due wholly to the Mn-doped film (Fig. 5.73).

### 5.3.4 Mössbauer Spectroscopy

Transmission Mössbauer spectroscopy of the ceramic targets doped with $^{57}$Fe shows that 91% of the iron in the target is ordered magnetically, with a hyperfine field of $B_{HF} = 50.0\,\mathrm{T}$, an quadrupole shift of $2\varepsilon = -0.19\,\mathrm{mm\,s^{-1}}$ and an isomer shift of

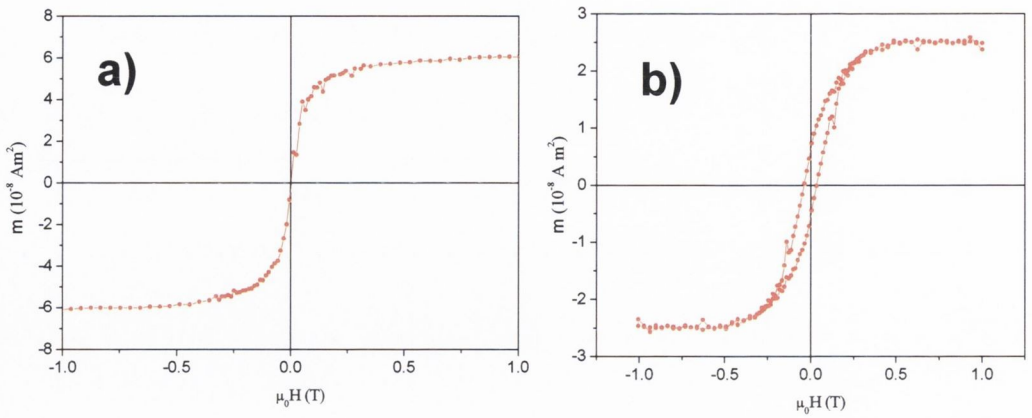



Figure 5.69. a) M-H loop for a Mn-doped ITO thin film. The loop is practically anhysteretic. b) M-H loop for an Fe-doped thin fims, which exhibits coercivity.

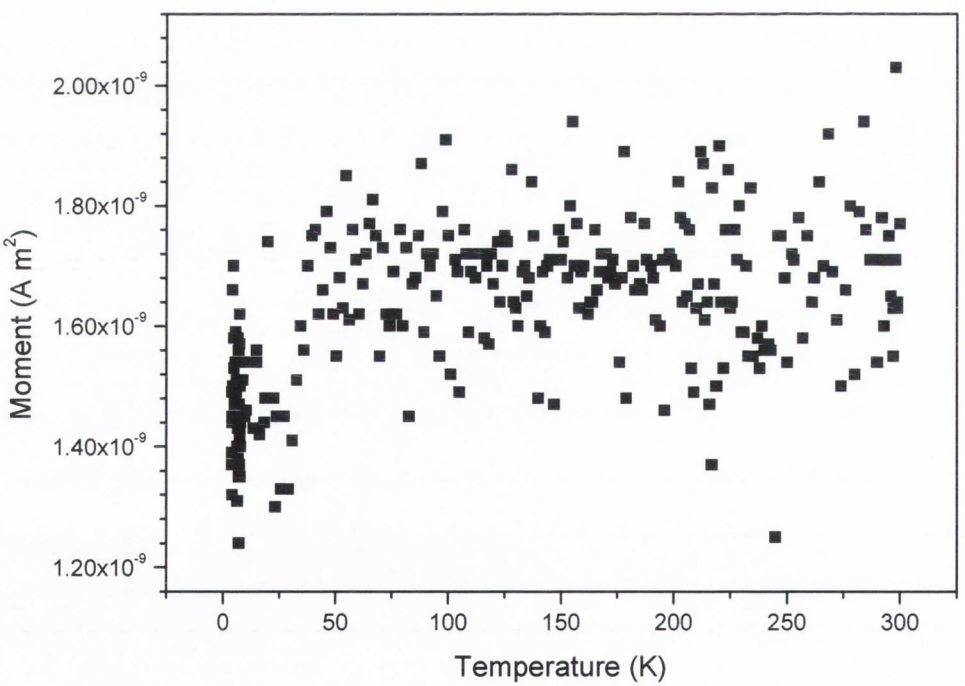



Figure 5.70. Remanent magnetization versus temperature for a thin film of composition $(In_{0.875}Sn_{0.1}Mn_{0.025})O_3$.

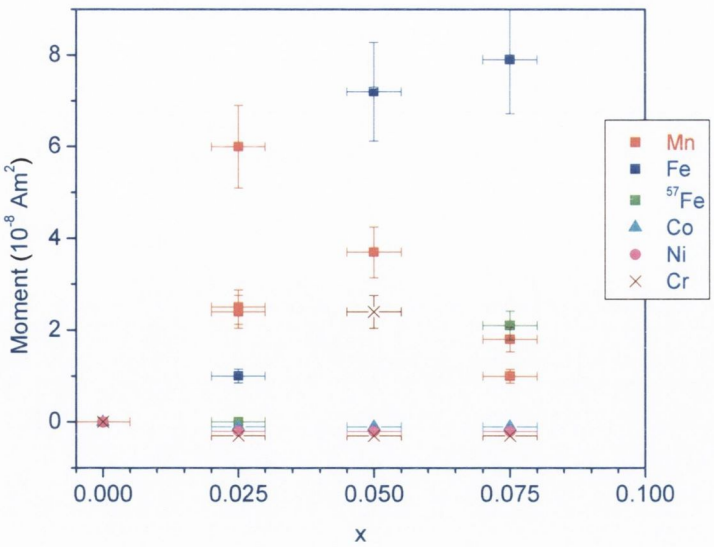



Figure 5.71. A graph of moment versus $x$ for $(In_{0.9-x}Sn_{0.1}M_x)_2O_3$ 140 nm thin films. Some values that are zero have been shifted slightly negative for clarity.

$\delta = 0.36\,\mathrm{mm\,s^{-1}}$ relative to Fe, indicating that most of the Fe in the target is in the form of hematite (Fig 5.74).

9% of the iron is not magnetically ordered and has an isomer shift of $\delta = 0.35\,\mathrm{mm\,s^{-1}}$ and a quadrupole splitting of $2\varepsilon = 0.958\,\mathrm{mm\,s^{-1}}$, indicating that it is also $Fe^{3+}$. The CEMS spectra for the 2.5% $^{57}$Fe-doped thin films (Fig. 5.76) reveal no hyperfine splitting, but instead two quadrupole split doublets are seen, one with a isomer shift of $\delta = 0.41\,\mathrm{mm\,s^{-1}}$ ($Fe^{3+}$) and the other with $\delta = 0.97\,\mathrm{mm\,s^{-1}}$ ($Fe^{2+}$). The $Fe^{3+}$ site accounts for 60% of the iron, the rest attributable to $Fe^{2+}$.

The quadrupole splitting on the $Fe^{2+}$ site is large, with $2\varepsilon = 2.46\,\mathrm{mm\,s^{-1}}$, while that on the $Fe^{3+}$ site is smaller, with $2\varepsilon = 0.84\,\mathrm{mm\,s^{-1}}$. The CEMS spectra for the 7.5% $^{57}$Fe-doped thin film (Fig. 5.76) exhibit similar $Fe^{3+}$ and $Fe^{2+}$ quadrupole-split doublets observed in the 2.5% doped films (with $\delta_{Fe^{3+},Fe^{2+}} = 0.20\,\mathrm{mm\,s^{-1}}, 1.03\,\mathrm{mm\,s^{-1}}$ and $2\varepsilon_{Fe^{3+},Fe^{2+}} = 0.95\,\mathrm{mm\,s^{-1}}, 2.27\,\mathrm{mm\,s^{-1}}$). However, this only accounts 69% of the iron. The remaining 31% can be fit with the parameters associated with magnetite.

Given 31% of the iron in the thin film is magnetite, we can estimate the moment due to the impurity. If 31% of the iron is in the form of magnetite, that implies that 2% of the mass of the film is magnetite. Thus, there is $1.78 \times 10^{-8}\,\mathrm{kg}$ of magnetite in the sample. Magnetite has a saturation magnetization of $92\,\mathrm{A\,m^2\,kg^{-1}}$. Therefore,

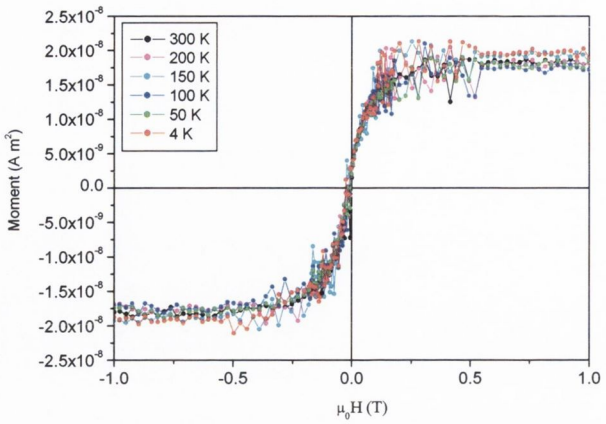



Figure 5.72. Magnetization curves at different temperatures for a thin film of composition $(In_{0.875}Sn_{0.1}Mn_{0.025})O_3$. The diamagnetic background has been subtracted.

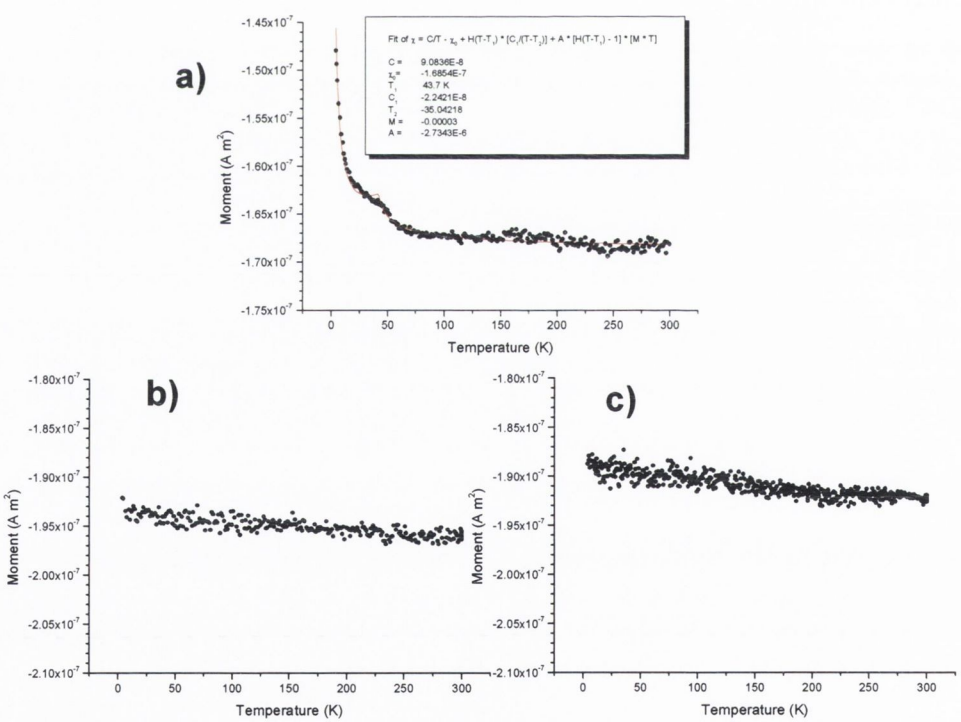



Figure 5.73. Magnetization at 1 T versus temperature for a 2.5 at% Mn-doped film (top), the same for a blank subtrate (bottom left) and an undoped ITO film (bottom right).

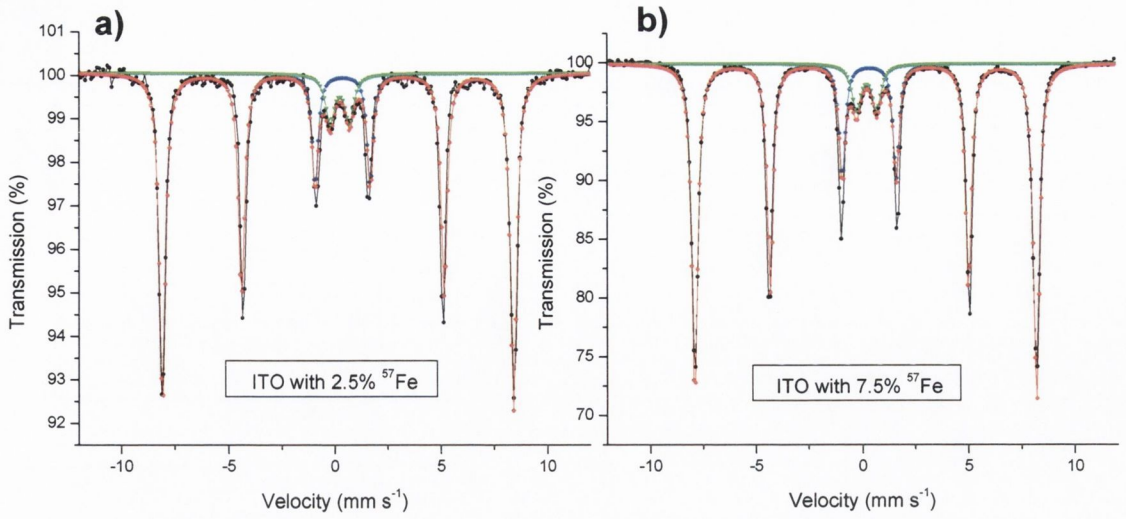



Figure 5.74. $^{57}$Fe transmission Mössbauer spectra for a) $(In_{0.875}Sn_{0.1}Fe_{0.025})_2O_3$ ceramic target and b) $(In_{0.825}Sn_{0.1}Fe_{0.075})_2O_3$ ceramic target.

we would expect a moment of $3.389 \times 10^{-8}\,\mathrm{A\,m^2}$ from the thin film due to magnetite alone.

Transmission Mössbauer spectra were taken for a 280 nm $Sn_{0.97}Fe_{0.03}O_2$ thin film (Fig. 5.77a and b). For this sample, 85% of the iron in is the form of magnetite. The thin film exhibits a moment of $20 \times 10^{-8}\,\mathrm{A\,m^2}$ at room temperature. Using a similar argument as the above paragraph, we would expect the magnetite to contribute a moment of $19 \times 10^{-8}\,\mathrm{A\,m^2}$.

### 5.3.5 Electrical Conductivity

The resistivity versus temperature data also indicate a clear difference between the manganese- and iron-doped films. The undoped and manganese doped films exhibit a metallic behaviour to their resistivity when $T \gtrapprox 100\,\mathrm{K}$. When $T \lessapprox 100\,\mathrm{K}$, the thermal coefficient of resistivity (TCR) changes sign, as has previously been observed for ITO thin films [36]. Typical R(T) curves for the undoped and Mn-doped thin films are shown in Fig 5.75.

This behaviour can be explained by ionized impurity scattering (IIS) dominating the resistivity at lower temperatures, while at higher temperatures, phonon effects dominate [37]. The temperature of the resistivity minimum, $T_{R_{min}}$ increases with manganese doping, due to the introduction of more impurity scattering centres, allowing

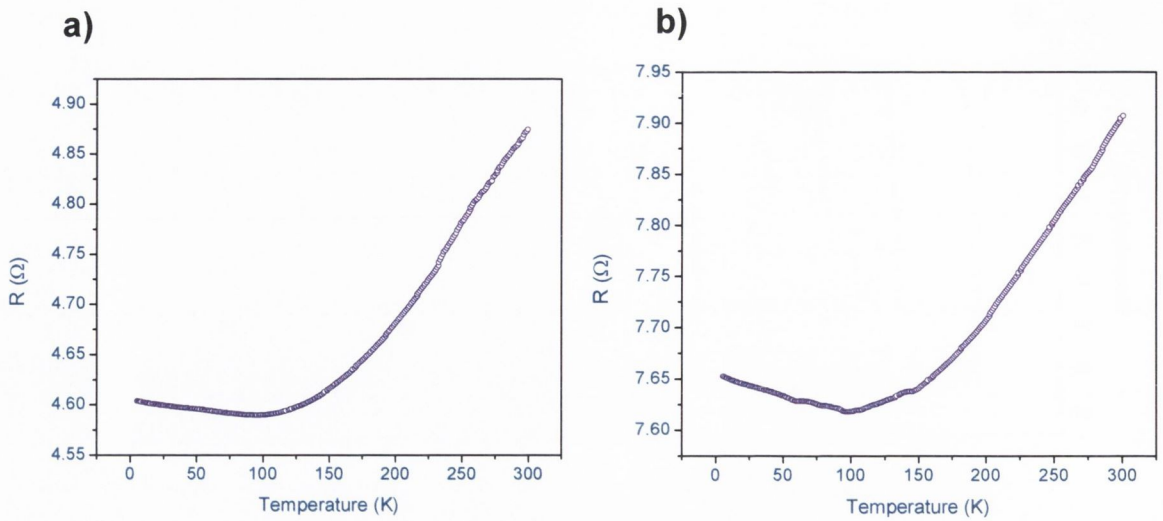



Figure 5.75. Resistance versus temperature graphs for undoped ITO (a) and Mn-doped ITO (b). The Mn-doped sample is a $(In_{0.875}Sn_{0.1}Mn_{0.025})_2O_3$ sample.

IIS to dominate at higher temperature (Fig. 5.81b). The resistivities of the films range from $4 \times 10^{-4} - 1.4 \times 10^{-3}\,\Omega\,\mathrm{cm}$ (Fig. 5.81a). A comparison between $T_{R_{\mathrm{min}}}$ and $\rho$ indicated that scattering increases as the dopant level is increased.

The iron-doped films show no such minima below 300 K, indicating that the presence of magnetite clusters may allow IIS to dominate at even higher temperature (Fig 5.78). The resistivity at 300 K of the Fe-doped films also increases with Fe concentration, from $4 \times 10^{-4} - 1.36 \times 10^{-3}\,\Omega\,\mathrm{cm}$.

### 5.3.6 Magneto-Optical Kerr Effect (MOKE)

Magnetic Mn-doped and Fe-doped thin films were examined for a Kerr signal. However, MOKE measurements showed no measureable Kerr effect in the magnetic samples in fields of up to 100 mT.

### 5.3.7 Hall Effect

Hall measurements were performed on undoped and Mn-doped ITO thin films (both magnetic and non-magnetic). No evidence of the anomolous Hall effect was seen in any of the thin films.

The carrier type is $n$-type, as to be expected. The undoped film shows a high carrier concentration of $7.5 \times 10^{22}\,\mathrm{cm}^{-3}$ which is virtually temperature independent.

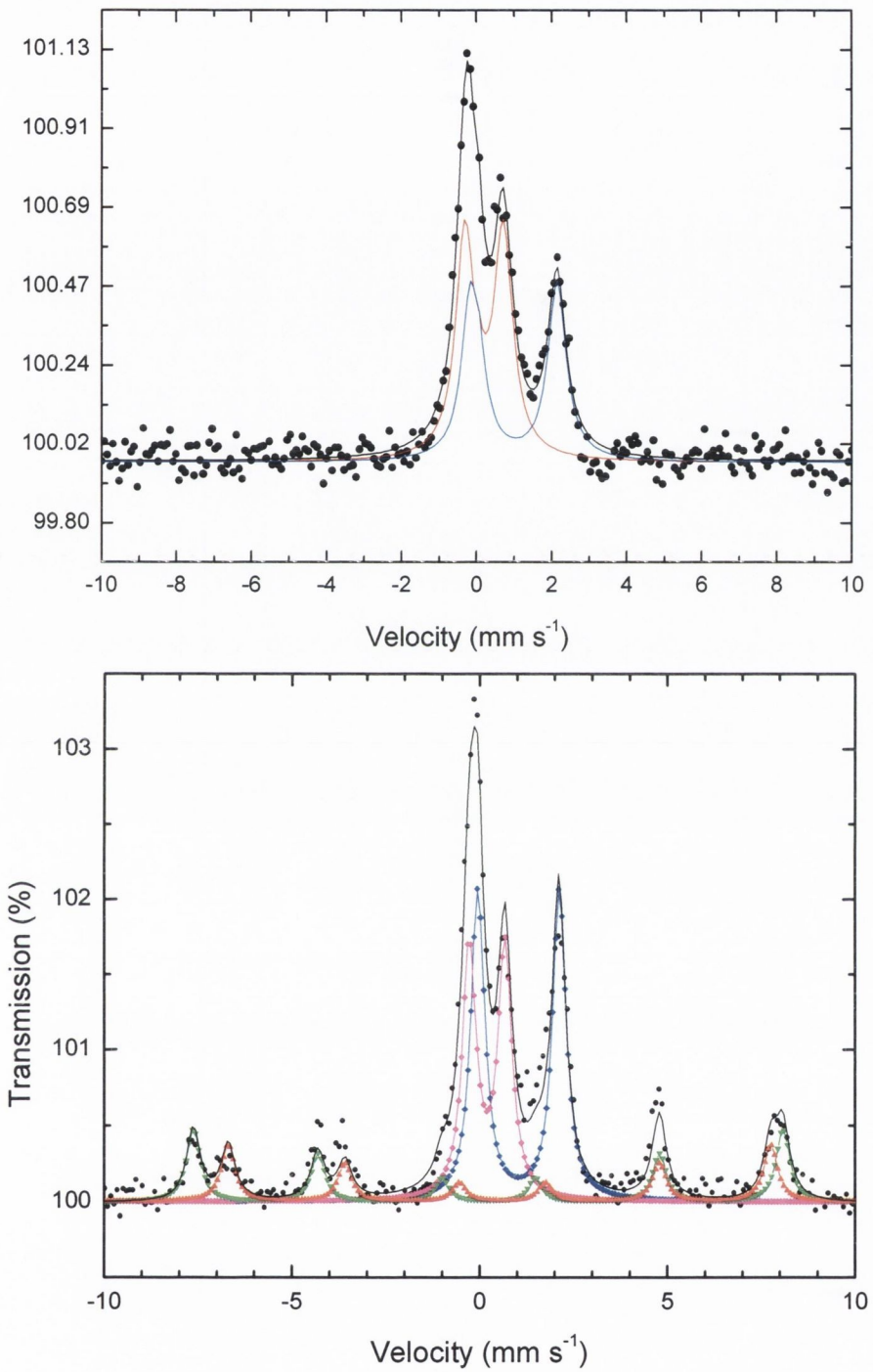



Figure 5.76. CEMS spectra of a 140 nm $(In_{0.875}Sn_{0.1}Fe_{0.025})_2O_3$ thin film that shows no magnetization (top) and 140 nm $(In_{0.825}Sn_{0.1}Fe_{0.075})_2O_3$ thin film that shows a magnetization of $2.5 \times 10^{-8}$ A m$^2$.

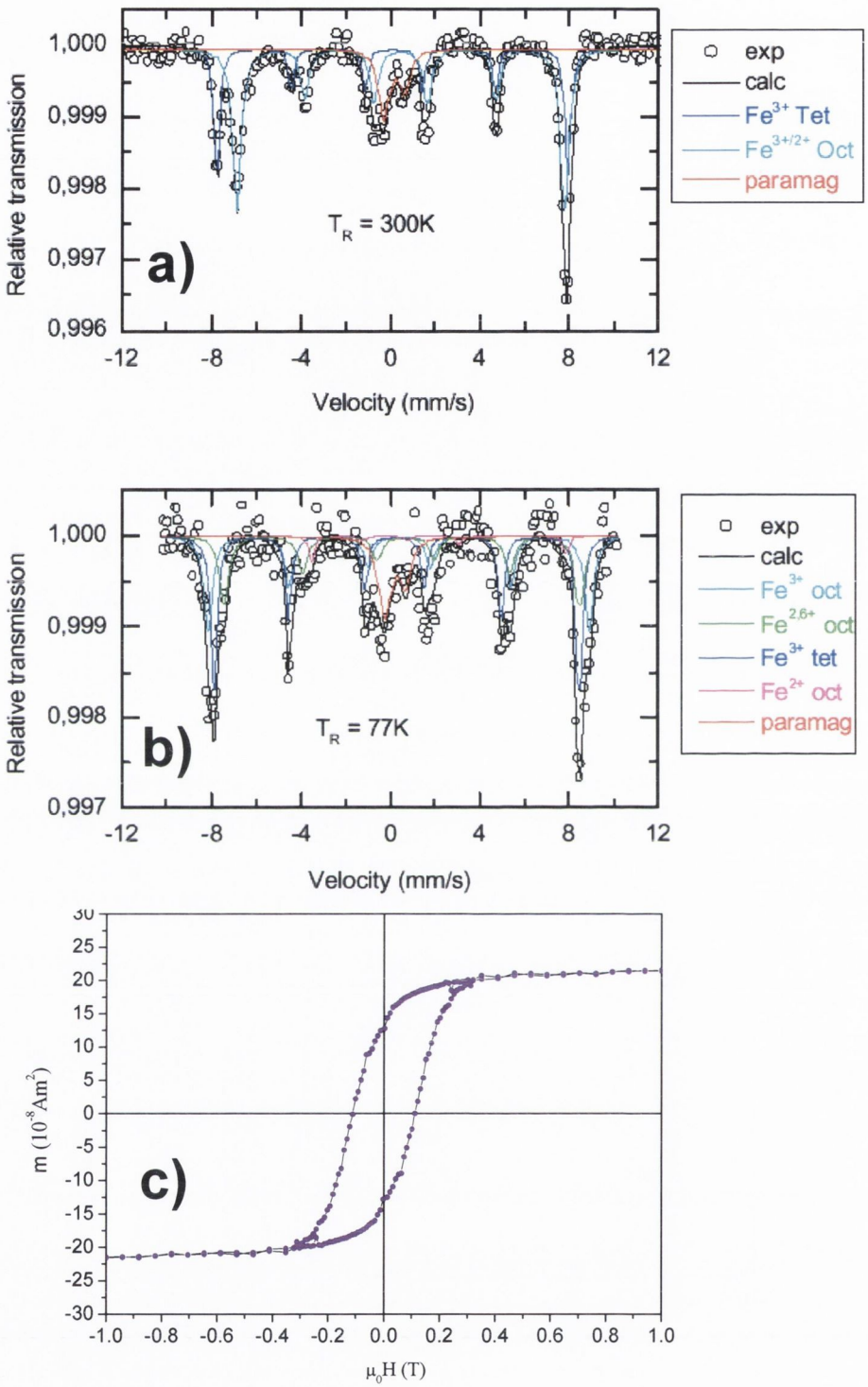



Figure 5.77. a) A transmission Mössbauer spectrum of a $Sn_{0.97}Fe_{0.03}O_2$ thin film at room temperature. b) A transmission Mössbauer spectrum of a $Sn_{0.97}Fe_{0.03}O_2$ thin film at 77K. c) The M-H loop for the same sample.

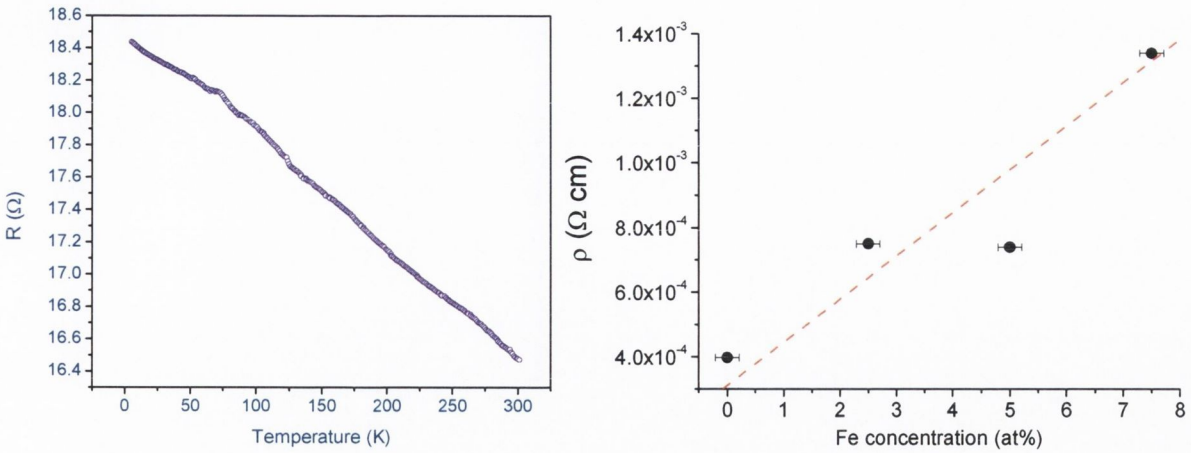



Figure 5.78. Left: A graph of resistance versus temperature for an Fe-doped film. The Fe-doped film has the composition $(In_{0.825}Sn_{0.1}Fe_{0.075})O_3$. Right: A graph of resistivity versus Fe at%.

The Mn-doped films show a lower carrier concentration, with $4.75 \times 10^{22}\,cm^{-3}$ for magnetic (deposited on C-cut) $In_{1.75}Sn_{0.2}Mn_{0.05}O_3$ and $4.0 \times 10^{22}\,cm^{-3}$ for non-magnetic (deposited on R-cut) $In_{1.75}Sn_{0.2}Mn_{0.05}O_3$. Again, both concentrations are virtually temperature independent (Fig. 5.80).

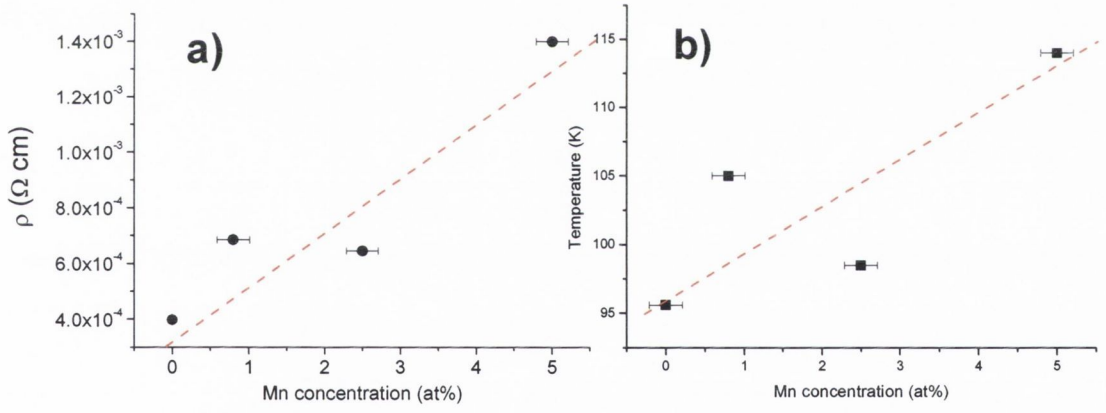



Figure 5.81. a) The resistivity of the Mn-doped films as a function of Mn-dopant concentration and b) the temperature of minimum resistivity versus Mn at% for Mn-doped ITO thin films.

### 5.3.8 Optical transmission

The optical transmission from 0.5 eV to 6 eV of the thin films was measured by a conventional Cary photospectrometer (Fig.5.82). The optical bandgap was measured using optical transmission. For the Mn-doped films, the bandgap values lay between

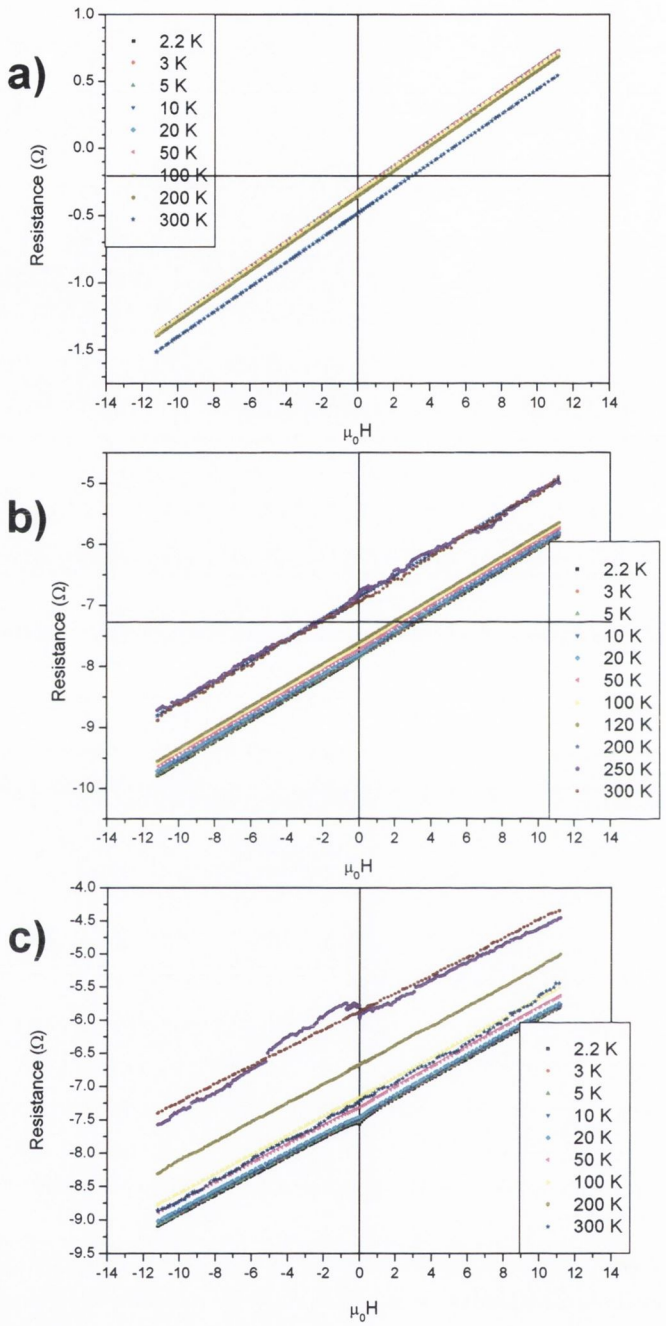



Figure 5.79. Hall effect measurements at different temperatures for a) an undoped ITO thin film, b) a $(In_{0.825}Sn_{0.1}Mn_{0.025})_2O_3$ on r-cut sapphire and c) $(In_{0.825}Sn_{0.1}Mn_{0.025})_2O_3$ deposited on c-cut sapphire.

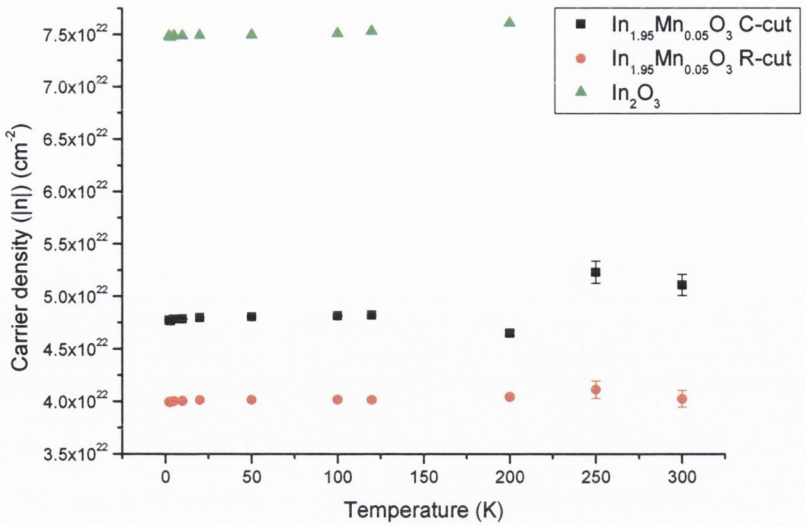



Figure 5.80. A plot of carrier concentration versus temperature for an undoped ITO thin films, a magnetic (deposited on C-cut) $(In_{0.875}Sn_{0.1}Mn_{0.025})_2O_3$ thin film and a non-magnetic (deposited on R-cut) $(In_{0.875}Sn_{0.1}Mn_{0.025})_2O_3$ thin film.

3.83 eV and 4.05 eV, while for the Fe-doped films, the bandgap lay between 3.95 eV and 3.97 eV. The undoped films showed a bandgap of 3.80 eV. There was no systematic shift in the bandgap with metal ion dopant.

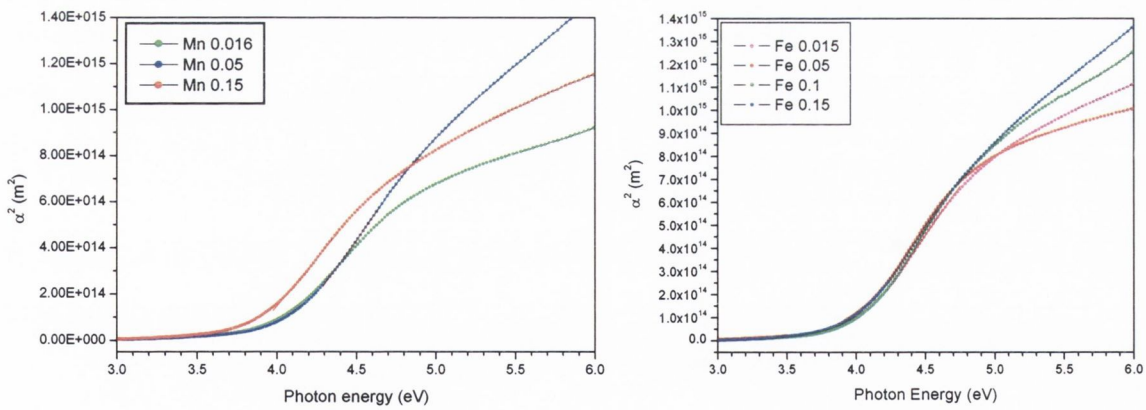



Figure 5.82. Optical bandgap measurements of both the Mn-doped (left) and Fe-doped (right) thin films.

## 5.4 Discussion

The magnetic properties of Fe-doped thin films can be comfortably explained by the presence of $Fe_3O_4$ grains as a secondary phase in the ITO films. Much of the iron is paramagnetic, in the $Fe^{2+}$ and $Fe^{3+}$ charge states, presumably in substituted sites of the bixbyite structure.

No such comfortable explanation is available for the ferromagnetic manganese or chromium doped samples. No known high temperature ferromagnetic or ferrimagnetic oxides from the elements involved. The magnetic properties are symptomatic of the syndrome that besets other dilute magnetic oxides [39], and for which there yet so far no accepted explanation. An unusual feature of this abnormal ferromagnetism is that is it practically anhysteretic, with a magnetization curve that does not depend on temperature. The moment per dopant increases as the dopant concentration decreases for the Mn-doped thin films, which is another of the recognised unusual features of this sort of magnetism.

There is substantial evidence that this unusual ferromagnetic moment is now observed in well-crystallized bulk or thin film material [40][41][42]. It is somehow associated with the defects, although the nature of these defect responsible remains to be clarified. It is suggested they may be electronic defects, ligand holes created in response to cation defects or doping [43][44][45].

In the Mn- and Cr- doped ITO, the $3d$ dopant cations behave paramagnetically. They exhibit a Curie-like susceptibility. This means that the ferromagnetism does not involve the $3d$ dopants directly. The small size of the ITO requires many grain boundaries.

The reports of $d^0$ ferromagnetism in thin films of undoped HfO2 [46] or TiO2 [47] describe a similar syndrome to the "phantom" ferromagnetism we are describing here. The two appear to be manifestations of the same phenomenon.

The "phantom" aspect relates to the reported instability of the moment in time. The absence of phenomena that depend on spin-orbit coupling (anomalous Hall effect, anisotropic magnetoresistance) is consistent with an argument of the magnetization that is unrelated to the $3d$ cations.

# References

[1] M. Marezio, Acta Cryst. 20, 723 (1966)

[2] N. Nadaud, H. Lequeux, M. Nanot, J. Jove, T. Riscnel, J. Solid States Chem. 135, 140 (1998)

[3] H. L. Hartnagel, A. L. Dawar, A. K. Jain and C. Jagadish, "Semiconducting transparent thin films" (London, 1995)

[4] J. C. C. Fan, F. J. Bachner amd G. H. Foley, Appl. Phys. Lett. 31, 773 (1977)

[5] S. Kulaszewicz, Thin Solid Films 76, 89 (1981)

[6] H. Binczycka, M. Uhrmacher, M. L. Elidrissi-Moubtassim, J.-C. Jumas, and P. Schaaf, phys. Stat. Sol (b) 242, 1100 (2005)

[7] N. Balasubramanian and A. Subrahmanyam, J. Phys. D: Appl. Phys. 22, 206 (1989)

[8] J. Philip, N. Theodoropoulou, G. Berera, J. S. Moodera, and B. Satpati, J, Appl. Phys. Lett. 85, 777 (2004)

[9] J. C. C. Fan, F. J. Bachner, and G. H. Foley, Appl. Phys. Lett 31, 773 (1977)

[10] M. Higuchi, S. Uekusa, R. Nakano, and K. Yokogawa, Jap. J. Appl. Phys. 33, 302 (1994)

[11] H. Haitjema and J. J. Ph. Elich, Thin Solid Films 205, 93 (1991)

[12] M. Buchanan, J. B. Webb and D. F. Williams, Thin Solid Films 80, 373 (1981)

[13] J. Bregman, Y. Shapira and H. Aharoni, J. Appl. Phys. 67, 3750 (1990)

[14] D. L. Peng, K. Sumiyama, N. Nozawa, T. Hihara and H. Morikawa, IEEE Trans. Magnetics 41, 3406 (2005)

[15] H. S. Kim, S. H. Ji, H. Kim, S.-K. Hong, D. Kim, Y.E. Ihm and W. K. Choo,

Solid State Communications 137, 41 (2006)

[16] G. Peleckis, X. Wang, and S. X. Dou, Appl. Phys. Lett. 89, 022501 (2006)

[17] S.G. Yang, A.B. Pakhomov, S.T. Hung, and C.Y. Wong, Appl. Phys. Lett. 81, 2418 (2002)

[18] Ogale et al, Phys. Rev. Lett. 91, 077205 (2003)

[19] Y. Matsumoto, M. Murakami, T. Shono, T. Hasegawa et al, Science 291 854 (2001)

[20] K. Ueda, H. Tabata and T Kawai, Appl. Phys Lett. 79, 988 (2001)

[21] M. Zajac, R. Doradzinski, J. Gosk, J. Szczytko, M. Lefeld-Sosnowaka, M. Kaminska, A. Twardowski, M. Placzewska, E. Grzanka and W. Gebicki: Appl. Phys.Lett. 78, 1276 (2001)

[22] J. M. D. Coey, A. P. Douvalis, C. B. Fitzgerald and M. Venkatesan, Appl. Phys. Lett. 84 1332 (2004)

[23] N. H. Hong, J. Sakai, W. Prellier, and A. Hassini, J. Phys.: Condens. Matter 17, 1697 (2005)

[24] N. H. Hong and J. Sakai, Physica B 358, 265 (2005)

[25] N. H. Hong, A. Ruyter, W. Prellier, J, Sakai, and N. T. Huong, J. Phys.: Condens. Matter 17, 6533 (2005)

[26] C. B. Fitzgerald, M. Venkatesan, L. S. Dorneles, R. Gunning, P. Stamenov, J. M. D. Coey, P. A. Stampe, R. J. Kennedy, E.C. Moreira, U. S. Sias, Phys. Rev. B (in press)

[27] J. He, S. Xu, Y. K. Yoo, Q. Xue, H.-C. Lee, S. Cheng, X.-D. Xiang, G. F. Dionne, and I. Takeuchi, Appl. Phys. Lett. 86, 052503 (2005)

[28] G. Peleckis, X. Wang, and S. X. Dou, Appl. Phys. Lett. 88, 132507 (2006)

[29] K.L. Chopra, S. Major and D. K. Pandya, Thin Solid Films 102, 1 (1983)

[30] M. Fiebig, D. Fröhlich, Th. Lottermoser, and R. V. Pisarev, Phys. Rev. B 65, 224421 (2002)

[31] R. Newman and R. M. Chrenko, Phys. Rev. 115, 882 (1959)

[32] M. Regulski, R. Przeniosło, I. Sosnowska, D. Hohlwein, and R. Schneider, J. All. Comp. 362, 236 (2004)

[33] L. W. Guo, D. L. Peng, H. Makino, T. Hanada, S. K. Hong, K. Sumiyama, T. Yao and K. Inaba, J. Appl. Phys. 90, 351 (2001)

[34] W. S. Seo, H. H. Jo, K. Lee, B. Kim, S. J. Oh, and J. T. Park, Angew. Chem. Int. Ed. 43, 1115 (2004)

[35] S. H. Kim, B. J. Choi, G. H. Lee, S. J. Oh, B. Kim, H. C. Choi, J. Park, Y. Chang, J. Korean Phys. Soc. 46, 941 (2005)

[36] J. Ederth, P. Johnsson, G. A. Niklasson, A. Hoel, A. Hultåker, C. G. Granqvist, A. R. van Doorn, M. J. Jongerius, and D. Burgard, Phys. Rev. B 68, 155410 (2003)

[37] D. Chattopadhyay and H. J. Queisser, Rev. Mod. Phys. 53, 745 (1981)

[38] T. S. Moss, Proc. of the Physical Society B76 (1954) 775-782, E. Burstein, Phys. Rev. 93 (1954) 632-633.

[39] J. M. D. Coey, Solid State Sciences 7, 660 (2005)

[40] S.R. Shinde, S.B. Ogale, J.S. Higgins, H. Zheng, A.J. Millis, V.N. Kulkarni, R. Ramesh, R.L. Greene and T. Venkatesan, Phys. Rev. Lett. 92 166601 (2004).

[41] K. Rode, A. Anane, R. Mattana, J. P. Contuor et al J. Appl. Phys. 93 7676 (2003).

[42] S. Ramachandran, A. Tiwari and J. Narayan, Appl. Phys. Letters 84 5255 (2004).

[43] C. Das Pemmaraju and S. Sanvito, Phys. Rev. Lett. 94, 217205 (2005)

[44] A. M. Stoneham, Theory of defects in solids, Ch.16, Clarendon Press, Oxford (1975)

[45] A. M. Stoneham, A.P. Pathak, R.H. Bartram, J. Phys. C, 9, 73 (1976)

[46] M. Venkatesan, C.B. Fitzgerald and J.M.D. Coey, Nature 430, 630 (2004)

[47] S. D. Yoon, Y. Chen, A. Yang, T. L. Goodrich, X. Zuo, D. A. Arena, K. Ziemer, C. Vittoria and V. G. Harris 2006 J. Phys.: Condens. Matter, 18, L355-L361 (2006)

# Chapter 6

# Al-doped Co:ZnO

"I did that before and its easy. I don't remember how, but it's easy"

Mike, another *clear* explanation

## 6.1 Introduction

Zinc oxide (ZnO) is a transparent oxide that crystallizes in the hexagonal wurtzite structure (space group $P6_3mc$). The zinc atoms arrange in almost hexagonal close packed arrangement, and the oxygen atoms form tetrahedra around the zinc atoms pointing in the direction of the c-axis (Fig. 6.83). The lattice constants for bulk ZnO are $a = 3.24\,\text{Å}$ and $c = 5.19\,\text{Å}$ [1]. ZnO is almost insoluble in water, but is dissolved by acids and bases. Zinc oxide has a melting point of 1975 °C, and decomposition occurs upon melting. Bulk ZnO has a density of $5660\,\text{kg}\,\text{m}^{-3}$.

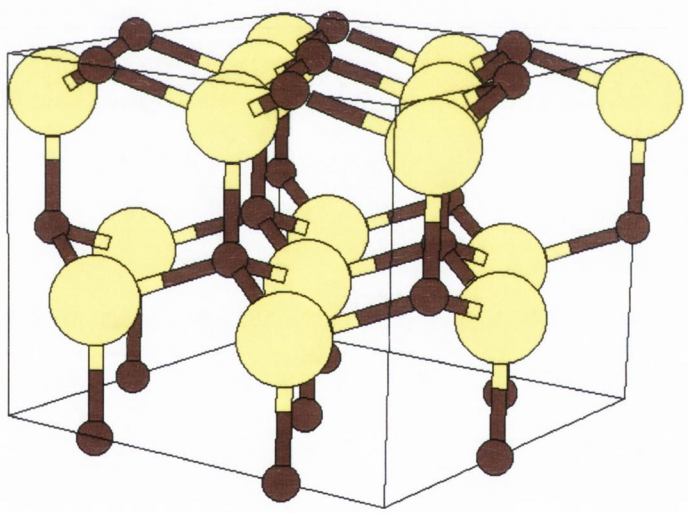


Figure 6.83. The wurtzite crystal structure of ZnO, with Zn atoms as small brown spheres and O atoms as large yellow spheres.

### 6.1.1 Conduction in Al-doped ZnO

ZnO has a wide, direct bandgap, in the region of $3.2 - 3.3\,\text{eV}$. It is an $n$-type semiconductor when undoped, but $p$-type conductivity can be induced by co-doping

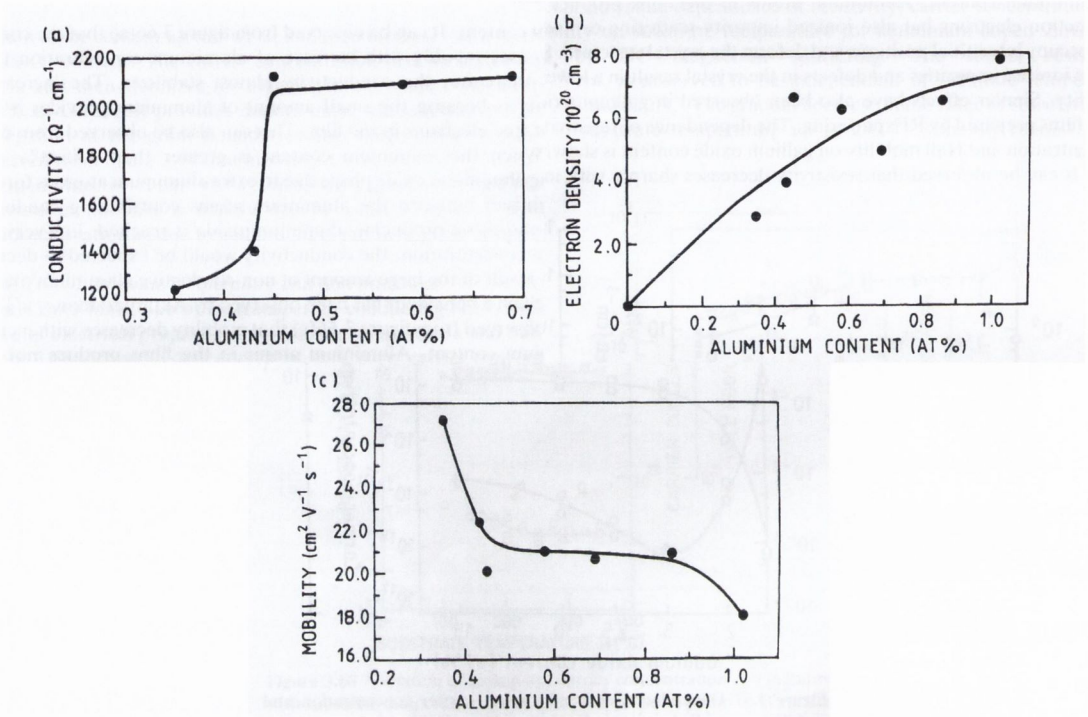



Figure 6.84. Dependence of (a) conductivity, (b) carrier concentration and (c) mobility on Al content in ZnO films. From [4].

Ga and N [2]. The surface of a ZnO crystal is susceptible to defect formation due to oxygen chemisorption and desorption, and this leads to unstable electrical properties in ZnO [3]. Oxygen vacancies in zinc oxide insert shallow donor levels in the bandgap, with a donor level energy of $E_d \approx 0.02 - 0.05\,\text{eV}$ [1]. Zn interstitials also play a role in donating electrons to the conduction band.

The doping of ZnO with aluminum improves the electrical properties in two ways - by providing extra carriers and also by stabilizing the electrical properties with respect to oxygen absorption and desorption. As $Al^{3+}$ replaces $Zn^{2+}$, it provides one extra conduction electron - thereby increasing the carrier concentration, $n$, and the conductivity, $\sigma$. However, the aluminum also produce ionized impurity scattering centres by occupying interstitial sites and deforming the lattice. This reduces the mobility, $\mu$, which also reduces the conductivity. However, for low enough concentrations of Al ($< 1\%$), the increase in $n$ dominates over the decrease in $\mu$, resulting in a net increasing in conductivity (Fig. 6.84).

The increase in conductivity would not be expected to continue for higher concentrations, as the aluminum would segregate into clusters of insulating $Al_2O_3$.

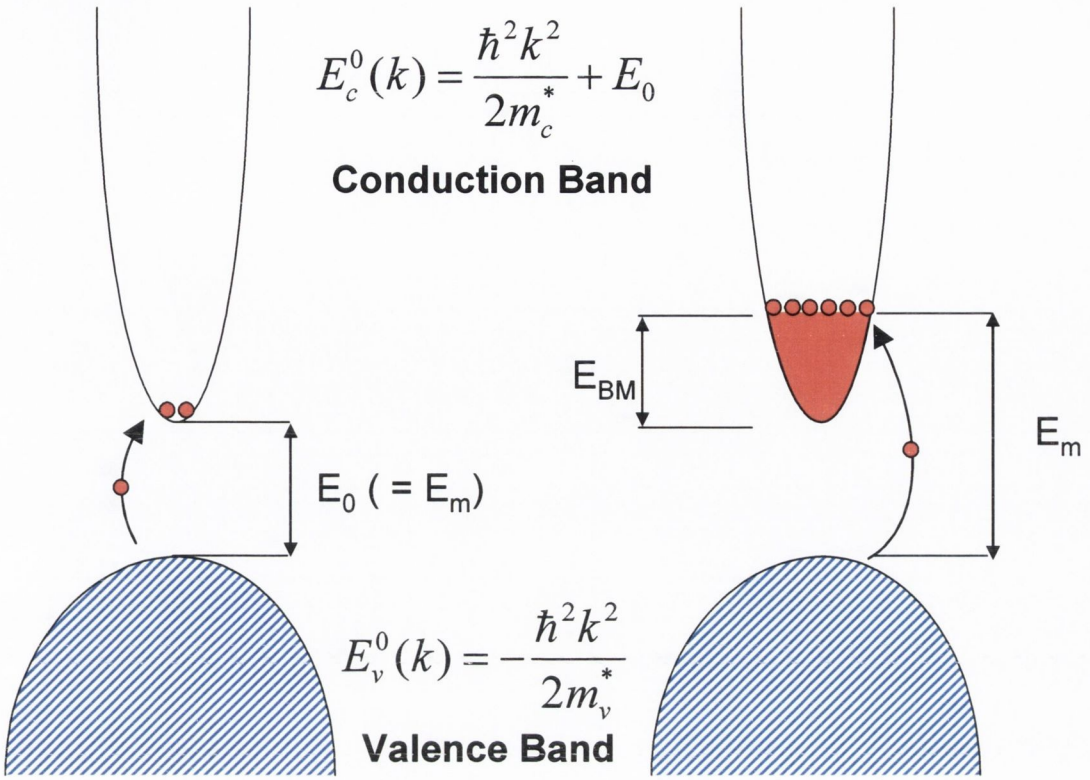



Figure 6.85. A schematic representation of the Burstein-Moss shift. On the left is an undoped material that experiences no shift. On the right is a doped material. The conduction band has been partially filled by the donor behaivour of the dopant.

### 6.1.2 Burstein-Moss Shift

The Burstein-Moss shift (BMS) was reported by both Burstein and Moss in 1954 [8]. It is a positive shift in the bandgap of a material, owing to the filling of the conduction band by donor electrons from dopants in semiconductors 6.85. Thus, the measured gap, $E_m$ becomes

$$E_m = E_0 + \Delta E_{BM} \tag{33}$$

where $E_0$ is the optical gap of the undoped material and $\Delta E_{BM}$ is the Burstein-Moss shift.

If we assume the shape of the both the valence and conduction bands to be parabolic and characterized by effective hole and electron masses ($m_v^*$ and $m_c^*$, respectively), the dispersion relations for the valence and conduction bands can be expressed as

$$E_v^0(k) = -\frac{\hbar^2 k^2}{2m_v^*} \tag{34}$$

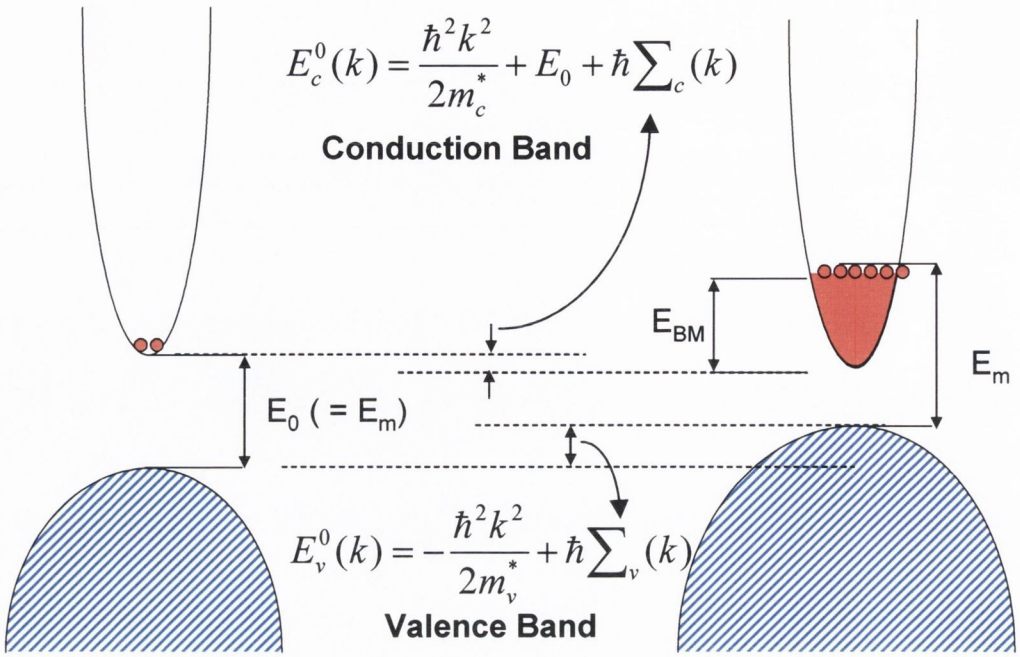



Figure 6.86. Schematic representation of the two competing mechanisms both widening and narrowing the bandgap

and

$$E_c^0(k) = E_0 + \frac{\hbar^2 k^2}{2m_c^*} \tag{35}$$

respectively. Combining these equations with (33) for direct transitions, $\Delta E_{BM}$ can be expressed as

$$\Delta E_{BM} = \frac{\hbar^2 k_F^2}{2}\left(\frac{1}{m_v^*} + \frac{1}{m_c^*}\right) \tag{36}$$

Using a reduced effective mass, $m_{vc}^*$ and expanding the Fermi wave number, we get

$$\Delta E_{BM} = \frac{\hbar^2}{2m_{vc}^*}\left(3\pi^2 n_e\right)^{\frac{2}{3}} \tag{37}$$

giving a energy-gap shift proportional to $n_e^{2/3}$.

The BMS only dominates for light doping. For heavy doping, a bandgap *narrowing* may be observed [6], due to a competing mechanism arising from the increasing free electron concentration. The increased number of free electrons induce a downward shift of the conduction band owing to their mutual exchange and Coloumb interaction, and also by the attractive impurity scattering. These electron-electron ($ee$) and electron impurity ($ei$) interactions have the opposite effect on the valence band, shifting it upwards and therefore effectively narrowing the gap (Fig. 6.86).

The dispersion equations are subsequently altered, giving

$$E_v(k,\omega) = E_v^0(k) + \hbar\Sigma_v(k,\omega) \tag{38}$$

and

$$E_c(k,\omega) = E_c^0(k) + \hbar\Sigma_c(k,\omega) \tag{39}$$

Combining these equations with (37), we can represent the total shift of the gap, $\Delta E$, by$\approx$

$$\Delta E = \frac{\hbar^2}{2m_{vc}^*}\left(3\pi^2 n_e\right)^{\frac{2}{3}} + [\hbar\Sigma_c(k,\omega) - \hbar\Sigma_v(k,\omega)]$$

These two mechanisms, i.e. the first and second terms in the above equation, compete against each other. For Al-doped ZnO and Sn-doped $In_2O_3$[21], the resultant shift is a widening of the gap.

### 6.1.3 Uses of ZnO

ZnO is used in gas sensors and as a component of blue and UV LEDs, which are used in the field of optical information storage. Nanostoichiometric ZnO is a transparent conducting oxide, but the poor stability of its electrical properties renders it of lesser importance than other TCOs.

Zinc oxide is an essential ingredient in industrial rubber as it accelerates the curing in the vulcanization process.

Chinese white is a pigment based on ZnO and is used in paints and as a opacifier.

Zinc oxide reflects ultra-violet light, and as a result can be used as a base for sun tan lotion. When mixed with small amounts of hematite it forms a mineral known a calamine, which can neutralize acidity and is anti-bactericial and had wide medical applications.

### 6.1.4 Ferromagnetism in Co-doped ZnO

ZnO was first reported as exhibiting room temperature ferromagnetism by Ueda et al [11] in (2001) for $Zn_{1-x}Co_xO$ thin films with $x = 0.05 - 0.25$, with a moment of up to 1.8 $\mu_B$ per cobalt ion for $x = 0.05$. The presence of a moment in Co-doped ZnO was confirmed by several groups [12][13][14][15][10], but without any consistency in the magnitude of the magnetic moments.

Maurice et al [9] reported room temperature ferromagnetism in Al-doped $Zn_{0.7}Co_{0.3}O$ grown by pulsed laser deposition on sapphire, with a moment of 0.7 $\mu_B$/Co ion. A sec-

| Sample | Composition | Moment ($\mu_B$/Co) | Thickn. (nm ± 1 nm) | $\Delta E_g$ (eV) |
|---|---|---|---|---|
| 197ZCO2 | $Zn_{0.95}Co_{0.05}O$ | 0.06 ± 0.01 | 160 | 3.2 |
| 207ZCO1 | $Zn_{0.95}Co_{0.05}O$ | 0.50 ± 0.1 | 160 | 3.2 |
| 216ZCAL1 | $Zn_{0.95}Co_{0.05}O$ + 0.1% Al | 0.06 ± 0.01 | 180 | 3.44 |
| 226ZCAL1 | $Zn_{0.95}Co_{0.05}O$ + 0.1% Al | 0.19 ± 0.04 | 60 | - |
| 226ZCAL2 | $Zn_{0.95}Co_{0.05}O$ + 0.2% Al | 0.46 ± 0.08 | 50 | - |
| 236ZCAL2 | $Zn_{0.95}Co_{0.05}O$ + 0.2% Al | 0.10 ± 0.02 | 145 | 3.48 |
| 246ZCAL1 | $Zn_{0.95}Co_{0.05}O$ + 0.5% Al | 0.18 ± 0.03 | 55 | - |
| 276ZCAL1 | $Zn_{0.95}Co_{0.05}O$ + 0.5% Al | 0.07 ± 0.01 | 165 | 3.55 |
| 286ZCAL1 | $Zn_{0.95}Co_{0.05}O$ + 0.7% Al | 0.06 ± 0.01 | 45 | - |
| 296ZCAL1 | $Zn_{0.95}Co_{0.05}O$ + 0.7% Al | 0.04 ± 0.007 | 160 | 3.61 |
| 296ZCAL2 | $Zn_{0.95}Co_{0.05}O$ + 1% Al | 0.07 ± 0.01 | 55 | - |
| 017ZCAL1 | $Zn_{0.95}Co_{0.05}O$ + 1% Al | 0.07 ± 0.01 | 205 | 3.65 |
| 217ZCAL1 | $Zn_{0.95}Co_{0.05}O$ + 0.1% Al | 0.42 ± 0.08 | 160 | 3.28 |
| 227ZCAL1 | $Zn_{0.95}Co_{0.05}O$ + 0.2% Al | 0.48 ± 0.08 | 160 | 3.37 |
| 227ZCAL2 | $Zn_{0.95}Co_{0.05}O$ + 0.5% Al | 0.30 ± 0.06 | 160 | 3.53 |
| 257ZCAL1 | $Zn_{0.95}Co_{0.05}O$ + 0.7% Al | 0.35 ± 0.08 | 160 | 3.64 |
| 257ZCAL2 | $Zn_{0.95}Co_{0.05}O$ + 1% Al | 0.06 ± 0.1 | 160 | 3.68 |
| 58ZCUO1 | $Zn_{0.9}Cu_{0.1}O$ | 0 | 160 | - |
| 58ZCUO2 | $Zn_{0.9}Cu_{0.1}O$ | 0 | 160 | - |
| 68ZCUO1 | $Zn_{0.95}Cu_{0.05}O$ | 0 | 160 | - |
| 68ZCUO2 | $Zn_{0.98}Cu_{0.02}O$ | 0 | 160 | - |
| 88ZFEO1 | $Zn_{0.9}Fe_{0.1}O$ | 0 | 200 | - |
| 88ZFEO2 | $Zn_{0.95}Fe_{0.05}O$ | 0 | 200 | - |
| 98ZFEO1 | $Zn_{0.95}Fe_{0.05}O$ | 0 | 200 | - |
| 108ZEO1 | $Zn_{0.98}Fe_{0.02}O$ | 0 | 200 | - |
| 108ZCFO1 | $Zn_{0.94}Fe_{0.05}Cu_{0.01}O$ | 0 | 200 | - |
| 108ZCFO2 | $Zn_{0.94}Fe_{0.05}Cu_{0.01}O$ | 0 | 200 | - |

Table 11.A table of thin films prepared.

ondary phase of metallic cobalt was observed, with 10% of the cobalt crystallizing as hexagonal metallic cobalt. The authors attribute the majority of the moment to the cobalt that does not segregate into cobalt metal . Bulk ZnO doped with Co and Al has, however, been reported not to exhibit ferromagnetic behaviour [5].

## 6.2 Sample Preparation

Ceramic targets of pure and Al doped (0.1 at.% to 1 at. %) $Zn_{0.95}Co_{0.05}O$ were first prepared by solid-state reaction of high purity ZnO, CoO and $Al_2O_3$ at 1000 °C. The thin films were deposited at 450 °C, both on c-cut and r-cut sapphire substrates at a repetition rate of 10 Hz. Laser fluence on the target was 1.8 J cm$^2$. The films were deposited at an oxygen partial pressure of $4 \times 10^{-5}$ mbar. A series of thin films ($t \approx 50$ nm) was produced to calibrate the deposition rate by measurement with XRR. Thicker films were then produced ($t \approx 50 - 150$ nm) for electrical, optical and magnetic measurements. A list of thin films prepared is given in Table 11.

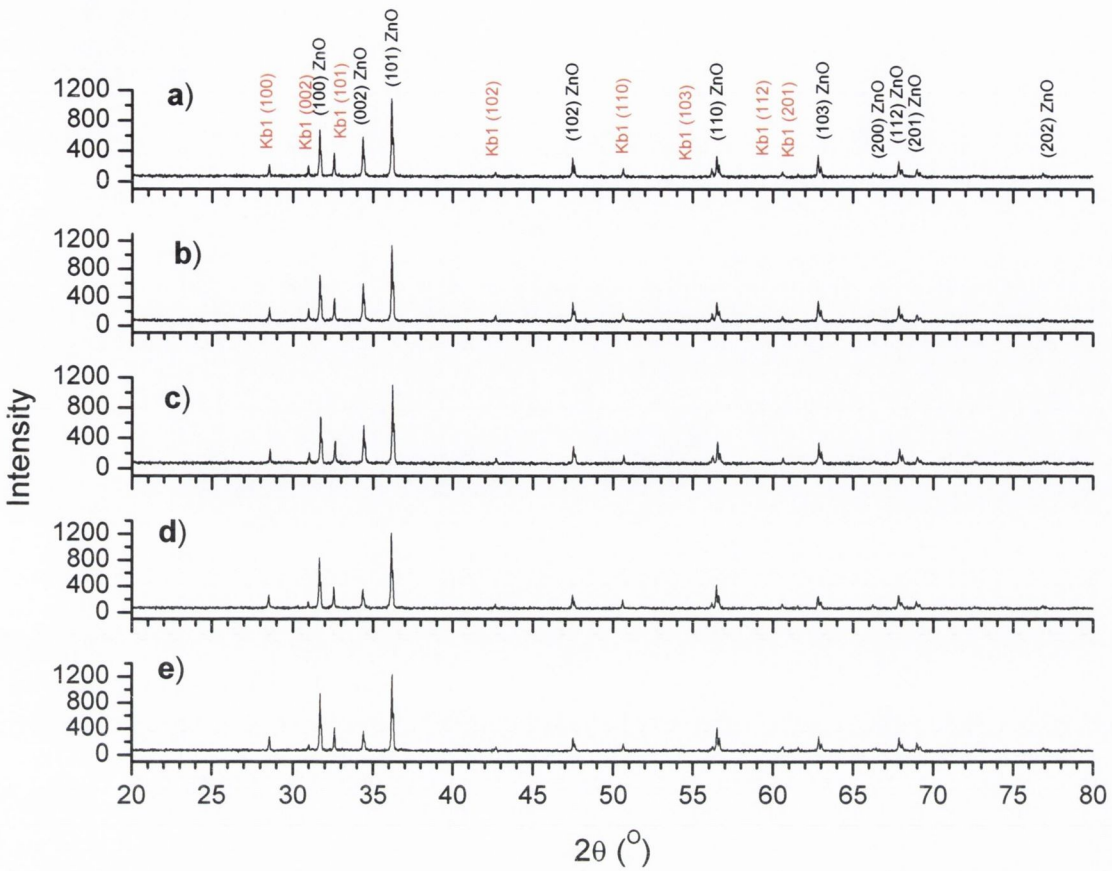



Figure 6.87. X-ray diffractograms of the a) 0.1%, b) 0.2%, c) 0.5%, d) 0.7% and e) 1% Al-doped ceramic $Zn_{0.95}Co_{0.05}O$ targets.

## 6.3 Sample Characterization

### 6.3.1 X-ray Diffraction

X-ray diffractograms of the ceramic targets (Fig. 6.87) matched the expected pattern for polycrystalline ZnO. No secondary Co or Al phases were seen for any concentrations of Al dopant.

All films are highly epitaxial and x-ray diffraction pattern on c-cut and r-cut sapphire substrates showed (002) and (110) reflections. There is no evidence of secondary phases, in particular Co metal precipitation (Fig 6.88).

### 6.3.2 Magnetization

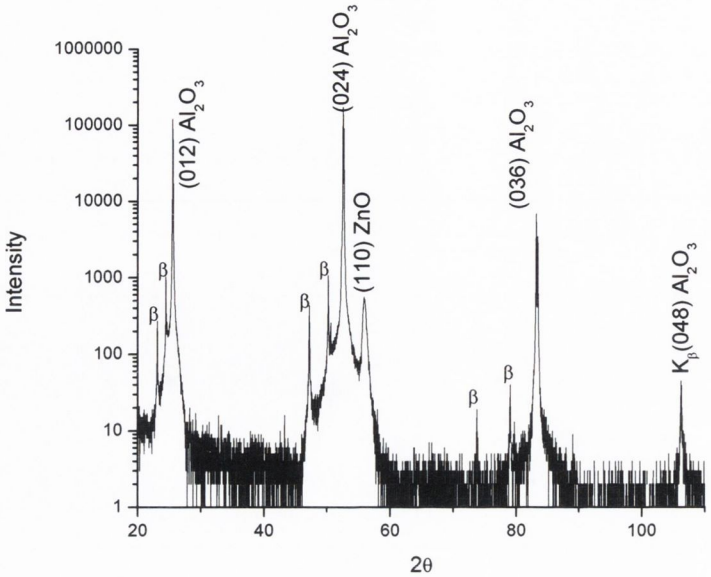



Figure 6.88. An x-ray diffractogram of a 1% Al-doped $Zn_{0.95}Co_{0.05}O$ thin film. The Cu $K_\beta$ are marked with a $\beta$.

These measurements were made with the field applied perpendicular to the substrate plane. The blank $Al_2O_3$ substrate subjected to the same thermal cycle in the deposition chamber as one with a thin film deposited on it exhibits pure diamagnetism. The susceptibility $-4.8 \times 10^{-9}\,m^3\,kg^{-1}$ is in agreement with the handbook value for $Al_2O_3$, $-4.6 \times 10^{-9}\,m^3\,kg^{-1}$. Fig. 6.89 show the ferromagnetic signal of Co:ZnO film on both c- and r-cut sapphire for 0.1% Al doping, after subtraction of the linear diamagnetic background signal arising from the substrate. Moments are quite variable, depending on the substrate as shown in Table 11. The observed moments per Co atom of doped films on c-cut sapphire substrates are always greater than on r-cut substrates.

Figure 6.90 shows a summary of the magnetization measurements for the Al-doped $Zn_{0.95}Co_{0.05}O$ thin films. The ferromagnetic moment is larger for the films deposited on c-cut sapphire than for the same compositions deposited on r-cut sapphire. The moment decreases with Al concentration. The films deposited on r-cut sapphire show small saturation magnetizations ($< 1 \times 10^{-8}\,A\,m^2$) in comparison with the c-cut films. The moment in the r-cut films shows no dependence on the Al concentration.

### 6.3.3 Optical Spectroscopy

The optical absorption spectra for the films deposited on both C-cut and R-cut

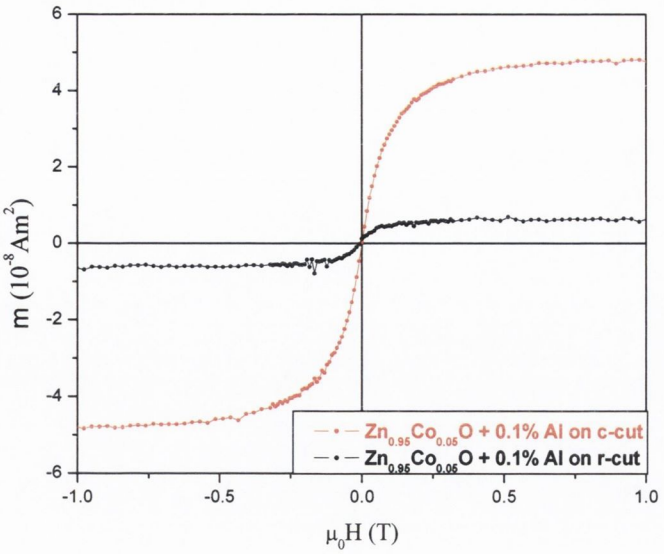



Figure 6.89. M-H curves for 0.1% Al-doped $Zn_{0.95}Co_{0.05}O$ thin films deposited on c-cut and r-cut $Al_2O_3$.

are displayed in Figure 6.92. The optical bandgap increases with Al content, from a value for 0.1% Al of $\Delta E_g = 3.28\,\text{eV}$ and $3.44\,\text{eV}$ (for c- and r-cut respectively) to $\Delta E_g = 3.68\,\text{eV}$ and $3.65\,\text{eV}$ for 1% Al (Fig. 6.91). This shift is explained by Burstein-Moss effect [8], as conduction electrons donated from the $Al^{3+}$ occupy the lower levels of the conduction band.

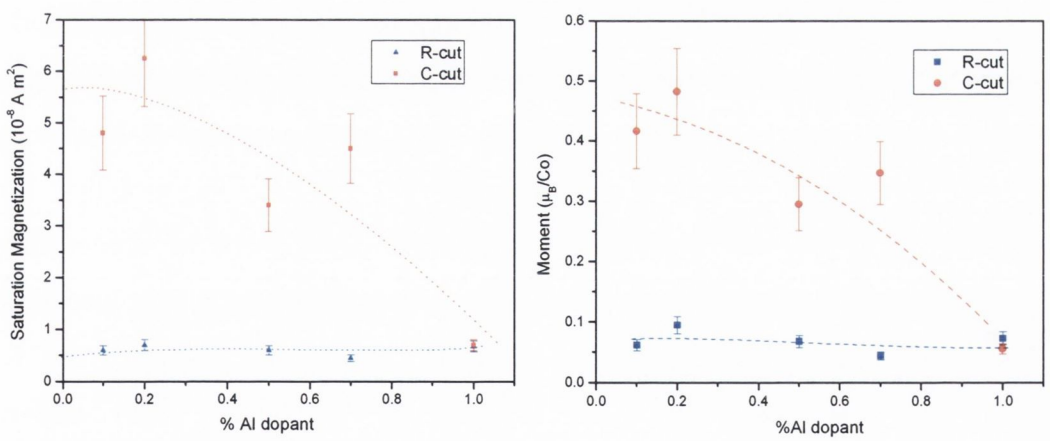



Figure 6.90. Plots of the saturation magnetization (left) and $\mu_B$/Co against Al concentration (right).

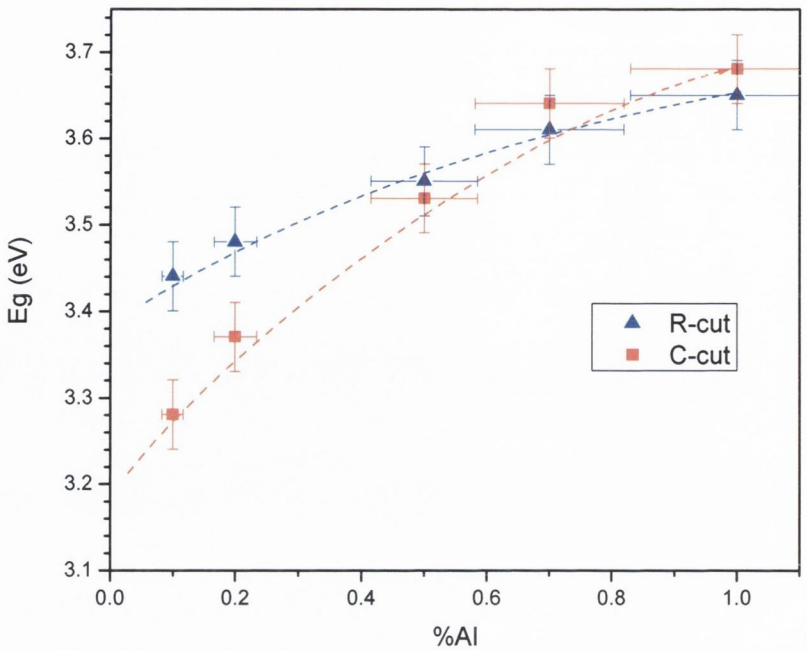



Figure 6.91. A plot of the optical band gap versus the Al dopant concentration. The dotted lines serve as guides for the eye.

### 6.3.4 Electrical Conductivity

Transport measurements[5], in the temperature interval $2-300\,\mathrm{K}$, were performed on samples contacted by shadow masking and thermal evaporation of Al/Au bi-layer at pressures below $10^{-6}\,\mathrm{mbar}$. Hall resistance were extracted by symmetrizing and anti-symmetrizing with respect to field the measured $R_{xy}$ in the van der Pauw geometry. All samples exhibit appreciable magnetoresistance only below about 30 K with strong temperature dependence governed by both carrier concentration and mobility. The acquired apparent carrier concentrations have non-linear dependence on Al concentration (Fig. 6.93) and show saturation at about 0.2 % Al evidence for either low solubility limit for Al or the complete degeneration of the electron gas at $n > 2\times10^{20}\,\mathrm{cm}^{-3}$. Mobilities are found to be in the region $0.4-11.4\,\mathrm{cm}^2\,\mathrm{V}^{-1}\,\mathrm{s}^{-1}$ at 2 K. The temperature dependence of the Hall resistance reveals almost degenerate electronic concentrations even for 0 % Al, and virtually no temperature dependence for the films with more than 0.2% Al.

The remarkable finding is that the resistivity of Co-doped ZnO film doped with

[5] These measurements were performed by P. Stamenov

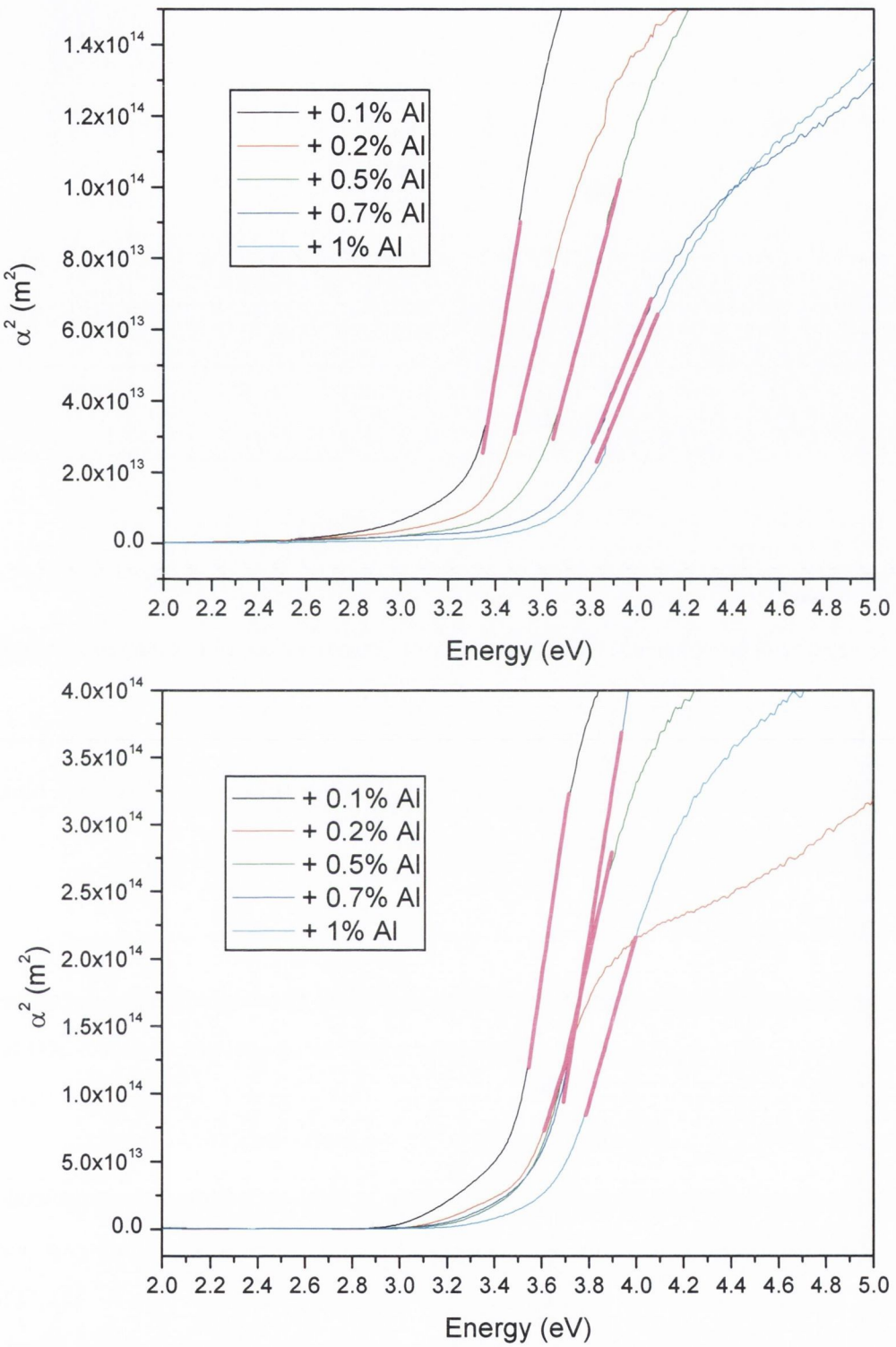



Figure 6.92. A graph of $\alpha^2$ against photon energy for Al-doped $Zn_{0.95}Co_{0.05}O$ thin films deposited on C-cut sapphire (top) and R-cut sapphire (bottom). The sections in magneta are the slopes used to measure the optical band gap.

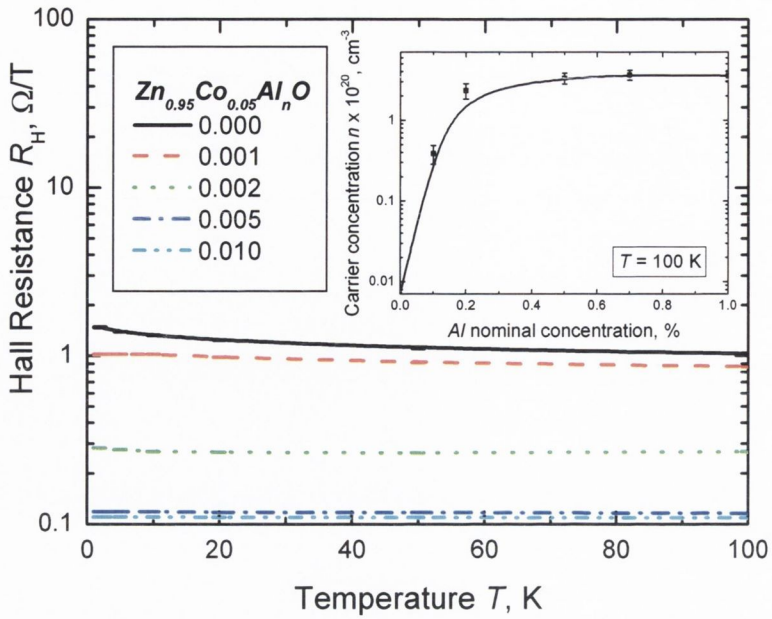



Figure 6.93. The Hall resistance as a function of temperature for different Al-dopings of $Zn_{0.95}Co_{0.05}O$. Inset: The carrier concentration as a function of Al-doping.

more than 0.2% Al drastically decreases in the whole temperature region $2 - 300\,K$, while preserving its macroscopic magnetisation. This system may therefore be considered a degenerate semi-magnetic semiconductor.

## 6.4 Discussion

The remarkable finding is that the resistivity of Co-doped ZnO film doped with more than 0.2% Al drastically decreases in the whole temperature region 2-300 K, while preserving its macroscopic magnetisation. This system may therefore be considered a degenerate semi-magnetic semiconductor.

Optical transmission spectra for Al-doped Co:ZnO thin films are compared in Fig. 6.91. Another striking feature of Al codoped ZnO:Co films is the band-gap widening. Band gap is shifted from 3.7 eV (ZnO:Co) to 4.1 eV (ZnO:Co:0.2 at.% Al). The shift occurs as a result of the blocking of the lowest states in the conduction band and is explained by Burstein-Moss effect [8] involving transfer of associated electrons to the conduction band. The filling of the density of states in the conduction band at high Al doping levels is illustrated by the shift of the direct-gap optical absorption edge as a function of carrier concentration as illustrated on Figure 6.91. The expected functional

dependence [21] verifies well within the experimental errors and yields for the mean harmonic mass defined as , $m^* = 0.26(3)\ m_e$, which is in good agreement with the accepted values of $m_e = 0.23$ and $m_h = 0.59$ for Al-doped ZnO [22].

In summary, it has been demonstrated that the magnetic, magnetotransport and optical properties of Co:ZnO films depend critically on Al doping. Magnetization decreases with increasing Al content. The conductivity is enhanced significantly in 0.2% Al doped $Zn_{0.96}Co_{0.04}O$ while maintaining significant room temperature magnetic moment. Magnetoresistance is observed only up to 30 K. Hall measurements reveal degenerate semiconducting behaviour for Al concentrations $> 0.2$ %. Optical band gaps were widened in proportion to the Al doping due to Burstein-Moss effect.

# References

[1] H. L. Hartnagel, A. L. Dawar, A. K. Jain and C. Jagadish, "Semiconducting transparent thin films" (London, 1995)

[2] M. Joseph, H. Tabata and T. Kawai, Jpn. J. Appl. Phys. 38, L2505 (1999)

[3] W. Göpel and U. Lampe, Phys. Rev. B 22, 6447–6462 (1980)

[4] J. Hu and R. G. Gordon, J. Appl. Phys. 71, 880 (1992)

[5] J. Alaria, H. Bieber, S. Colis, G. Schmerber, A. Dinia, Appl. Phys Letters 88, 112503 (2006)

[6] A. P. Roth J. B. Webb and D. F. Williams, Phys. Rev. B 25, 7836 (1982)

[7] K. Ando, H. Saito, Z-W Jin, T. Kukumura et al Appl. Phys. Lett. 78, 2700 (2001)

[8] E. Burstein, Phys. Rev. 93 632 (1954); T.S. Moss, Proc. Phys. Soc. London, Ser. B 67, 775 (1954)

[9] J.-L. Maurice, K. Rode, A. Anane, D. Imhoff and J.-P. Contour, Eur. Phys. J. Appl. Phys. 33, 109-113 (2006)

[10] D. P. Norton, M. E. Overberg, S. J. Pearton, K. Preusser et al, Appl. Phys Letters 83, 5488 (2003)

[11] K. Ueda, H. Tabata and T Kawai, Appl. Phys Lett. 79, 988 (2001)

[12] Y. M. Cho, W. K. Choo, H. Kim, D. Kim and Y. E. Ihm, Appl. Phys Lett. 80, 3358 (2001)

[13] H. J. Lee, S. Y. Jeong, C. R. Cho and C. H. Park, Appl. Phys Lett. 81, 4020 (2002)

[14] K. Rode, A. Anane, R. Mattana, J. P. Contuor et al J. Appl. Phys. 93, 7676 (2003)

[15] W. Prellier, A. Fouchet, B. Mercey, C. Simon and B. Raveau, Appl. Phys Letters 82, 3490 (2003)

[16] K. J. Kim and Y. R. Park Appl. Phys. Lett. 81, 1420 (2001)

[17] D.A. Schwartz, N. S. Norberg, Q. P. Nguyen, J. M. Parker and D. M. Gamelin, J. Am. Chem. Soc 125, 13205 (2003)

[18] S. Ramachandran, A. Tiwari and J. Narayan, Appl. Phys. Lett. 84, 5255 (2004)

[19] P. Stamenov, M. Venkatesan, et al, J. Appl. Phys., (in press)

[20] T. Andrearczyk, J. Jaroszynski, et al, Phys. Rev. B 72, 121309R (2005)

[21] I. Hamberg and C. G. Granqvist, Phys. Rev. B 30 3240 (1984)

[22] B. E. Sernelius, K. F. Berggren at al, Phys. Rev. B 37 10244 (1988)

# Chapter 7

# Carbon

"I believe that you can reach the point where there is no longer any difference between developing the habit of pretending to believe and developing the habit of believing."

Umberto Eco

## 7.1 Introduction



Figure 7.94. The scrolls on the unbroken tube surface. The photograph was taken with an optical microscope.

The diamagnetic nature of various carbon polymorphs has long been established experimentally [1]. Small, temperature-independent susceptibilities, $\chi \approx -5 \times 10^{-9}\,\mathrm{m^3\,kg^{-1}}$, are associated with the atomic orbital diamagnetism in the insulating polymorphs such as diamond, whereas much larger, temperature-dependent susceptibilities in the range $-100$ to $-300 \times 10^{-9}\,\mathrm{m^3\,kg^{-1}}$ are associated with the Landau

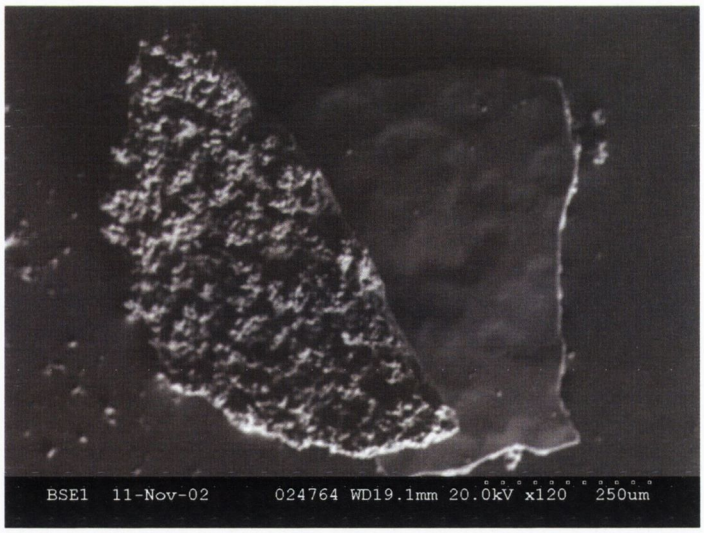



Figure 7.95. SEM image of a flake of soot broken in half and folded over itself. On the left we can see the "shiny" side of the soot flake, which is the side in contact with the quartz during deposition, while on the right we see the side which shows the conglomerate of spherical particles.

diamagnetism [2] of carriers with low effective mass in semimetallic polymorphs such as graphite or carbon nanotubes.

More recently, evidence has been accumulating for the presence of a variable ferromagnetic moment in certain forms of carbon [3], where it may be associated with the presence of atomic defects [4], or else induced by contact with ferromagnetic impurities [5]. There are reports of weak magnetic moments ($10^{-3} < \sigma < 10^{-1}\,\mathrm{A\,m^2\,kg^{-1}}$) in graphite [6], rhombohedral $C_{60}$ [7] and carbon foam [8] as well as in irradiated graphite [4]. Much larger ferromagnetic moments have been reported in pyrolysis products of carbon-containing precursors, notably 1,2-diaminopropane ($10.5\,\mathrm{A\,m^2\,kg^{-1}}$) [9] and trialkyl boranes ($32\,\mathrm{A\,m^2\,kg^{-1}}$) [10]. Contact induced magnetism, first suggested as an explanation for the ferromagnetism of meteoritic graphite [11], can result in magnetic moments ($\sim 0.05\ \mu_B$/C; note that $1\ \mu_B/\mathrm{C} = 465\,\mathrm{A\,m^2\,kg^{-1}}$) for atoms near the surfaces of multiwalled carbon nanotubes [5] or thin films in C/Fe multilayer stacks [12]. There are inevitable concerns regarding the possible presence of ferromagnetic impurities, especially for the samples with very small magnetization. The reports of large moments obtained by pyrolysis of organic precursors [3],[9], [10],[13] are of special interest. The carbon-based powders produced in this way are reported to have a saturation magnetization, $\sigma_S$, that is dependent on the ratio of hydrogen to carbon in the starting materials (precursors) [9]. It is also reported that the magnetic properties of the pyrolysis product depend on the pyrolysis temperature [3].

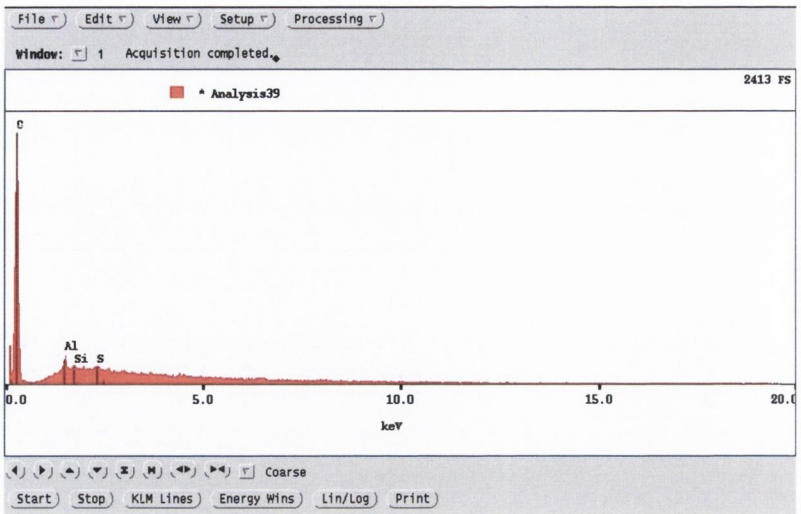



Figure 7.96. An EDAX spectrum of the pyrolysis products of 1,2-diaminopropane.

In an effort to confirm the reports of large ferromagnetic moments in carbon based materials and relate them to the moments observed in dilute magnetic oxides, we have undertaken an analysis of the pyrolysis product of 1,2-diaminopropane (DAP) and of allylamine (AA). We find $CN_x$ products that resemble the graphite whisker scrolls first described by Bacon in 1960 [14]. The most remarkable property of those whiskers was their tensile strength and Young's modulus – which Bacon measured to be 20 G Pa and 700 G Pa, respectively. More recently, whiskers have also been produced by potassium-GIC [15] and the energetic process of ball-milling [16].

## 7.2 Carbon Whiskers

### 7.2.1 Pyrolysis

A small quantity of the precursor (1,2-diaminopropane or allylamine), 3 ml, was placed into a quartz tube and frozen in liquid nitrogen. The tube was evacuated to $\sim 10^{-6}$ mbar and pumped out for 12 hours before sealing under vacuum. The tube was allowed to warm to room temperature and it was then placed in a furnace for 30 minutes at 950 °C to pyrolyse (for the diaminopropane) or at 900 °C (for the allylamine), which is within the "transition range" [17]. This temperature is also close to the range where "mesoscopic origami" and bond rearrangements are reported to take place in graphitic structures [18]. Pyrolysis at higher temperatures failed to deposit recoverable amounts of sample, as the gas mixture in the tube became explosive. The tube was rapidly

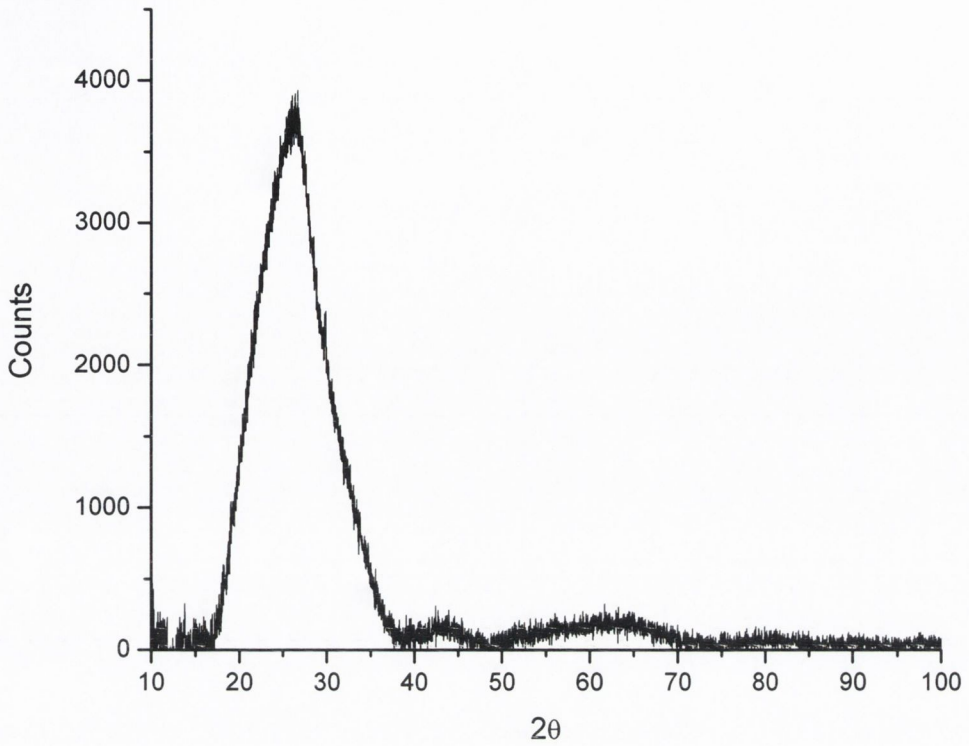



Figure 7.97. X-ray diffractogram of the carbon-nitrogen scrolls

removed from the furnace after pyrolysis and allowed to cool in ambient air. The black deposit on the tube walls began to peel away after $\sim 5 - 10\,\mathrm{s}$ of cooling to form the whiskers, a process which continues until most of the deposit on the inner surface has peeled off. The scrolls were originally viewed in the still-sealed tube under and optical microscope (Fig. 7.94). The tube was then broken open and the whiskers removed. Plastic tweezers and spatulas were used at all times. Assuming ideal gas behaviour, the pressure in the tube at pyrolysis temperature is in the region of 0.5 M Pa.

The conditions of the pyrolysis and cooling were varied to investigate the effect of cooling rate on the formation of whiskers. The scroll formation was not seen for higher pyrolysis temperature or for a slower cooling rate. A rate of $5\,\mathrm{K\,min^{-1}}$ was achieved using electronically controlled cooling of the furnace. Instead of following the scrolling behaviour, the deposit remained attached to the tube wall. This deposit, which we call "soot" was removed by scraping with a non-magnetic spatula. Under examination in a microscope, the whiskers appeared as shiny needles. The soot was shiny on one side, but dark on the other (Fig. 7.95).The pyrolysis of various precursors was carried

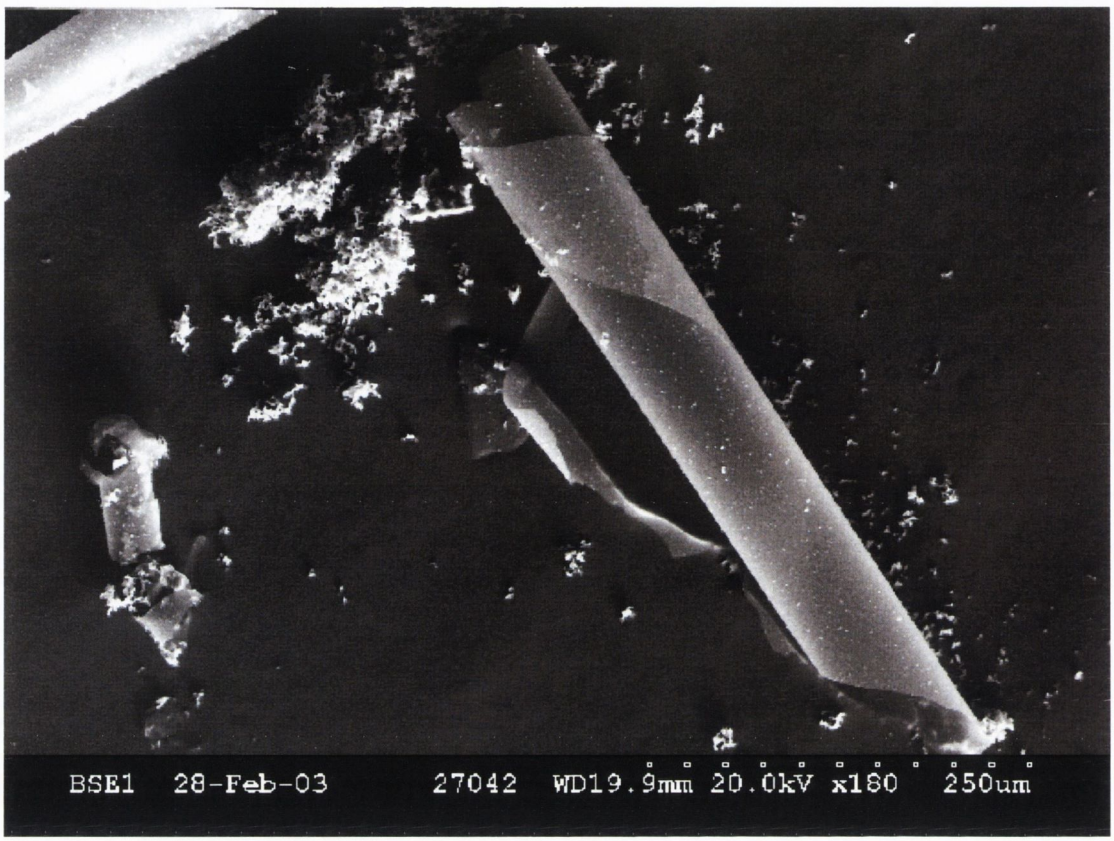



Figure 7.98. An SEM image showing a carbon whisker on the right together with some "soot" (top left).

out at a range of different temperatures. We were unable to produce whiskers by decomposition of propyne under similar conditions.

### 7.2.2 Combustion Analysis

Combustion analysis was performed on various different samples - some were mostly comprised of soot while others were mostly comprised of scrolls. Table 12 below shows a summary of the results.

It can be seen that the scrolled samples have a very low percentage of nitrogen by mass compared to the soot samples.

### 7.2.3 ICP

Inductively Coupled Plasma Mass Spectrometry (ICP) was performed to determine to the metal content of the 1,2-diaminopropane and allylamine used as precursors for the pyrolysis. A small amount, 3 ml, was placed into the quartz tube as per the pyrolysis procedure, to ensure the liquid being examined was as close to the precur-

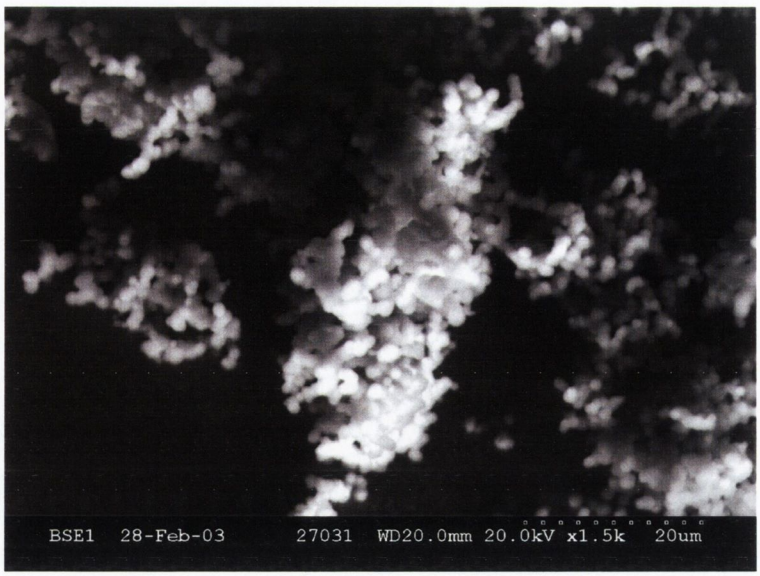



Figure 7.99. SEM image of the soot showing agglomerates of $\sim 1\,\mu$m particles.

sor used as possible. The liquid was then drained from the tube. The ICP method utilizes a hot argon plasma to excite atoms of the the material under investigation to metastable excited states. The relaxation of the atoms causes light to be emitted at characteristic wavelenghts, or lines. ICP can measure about 70 elements in aqueous solutions, including most metals. Importantly for this work, it can measure Fe, Ni, and Co - three elements that are prevalent in many magnetic compounds. The dissolved solids in sample solutions must be less than 1%. The optimum working range for element concentrations is from 0.5 to 100 parts per million (ppb) by weight. Determinations down to 100 parts per billion (ppb) or less are possible for many elements in clean solutions.

The ICP was conducted in the Centre for Microscopy and Analysis (CMA).

The results showed the levels of Fe, Ni, Co to be $< 50$ ppb in the precursors. Levels of contaminant this low would not lead to a measureable magnetic moment in the material.

| Sample | Form | C wt% | H wt% | N wt% |
|---|---|---|---|---|
| DAP02 | Scrolls | 91.2 | 0.4 | 7.7 |
| DAP03 | Soot | 52.4 | 3.9 | 43.7 |
| DAP04 | Mix | 86.8 | 1 | 11.8 |
| DAP05 | Soot | 52.9 | 3.5 | 43.5 |
| DAP06 | Soot | - | - | - |
| DAP07 | Scrolls | 91 | 0 | 8 |

Table 12.A table of elemental analysis results from combustion and subsequent mass spectrometry of the soot and scroll samples.

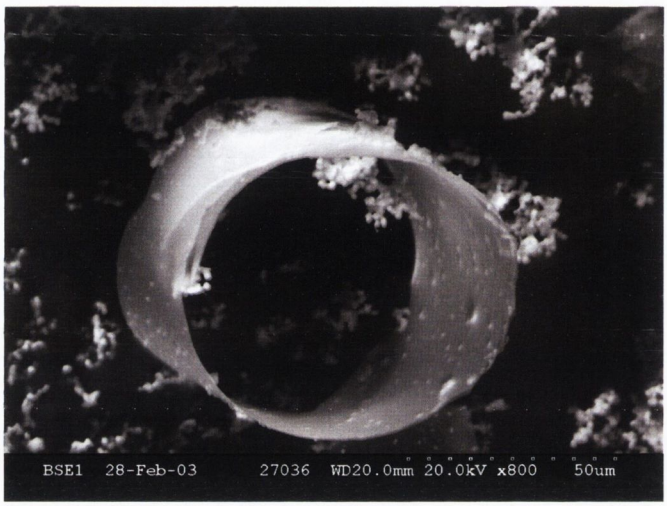



Figure 7.100. Cross-section of a whisker as viewed in the SEM. The diameter of this scroll is $\sim 25\,\mu$m, a typical value for the whisker.

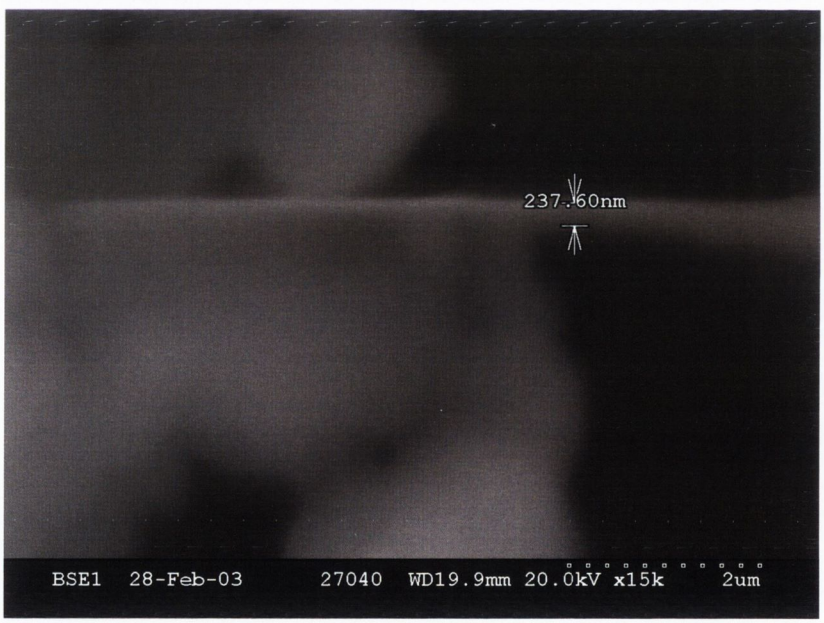



Figure 7.101. An SEM of one layer of the whisker, magnified. This provides a measurement of the thickness of the layers which wrap around themselves to form the scrolls.

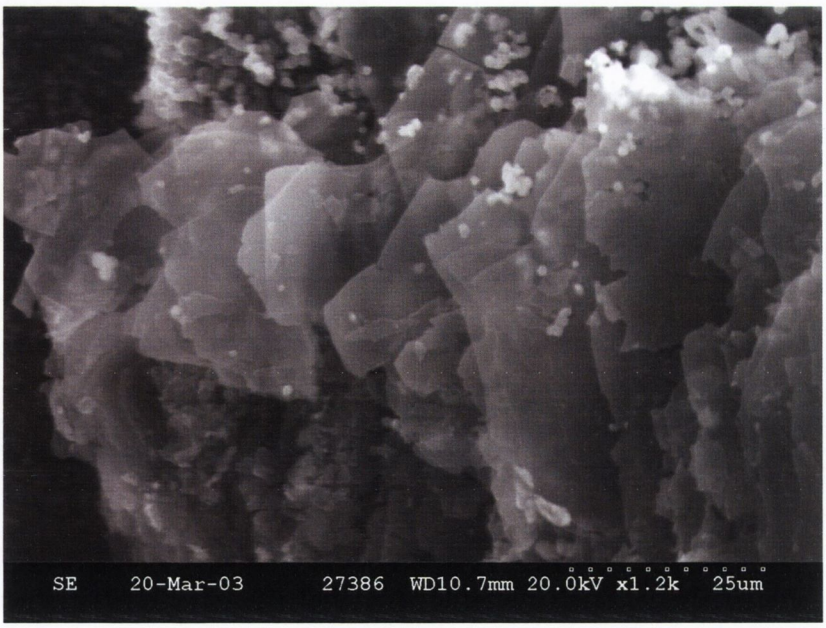



Figure 7.102. An SEM image of some soot which has intercalated layers of graphite-like material which resemble the graphine layer that fold to create the whiskers.

### 7.2.4 EDAX

A typical EDAX spectrum of the scrolls is shown in Fig.7.96. The strong peak is carbon, which is responsible for 99.4% of the signal (by weight). The Al and S are background signals due to the holder and the Si is not determined within experimental accuracy. The EDAX is unable to determine N or H accurately, due to the fact that a variable pressure SEM was used to avoid sample charging.

### 7.2.5 XRD

The XRD pattern of scrolls exhibits a broad peak at $d = 0.34\,\text{nm}$ (Fig. 7.97). This $d$ spacing is that of the (002) spacing of graphite. This shows that the carbon in the sample is practically amorphous, with a roughly graphitic structure to it. The coherence length of the crystalline regions deduced from the width of the peak by using the Scherrer formula is $8 \pm 1\,\text{nm}$.

### 7.2.6 Microscopy and SEM

When viewed in the SEM, the two phases of the material were immediately apparent. In Fig.7.98 we see the scroll on the right, which appears as semi-transparent to the SEM beam. On the left, there is a dahlia-like conglommeration, which is the

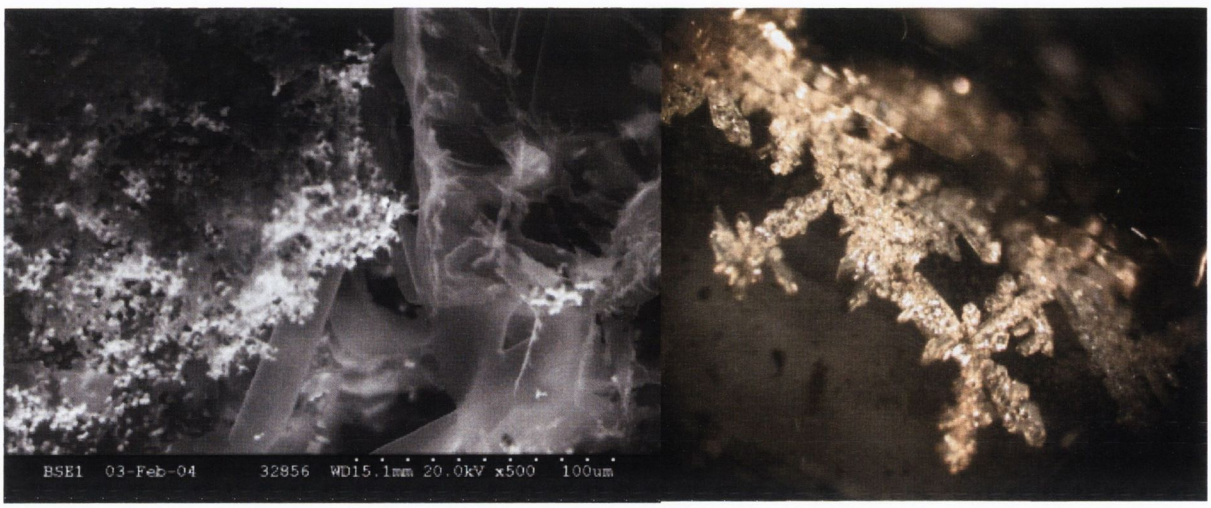



Figure 7.103. Crystallite formation on tube surface (right) and in SEM (left). The phase is possibly adamantane.

"soot" that we have described in the previous section.

Taking a closer look at the soot, we see that one side of it is composed of spherical particles of approximately 1 micron in diameter (Fig. 7.99). These dahlia-like conglommerations seem to form a smooth side to the tube, with the dahlia side facing in, as can be seen in Fig. 7.95. In this picture we can see one side of the flake is completely smooth while the other shows the dahlia pattern.

The soot is of relatively little interest compared to the scrolls and can be seen as an undesirable by product that seems to always accompany the formation of the scrolls. Further microscopy of the scrolls reveals some interesting characteristics. Fig.7.100 shows the cross-section of a scroll. This particular scroll seem wrapped over on itself twice or three times. Closer magnification on the surface of the scroll reveals a layer thickness of about less than 250 nm (Fig. 7.101).

While the phases are quite distinctive, the spherical particles tend to inhabit the surface of the scrolls, and there seems to be some unusual interplay between the two phases. For instance, Fig. 7.102 shows some sort of intercalation of the scroll layers between the dahlia formations.

Examination of the pyrolysed tube of the allylamine under the microscope revealed what seemed to be some transparent unusual crystal formations on the tube surface (Fig. 7.103). Further examination of this material in the SEM showed that there seemed to be very little coordination in this phase. There was far too little of this material to examine it in the XRD. The material appeared in all tubes after pyrolysis,

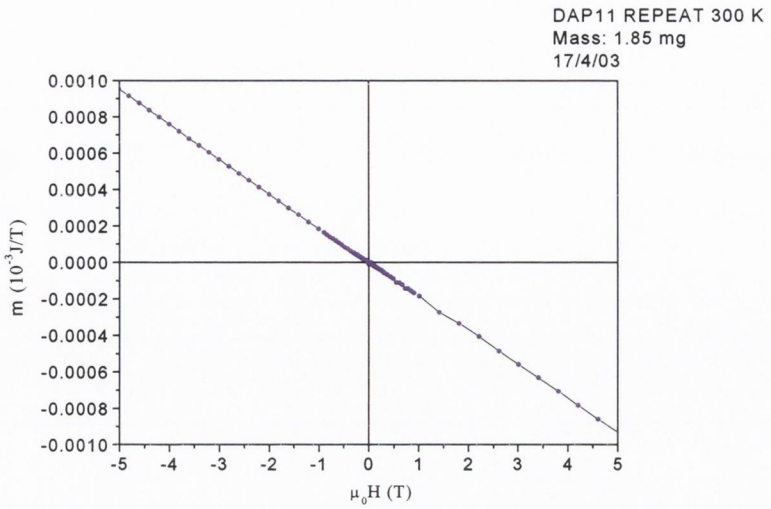



Figure 7.104. M-H loop of soot product. $\chi = -27 \times 10^{-9}\,\mathrm{m^3\,kg^{-1}}$. The sample holder contributes a diamagnetic moment of $\chi = -1.37 \times 10^{-7}\,\mathrm{A\,m^2\,T^{-1}}$.

but due to the minute quantities, its properties, structure and elemental make-up have remained largely undetermined. It is a minor phase and it's appearance would suggest adamantane as a possible candidate. Adamantane (Tricyclo[3.3.1.$1^{3,7}$]decane), with a formula $C_{10}H_{16}$, is a cycloalkane. It is an off-white powder that forms face-centred cubic crystals.

### 7.2.7 FTIR

The scroll surfaces and one side of the soot (the one which faces the tube) are quite shiny, so it would be expected that they would respond well to FTIR spectroscopy. However, despite the fact that many different samples were measured, nothing significantly distinctive from the background taken was ever observed.

### 7.2.8 SQUID Magnetometry

For the magnetic measurement, a typical sample mass was 1 mg. Measurements were taken at room temperature and at 5 K. The diamagnetic signal from the sample holder, which was a gel cap mounted in a drinking straw, was measured and subtracted from the data. For selected samples, magnetization loops were also acquired at intermediate temperatures.

The soot samples were perfectly diamagnetic at all temperatures with room

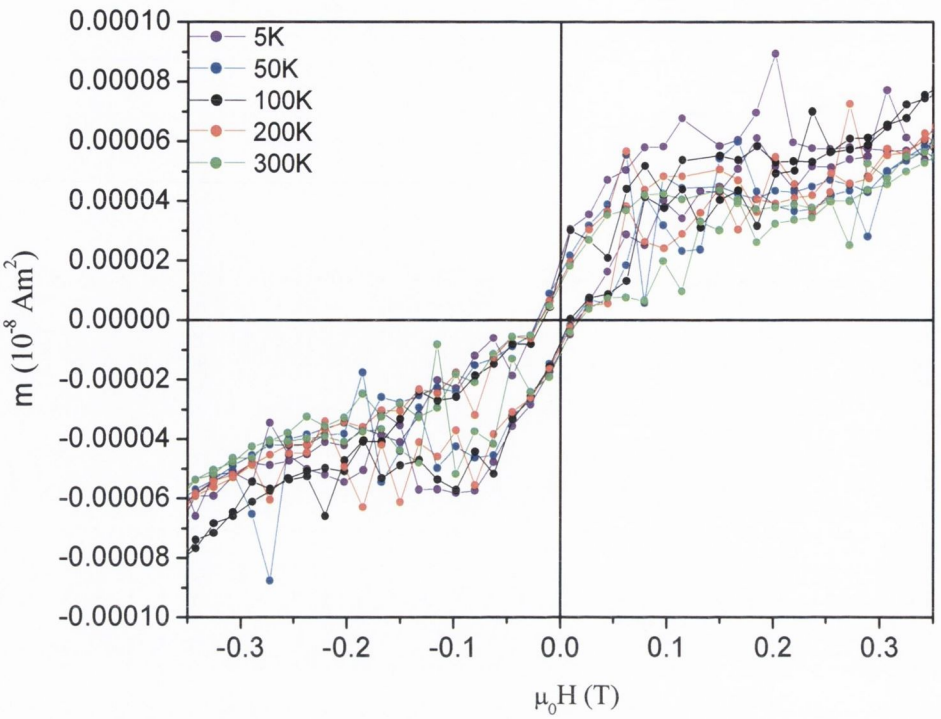



Figure 7.105. Magnetization measurements of a scroll sample at different temperatures.

temperature susceptibilities ranging from $\chi = -26 \times 10^{-9}\,\mathrm{m^3\,kg^{-1}}$ to $\chi = -72 \times 10^{-9}\,\mathrm{m^3\,kg^{-1}}$. A typical measurement is shown in Fig. 7.104 . These measurements were repeatible and the diamagnetic susceptibility had no time dependence.

The whisker samples had a mainly diamagnetic susceptibility, with small ferromagnetic loops sometimes observable at low fields having a magnetization value of up to $0.2\,\mathrm{A\,m^2\,kg^{-1}}$ (Fig. 7.106). The large ferromagnetic moments reported previously [9] were never observed. The high-field diamagnetic susceptibility at room temperature ranged from $\chi = -84 \times 10^{-9}\,\mathrm{m^3\,kg^{-1}}$ to $\chi = -171 \times 10^{-9}\,\mathrm{m^3\,kg^{-1}}$. No anisotropy of the susceptibility was observed in attempts to orient a suspended scroll in a magnetic field. The moment shows very little temperature dependence (Fig.7.105).

Only the scrolls produced from the pyrolysis of 1,2 diaminopropane exhibited this ferromagnetic behaviour. Both the soot and scrolled samples from the pyrolysis of the allylamine failed to produce a measurable ferromagnetic moment. Typical results from all four conditions are shown in Fig.7.106. The magnetic behaviour of the soot from both samples is quite similar. The absence of a ferromagnetic signal notwithstand-

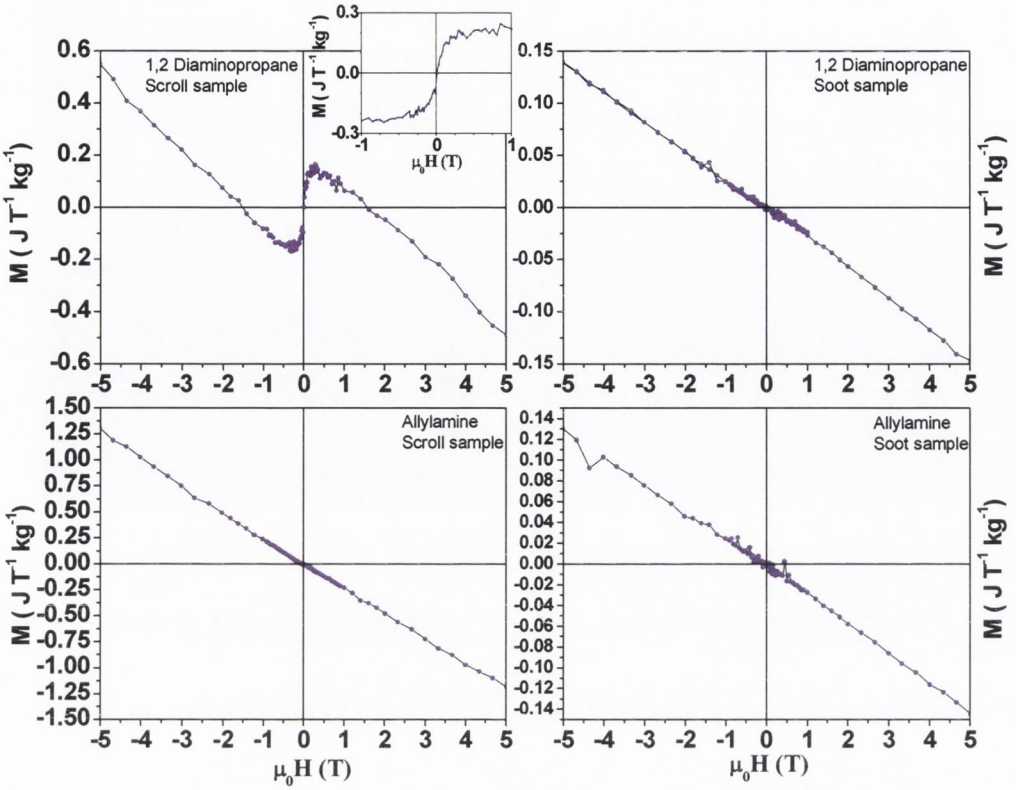



Figure 7.106. Room temperature magnetization data for scroll and soot products of the two precursors

ing, the scrolls from the allylamine precursor still demonstrate the large diamagnetic susceptibility, comparable to that of graphite, $\chi = -169 \times 10^{-9}\,\mathrm{m^3\,kg^{-1}}$.

### 7.2.9 MFM

An AFM of the surface of one of the scrolls is shown in Fig. 7.107. The micron diameter circles are likely to be the soot which attaches itself to the surface of the scrolls which has already been observed in the SEM. Smaller irregular features can be seen on the surface of the scroll. The MFM shows no magnetic contrast.

### 7.2.10 EPR

The EPR spectrum of a typical soot sample is shown in Fig. 7.108. The spectrum is best fit when there are two components used, one with a broad line and one with a narrow. Table 13 shows the difference between scroll and a soot samples from a 1,2

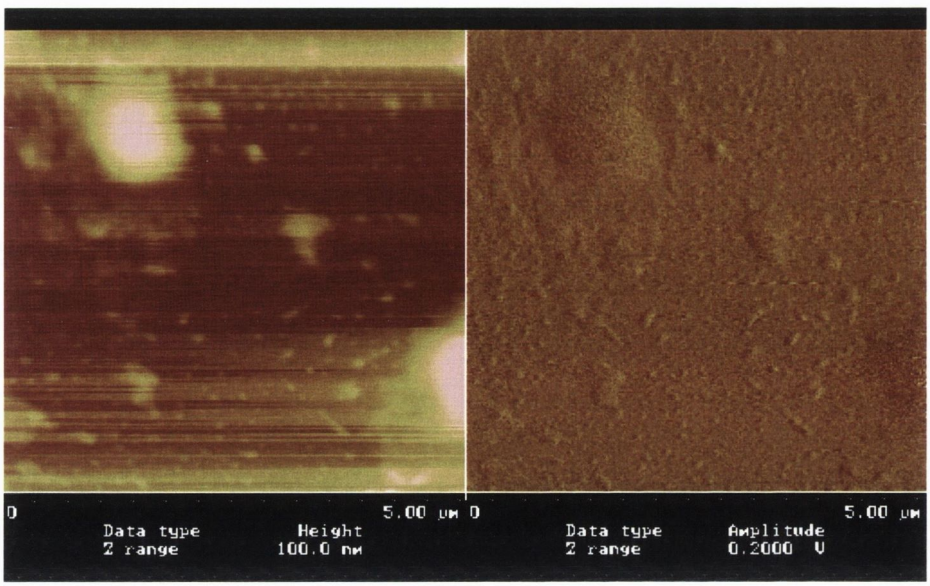



Figure 7.107. AFM of scroll surface

| Data | Scroll | Soot |
|---|---|---|
| Spin density/$m^{-3}$ | $4.45 \times 10^{24}$ | $1.43 \times 10^{24}$ |
| $g_1$ | 2.00280(4) | 2.00274(6) |
| $FWHM_1/G$ | 2.20(3) | 2.30(7) |
| $\Delta B_{pp1}/G$ | 1.27(2) | 1.33(4) |
| $g_2$ | 2.00267(12) | 2.00278(5) |
| $FWHM_2/G$ | 12.0(8) | 6.7(6) |
| $\Delta B_{pp2}/G$ | 6.9(5) | 3.9(4) |

Table 13.Fit parameters for the EPR spectra

diaminopropane precursor.

The intensity of the two components is equal for the scroll samples but the ratio of $L_1$ to $L_2$ is 1.37 for the soot samples. The spin density for the scrolls is three times higher for the scrolls than the soot. The spin density corresponds to one unpaired spin per $2 \times 10^4$ atoms.

### 7.2.11 RGA

The residual gas analysis of the atmosphere in a tube of pyrolysed 1,2-diaminopropane precursor is shown in Fig. 7.109. The background is normalised to the water vapour peak. The background is low compared to the signal when the residual gas is bled in the chamber.

The main peak observable is the 15 a.m.u. peak. This may be $CH_3$ or NH, as these are the only two combinations of the atoms possibly present in the gas that may

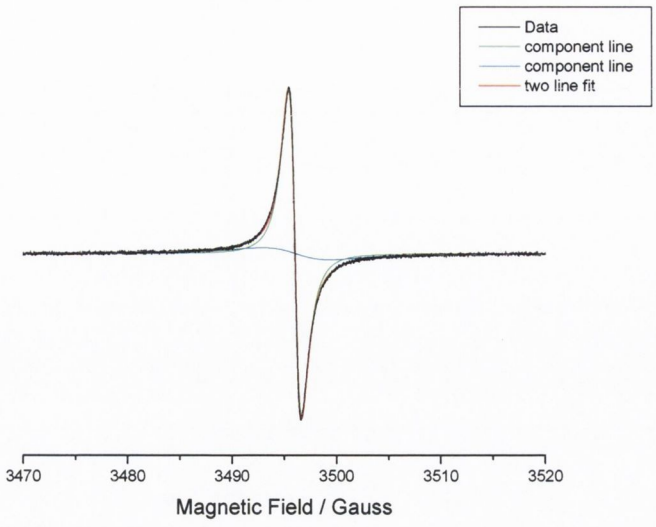



Figure 7.108. EPR spectrum of a soot sample from a 1,2 diaminopropane precursor.

have a molecular weight of 15. Also important are the 16, 17 and 28 a.m.u. peaks. The 16 and 17 a.m.u. peaks are most likely due to methane and ammonia. These are the by-products of the pyrolysis. The 28 a.m.u. peak can be attributed to nitrogen. This may be a by-product of the pyrolysis, but there might also be some residual nitrogen left in the antechamber after pumping.

The residual gas analysis of the allylamine shows a spectrum quite similar to the 1,2-diaminopropane (Fig. 7.110). The main difference is that the 16 a.m.u. peak is less prevalent (by about a factor of 2) in the allylamine spectrum than in the 1,2-diaminopropane spectrum. There is also a slight difference in the 27/28/29 a.m.u. peaks, with the 29 peak more prevalent in the allylamine residue, and the 28 more prevalent in the diaminopropane residue.

### 7.2.12 Gas Absorption Analysis

Hydrogen absorption of the soot samples was measured in a thermo-piezic analyser (TPA), but no measurable absorption was seen up to 600 °C. It is concluded that any hydrogen absorption is less than 1 at%.

### 7.2.13 Transport

A typical R(T) curve of a scroll is shown in Fig. 7.111. The scrolls usually show a

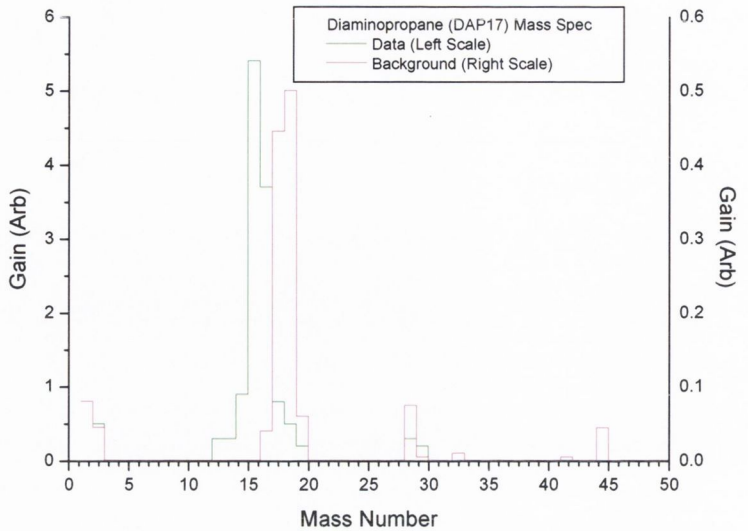



Figure 7.109. Residual gas analysis of the remaining gas following pyrolysis of 1,2-diaminopropane.

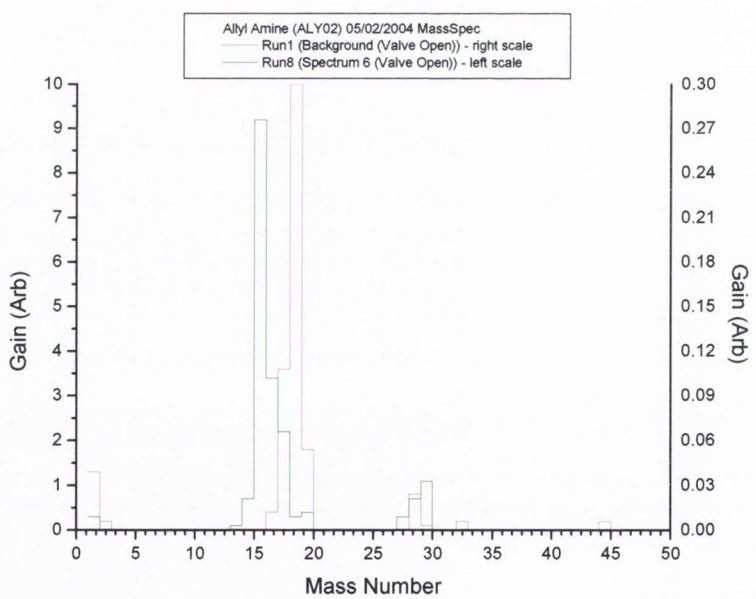



Figure 7.110. Residual gas analysis of the remaining gas following pyrolysis of allylamine.

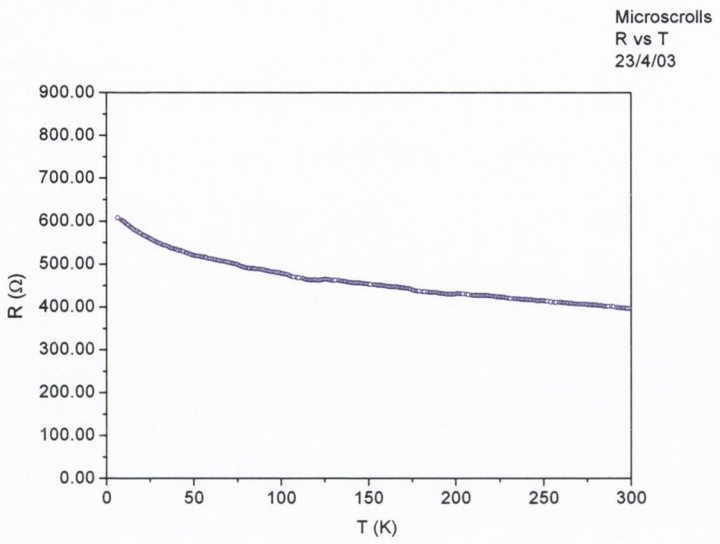



Figure 7.111. A typical R(T) curve of a scroll

semiconducting temperature dependence of resistance, but a few seem to show metallic characteristics. The resistivity of these scrolls is approximately $\sim 10^{-6}\ \Omega\,\mathrm{m}$, which is at the limit of metallic conductivity. Magnetic fields of up 1 T did not change the resistance.

### 7.2.14 Hall Effect

The Hall effect was measured on broken shards of the scrolls (Fig.7.112).

A typical plot of the Hall resistance of a scroll piece as a function of field is shown in Fig. 7.113. From the plot, using a thickness of 0.25 $\mu$m, the carrier concentration, $n$, is determined as $1.6 \times 10^{27}\,\mathrm{m}^{-3}$, or $1.43 \times 10^{-2}$ carriers per carbon. Coherent electronic transport around the tube is precluded by the short mean free path.

## 7.3 Carbon Manganese

### 7.3.1 Sample Preparation

Graphite powder from Aldrich of unquoted purity ($> 99\%$) and Mn powder were mechanically mixed by hand in an agate mortar and pestle. The powder was pressed into a pellet and sintered for 12 hours at 900 K under a vacuum of $10^{-5}$ mbar.

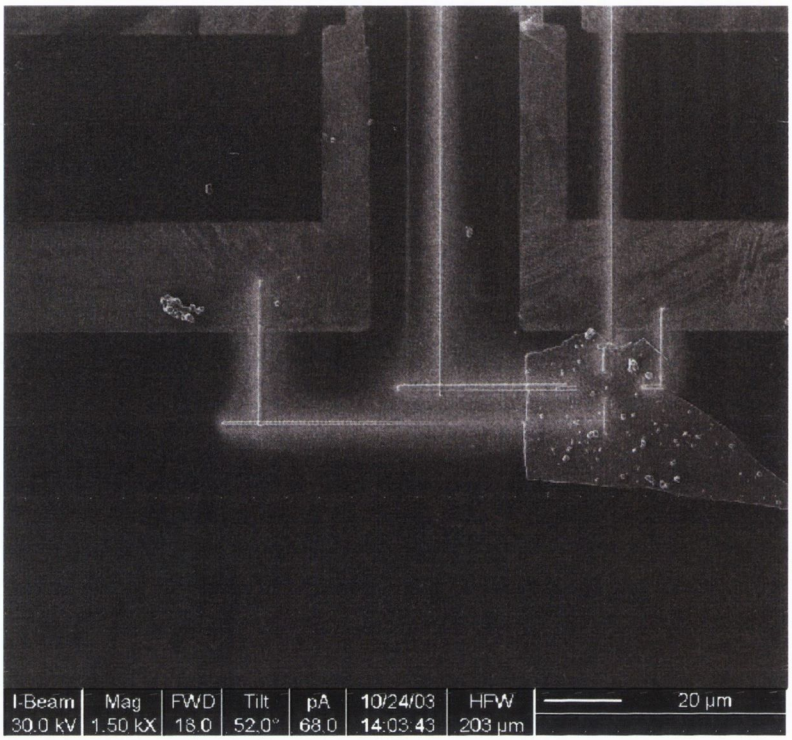



Figure 7.112. An scanning electron microscopy image of the contacts made to a broken scroll in order to measure the Hall Effect.

### 7.3.2 XRD

The XRD pattern of C-Mn show peaks of both graphite and manganese. No other peaks (e.g. for Fe) were observed.

### 7.3.3 SEM/EDAX

The EDAX results shown in Fig. 7.115 show some clustered areas of bright contrast. The bright contrast indicated higher atomic number. From this, we can see that significant clustering of the Mn in the sample has occurred.

The EDAX analysis of the sample (Fig. 7.116) shows that there is a indication that Fe might be present. Since the secondary Mn peak and the primary Fe peak are close the each other, the EDAX system has difficulty in precisely resolving the two peaks. Quantative analysis reveals that the sample contains 0.2 at% Fe, within an experimental error of 0.16%.

### 7.3.4 VSM

A typical M(H) loop is shown in Fig. 7.117. A clear ferromagnetic loop with a

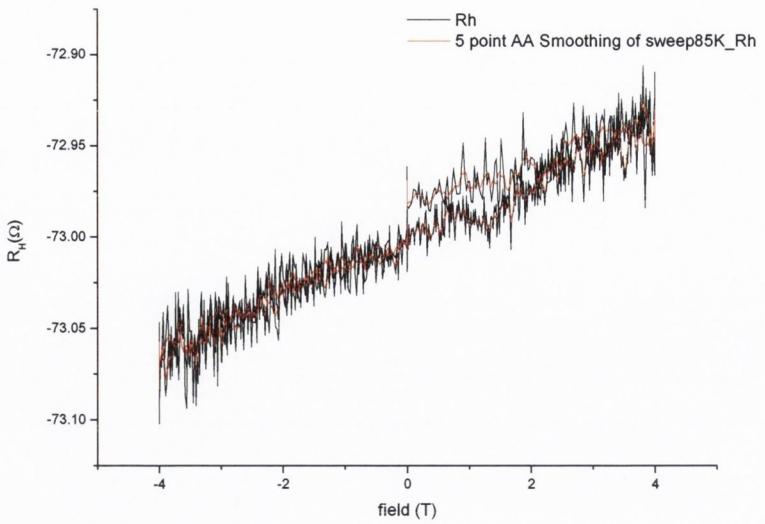



Figure 7.113. Hall resistance of a scroll piece as a function of field.

saturation magnetisation of about $0.2\,\mathrm{J\,T^{-1}\,kg^{-1}}$. This corresponds to 5% Mn doping. The ferromagnetic signal was not seen for higher percentage doping. Loops of the pure Mn, C and sample holder were also taken. The Mn was gives a perfectly paramagnetic response. The sensitivity of the VSM was the limiting factor in the other two measurements. The SQUID was therefore used to investigate the magnetic properties of the pure graphite.

### 7.3.5 SQUID Magnetometry

For the doped samples, the SQUID loops verified the VSM measurements, with a saturation magnetization of $0.2\,\mathrm{J\,T^{-1}\,kg^{-1}}$.

However, a measurement of the Aldrich graphite (Fig. 7.119) also revealed a ferromagnetic loop, again with a saturation magnetization of $0.2\,\mathrm{J\,T^{-1}\,kg^{-1}}$. This was overlayed on a strong diamagnetic signal, as one would expect from graphite.

Measurements of 99.9995% purity graphite from Alfa Aesar revealed a perfect diamagnetic response, with $\chi = -92 \times 10^{-9}\,\mathrm{m^3\,kg^{-1}}$ at room temperature (Fig. 7.120).

### 7.3.6 $^{57}$Fe Mössbauer Spectrometry

The Mössbauer spectrum of the $C_{95}Mn_5$ (Fig. 7.121a) shows a doublet at the centre, due to iron in the Be-window of the detector (Fig. 7.121d). The peaks at

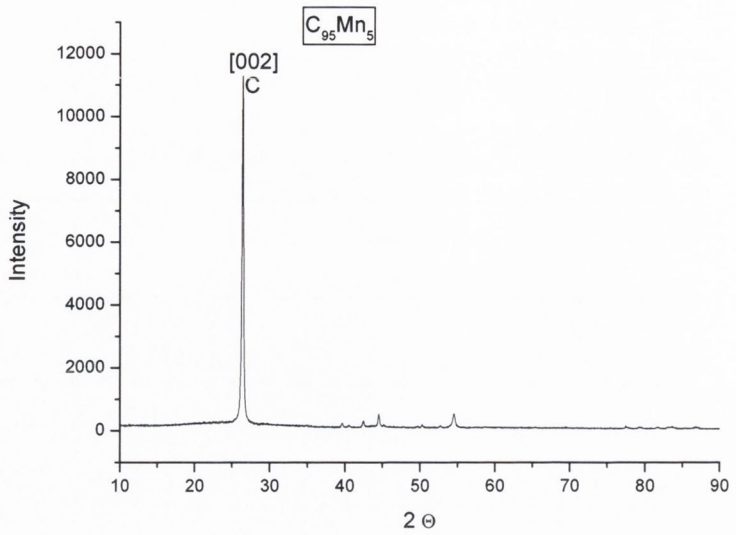



Figure 7.114. X-ray diffraction pattern of C-Mn. All the peaks are those of polycrystalline graphite and Mn metal.

$+6\,\mathrm{mm\,s^{-1}}$ indicates the possibility of the presence of some form of magnetically formed iron. A spectrum of the Aldrich graphite (Fig. 7.121b) shows an Fe sextet and a wider sextet due to an iron oxide (most probably $Fe_3O_4$). The Aesar 99.9995% graphite only show an Fe-doublet which is due to the iron in the Be counter window (Fig. 7.121c).

## 7.4 Discussion

### 7.4.1 Whiskers

We were unable to reproduce the ferromagnetic properties reported previously by Murata et al. [9] for carbon produced by pyrolysis of 1,2-diaminopropane. The main pyrolysis products were found to be microscroll whiskers of poorly crystalline $CN_x$, with $x \approx 0.07$, and/or a soot of approximate composition $CN_x$ with $x \approx 0.25$.

From the fact that the pyrolysis of 1,2-diaminopropane and of allylamine produce similar results, with the main difference being a disparity in the amount of $CH_4$ that remains in the tube as a residual gas, and from consideration of bond strengths, it can be surmised that the first step in the pyrolysis of the 1,2-diaminopropane is probably

$$CH_3CH(NH_2)CH_2NH_2 \rightarrow CH_2 = CH - CH_2NH_2 + NH_3$$

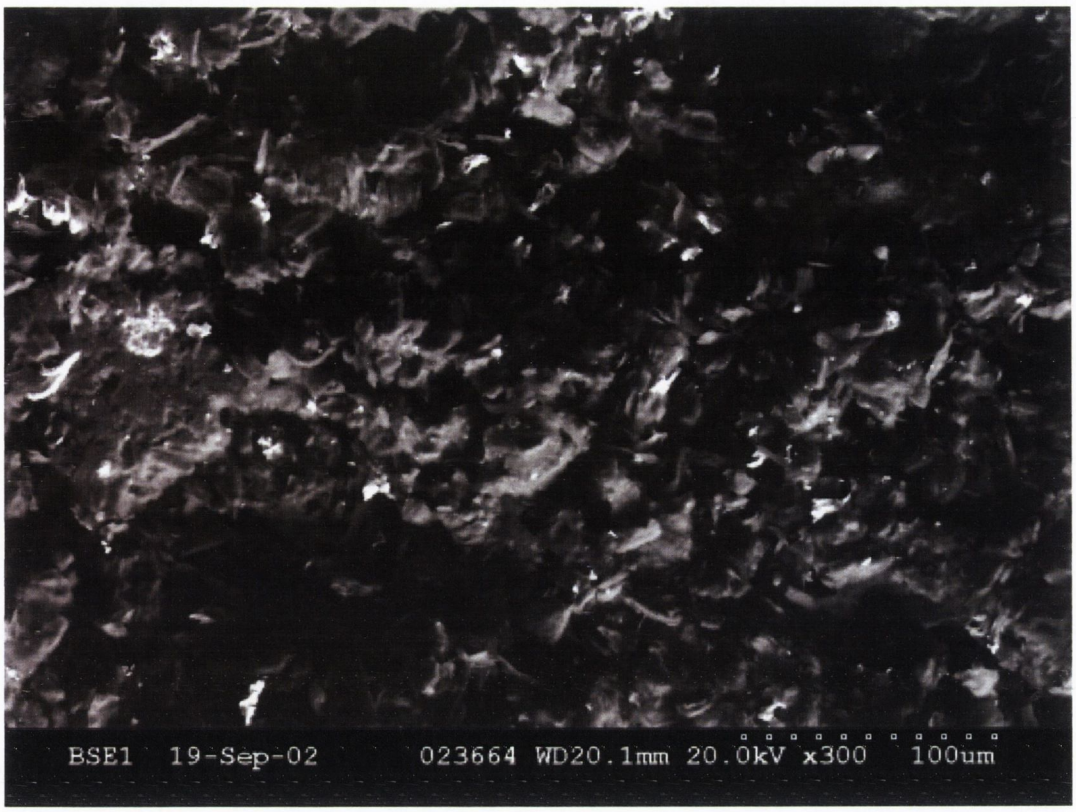



Figure 7.115. SEM image of the C-Mn

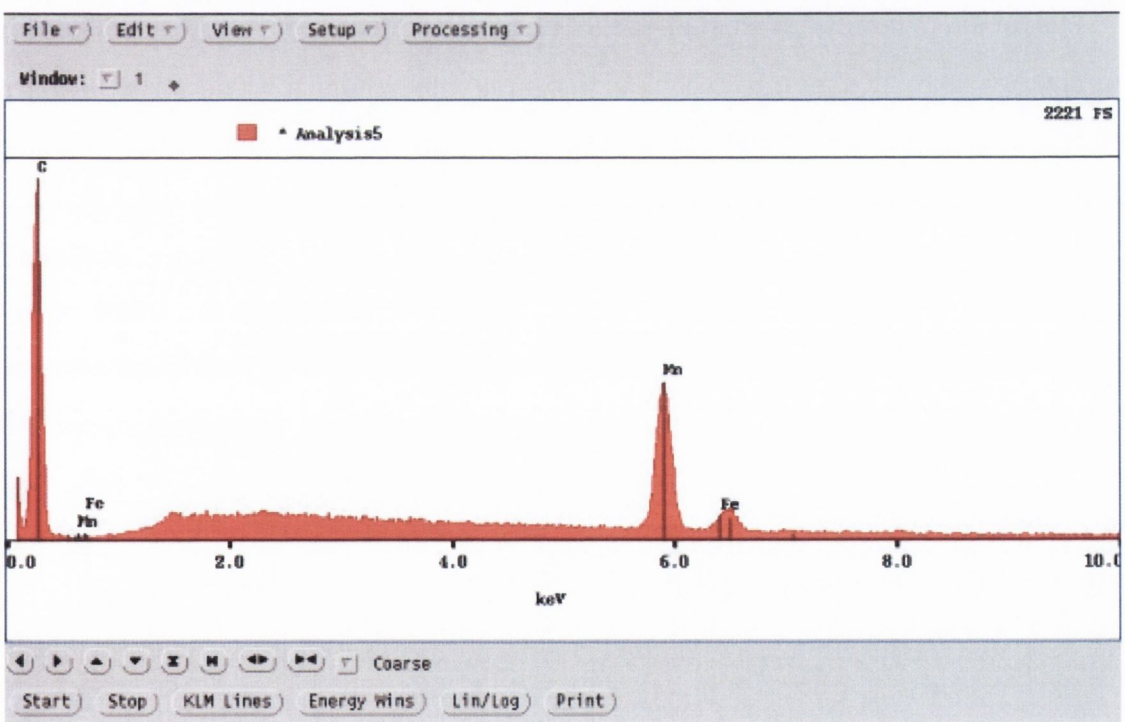



Figure 7.116. EDAX of C-Mn

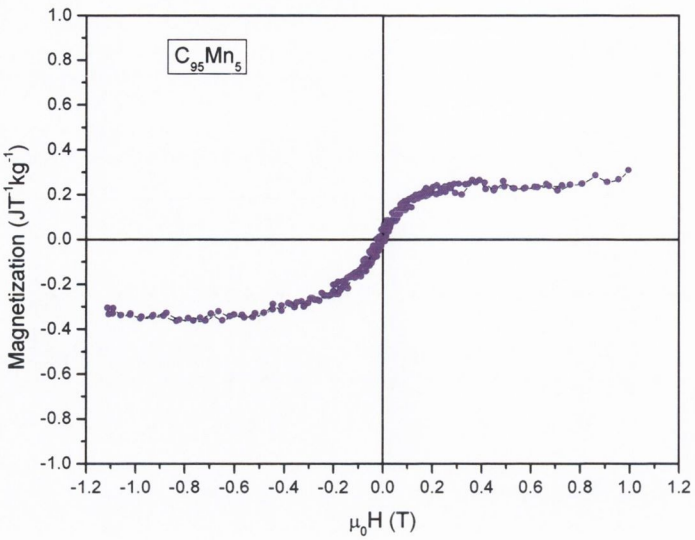



Figure 7.117. VSM M-H loop of C-Mn

The chain after this is likely to largely involve decomposition to radicals, such as propargyl ($C_3H_3$) [19]. These radicals may then polymerise, incorporating a smaller number of nitrogen-containing species to give $CN_x$ films observed.

The scrolls are fragile and break easily. They do not show the high flexibility, tensile strength and Young's modulus that was associated with graphite whiskers [14], nor do they exhibit the anisotropic susceptibility of graphite. The structure is not formed of graphene sheets parallel to the scrolls surface. The material is isotropic a poorly crystallized.

The whiskers made from both precursors reveal a large isotropic diamagnetic susceptibility of $\chi = -170 \times 10^{-9}\,\mathrm{m^3\,kg^{-1}}$. These fall within the measured range of values for graphite, where $\chi = -3.8 \times 10^{-9}\,\mathrm{m^3\,kg^{-1}}$ parallel to the basal plane and $\chi = -251 \times 10^{-9}\,\mathrm{m^3\,kg^{-1}}$ perpendicular to it [1]. Randomly orientated graphite has $\chi = -169 \times 10^{-9}\,\mathrm{m^3\,kg^{-1}}$, similar to the scrolls. The bonding should be $sp^2$. As for the soot, it shows a smaller susceptibility, with $\chi \approx -40 \times 10^{-9}\,\mathrm{m^3\,kg^{-1}}$. There is a significant proportion of $sp^3$ bonds in the soot. The $sp^2$:$sp^3$ ratio is about 4:1.

While EDAX shows no ferromagnetic metallic impurities in the samples and ICP reveal $< 50$ pbb in all precursors, the ferromagnetic component with $\sigma_S$ of up to $0.2\,\mathrm{A\,m^2\,kg^{-1}}$ would represent 0.1% by mass of iron, or somewhat more cobalt. The moments are comparable in magnitude to those that have been reported in graphite

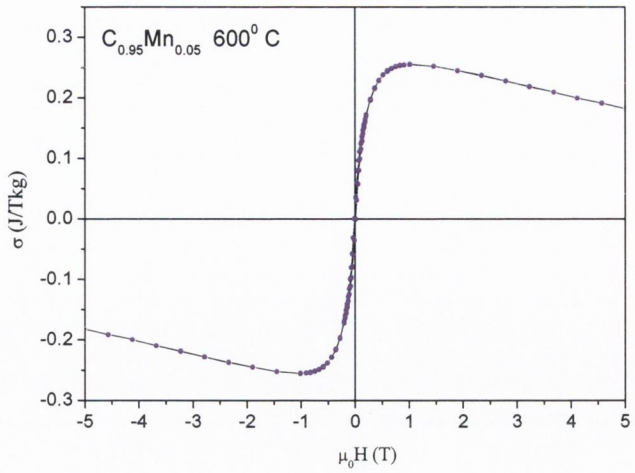



Figure 7.118. M(H) loop from SQUID measurements of the C-Mn sintered at 600 °.

[6] of rhombohedral $C_{60}$ [7].

The absence of moments in soot samples from the same batches points to an origin of the ferromagnetic moment in defects that are present in the scrolls, but not in the soot. The puzzle here is not that defects with unpaired spin can exist in highly disordered graphite, but that exchange interactions might exist that couple them together into a ferromagnetically ordered state at room temperature [20].

The diamagnetic susceptibility of the carbon microscrolls is large and isotropic, similar to that of graphite powder. The small and variable moment found in some of the scrolls, but not in soot from the same batches corresponds to at most $5 \times 10^{-4}$ $\mu_B$/C. This moment may be regarded as a further example of defect-related '$d^0$ ferromagnetism' [21], but the origin remains unclear.

The similarity of the magnetization curves to those of the Aldrich graphite makes it difficult to make a strong claim. It would be worth examining the whiskers by STEM.

### 7.4.2 C-Mn

The magnetism seen in the C-Mn system is due to impurities in the graphite. Careful measurements of the starter material (Aldrich graphite) reveals a ferromagnetic loop. Mössbauer analysis of this graphite shows the presence of iron and iron oxide in these samples. Pure graphite (purity = 99.9999%) shows perfect diamagnetism and no trace of iron in its Mössbauer spectrum. It must be concluded that the ferromagnetism

observed is due to the Aldrich graphite Fe impurities.

While we have not discounted the possibility of carbon-based Mn-doped DMS, our attempts have shown that a different technique would be needed to produce such a material.

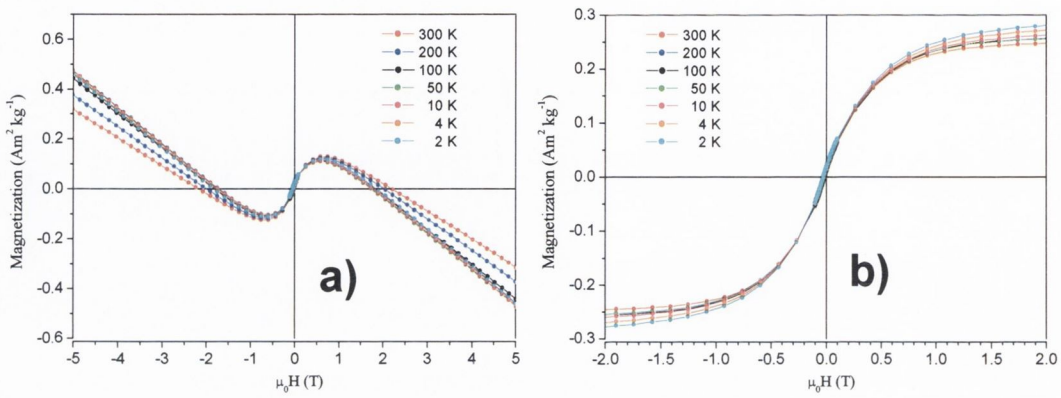



Figure 7.119. a) M(H) loops at different temperatures of "pure" graphite from Aldrich and b) with diamagnetic signal removed

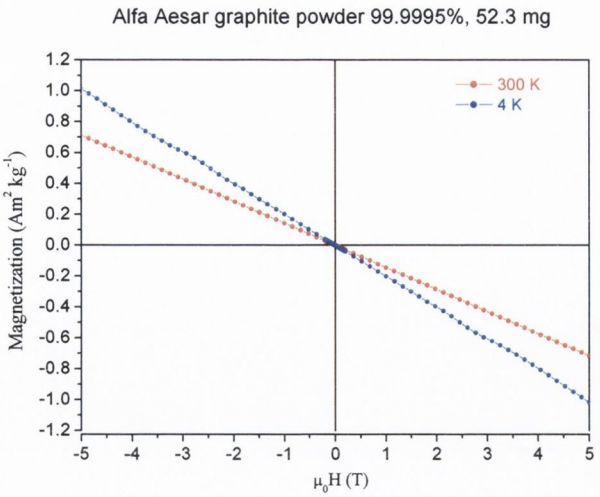



Figure 7.120. M-H loops at 300 K and 5 K for 99.9995% pure graphite from Aesar.

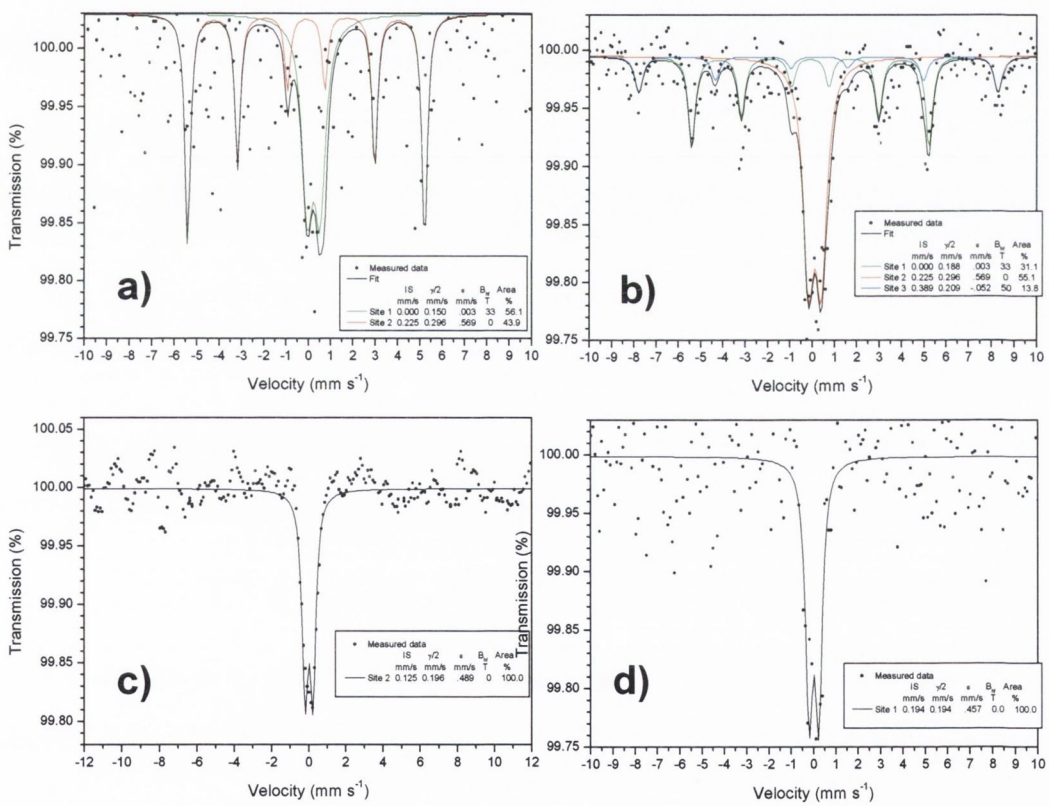



Figure 7.121. a) Transmission Mössbauer spectrum of $C_{95}Mn_5$ powder. b) Transmission Mössbauer spectrum of Aldrich graphite powder. c) Transmission Mössbauer spectrum of Alfa Aesar 99.9995% purity graphite powder. d) Transmission Mössbauer spectrum background due to iron in the Be window. Spectrum a) has a simulation (not a fit) overlayed on top of it. Spectra b), c) and d) have fits overlaid upon the. The folding point was determined through drive calibration with an Fe powder.

# References

[1] J. Heremans, C.H. Olk, D. T. Morelli, Phys. Rev. B 49, 15122 (1994)

[2] P. Stamenov, J. M. D. Coey, J. Magn. Magn. Mat. 290-291, 279 (2005)

[3] T. L. Makarova, In: Narlikar A. Studies of High-Tc Superconductivity, vol 44-45, New York; Nova Science (2003)

[4] P. Esquinazi, D. Spemann, R. Hohne, A. Setzer, K.-H. Han, T. Butz, Phys Rev Lett. 91, 227201 (2003)

[5] O. Céspedes, M. S. Ferreira, S. Sanvito, M. Kociak, J. M. D. Coey, J. Phys.: Condens. Matter 16, L155 (2004)

[6] P. Esquinazi, A. Setzer, R. Hohne, C. Semmelhack, Y. Kopelevich, D. Spemann, et al., Phys. Rev. B 66, 024429 (2002)

[7] T. L. Makarova, B. Sundqvist, R. Hohne, P. Esquinazi, Y. Kopelevich, P. Scharff, et al., Nature 413, 716 (2001)

[8] A. V. Rode, E. G. Gamaly, A. G. Christy, J. G. Fitzgerald, S. T. Hyde, R. G. Elliman, et al., Phys Rev B 70, 054407 (2004)

[9] K. Murata, H. Ushijima, H. Ueda, K. Kawaguchi, J Chem Soc, Chem Commun. 7, 567 (1992)

[10] K. Murata, H. Ushijima, J Appl Phys. 79, 978 (1996)

[11] J. M. D. Coey, M. Venkatesan, C. B. Fitzgerald, A. P. Douvalis, I. S. Sanders, Nature 420, 156 (2002)

[12] H.-Ch. Mertins, S. Valencia, W. Guda, P. M. Oppeneer, O. Zaharko, H. Grimmer, Europhys. Lett. 66, 743 (2004)

[13] K. Murata, H. Ueda, K. Kawaguchi, Synthetic Metals 44, 357 (1991)

[14] R. Bacon, Jour. Appl. Phys. 31, 283 (1960)

[15] H. Shioyama, T. Akita, Carbon 41, 179 (2003)

[16] J. L. Li, Q. S. Peng, G. Z. Bai, W. Jiang, Carbon 43, 2830 (2005)

[17] M. J. Matthews, M. S. Dresselhaus, N. Kobayashi, T. Enoki, M. Endo, K. Nishimura, Phys. Rev. B 60, 4749 (1998)

[18] D. Tománek, Physica B: Condensed Matter 323, 86 (2002)

[19] A. Lifshitz, M. Frenklach, A. Burcat, J. Phys. Chem. 80, 2437 (1976)

[20] J. M. D. Coey, S. Sanvito, Physics World 17, 33 (2004)

[21] J. M. D. Coey, Solid State Sciences 7, 660 (2005)

# Chapter 8

# Discussion

"If two things don't fit, but you believe both of them, thinking that somewhere, hidden, there must be a third thing that connects them, that's credulity"

Umberto Eco

## 8.1 Introduction

In the present work, room temperature ferromagnetism is observed in Cr-doped $In_2O_3$, Fe/Mn/Cr-ITO, Fe-doped $SnO_2$, Fe-doped $TiO_2$ and Al-doped Co:ZnO films grown by pulsed laser deposition, as well as in impure graphite and carbon whiskers. In all systems, the actual concentration of $3d$ dopants in the films always exceeds that in the targets. No magnetic moment is observed in undoped ZnO, $In_2O_3$, ITO, $TiO_2$ films grown on sapphire substrates under similar conditions.

## 8.2 Magnetization and Susceptibility

The question is whether the magnetization is due to inclusions of a ferromagnetic impurity phase or whether is it an intrinsic property of the material. The magnetization curves usually show little coercivity or remanence. A remanence ratio at room temperature of $5-10\%$ and a coercivity of $5-10$ mT is typical of these dilute systems.

In previous studies, the observed magnetic moments were sometimes remarkably large, when related to the doping level, sometimes exceeding the spin-only moment of the dopant cations and quite often exceeding the value corresponding to any postulated impurity phase such as metallic cobalt or $Fe_3O_4$ [2]. Giant magnetic moments were reported first in lightly doped systems - Co- or Mn-doped $SnO_2$ (7.5 $\mu_B$/Co, 4.8 $\mu_B$/Co and 7.0 $\mu_B$/Mn ) [3][4] followed by Co- ZnO and V-doped $TiO_2$ (5.8 $\mu_B$/Co, 4.2 $\mu_B$/V) [5][6]. There is no proportionality between the moments and doping concentration or film thickness. The observed magnetization seemed to be the sum of two contributions – one due to transition-metal doping, and a second which was roughly constant for any film with a value of about 200 $\mu_B$ nm$^{-2}$. There is no reason to expect the profile of the dopant element to be uniform across the film. The dopant may be concentrated

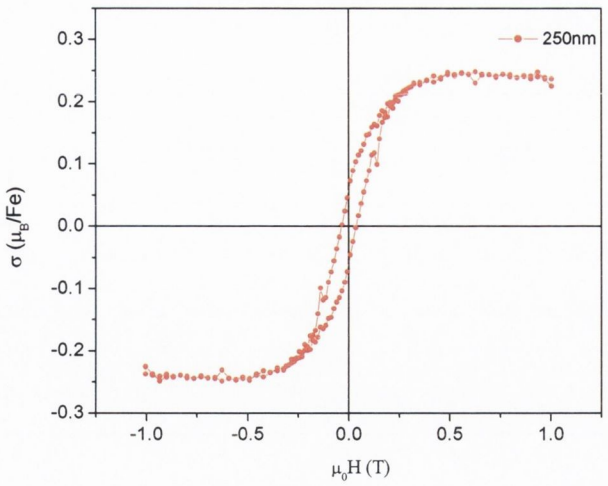



Figure 8.122. A M-H loop of a thin film of $(In_{0.825}Sn_{0.1}Fe_{0.075})_2O_3$ at 300 K, which shows hysteresis due to magnetic inclusions.

near either surface, or else it may cluster near defects.

Among the systems we have studied, only Fe:$TiO_2$ (1%, oxidized) exhibits a giant moment of 6.9 $\mu_B$/Fe. Saturation magnetic moment of 1.6 $\mu_B$/Mn, 0.8 $\mu_B$/Cr is obtained for $In_{1.75}Sn_{0.2}Mn_{0.05}O_3$ and $In_{1.7}Sn_{0.2}Cr_{0.1}O_3$ respectively. In $In_{1.8}Cr_{0.2}O_3$, the corresponding moment is 1.0 $\mu_B$/Cr. Films grown on c-$Al_2O_3$ substrates exhibit higher moments than on r-$Al_2O_3$ substrates. The Mn or Cr doped ITO and Cr-doped ITO are useful systems because we can dismiss the problem of precipitated ferromagnetic clusters.

The magnetization curves of these oxide films usually show little or no hysteresis. It is only at doping levels approaching the percolation limit that significant hysteresis appears. Development of coercivity at higher concentration would often imply the presence of ferromagnetic clusters in the host matrix. Fig. 8.122 shows the magnetization at 300 K of an Fe-doped ITO film grown using the target of 7.5 at% Fe content. The films are ferromagnetic at room-temperature with evident hysteresis. Mössbauer spectroscopy shows the presence of magnetite clusters, in a sufficient quantity to explain the room temperature moment. Coercivity increases from 10 m T at $x = 0.025$ to 36 m T at $x = 0.075$. On the other hand, the coercivity values of Mn doped ITO and Cr-doped $In_2O_3$ are only about 4 m T at room temperature.

There are technical difficulties to measure the ordering temperature in dilute

magnetic oxide systems. Except in a few systems Co:$SnO_2$ (650 K, [3]), Fe:$SnO_2$ (610 K, [7]) and Fe:$In_2O_3$ (750 K, [8]), there are no reports of a reversible $T_c$ in the literature. In some cases, Curie temperature exceeds the growth tempeature of films, which in turn affects the stability and magnetic properties of films.

Analysis of the susceptibily versus temperature measurements allows us to estimate the contribution from each paramagnetic dopant cation in the films. A full derivation of the method is given in Appendix B. The susceptibility, $\chi$, can be expressed as

$$\chi = \frac{C}{T} + \chi_0 \tag{40}$$

where $T$ is the temperature, $C$ is the Curie constant for the material and $\chi_0$ is a constant. $C$ can be expressed as

$$C = \frac{\mu_0 N m_{eff}^2}{3k_B} \tag{41}$$

where $\mu_0$ is the permitivity of free space, $N$ is the density of atoms per $\mathrm{m}^3$, $k_B$ is the Boltzmann constant and $m_{eff}^2$ is the effective moment per atom. $C$ then takes units of K, since the volume susceptibility is dimensionless. We define $p_{eff}$ by the relation

$$m_{eff} = \mu_B p_{eff} \tag{42}$$

where $\mu_B$ is the Bohr magneton. Substituting the values, we get

$$C = 2.08 \times 10^{-24} \left(\mu_0 N \cdot p_{eff}^2\right) \mathrm{m}^3\,\mathrm{K} \tag{43}$$

We have applied this analysis to Mn-doped ITO ($x = 0.025$) and oxidized Fe-doped $TiO_2$ ($x = 0.01$). The fit for $In_{1.75}Sn_{0.2}Mn_{0.05}$ gives $C = 1.23 \times 10^{-13}\,\mathrm{m}^3\,\mathrm{K} \pm 2 \times 10^{-16}\,\mathrm{m}^3\,\mathrm{K}$ (Fig. 8.123a). Given that the density of Mn atoms in the film is $7.7 \times 10^{26}\,\mathrm{m}^{-3} \pm 0.5 \times 10^{26}\,\mathrm{m}^{-3}$, we get

$$p_{eff} = 4.31 \pm 0.06$$

Given that for $Mn^{3+}$, $p_{eff} = 4.9$ and for $Mn^{4+}$, $p_{eff} = 3.87$, we can estimate 57% of the Mn atoms are $Mn^{4+}$ and 43% are $Mn^{3+}$.

For $Ti_{0.99}Fe_{0.01}O_3$, $C = 6.1 \times 10^{-14}\,\mathrm{m}^3\,\mathrm{K} \pm 1 \times 10^{-15}\,\mathrm{m}^3\,\mathrm{K}$ (Fig. 8.123b) and the density of Fe atoms in the film is $2.38 \times 10^{26}\,\mathrm{m}^{-3} \pm 0.3 \times 10^{26}\,\mathrm{m}^{-3}$. Therefore, we have

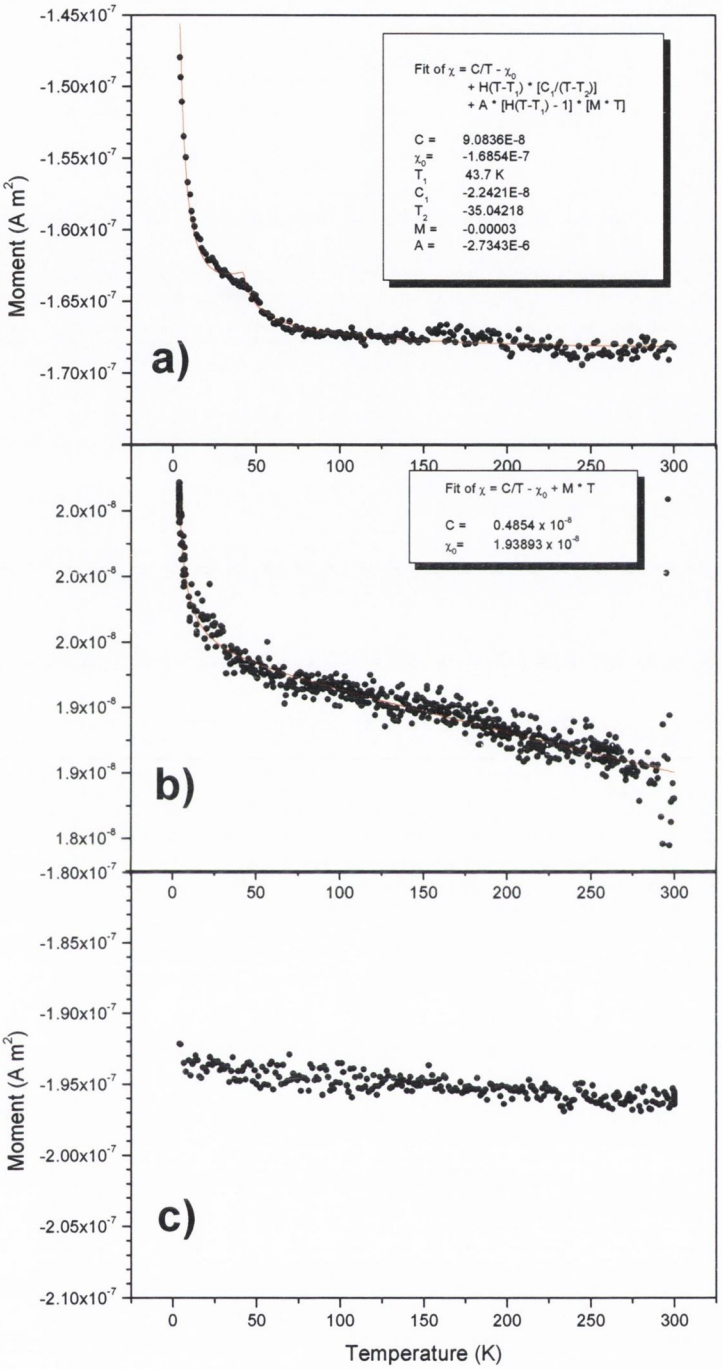



Figure 8.123. Susceptibility versus temperature measurements for a) a $(In_{0.875}Sn_{0.1}Mn_{0.025})_2O_3$ thin film b) a $Ti_{0.99}Fe_{0.01}O_2$ c) a blank substrate that has be treated in "mock" deposition conditions. Figure a) is fit with an extra term to account for trapped anti-ferromagnetic oxygen.

for $Ti_{0.99}Fe_{0.01}O_3$, that

$$p_{eff} = 5.4 \pm 0.2$$

The expected values of $p_{eff}$ for $Fe^{2+}$ and $Fe^{3+}$ are 4.9 and 5.9. The Conversion Electron Mössbauer spectrum of this film indicates that $75\% \pm 3\%$ of the Fe is in the 2+ state and $25\% \pm 3\%$ is in the 3+ state. From this, we would expect an average of $p_{eff} = 5.15 \pm 0.05$.

The remarkable result is that these ferromagnetic films exhibit a paramagnetic susceptibility which corresponds to the $3d$ dopant concentrations. The blank substrates show no significant temperature dependent susceptibility on this scale. The ferromagnetism is therefore not due to the dopants directly. The materials are not dilute magnetic semiconductors in the accepted sense. In the case of the iron-doped films, the paramagnetism is independently confirmed by Mössbauer spectroscopy.

Regarding the stability and reproducibility of the magnetic properties of the Fe:$TiO_2$, Co:ZnO films, contradictory results have been reported by different research groups. This controversy between research teams may result from the growth method used and/or from the growth conditions (oxygen pressure, deposition temperature, etc). Small changes in deposition conditions can yield films with no magnetic moment, but with identical X-ray diffraction patterns (Fig. 8.124). Another striking observation is that the conditions needed to develop ferromagnetism in may be very restricted. Films with enhanced and reproducible moments can be produced in a narrow temperature window.

## 8.3 Electrical Properties

Mn–ITO films exhibit degenerate semiconducting behavior and the zero-field electrical resistivity at room temperature ranged from 0.4 to 1.2 $m\Omega\,cm$. Normal Hall effect measurements at high fields show $n$-type conduction with a carrier density, $n$, in the range of $10^{22}\,cm^{-3}$. The calculated mobility for the 5% Mn–ITO is about 0.23 $cm^2\,V^{-1}\,s^{-1}$. The high conductivity, ferromagnetic behavior at room temperature and semiconducting nature of Mn–ITO could be promising for spin injection into semiconductors. The temperature independence of the carrier concentration (determined from the temperature dependence of the Hall effect) implies the resistivity function of temperature is dominated by the temperature behaviour of the mobility (Fig. 8.125).

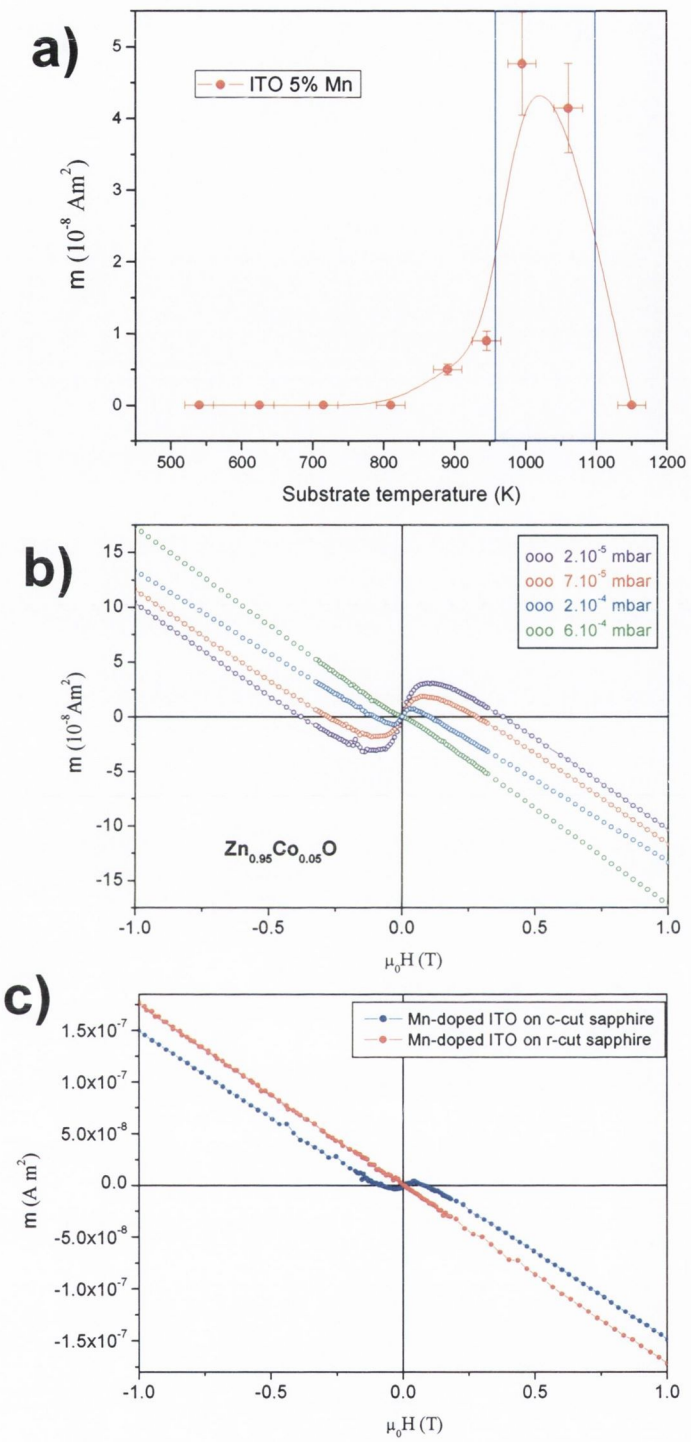



Figure 8.124. a) A plot of moment versus substrate temperature for $(In_{0.875}Sn_{0.1}Mn_{0.025})_2O_3$ thin films. b) M-H loops of $Zn_{0.95}Co_{0.05}O$ for different deposition pressures c) M-H loops of $(In_{0.875}Sn_{0.1}Mn_{0.025})_2O_3$ deposited on different cuts of sapphire during in the same deposition.

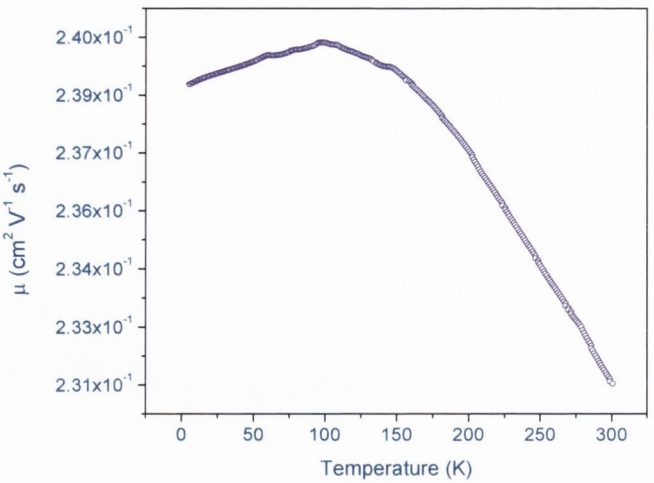



Figure 8.125. The mobility as a function of temperature of a $(In_{0.875}Sn_{0.1}Mn_{0.025})_2O_3$ thin film.

The resistivity versus temperature data also indicate a clear difference between the manganese- and iron-doped ITO films. The undoped and manganese doped films exhibit a metallic behaviour to their resistivity when T > 100 K. When T < 100 K, the thermal coefficient of mobility (TCM) changes sign, as has previously been observed for ITO thin films [9]. This behaviour can be explained by ionized impurity scattering (IIS) dominating the resistivity at lower temperatures, while at higher temperatures, phonon effects dominate [10]. The temperature of the mobility maximum increases with manganese doping, due to the introduction of more impurity scattering centres, allowing IIS to dominate at higher temperature. The iron-doped films show no such maxima below 300 K, indicating that the presence of magnetite clusters may allow IIS to dominate at even higher temperature.

The remarkable finding is that the resistivity of Co-doped ZnO film doped with more than 0.2% Al drastically decreases in the whole temperature region $2 - 300$ K, while preserving its macroscopic magnetisation. Magnetoresistance is observed only up to 30 K. Hall measurements reveal degenerate semiconducting behaviour for Al concentrations > 0.2 %.

## 8.4 Optical Properties

Optical absorption structures are observed in Co:ZnO and interpreted as due to the transitions between the crystal-field-split $3d$ levels of tetrahedral $Co^{2+}$ ions

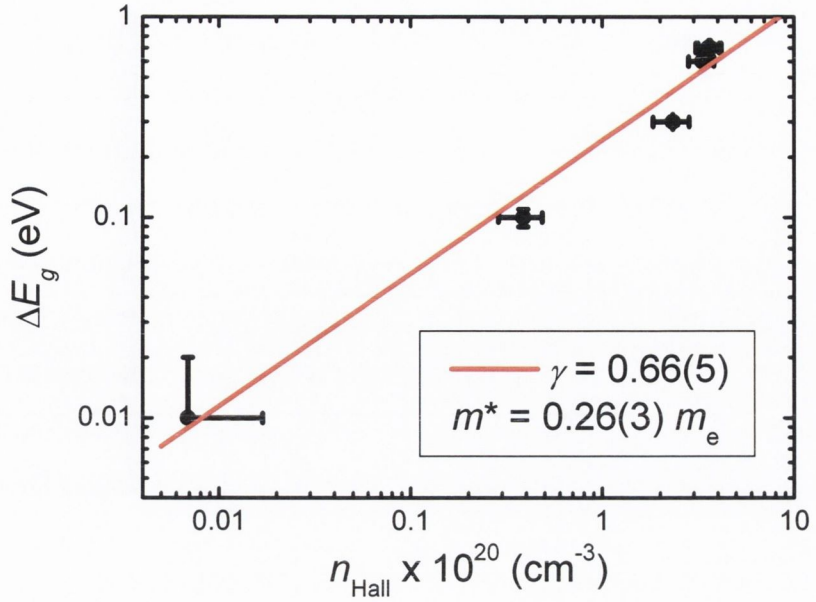



Figure 8.126. The band gap shift of Al-doped $Zn_{0.95}Co_{0.05}O$ thin films as a function of carrier concentration, determined from Hall effect measurements.

substituting for $Zn^{2+}$ ions. In the case of Al-doped Co:ZnO films, Striking feature of Al codoped ZnO:Co films is the band-gap widening. Band gap is shifted from 3.24 eV (ZnO:Co) to 3.68 eV (ZnO:Co:1 at.% Al). The shift occurs as a result of the blocking of the lowest states in the conduction band and is explained by Burstein-Moss effect [11] involving transfer of associated electrons to the conduction band. The filling of the density of states in the conduction band at high Al doping levels is illustrated by the shift of the direct-gap optical absorption edge as a function of carrier concentration as illustrated on Fig. 8.126[6]. The expected functional dependence

$$\Delta E_g = \frac{\hbar}{2m^*} \left(3\pi^2 n_e\right)^{\frac{2}{3}}$$

is well verified well within experimental error and yields the mean harmonic mass defined as

$$\frac{1}{m^*} = \frac{1}{m_h} + \frac{1}{m_e}$$

where $m^* = 0.26(3)m_e$, which is in good agreement with the accepted values of $m_e = 0.23$ and $m_h = 0.59$ for Al-doped ZnO.

[6] The Hall effect measurements were carried out by P. Stamenov.

## 8.5 Extrinsic Mechanisms of Ferromagnetism

The interest in dilute magnetic semiconductors and dilute magnetic transparent conducting oxides is due to their possible applications in spin electronics. The usefulness of these materials is conditional on the mechanism that induces ferromagnetism in them. Extrinsic causes of ferromagnetism, such as segregation of dopants into ferromagnetic impurity phases and, especially, contamination of the materials by sample handling would discount the material for possible spintronic use. Therefore, for a material to be considered useful, the possibility of an extrinsic mechanism of ferromagnetism must be ruled out. In this section, we shall consider ferromagnetic impurities which may arise from the materials used in this work. Then we shall then discuss the precautions taken against contamination of the samples and the equipment used for measurement.

### 8.5.1 Ferromagnetic Impurities

While there has been quite a variation in the measured room temperature magnetization of dilute magnetic oxide films in the literature, the absolute moments are quite small. Assuming a sample deposited on a $25\,\mathrm{mm}^2$ substrate with a thickness of a few hundred nanometres, the typical moment measured is in the range of $m = 10^{-8} - 10^{-7}\,\mathrm{A\,m}^2$.

It is instructive to examine the different amounts of impurity phases required to explain these moments. A knowledge of the quantity of possible impurity phase is essential for choosing experimental techniques to discount them from contributing to observed ferromagnetism. Table 14 lists some commonly expected impurity phases in dilute magnetic semiconductors. The last column gives the volume fraction of the sample that would be occupied by that phase were it to cause a moment of $10^{-7}\,\mathrm{A\,m}^2$ at room temperature. This figure allows us to rule out a number of impurity phases. Anything over 100% clearly cannot cause the observed moments. Thus, weakly ferromagnetic phases such as hematite cannot be responsible.

#### 8.5.1.1 Materials purity

The purity of the starter materials is typically 99.999% or better for all the host materials and over 99.97% for the dopants. Typically, 1 g of host material and 0.01 g

of the dopant oxides are used to produce the ceramic targets. That implies that at most, 10 $\mu$g of impurity may exist in total in the host material and 3 $\mu$g may exist in the dopant material. Therefore, a maximum 13 $\mu$g of impurity may exist in the whole of the 1 g ceramic target. For an impurity from the target to cause $\sim$1 g of magnetic phase in a thin film we must assume that:

1. 10% or more of the target impurity must be concentrated in the material ablated by the laser. Typically, laser ablation removes $> 5\%$ of target.

2. The impurity must travel selectively to the substrate and not disperse in the plume. The surface area of the plume when it reaches the substrate must be $2\pi r^2$, assuming a hemispherical expansion of the plume, with $r = 35\,\text{mm}$. Thus $A = 1225\,\text{mm}^2$, and the fraction of the substrate area to the plume area is 0.02.

If we estimate the impurity level due to the purity of the material, assuming uniformity dispersion of the impurity in the target and plume, we get

$$\begin{aligned} m_{imp} &= 13\,\mu\text{g} \times 0.05 \times 0.02 \\ &= 0.013\,\mu\text{g} \end{aligned}$$

assuming minimum purity of the starter materials.

#### 8.5.1.2 XRD

The limits of detection of XRD for oriented impurity phases is roughly 1-5%. This figure is dependent on a few factors:

1. The intensity/length of scan/detector quality. The signal to noise ratio of x-ray diffraction measurements is largely determined by the average number of counts in a scan. A strong source - such a synchotron, a long scanning time or an advanced detector (such as the X'Celerator used in this work) increases the sensitivity and thus the lower limit of detectable phases.

2. Impurity orientation. An oriented impurity will typically exhibit one XRD peak which has a relatively large intensity. A polycrystalline impurity exhibits many low intenstiy peaks, which may not show above the noise level. Therefore, the more oriented an impurity phase, the easier it is to detect.

3. X-ray fluoresence. Certain x-ray energies cause a range of atoms to fluoresce. Cu $K_\alpha$, for instance, causes Fe to fluoresce. This increases the background noise and reduces the definition of Bragg reflections. Therefore it is prudent to choose x-ray

| **Phase** entry | $\rho$ ($kg\,m^{-3}$) | $T_C$ (K) | $\sigma$ ($A\,m^2\,kg^{-1}$) | Mass ($\mu g$) | Volume Percentage (%) |
|---|---|---|---|---|---|
| Fe | 7874 | 1040 | 220 | 0.45 | 0.9 |
| Co | 8900 | 1382 | 170 | 0.59 | 1.1 |
| Ni | 8908 | 627 | 55 | 1.82 | 3.3 |
| CdTe | 5850 | 340 | 20 | 5 | 13.7 |
| MnAs | 6170 | 318 | 5 | 20 | 51.9 |
| MnSb | 6885 | 587 | 118 | 0.85 | 2.0 |
| $Mn_3Sn$ | 7465 | 325 | 0.2 | 507.29 | >100% |
| $Mn_3Ga$ | 7804 | 743 | 48 | 2 | 4.1 |
| $Mn_2Ga$ | 7910 | 680 | 47 | 2 | 4.0 |
| MnGa | 7700 | 300 | 50 | 2 | 4.2 |
| $Mn_4N$ | 6823 | 745 | 5 | 20 | 46.9 |
| MnP | 5799 | 291 | 51 | 1.96 | 5.4 |
| FeCu | 7874 | 505 | 80 | 1.25 | 2.5 |
| $Fe_4N$ | 7212 | 760 | 150 | 0.67 | 1.5 |
| FeP | 7184 | 215 | 30 | 3.33 | 8.8 |
| $Fe_2P$ | 6070 | 278 | 43 | 3.5 | 10.5 |
| $Fe_3P$ | 5079 | 716 | 32 | 3.4 | 7.5 |
| FeB | 7142 | 589 | 180 | 0.56 | 1.2 |
| $Fe_2B$ | 7150 | 1015 | 190 | 0.53 | 1.2 |
| $CrO_2$ | 4900 | 390 | 110 | 0.91 | 3.0 |
| $\alpha$-$Fe_2O_3$ | 5270 | 960 | 0.4 | 250.0 | >100% |
| $\gamma$-$Fe_2O_3$ | 4856 | 743 | 82 | 1.22 | 4.0 |
| $Fe_3O_4$ | 5180 | 860 | 80.2 | 1.25 | 3.9 |

Table 14.A table listing common impurities phases in dilute magnetic semiconductors, quoting the phase, its denstiy, Curie temperature, saturation magnetization, the mass of phase need to explain commonly measured moments in dilute magnetic semconductors and the volume fraction of sample that phase would take.

energies that will not fluoresce on the sample being measured.

As the x-ray diffractometer used in this study was used Cu $K_\alpha$ x-rays, the impurity phases that are the most difficult to detect are Fe and its compounds and Co (which also fluoresce when irradiated with Cu $K_\alpha$ x-rays), though all the others mentioned in Table 14 should be detectable by XRD.

#### 8.5.1.3 Mössbauer Spectrometry

The use of $^{57}Fe$ Mössbauer Conversion Electron Spectrometry enables the determination of the nature of all the iron in the thin films. Clusters of metallic Fe or its oxide are detectable. It is also possible to determine the oxidation state and the specific oxide present. All our Fe-doped samples were created using $^{57}Fe$, which allows for good signal-to-noise ratio in Mössbauer spectra. Metallic Fe was identifed in highly reduced $TiO_2$ thin films and hematite was observed in the oxidized $TiO_2$. $Fe_3O_4$ was found to be present in Fe-doped ITO and $SnO_2$.

| Material | Dopant | Possible Impurities | Level detected (%) | Impurity moment (%) | Intrinsic or Extrinsic |
|---|---|---|---|---|---|
| ITO | Mn | $Mn_4N$ | 0 | 0 | Intrinsic |
| | Fe | Fe | 0 | 0 | |
| | | $Fe_3O_4$ | $33 \pm 5$ | 100 | Extrinsic |
| | | $\alpha, \gamma - Fe_2O_3$ | 0 | 0 | |
| | Cr | $CrO_2$ | 0 | 0 | Intrinsic |
| $TiO_2$ (oxidized) | Fe | Fe | 0 | 0 | |
| | | $Fe_3O_4$ | 0 | 0 | Intrinsic |
| | | $\alpha, \gamma - Fe_2O_3$ | $60 \pm 5$ | <0.15 | |
| $TiO_{2-\delta}$ (reduced) | Fe | Fe | $90 \pm 3$ | $80 \pm 2$ | |
| | | $Fe_3O_4$ | 0 | 0 | Extrinsic |
| | | $\alpha, \gamma - Fe_2O_3$ | 0 | 0 | |
| $In_2O$ | Cr | $CrO_2$ | 0 | 0 | Intrinsic |
| Sn | Fe | Fe | 0 | 0 | |
| | | $Fe_3O_4$ | $80 \pm 10$ | >100% | Extrinsic |
| | | $\alpha, \gamma - Fe_2O_3$ | 0 | 0 | |
| ZnO:Al | Co | Co | < 5% | <80% | Intrinsic |
| Whiskers | - | TM | < 0.1% | <10% | Intrinsic |
| Graphite | - | Fe | > 1% | 100% | Extrinsic |

Table 15.A table of materials that were found to exhibit ferromagnetic behaviour. Included is the possible ferromagnetic impurities present, the levels detect (as a percentage of the total dopant in the sample, and the contribution of the impurity to the moment

#### 8.5.1.4 Other considerations

The feasibilty of the presence of certain impurities must also be examined. $CrO_2$, for instance, only forms under very particular conditions and is easily reduced to $Cr_2O_3$ [12], the stable phase in ambient conditions. Therefore, $CrO_2$ is unlikely to form. For the Cr-doped thin films presented in this thesis, the impurity phase identified was $Cr_2O_3$ because the conditions of deposition are insufficiently oxidizing to produce $CrO_2$.

A list of the materials found to be ferromagnetic in this work is given in Table 15, along with the possible room temperature ferromagnetic impurities and the amounts of those impurities detected.

It is evident that impurities of iron and its oxides are responsible for moments in ITO:Fe, $SnO_2$:Fe and reduced $TiO_{2-\delta}$, though only in part for the moment in $TiO_{2-\delta}$.

### 8.5.2 Contamination

From Table 14, we can see that tiny amounts of metallic contaminants may be responsible for the measured moments. It is therefore important to ensure that the samples do not become contaminated by even a small amount of stray ferromagnetic particles.

#### 8.5.2.1 Sample Handling

The samples were handled at all times by zirconia toughened aluminum oxide ceramic tweezers from Electron Microscopy Sciences, Ltd. The substrate was attached to the heater by silver paint which is paramagnetic and could easily be removed by a solvent. The heater was thoroughly cleaned in between deposition by washing with acetone, scraping with pure tantalum metal and washing again with acetone. The thin films were cleaned thoroughly by methanol before measurement in the SQUID, which was the first measurement to be performed on each sample.

#### 8.5.2.2 Background Checks

To ensure any signal observed was not due to the substrate or the host material, a careful series of background measurement was performed (Fig. 8.127). Blank substrates were exposed to "mock" deposition conditions in which a deposition was simulated, without the laser beam entering the deposition chamber. No ferromagnetic signal ($> 10^{-9}\,\mathrm{A\,m^2}$) was observed from these samples. This is important to lend credence to the measured ferromagnetic moments. Each host transparent conducting oxide was produced undoped in the conditions that produced ferromagnetic thin films ablated from doped ceramic targets. No ferromagnetism was observed in any of these undoped samples.

## 8.6 Models for Ferromagnetism in Dilute Magnetic Semiconductors

Whenever it is possible to exclude the possibility of extrinsic factors governing the ferromagnetism of thin films of DMTCOs, a model for an intrinsic mechanism should be found. We consider first the standard explanations.

### 8.6.1 Superexchange

Superexchange [13] is a process in which the spins of two ions are correlated due to the spin-dependent kinetic exchange interaction between each of the two ions and the valence $p$ electrons of a mediating oxygen. The sign of the superexchange (i.e. if it results in ferro- or antiferro-magnetic coupling of the pair) follows the *Goodenough-Kanamori* rules. These state that if two cations have lobes of occupied $3d$ orbitals which

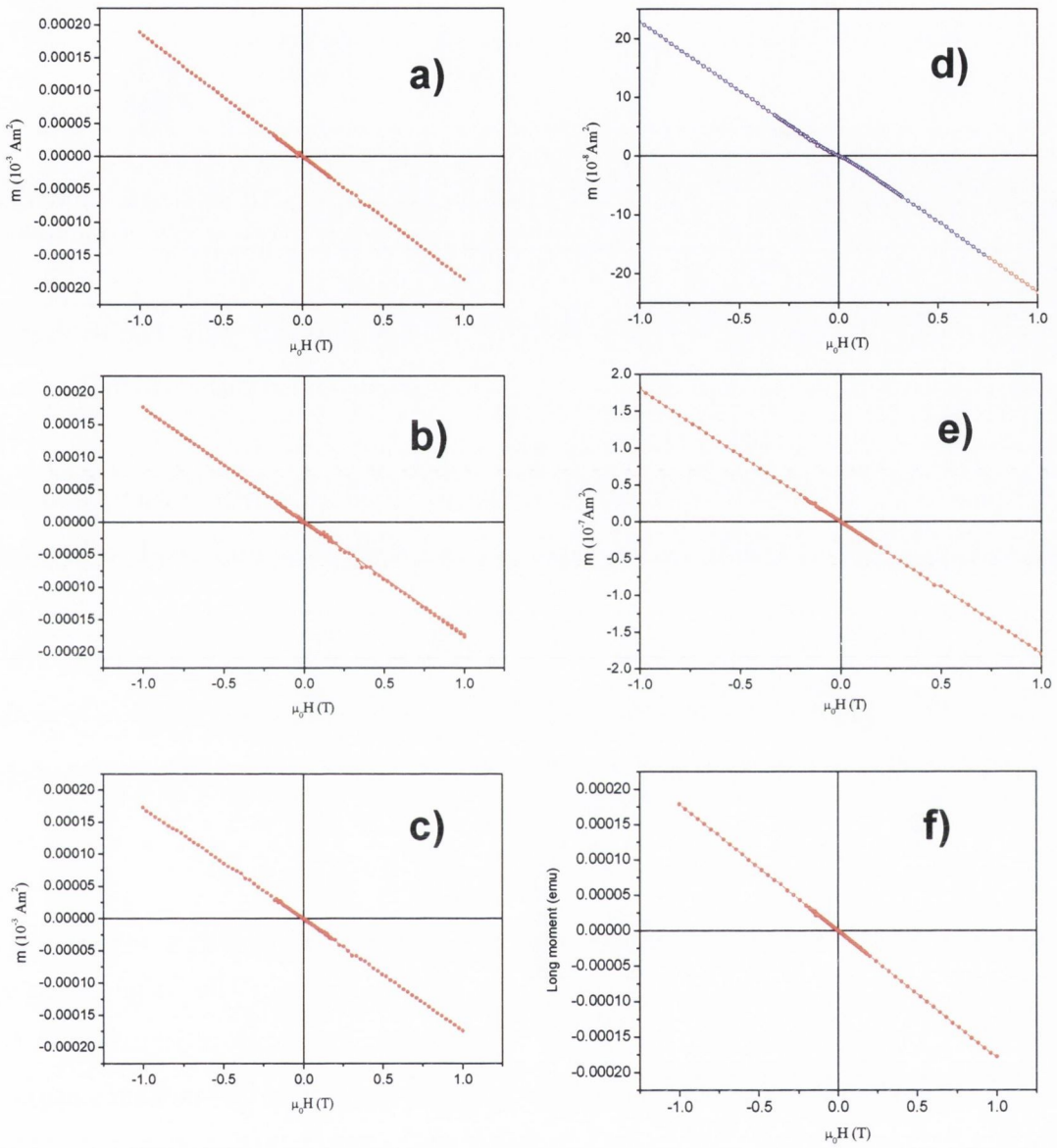



Figure 8.127. A representative set of background room temperature SQUID measurements. a) A blank $Al_2O_3$ substrate exposed to "mock" deposition b) 140 nm thick ITO thin film c) 140 nm thick $In_2O_3$ thin film d) 160 nm thick ZnO thin films e) 200 nm thick $TiO_2$ thin film f) 140 nm thick $Cr_{1.9}In_{0.1}O_2$ thin film

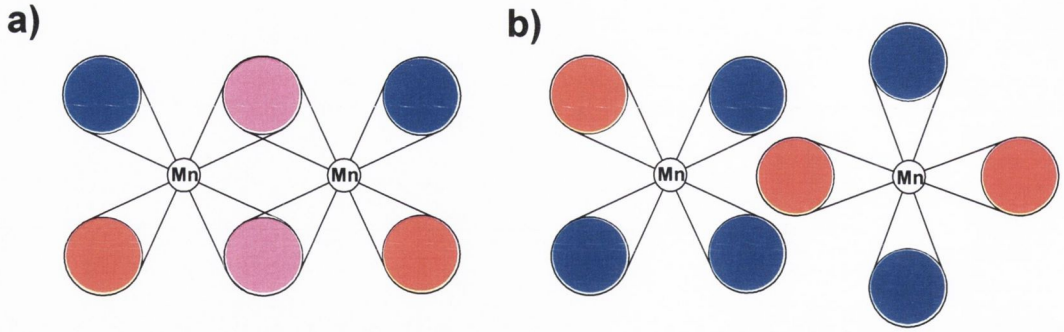



Figure 8.128. The superexchange. a) With a non-zero overlap giving AF exchange. b) With zero overlap giving FM exchange. Red denotes positive and blue denote negative sign of wavefunction. Pink denotes non-zero overlap

point towards each other giving large overlap and hopping integrals, the exchange is antiferromagnetic and strong. If the two cations have an overlap which is zero by symmetry, the exchange is ferromagnetic and weak (Fig. 8.128).

Superexchange, therefore, is short ranged and predominantly antiferromagnetic. Its short range demands that the dopant ion concentration would need to be greater than the percolation threshold, $x_p$, which for nearest-neighbour cation coupling is approximately $\frac{2}{Z}$ where $Z$ is the cation co-ordination number ($0.25 < x_p < 0.16$). This is not the case in the samples presented. Also, ferromagnetic superexchange is a weak interaction, which is completely insufficient to account for the large Curie temperatures observed.

### 8.6.2 Zener Double Exchange

Zener proposed double exchange [14] in 1951 to explain the large moment in mixed valence manganites. In this model, an electron hops from a $3d$ cation A to an anion whilst an electron simultaneously hops from that anion to another cation $A^+$. The lowest energy of this system is such that the spins on the cations are aligned. This model requires mixed valence and a high concentration for exchange, neither of which are necessary conditions for ferromagnetism in dilute magnetic transparent conducting oxides. The percolation threshold must again be attained before long-range ferromagnetic ferromagnetism can set in.

### 8.6.3 The RKKY Interaction

The RKKY interaction is a long-range interaction that occurs in systems where

there is overlap between electrons in a conduction band and the spin of magnetic ions. The spin polarized electron then couples to a neighbouring ionic spin. The sign of the interaction oscillates with distance, coupling the ionic spins ferromagnetically or antiferromagnetically depending on their separation. The RKKY interaction only becomes efficient when the carrier concentration is high [15]. Quantitative estimations indicate, however, that in II–VI dilute magnetc oxides even for the highest available electron densities no transition to the ferromagnetic phase can be expected above 1 K [?]. The transition to a ferromagnetic phase is possible for $p$-type doping of higher than $p \approx 2 \times 10^{19}\,\mathrm{cm}^{-3}$. Oxides are generally $n$-type, and Hall measurements confirm that the films in this study are $n$-type, removing the RKKY interaction as a possible mechanism for ferromagnetism in the magnetic films present in this thesis.

### 8.6.4 Impurity Band Exchange and Magnetic Polarons

The impurity band exchange model [17] is based on the idea that donor electrons becomes trapped by a lattice defect, such as an oxygen vacancy. The electron is confined in a hydrogenic orbital of radius

$$r_H = \varepsilon(\frac{m}{m^*})a_0$$

, where $\varepsilon$ is the high-frequency dielectric constant, $m$ is the electron mass, $m^*$ is the effective mass of the donor electrons and $a_0$ is the Bohr radius (53 pm). If $r_H$ is large enough, the electron will interact with more than one $3d$ cation and couple them ferromagnetically. For a high enough defect concentration, $\delta_{crit}$, the trapped electron orbitals will overlap and couple to each other, ordering the material ferromagnetically (Fig. 8.129).

Transparent conducting oxides, like oxide semiconductors, owe their high conductivity to oxygen defects - which are present in large numbers due to sub-stoichiometry. The oxides also tend to have relatively high dielectric constants ($\sim$ 10), which are needed for the trapped electrons to couple dilute magnetic ions in a low concentration. A detailed analysis of the model shows that the magnetic ordering temperature should not exceed 20 K for 5% dopant [17].

The Mössbauer results show, however, that in oxidized Fe-doped $TiO_2$, there is no evidence of magnetic ordering between ions which have substituted into the lattice or placed themselves interstitially. The magnetic ordering in this material must be

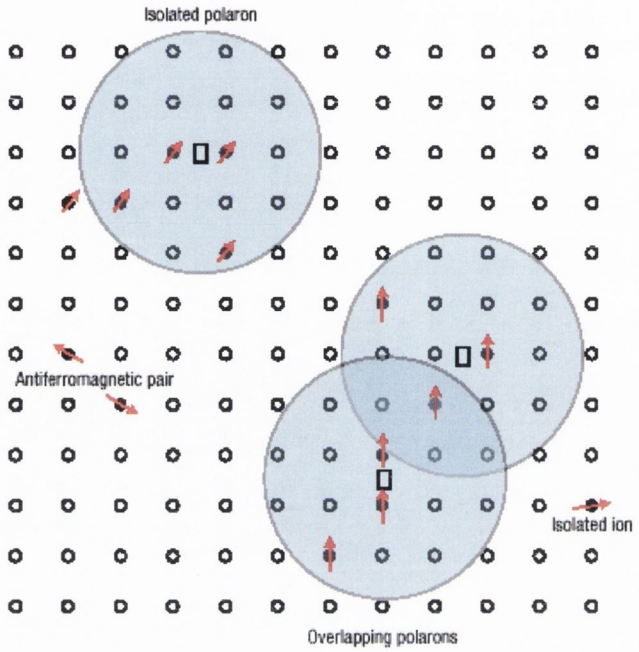



Figure 8.129. Representation of magnetic polarons. A donor electron in its hydrogenic orbit couples with its spin antiparallel to impurities with a 3d shell that is half-full or more than half-full. The fi gure is drawn for $x = 0.1$, $\gamma = 12$. Cation sites are represented by small circles. Oxygen is not shown; the unnoccupied oxygen sites are represented by squares. From [?].

mediated by something other than the dilute $3d$ ion. The stated explanations are unable to explain the high temperature ferromagnetism observed in the films.

### 8.6.5 Other Mechanisms

The low Curie temperatures predicted by the above models discount them as a possible explanation for the ferromagnetism observed in the films. Clearly, more exotic mechanisms must be considered which can satisfy the demand for a Curie temperature well above room temperature.

Das and Sanvito [18] have performed DFT calculations investigating the possibility of intrinsic defect driven ferromagnetism in $HfO_2$. While they found that oxygen vacancies form nonmagnetic impurity levels, Hf vacancies show a high-spin state with an associated magnetic moment of 3 $\mu_B$. These are ferromagnetically coupled via minority-spin electron delocalization across bridging Hf sites, with a large coupling strength suggesting high Curie temperatures.

Hernando et al [19] have accounted for the giant moments observed in thiol-capped gold thin films by proposing that the broken symmetries at thin film surfaces lead to

orbital states that can have quite a large radius, and subsequently, a large orbital momentum. These orbital momenta can align due to intraorbital ferromagnetic spin correlations, leading to the giant orbital moments that have been observed.

# References

[1] A. M. Nazmul and S. Sugahara, Phys. Rev. B 67, 241308 (2003)

[2] Y.J. Kim, S. Thevuthasan, T. Droubay, A.S. Lea, C.M. Wang, V. Shutthanandan, S.A. Chambers, R.P. Sears, B. Taylor and B. Sinkovic, Appl. Phys. Lett., 84 3531 (2004)

[3] S. B. Ogale, R. J. Choudhary, J. P. Buban, S. E. Lofland, S. R. Shinde, S. N. Kale, V. N. Kulkarni, J. Higgins, C. Lanci, J. R. Simpson, N. D. Browning, S. Das Sarma, H. D. Drew, R. L. Greene and T Venkatesan, Phys. Rev. Lett. 91, 077205 (2003)

[4] C. B. Fitzgerald, M. Venkatesan, L. S. Dorneles, R. Gunning, P. Stamenov, J. M. D. Coey, P. A. Stampe, R. J. Kennedy, E. C. Moreira, U. S. Sias, Phys. Rev. B 74, 115307 (2006)

[5] M. Venkatesan, C.B. Fitzgerald, J.G. Lunney and J.M.D. Coey, Phys. Rev. Lett. 87, 026601 (2004)

[6] N. Y. H. Hong, J. Sakai and A. Hassini, Appl. Phys. Lett. 84, 2602 (2004)

[7] J.M.D. Coey, A. P. Douvalis, C. B. Fitzgerald, M. Venkatesan, Applied Physics Letters 84, 1332 (2004)

[8] J. He, S. Xu, Y. K. Yoo, Q. Xue, H.-C. Lee, S. Cheng, X.-D. Xiang, G. F. Dionne, and I. Takeuchi, Appl. Phys. Lett. 86, 052503 (2005)

[9] J. Ederth, P. Johnsson, G. A. Niklasson, A. Hoel, A. Hultåker, C. G. Granqvist, A. R. van Doorn, M. J. Jongerius, and D. Burgard, Phys. Rev. B 68, 155410 (2003)

[10] D. Chattopadhyay and H. J. Queisser, Rev. Mod. Phys. 53, 745 (1981)

[11] E. Burstein, Phys. Rev. 93 632 (1954); T.S. Moss, Proc. Phys. Soc. London, Ser.

B 67, 775 (1954)

[12] M. Rabe, J. Dreßen, D. Dahmen, J. Pommer, H. Stahl, U. Rüdiger, G. Güntherodt, S. Senz and D. Hesse, J. Magn. Magn. Mat. 211, 314 (2000)

[13] J. B. Goodenough, *Magnetism and the Chemical Bond,* Interscience, New York (1963)

[14] C. Zener, Phys. Rev. 82, 403–405 (1951)

[15] P. Kacman, Semicond. Sci. Technol. 16, R25 (2001)

[16] T. Dietl, J. Cibert, D. Ferrand and Y. M. d'Aubigné, Mater. Sci. Eng. B 63, 103 (1999)

[17] J. M. D. Coey, M. Venkatesan, C. B. Fitzgerald, Nature Materials 4, 173 (2005)

[18] C. Das Pemmaraju and S. Sanvito, Phys. Rev. Lett. 94, 217205 (2005)

[19] A. Hernando, P. Crespo, and M. A. García, Phys. Rev. Lett. 96, 057206 (2006)

# Chapter 9

# Conclusions

"But now I have come to believe that the whole world is an enigma, a harmless enigma that is made terrible by our own mad attempt to interpret it as though it had an underlying truth."

Umberto Eco

## 9.1 Conclusions

The materials investigated can been segregated into two sets. The first set of materials contains Fe-doped ITO, $SnO_2$ reduced $TiO_2$ and non-ultrapure carbon. For these materials, Mössbauer analysis has shown that the moment observed in some Fe-doped transparent conducting oxides is due, in part or wholly, to ferromagnetic impurity phases. Magnetite ($Fe_3O_4$) is responsible for the moment observed in Fe-doped ITO and $SnO_2$, while clusters of iron metal contribute to the observed moment in reduced Fe-doped $TiO_2$ and are a significant impurity in non-ultrapure carbon. Two conclusions can be drawn from this set. Firstly, the Fe-doping of semiconducting oxides to produce ferromagnetic semiconductors is likely to produce extrinsic ferromagnetism due to phase segregation. If this route is to be used to produce ferromagnetic semiconducting oxides, due care must to taken to ensure that the iron does not segregate into a ferro- or ferri-magnetic secondary phase, and any Fe-doped oxide purporting to exhibit unaccountable ferromagnetism must be carefully examined for secondary phases. Secondly, for all research into areas involving unexplained small magnetizations, the purity of the starting materials must be established before any claims as to the origin of these magnetization are made.

The second set, comprised of the Mn- and Cr-doped ITO and oxidized Fe:$TiO_2$, is more interesting. Here the dopant ions behave paramagnetically down to 4 K, despite the unusual ferromagnetism of the film up to room temperature and above, which is similar to that in other systems including $d^0$ ferromagnetism. The main conclusion is that these materials are not dilute magnetic semiconductors. It is misleading to regard them in these terms. The magnetism is not caused by the $3d$ dopants. Some

sort of defect mechanism must be involved, but the nature of these defects requires clarification.

There has been a plethora of reports of ferromagnetism in doped semiconducting oxides [1] which cannot be explained with conventional models of ferromagnetism. In these reports, however, it has generally been assumed that the dopant cation is directly involved in the ferromagnetic interaction and orders itself. The paramagnetic nature of the dopant cations in the results presented in this thesis suggests that this is not the case. A novel theoretical explanation is urgently needed to explain the data. Present explanations fail because of their dependence on the unfilled $3d$ electron shells to mediate the interaction to exist far above room temperature. There is now direct evidence that this is not the case in some materials, yet the moment persists above room temperature.

## 9.2 Future Work

Three strong candidates for intrinsic ferromagnetic transparent conducting oxides have emerged based on these results, namely Mn:ITO, Cr:ITO/$In_2O_3$ and oxidized Fe:$TiO_2$. An explanation of the magnetic properties of these materials is required, but more experimental work is required to examine the exact nature of the ferromagnetism.

For the Mn:ITO thin films, $^{119}$Sn Mössbauer spectroscopy (an analogue to $^{57}$Fe Mössbauer spectroscopy) would allow probing of the Sn atoms in a similar fashion to how the Fe atoms were probed in this work. This would allow for a greater understanding of the role and placement of Sn in the lattice.

For all the films, magnetic x-ray circular dichroism (XMCD) may prove useful. XMCD measures the difference in the absorption of left- and right-circular polarized photons. The absorption can be measured for specific elements in the lattice as the absorption is measured at the absorption edges of the relevant elements. The difference in the absorption of the two polarizations can reveal magnetic information about the sample that is element specific. Since it has been show that the 3d cations are not magnetically ordered, this technique would be useful in finding the mechanism before the long-range ordering.

Since it is strongly suspected that oxygen vacancies play a large role in mediating the ferromagnetic exchange in these materials, a direct measurement of the

off-stoichiometry of the oxide thin films would allow the examination of a relationship between this value and the magnetization of the oxides. The development of atomic resolution measurement of oxygen vacancies may enable this in the future [2], but no such measurement exists yet.

# References

[1] S J Pearton, W H Heo, M Ivill, D P Norton and T Steiner, Semicond. Sci. Technol. 19, R59-R74 (2004)

[2] C. L. Jia and K. Urban, Science 303, 5666 (2004)

# Publications

[1] M. Venkatesan, F.M.F. Rhen, R. Gunning , and J.M.D Coey, "Effect of Fe, Cu, Zr, and Ti on the magnetic properties of SmCo-1:7 magnets", IEEE Transactions on Magnetics 38, 2919-2921 (2002)

[2] E. Clifford, M. Venkatesan, R. Gunning, J. M. D. Coey, "Magnetoresitance in point contacts of the Heusler alloy $Co_2Cr_{0.6}Fe_{0.4}Al$", Solid State Communications 131, 61-64 (2004)

[3] S. A. Corr, Y. K. Gun'ko, S. J. Byrne, A. P. Douvalis, M. Venkatesan, R. D. Gunning, "Magnetite nanocrystals from a single source metallorganic precursor: metallorganic chemistry vs. biogeneric bacteria", Journal of Materials Chemistry 14, 944-946 (2004)

[4] S. A. Corr, Y. K. Gun'ko, S. J. Byrne, A. P. Douvalis, M. Venkatesan, R. D. Gunning, "New two in one magnetic fluorescent nanocomposites", Opto-Ireland 2005: Nanotechnology and Nanophotonics 5824, 71-78 (2005)

[5] R.D.Gunning, M. Venkatesan, D. H. Grayson, J. M. D. Coey., "Magnetic properties of CNx whiskers", Carbon 44, 3213 (2006)

[6] C. B. Fitzgerald, M. Venkatesan, L. S. Dorneles, R. Gunning, P. Stamenov, J. M. D. Coey, P. A. Stampe, R. J. Kennedy, E. C. Moreira, U. S. Sias, Phys. Rev. B 74, 115307 (2006)

[7] R.D. Gunning, M. Venkatesan, K. Paul and J.M.D. Coey, "Magnetism of TiO2 thin films doped with iron", submitted, Applied Physics Letters (2006)

# Appendix A
# Units

## A.1 The SI and cgs conventions

While the SI unit system has many advantages over the cgs system, the cgs system still enjoys much popularity. A table of unit conversions are given in Table 16.

| **Unit** | **Multiplied by** | **Gives value in** |
|---|---|---|
| emu | $10^{-3}$ | $\mathrm{A\,m^2}$ |
| emu $\mathrm{g^{-1}}$ | 1 | $\mathrm{A\,m^2\,kg^{-1}}$ |
| Oe | 79.577 | $\mathrm{A\,m^{-1}}$ |
| G | $10^{-4}$ | T |
| $\mathrm{A\,m^2}$ | $10^3$ | emu |
| $\mathrm{A\,m^2\,kg^{-1}}$ | 1 | emu $\mathrm{g^{-1}}$ |
| $\mathrm{A\,m^{-1}}$ | $1.2566 \times 10^{-2}$ | Oe |
| T | $10^4$ | G |

Table 16.A table of cgs to SI and SI to cgs unit conversions

# Appendix B
# Calculations and Derivations

## B.1 Curie Susceptibility vs. Temperature to Obtain $p_{eff}^2$

For this measurement, we use the Curie Law

$$\chi = \frac{C}{T} + \chi_0$$

together with the expression for $C$

$$C = \frac{\mu_0 \cdot N \cdot p_{eff}^2}{3k_B} \tag{44}$$

where $\mu_0$ is the permittivity of free space, $k_B$ is the Boltzmann constant and $N$ is the number of dipoles.

Typically, the Curie susceptibility will be measured in the SQUID as a function of temperature, $T$, obtaining a set of values with moment, $m$, in *emu* as a function of temperature, for a constant magnetic field strength in *Oersted* (Oe), as the SQUID uses cgs units. The moment, $m$, in *emu* is converted to $\mathrm{A\,m^2}$ by multiplying by a factor of $10^{-3}$. The field strength, $H$, is converted to $\mathrm{A\,m^{-1}}$ by multiplication by 79.577. Fitting the equation

$$\frac{m}{H} = \frac{C_{Fit}}{T} + \chi_0 \tag{45}$$

will give a value for $C_{Fit}$ in units of $\mathrm{m^3\,K}$. Using Eqn. (44) and substituting the known constants, $C_{Calc}$ is given by

$$C_{Calc} = 2.6 \times 10^{-30} \cdot N \cdot p_{eff}^2 \tag{46}$$

where $N = m \times N_m = V \times N_V$, $m$ being the mass and $N_m$ the number of atoms per kg, and $V$ being the volume and $N_V$ the number of atoms per $\mathrm{m^3}$. This will give $C_{Calc}$ in units of $\mathrm{m^3\,K}$. Equatings Eqn. (45) and (46), we get

$$p_{eff} = \sqrt{\frac{C_{Fit}}{2.6 \times 10^{-30} \cdot N}}$$

The theoretical value of $p_{eff}$ can be calculated from the relation

$$p_{eff} = g\sqrt{s\,(s+1)}$$

where $g$ is the gyromagnetic ratio.

## B.2 Substrate Temperature

The substrates in the PLD chamber are attached with silver paste to a SiN strip. The strips resistance causes its temperature to increase when a current is passed through it. A calibration has been performed to correlate the voltage applied to the temperature of the substrate (Fig. 9.130).

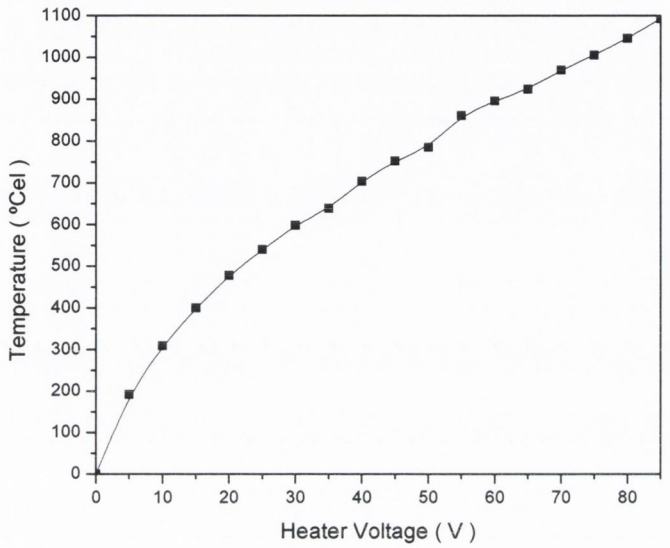



Figure 9.130. A plot of substrate temperature against heater voltage.

# Appendix C
# Error calculation and analysis

## C.1 Magnetization measurements

Magnetization measurements were performed in a Quantum Design SQUID. It returns measurement values in units of $\mathrm{A\,m^2}$. The moments measured in this thesis are typically quite small and of the order of $5 \times 10^{-8}\,\mathrm{A\,m^2}$, which is around 100 times smaller than the signal that would be measured for a similar sample of a "traditional" magnetic material such as magnetite.

There are two factors that need to be considered for the error analysis in the measurements of the moments measured in both the oxide thin films and the carbons. Firstly, the instrumental error must be determined. Secondly, there are large deviations in the magnitude of the moments measured for samples that are seemingly of the exact same composition and preparation method. These variations must also be taken into account.

### C.1.1 Instrumental Error

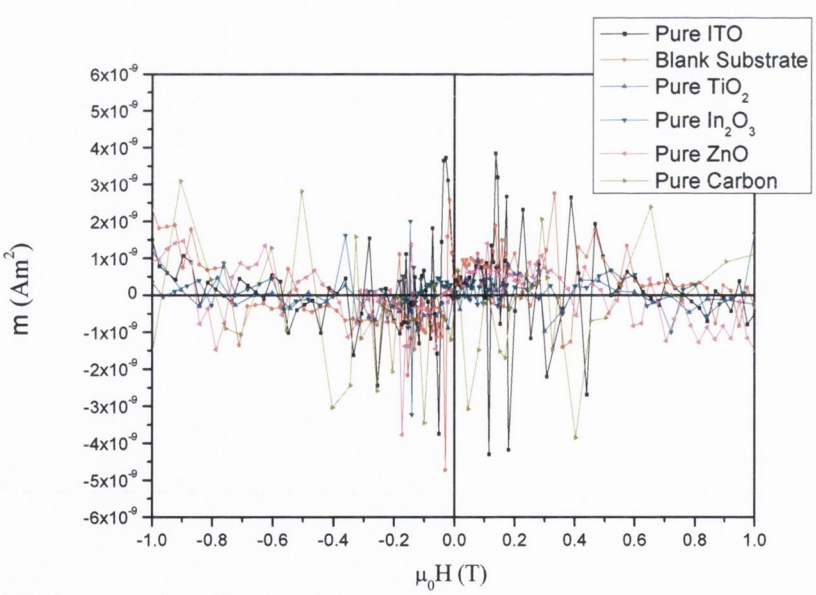



Figure 9.131. A plot of moment versus applied field for the "blank" materials. The diamagnetic signal has been subtracted, with only the SQUID noise remaining.

The sensitivity of the SQUID is quoted as $1 \times 10^{-11}\,\mathrm{A\,m^2}$ in the user's manual. However, it was more instructive to embark on an independent examination of the error in the measurement by using thin films similar to those investigated in the thesis.

A purely diamagnetic sample should exhibit a linear response to the magnetic field applied. Therefore, any deviations from linearity for a purely diamagnetic sample should provide a good estimation for the instrumental error.

A sapphire substrate, exactly identical to those used for the thin film deposition was measured. The linear term was subtracted and the absolute values of the deviations around zero were recorded. The instrumental error was determined from the standard deviation of these deviations. This was repeated on thin films of each of the undoped host oxides (Fig. 9.131). The average value of instrumental error was then taken as the error used throughout the thesis, which took a value of $6 \times 10^{-10}\,\mathrm{A\,m^2}$. This value was important in determining the accuracy of the moment in individual films.

For a typical moment of $5 \times 10^{-8}\,\mathrm{A\,m^2}$, this would represent an error of 1% in the values of moment measured.

| **Material** | **Standard Deviation** ($\mathrm{A\,m^2}$) |
|---|---|
| Sapphire | $6.5957 \times 10^{-10}$ |
| $TiO_2$ | $2.7987 \times 10^{-10}$ |
| $In_2O_3$ | $4.3154 \times 10^{-10}$ |
| ITO | $1.01675 \times 10^{-9}$ |
| ZnO | $4.97976 \times 10^{-10}$ |
| Carbon | $9.69573 \times 10^{-10}$ |
| Average | $6 \times 10^{-10}$ |

Table 17.The standard deviation of the noise measurements on the sample blanks and their average and standard deviation

### C.1.2 Sample variation

When examining the trends in magnetization with respect to another material property such as magnetization versus dopant concentration, the variation in the magnetization of nominally identical films is quite important.

To determine this, a sample known to be ferromagnetic was manufactured multiple times under the same conditions, where possible. The sample variation error is then defined as the standard deviation in the measured values of magnetization. This sample variation error was then used for the system as a whole (Table 18). The only system where this was not possible was for the carbon-nitrogen whiskers, due to the

small numbers of samples prepared and the inability to accurately control preparation conditions. Thin films of $Fe_3O_4$ were also produced and measured. It important to note that each of the Fe:$TiO_2$, Mn:ITO, and $Fe_3O_4$ series were produced in one day. The Cr:$In_2O_3$ and $Fe_3O_4$ films were not produced consecutively, thus increasing the probability of sample variation.

| | **S1** | **S2** | **S3** | **S4** | **Avg.** | **Std Dev** | **Ratio** |
|---|---|---|---|---|---|---|---|
| | ($10^{-8}$ A m$^2$) | | | | ($10^{-8}$ A m$^2$) | | (%) |
| Cr:$In_2O_3$ | 3.05 | 4.12 | 5.00 | 6.79 | 4.74 | 1.58 | 33 |
| Fe:$TiO_2$ | 6.34 | 6.36 | 6.41 | 7.34 | 6.61 | 0.49 | 8 |
| Mn:ITO | 4.77 | 4.15 | 4.05 | 3.9 | 4.22 | 0.4 | 9 |
| Co:ZnO | 6.66 | 5.10 | 4.76 | 4.50 | 5.25 | 1.00 | 18 |
| $Fe_3O_4$ | 119 | 127 | 103 | 111 | 115 | 10 | 9 |
| Average | | | | | | | 15 |

Table 18.A table giving the measured magnetization of four different samples of five series of films. Also quoted is the average, the standard deviation and the ratio of the standard deviation to the average.

The ratio of the standard deviation to the average measured magnetization is a good candidate for the error in the films. An average value of 15% of the measured magnetization is thus taken as the error due to sample variation in the magnetization measurements for the thin film oxide materials.

It is important to note that when relating two or more properties of an individual film determined from separate experiments on the same film[7], this "sample variation" error has no meaning. In this case, only the respective measurement errors have any significance. In samples where the possibility of the presence of a dopant or property (e.g. a magnetic moment) has been eliminated, the value will be taken as zero, and an error zero used.

## C.2 Other measurements

| | **Error** | **Typical Value** | **Ratio (%)** |
|---|---|---|---|
| XRR | 1 nm | 70 nm | 1.4 |
| XRD (Intensity) | The error is the square root of the count | | |
| XRD ($2\theta, d$) | 0.01 °, 0.01 Å | 40 °, 10 Å | 0.025, 0.1 |
| Resistance | This scales with sample resistance | | 0.1 |
| EDAX | 0.1 weight% | 1 weight% | 10 |

Table 19.A table showing the error due to a particular measurement, a typical measured value and the ratio between the two.

[7] Such as explaining the measured moment of an individual film by quantitative measurements of phases on that exact film

# Appendix D
# BASIC program for RGA spectrum acqisition

## D.1 Program 1: Simple Control

The first program is a simple control and read program that allows the user to control the RGA and returns spectra as a list of mass number and intensity.

```
10 REM **Mass Spec Terminal**
20 OPEN "COM1:19200,N,8,1" FOR RANDOM AS #3
30 ON COM(1) GOSUB 120
40 COM(1) ON
50 A$ = INKEY$
60 IF A$ = "" THEN GOTO 50
70 IF A$ = CHR$(27) THEN CLOSE : END
71 IF A$ = CHR$(115) THEN GOSUB 790
72 IF A$ = CHR$(13) THEN A$ = "(K5)"
73 IF A$ = CHR$(104) THEN A$ = "(K6)"
74 IF A$ = CHR$(112) THEN A$ = "(K7)"
75 IF A$ = CHR$(8) THEN A$ = "(K8)"
79 IF LEN(A$) = 2 THEN GOSUB 710
80 PRINT #3, A$
90 PRINT A$
100 GOTO 50
110 REM **Print characters received from the Vacscan**
120 B$ = INPUT$(LOC(3), #3)
130 PRINT B$
140 RETURN
710 REM **Arrow Key sub-routine**
711 null$ = CHR$(0)
712 IF A$ = null$ + "M" THEN A$ = "(K3)"
713 IF A$ = null$ + "K" THEN A$ = "(K2)"
714 IF A$ = null$ + "H" THEN A$ = "(K1)"
715 IF A$ = null$ + "P" THEN A$ = "(K4)"
716 RETURN
```

## D.2 Program 2: Control, Display And Save

The second program redraws the GUI of the Vacscan and will also save and organise files. It is an extension of program one.

```
DECLARE SUB GetCurrent () '*** Get the current drive and directory ***
DECLARE SUB FindDrives () '*** Find which drives are on the PC ***
DECLARE SUB SortArrays (SortArray$(), Low AS INTEGER, High AS INTEGER) '*** Put the
files and directories in order ***
DECLARE SUB DrawMenu () '*** Draw the fixed menu items ***
DECLARE SUB FillMenu () '*** Fill the variable menu items ***
DECLARE SUB DoWriteMenu () '*** Do File, Drive, Directory menu items ***
DECLARE SUB DoFileMenu () '*** Do the scrolling file menu ***
DECLARE SUB DoDirMenu () '*** Do the scrolling directory menu ***
DECLARE SUB ChkFile () '*** Check that a file exists ***
DECLARE SUB ChkDrv () '*** Check that a drive exists ***
DECLARE SUB ChkDir () '*** Check that a directory exists ***
DECLARE SUB ChngDir () '*** Change a directory ***
```

```
DECLARE SUB WriteSpec () '*** Write a spectrum to disk ***
DECLARE SUB ReadSpec () '*** Read a spectrum ***
10 REM **Mass Spec Terminal**
20 OPEN "COM1:19200,N,8,1" FOR RANDOM AS #3
30 REM **TEMP REMOVE: ON COM(1) GOSUB 120**
40 COM(1) ON
42 CLS
43 PRINT
44 PRINT
45 PRINT " WELCOME TO THE MASS SPEC CONTROL PROGRAM"
46 PRINT
47 PRINT
48 PRINT "Use the arrow keys, enter and backspace to navigate the Vacscan Terminal"
49 PRINT "Press 's' to save a spectrum to file and 'h' to access the Terminal help"
50 A$ = INKEY$
60 IF A$ = "" THEN GOTO 50
70 IF A$ = CHR$(27) THEN CLOSE : END
71 IF A$ = CHR$(115) THEN GOSUB 790
72 IF A$ = CHR$(13) THEN A$ = "(K5)"
73 IF A$ = CHR$(104) THEN A$ = "(K6)"
74 IF A$ = CHR$(112) THEN A$ = "(K7)"
75 IF A$ = CHR$(8) THEN A$ = "(K8)"
79 IF LEN(A$) = 2 THEN GOSUB 710
80 PRINT #3, A$
100 GOTO 50
110 REM **Print characters received from the Vacscan**
120 B$ = INPUT$(LOC(3), #3)
130 PRINT B$
140 RETURN
710 REM **Arrow Key sub-routine**
711 null$ = CHR$(0)
712 IF A$ = null$ + "M" THEN A$ = "(K3)"
713 IF A$ = null$ + "K" THEN A$ = "(K2)"
714 IF A$ = null$ + "H" THEN A$ = "(K1)"
715 IF A$ = null$ + "P" THEN A$ = "(K4)"
716 RETURN
790 REM **Sub routine for saving a spectrum**
791 'FileDir.bas
'A file / directory dialog / menu
OPTION BASE 1
'*** Global variables ***
DIM SHARED FileNo AS INTEGER 'File stream number
DIM SHARED DirName(500) AS STRING 'Directory names
DIM SHARED FileName(500) AS STRING 'File names
DIM SHARED CurrDrive AS STRING 'Current drive
DIM SHARED CurrDir AS STRING 'Current directory
DIM SHARED CurrPath AS STRING 'Current path
DIM SHARED NumDirs AS INTEGER 'Number of directories
DIM SHARED NumFiles AS INTEGER 'Number of files
DIM SHARED TabNum AS INTEGER 'Keep a track of what part of the menu
DIM SHARED YMenuPosn AS INTEGER 'Top right Y position of menu
DIM SHARED XMenuPosn AS INTEGER 'Top right X position of menu
DIM SHARED EndMenu AS INTEGER 'User pressed ESC or file opened properly
DIM SHARED HiLiteFile AS INTEGER 'Currently highlighted file
DIM SHARED HiLiteDir AS INTEGER 'Currently highlighted directory
DIM SHARED Message AS STRING 'Current field being edited
DIM SHARED Drive AS STRING 'Drives available on the computer
DIM SHARED ProgErr AS INTEGER 'Program error code
DIM SHARED OrigDrive AS STRING 'Original drive
DIM SHARED OrigDir AS STRING 'Original directory
DIM SHARED OrigPath AS STRING 'Original path
'*** Local variables ****
```

```
DIM Num AS INTEGER 'General integer variable
'*** The DIR command may give different results on different platforms ***
TabNum = 1
YMenuPosn = 3
XMenuPosn = 3
'*** Find the drives on the computer ***
ON ERROR GOTO DriveErr
FOR Count = 65 TO 90
ProgErr = 0
Message$ = CHR$(Count) + ":\"
FILES Message$
IF ProgErr = 0 THEN Drive$ = Drive$ + CHR$(Count)
NEXT Count
ON ERROR GOTO OopsError
GetCurrent '*** Get the current drive and directory ***
SortArrays FileName$(), 1, NumFiles
SortArrays DirName$(), 1, NumDirs
'*** Get the original info to reset on exit ***
OrigDrive$ = CurrDrive$
OrigDir$ = CurrDir$
OrigPath$ = CurrPath$
DrawMenu '*** Draw the fixed menu items ***
FillMenu '*** Fill the variable menu items ***
DO
'*** Relocate the cursor to the current field (by TabNum) ***
EndMenu = 0
IF TabNum <= 3 THEN
DoWriteMenu
END IF
IF TabNum = 4 THEN DoFileMenu
IF TabNum = 5 THEN DoDirMenu
LOOP UNTIL EndMenu > 0 '*** 1 = ESC was pressed, 2 = file found, 3 = file created ***
CLS
IF EndMenu = 1 THEN
PRINT
PRINT " Menu exited, ESC pressed"
END IF
IF EndMenu = 2 THEN
PRINT
PRINT " The file "; Message$; " was successfully found"
PRINT
PRINT " Press enter to take spectrum and overwrite current data"
WriteSpec
END IF
IF EndMenu = 3 THEN
PRINT
PRINT " The file "; Message$; " was successfully created"
PRINT
PRINT " Press enter to take spectrum and write to disk"
WriteSpec
END IF
'*** reset the drive and directory to the original ***
SHELL OrigDrive$
CHDIR OrigDir$
CLOSE
END
DriveErr:
IF ERR = 68 THEN ProgErr = 1
RESUME NEXT
OopsError:
CLS
PRINT
```

```
PRINT " The program has reported a fatal error and will now end"
PRINT
PRINT " The Error Code reported was"; ERR
PRINT
PRINT " Press any key to continue . . ."
DO
LOOP UNTIL INKEY$ <> ""
CLOSE
SHELL OrigDrive$
CHDIR OrigDir$
END
FileErr:
IF ERR > 0 THEN ProgErr = 1
RESUME NEXT
900 RETURN
SUB ChkDir
'*** There are two ways into this sub, either from a typed ***
'*** directory or one chosen from the directory menu ***
'*** Check that the chosen or typed directory exists ***
'*** It should already be in the FileName$ array,
'*** but refresh the array in case it was created while the program was running ***
DIM OldDir AS STRING 'A copy of the current directory name
DIM OldDrv AS STRING 'A copy of the current drive letter
DIM DirPosn AS INTEGER 'Place holder for splitting splitting directory string
OldDir$ = CurrDir$ '*** Keep a copy of the directory in case of errors ***
OldDrv$ = CurrDrive$ '*** Keep a copy of the drive in case of errors ***
IF TabNum = 5 THEN
GetCurrent
SortArrays FileName$(), 1, NumFiles
SortArrays DirName$(), 1, NumDirs
FOR Count = 1 TO UBOUND(DirName$)
IF UCASE$(DirName$(HiLiteDir)) = UCASE$(DirName$(Count)) THEN
IF DirName$(HiLiteDir) = ".." THEN
SHELL "CD .."
ELSE
IF RIGHT$(CurrDir$, 1) <> "\" THEN CurrDir$ = CurrDir$ + "\"
SHELL "CD " + CurrDir$ + DirName$(HiLiteDir)
END IF
EXIT FOR
END IF
NEXT Count
END IF
'*** Getting the directories from the typed in string is a bit more complicated
'*** If the string starts with a letter then a ":" then the drive needs changing too ***
'*** If the string sarts with a "\" then assume the ***
'*** directory list starts from the root of the drive ***
'*** If it doesn't then assume it starts from the current directory ***
ProgErr = 0
IF TabNum = 3 THEN
ON ERROR GOTO FileErr
IF RIGHT$(Message$, 1) = "\" THEN Message$ = LEFT$(Message$, LEN(Message$) - 1)
IF LEFT$(Message$, 1) = "\" THEN
CHDIR Message$
ELSE
IF MID$(Message$, 2, 2) = ":\" THEN
IF INSTR(UCASE$(Drive$), UCASE$(LEFT$(Message$, 1))) > 0 THEN
SHELL LEFT$(Message$, 2)
Message$ = MID$(Message$, 3)
CHDIR Message$
END IF
ELSE
Message$ = CurrDir$ + "/" + Message$
```

```
CHDIR Message$
END IF
END IF
'*** If possible make the typed directory ***
IF ProgErr = 1 THEN
ProgErr = 0
MKDIR Message$
IF ProgErr = 0 THEN
PRINT " created. Press any key"'
DO
LOOP UNTIL INKEY$ <> ""
END IF
END IF
IF ProgErr = 1 THEN
SHELL OldDrv$ + ":"
CHDIR OldDir$
END IF
ON ERROR GOTO OopsError
'*** Redo the command line ***
GetCurrent
LOCATE YMenuPosn + 5, XMenuPosn + 15
PRINT SPACE$(59);
Message$ = CurrDir$
LOCATE YMenuPosn + 5, XMenuPosn + 15
PRINT Message$;
END IF
HiLiteFile = 1
HiLiteDir = 1
GetCurrent
SortArrays FileName$(), 1, NumFiles
SortArrays DirName$(), 1, NumDirs
DrawMenu
FillMenu
END SUB
SUB ChkDrv
IF INSTR(1, Drive$, UCASE$(LEFT$(Message$, 1))) >= 1 THEN
Message$ = UCASE$(LEFT$(Message$, 1)) + ":"
SHELL Message$
GetCurrent '*** Get the current drive and directory ***
SortArrays FileName$(), 1, NumFiles
SortArrays DirName$(), 1, NumDirs
DrawMenu
FillMenu
END IF
END SUB
SUB ChkFile
DIM Count AS INTEGER
'*** Check that the chosen or typed file exists ***
'*** It should already be in the FileName$ array,
'*** but refresh the array in case it was created while the program was running ***
ProgErr = 0
GetCurrent
SortArrays FileName$(), 1, NumFiles
SortArrays DirName$(), 1, NumDirs
IF Message$ > "" THEN
FOR Count = 1 TO UBOUND(FileName$)
IF UCASE$(Message$) = UCASE$(FileName$(Count)) THEN
EndMenu = 2
EXIT FOR
END IF
NEXT Count
IF EndMenu = 0 THEN '*** Check the file can be created ***
```

```
ON ERROR GOTO FileErr
FileNo = FREEFILE
OPEN Message$ FOR OUTPUT ACCESS WRITE LOCK READ WRITE AS FileNo
CLOSE
IF ProgErr = 0 THEN EndMenu = 3
'*** If there was a problem creating this file then ProgErr = 1 ***
ON ERROR GOTO OopsError
END IF
END IF
END SUB
SUB DoDirMenu
'*** Scrolling directory menu ***
DIM UserIn AS STRING 'User input
DIM ChngTab AS INTEGER 'Tracks if menu movement keys are pressed
STATIC FirstDir AS INTEGER 'The first directory to be displayed
DIM YDirPosn AS INTEGER '
ChngTab = 0
IF HiLiteDir = 0 THEN HiLiteDir = 1
IF FirstDir = 0 THEN FirstDir = 1
XDirPosn = XMenuPosn + 59
LOCATE (YMenuPosn + 9) + HiLiteDir - FirstDir, XDirPosn
COLOR 0, 7
PRINT DirName$(HiLiteDir);
COLOR 7, 0
DO
'*** Print the up / down arrows ***
LOCATE YMenuPosn + 9, XMenuPosn + 71
PRINT " ";
LOCATE YMenuPosn + 18, XMenuPosn + 71
PRINT " ";
IF FirstDir > 10 THEN
LOCATE YMenuPosn + 9, XMenuPosn + 71
PRINT CHR$(24); CHR$(24)
END IF
IF FirstDir < NumDirs - 9 THEN
LOCATE YMenuPosn + 18, XMenuPosn + 71
PRINT CHR$(25); CHR$(25)
END IF
LOCATE (YMenuPosn + 9) + HiLiteDir - FirstDir, XDirPosn + LEN(DirName$(HiLiteDir))
DO
UserIn$ = INKEY$
LOOP UNTIL UserIn$ <> ""
'*** Process the key pressed ***
SELECT CASE UserIn$
CASE CHR$(27) '*** Esc pressed ***
EndMenu = 1
CASE CHR$(13) '*** Enter pressed ***
'*** Check the directory exists, if it does change it ***
'*** This should'nt be necessary but it may have ***
'*** been deleted while this program was running ***
ChkDir
CASE CHR$(9) '*** Tab pressed ***
TabNum = 1
ChngTab = 1
CASE CHR$(0) + CHR$(15) '*** Shift Tab pressed ***
TabNum = TabNum - 1
ChngTab = 1
CASE CHR$(0) + CHR$(80) '*** Down arrow pressed ***
IF DirName$(HiLiteDir + 1) <> "" THEN HiLiteDir = HiLiteDir + 1
CASE CHR$(0) + CHR$(72) '*** Up arrow pressed ***
IF HiLiteDir - 1 <> 0 THEN HiLiteDir = HiLiteDir - 1
CASE CHR$(0) + CHR$(71) '*** Home pressed ***
```

```
HiLiteDir = 1
CASE CHR$(0) + CHR$(79) '*** End pressed ***
HiLiteDir = NumDirs
CASE CHR$(0) + CHR$(73) '*** Page Up pressed ***
IF HiLiteDir > 10 THEN
HiLiteDir = HiLiteDir - 10
ELSE
HiLiteDir = 1
END IF
CASE CHR$(0) + CHR$(81) '*** Page Down pressed ***
IF HiLiteDir < NumDirs - 9 THEN
HiLiteDir = HiLiteDir + 10
ELSE
HiLiteDir = NumDirs
END IF
CASE ELSE
'*** For any other key press find the first directory ***
'*** starting with that key ***
FOR Count = 1 TO NumDirs
IF UCASE$(LEFT$(DirName$(Count), 1)) = UCASE$(UserIn$) THEN
HiLiteDir = Count
EXIT FOR
END IF
NEXT Count
END SELECT
'*** Clear the directory list area and reprint the new list ***
XDirPosn = XMenuPosn + 59
LOCATE YMenuPosn + 9, XDirPosn
FOR Count = FirstDir TO FirstDir + 9
PRINT SPACE$(LEN(DirName$(Count)));
LOCATE CSRLIN + 1, XDirPosn
NEXT Count
IF HiLiteDir > FirstDir + 9 THEN
DO
FirstDir = FirstDir + 10
LOOP UNTIL HiLiteDir < FirstDir + 10
END IF
IF HiLiteDir < FirstDir THEN
DO
FirstDir = FirstDir - 10
LOOP UNTIL HiLiteDir >= FirstDir
END IF
XDirPosn = XMenuPosn + 59
LOCATE YMenuPosn + 9, XDirPosn
FOR Count = FirstDir TO FirstDir + 9
PRINT DirName$(Count);
LOCATE CSRLIN + 1, XDirPosn
NEXT Count
XDirPosn = XMenuPosn + 59
LOCATE (YMenuPosn + 9) + HiLiteDir - FirstDir, XDirPosn
COLOR 0, 7
PRINT DirName$(HiLiteDir);
COLOR 7, 0
LOOP UNTIL EndMenu > 0 OR ChngTab = 1
END SUB
SUB DoFileMenu
'*** Scrolling Dir menu ***
DIM UserIn AS STRING 'User input
DIM ChngTab AS INTEGER 'Tracks if menu movement keys are pressed
DIM NumCols AS INTEGER 'Total number of Dir columns
STATIC FirstFile AS INTEGER 'The first file to be displayed
DIM XFilePosn AS INTEGER '
```

```
    NumCols = FIX((NumFiles + 9) / 10) '*** calculates the number of columns ***
    ChngTab = 0
    IF HiLiteFile = 0 THEN HiLiteFile = 1
    IF HiLiteFile = 1 THEN FirstFile = 1
    IF FirstFile = 0 THEN FirstFile = 1
    XFilePosn = XMenuPosn + 2
    LOCATE (YMenuPosn + 9) + ((HiLiteFile - FirstFile) MOD 10), XFilePosn + (FIX((HiLiteFile
- FirstFile) / 10) * 14)
    COLOR 0, 7
    PRINT FileName$(HiLiteFile);
    COLOR 7, 0
    DO
    '*** Print the << and / or the >> ***
    LOCATE YMenuPosn + 7, XMenuPosn + 2
    PRINT " "
    LOCATE YMenuPosn + 7, XMenuPosn + 54
    PRINT " "
    IF FirstFile > 10 THEN
    LOCATE YMenuPosn + 7, XMenuPosn + 2
    PRINT "<<"
    END IF
    IF FirstFile < NumFiles - 40 THEN
    LOCATE YMenuPosn + 7, XMenuPosn + 54
    PRINT ">>"
    END IF
    IF HiLiteFile > 1 THEN LOCATE (YMenuPosn + 9) + ((HiLiteFile - FirstFile) MOD 10), XFile-
Posn + (FIX((HiLiteFile - FirstFile) / 10) * 14) + LEN(FileName$(HiLiteFile))
    IF HiLiteFile = 1 THEN LOCATE (YMenuPosn + 9), XFilePosn + LEN(FileName$(HiLiteFile))
    DO
    UserIn$ = INKEY$
    LOOP UNTIL UserIn$ <> ""
    '*** Clear the user entry file box ***
    LOCATE CSRLIN, POS(0) - LEN(FileName$(HiLiteFile))
    COLOR 7, 0
    PRINT FileName$(HiLiteFile);
    LOCATE YMenuPosn + 1, XFilePosn + 13
    PRINT SPACE$(58)
    '*** Process the key pressed ***
    SELECT CASE UserIn$
    CASE CHR$(27) '*** Esc pressed ***
    EndMenu = 1
    CASE CHR$(13) '*** Enter pressed ***
    '*** ChkFile shouldn't be necessary but the chosen file ***
    '*** may have been deleted while this program was running ***
    ChkFile
    CASE CHR$(9) '*** Tab pressed ***
    TabNum = TabNum + 1
    ChngTab = 1
    CASE CHR$(0) + CHR$(15) '*** Shift Tab pressed ***
    TabNum = TabNum - 1
    ChngTab = 1
    CASE CHR$(0) + CHR$(80) '*** Down arrow pressed ***
    IF FileName$(HiLiteFile + 1) <> "" THEN HiLiteFile = HiLiteFile + 1
    CASE CHR$(0) + CHR$(72) '*** Up arrow pressed ***
    IF HiLiteFile - 1 <> 0 THEN HiLiteFile = HiLiteFile - 1
    CASE CHR$(0) + CHR$(75) '*** Left arrow pressed ***
    IF HiLiteFile > 10 THEN HiLiteFile = HiLiteFile - 10
    CASE CHR$(0) + CHR$(77) '*** Right arrow pressed ***
    IF HiLiteFile < (NumCols - 1) * 10 + 1 THEN HiLiteFile = HiLiteFile + 10
    IF HiLiteFile > NumFiles THEN HiLiteFile = NumFiles
    CASE CHR$(0) + CHR$(71) '*** Home pressed ***
    HiLiteFile = 1
```

```
CASE CHR$(0) + CHR$(79) '*** End pressed ***
HiLiteFile = NumFiles
CASE CHR$(0) + CHR$(73) '*** Page Up pressed ***
IF HiLiteFile > 40 THEN
HiLiteFile = HiLiteFile - 40
ELSE
HiLiteFile = 1
END IF
CASE CHR$(0) + CHR$(81) '*** Page Down pressed ***
IF HiLiteFile < NumFiles - 40 THEN
HiLiteFile = HiLiteFile + 40
ELSE
HiLiteFile = NumFiles
END IF
CASE ELSE
'*** For any other key press find the first file ***
'*** starting with that key ***
FOR Count = 1 TO NumFiles
IF UCASE$(LEFT$(FileName$(Count), 1)) = UCASE$(UserIn$) THEN
HiLiteFile = Count
EXIT FOR
END IF
NEXT Count
END SELECT
'*** Reprint the user entry file box ***
Message$ = FileName$(HiLiteFile)
LOCATE YMenuPosn + 1, XFilePosn + 13
PRINT Message$
'*** Clear the file list area and reprint the new columns ***
XFilePosn = XMenuPosn + 2
LOCATE YMenuPosn + 9, XFilePosn
FOR Count = FirstFile TO FirstFile + 39
PRINT SPACE$(12);
LOCATE CSRLIN + 1, XFilePosn
IF Count MOD 10 = 0 THEN
XFilePosn = XFilePosn + 14
LOCATE YMenuPosn + 9, XFilePosn
END IF
NEXT Count
IF HiLiteFile > FirstFile + 39 THEN
DO
FirstFile = FirstFile + 10
LOOP UNTIL HiLiteFile < FirstFile + 40
END IF
IF HiLiteFile < FirstFile THEN
DO
FirstFile = FirstFile - 10
LOOP UNTIL HiLiteFile >= FirstFile
END IF
XFilePosn = XMenuPosn + 2
LOCATE YMenuPosn + 9, XFilePosn
FOR Count = FirstFile TO FirstFile + 39
PRINT FileName$(Count);
LOCATE CSRLIN + 1, XFilePosn
IF Count MOD 10 = 0 THEN
XFilePosn = XFilePosn + 14
LOCATE YMenuPosn + 9, XFilePosn
END IF
NEXT Count
XFilePosn = XMenuPosn + 2
IF HiLiteFile > 1 THEN LOCATE (YMenuPosn + 9) + ((HiLiteFile - FirstFile) MOD 10), XFile-
Posn + (FIX((HiLiteFile - FirstFile) / 10) * 14)
```

```
IF HiLiteFile = 1 THEN LOCATE (YMenuPosn + 9), XFilePosn
COLOR 0, 7
PRINT FileName$(HiLiteFile);
COLOR 7, 0
LOOP UNTIL EndMenu > 0 OR ChngTab = 1
END SUB
SUB DoWriteMenu
'*** Do the user input for the file, drive and directory ***
DIM UserIn AS STRING 'User input
DIM CsrPosn AS INTEGER 'Cursor position
DIM InsFlag AS INTEGER 'The state of the Insert key
DIM ChngTab AS INTEGER 'Tracks if menu movement keys are pressed
DIM OldMessage AS STRING 'A copy of the original message
ChngTab = 0
IF TabNum = 1 THEN
IF HiLiteFile = 0 THEN
Message$ = FileName$(1)
ELSE
Message$ = FileName$(HiLiteFile)
END IF
END IF
IF TabNum = 2 THEN Message$ = CurrDrive$
IF TabNum = 3 THEN Message$ = CurrDir$
CsrPosn = LEN(Message$) + 1
DO
LOCATE YMenuPosn + (TabNum * 2) - 1, XMenuPosn + 15
PRINT Message$;
CsrPosn = LEN(Message$) + 1
IF InsFlag >= 0 THEN
LOCATE , XMenuPosn + 14 + CsrPosn, 1, 1
ELSE
LOCATE , XMenuPosn + 14 + CsrPosn, 1, 1, 30
END IF
UserIn$ = ""
DO
UserIn$ = INKEY$
LOOP UNTIL UserIn$ <> ""
SELECT CASE UserIn$
CASE CHR$(27) '*** Esc pressed ***
EndMenu = 1
CASE CHR$(8) '*** Backspace pressed ***
LOCATE , XMenuPosn + 15
PRINT SPACE$(LEN(Message$))
IF CsrPosn > 1 THEN
Message$ = LEFT$(Message$, CsrPosn - 2) + MID$(Message$, CsrPosn)
CsrPosn = CsrPosn - 1
END IF
CASE CHR$(0) + CHR$(83) '*** Delete key pressed ***
LOCATE , XMenuPosn + 15
PRINT SPACE$(LEN(Message$))
Message$ = LEFT$(Message$, CsrPosn - 1) + MID$(Message$, CsrPosn + 1)
CASE CHR$(0) + CHR$(82) '*** Ins key pressed ***
InsFlag = NOT InsFlag '*** Boolean toggle ***
CASE CHR$(0) + CHR$(75) '*** Left arrow pressed ***
IF CsrPosn > 1 THEN CsrPosn = CsrPosn - 1
CASE CHR$(0) + CHR$(77) '*** Right arrow pressed ***
IF CsrPosn <= LEN(Message$) THEN CsrPosn = CsrPosn + 1
CASE CHR$(0) + CHR$(71) '*** Home pressed ***
CsrPosn = 1
CASE CHR$(0) + CHR$(79) '*** End pressed ***
CsrPosn = LEN(Message$) + 1
CASE CHR$(0) + CHR$(15), CHR$(0) + CHR$(72) '*** Up arrow or SHIFT Tab pressed ***
```

```
LOCATE , XMenuPosn + 15
PRINT SPACE$(59);
LOCATE , XMenuPosn + 15
IF HiLiteFile = 0 THEN HiLiteFile = 1
IF TabNum = 1 THEN Message$ = FileName$(HiLiteFile)
IF TabNum = 2 THEN Message$ = CurrDrive$
IF TabNum = 3 THEN Message$ = CurrDir$
PRINT Message$
TabNum = TabNum - 1
IF TabNum = 0 THEN TabNum = 5
ChngTab = 1
CASE CHR$(9), CHR$(0) + CHR$(80) '*** Down arrow or Tab pressed ***
LOCATE , XMenuPosn + 15
PRINT SPACE$(59);
LOCATE , XMenuPosn + 15
IF HiLiteFile = 0 THEN HiLiteFile = 1
IF TabNum = 1 THEN Message$ = FileName$(HiLiteFile)
IF TabNum = 2 THEN Message$ = CurrDrive$
IF TabNum = 3 THEN Message$ = CurrDir$
PRINT Message$
TabNum = TabNum + 1
ChngTab = 1
CASE ELSE '*** Add / insert the character to messages ***
IF LEN(Message$) < 59 THEN
IF LEN(UserIn$) = 1 AND UserIn$ > CHR$(34) THEN
IF InsFlag = 0 THEN
Message$ = LEFT$(Message$, CsrPosn - 1) + UserIn$ + MID$(Message$, CsrPosn)
ELSE
Message$ = LEFT$(Message$, CsrPosn - 1) + UserIn$ + MID$(Message$, CsrPosn + 1)
END IF
CsrPosn = CsrPosn + 1
END IF
END IF
END SELECT
IF UserIn$ = CHR$(13) THEN
SELECT CASE TabNum
CASE 1 '*** Check the file exists, if it does then exit menu ***
ChkFile
CASE 2 '*** Check the drive exists, if it does then change the drive ***
ChkDrv
CASE 3
'*** Check the directory exists, if it does then change it
ChkDir
END SELECT
END IF
LOOP UNTIL EndMenu > 0 OR ChngTab = 1
END SUB
SUB DrawMenu
'*** Draw the fixed menu items ***
DIM FileCols AS INTEGER 'Number of columns in the file section
DIM Count AS INTEGER 'Loop counter
FileCols = NumFiles / 10
XFilePosn = 7
YFilePosn = 9
XDirPosn = 65
YDirPosn = 9
CLS
LOCATE YMenuPosn, XMenuPosn
PRINT CHR$(201);
PRINT STRING$(12, CHR$(205));
PRINT CHR$(209);
PRINT STRING$(60, CHR$(205));
```

```
PRINT CHR$(187)
LOCATE , XMenuPosn
PRINT CHR$(186);
LOCATE , XMenuPosn + 2
PRINT "File";
LOCATE , XMenuPosn + 13
PRINT CHR$(179);
LOCATE , XMenuPosn + 74
PRINT CHR$(186)
LOCATE , XMenuPosn
PRINT CHR$(199);
PRINT STRING$(12, CHR$(196));
PRINT CHR$(197);
PRINT STRING$(60, CHR$(196));
PRINT CHR$(182)
LOCATE , XMenuPosn
PRINT CHR$(186);
LOCATE , XMenuPosn + 2
PRINT "Drive";
LOCATE , XMenuPosn + 13
PRINT CHR$(179);
LOCATE , XMenuPosn + 74
PRINT CHR$(186)
LOCATE , XMenuPosn
PRINT CHR$(199);
PRINT STRING$(12, CHR$(196));
PRINT CHR$(197);
PRINT STRING$(60, CHR$(196));
PRINT CHR$(182)
LOCATE , XMenuPosn
PRINT CHR$(186);
LOCATE , XMenuPosn + 2
PRINT "Directory";
LOCATE , XMenuPosn + 13
PRINT CHR$(179);
LOCATE , XMenuPosn + 74
PRINT CHR$(186)
LOCATE , XMenuPosn
PRINT CHR$(199);
PRINT STRING$(12, CHR$(196));
PRINT CHR$(193);
PRINT STRING$(43, CHR$(196));
PRINT CHR$(194);
PRINT STRING$(16, CHR$(196));
PRINT CHR$(182)
LOCATE , XMenuPosn
PRINT CHR$(186);
LOCATE , XMenuPosn + 7
PRINT NumFiles; "files in "; CurrPath$;
LOCATE , XMenuPosn + 57
PRINT CHR$(179);
LOCATE , XMenuPosn + 58
PRINT NumDirs; "Directories";
LOCATE , XMenuPosn + 74
PRINT CHR$(186)
LOCATE , XMenuPosn
PRINT CHR$(199);
PRINT STRING$(56, CHR$(196));
PRINT CHR$(197);
PRINT STRING$(16, CHR$(196));
PRINT CHR$(182)
FOR Count = 1 TO 10
```

```
LOCATE , XMenuPosn
PRINT CHR$(186);
LOCATE , XMenuPosn + 57
PRINT CHR$(179);
LOCATE , XMenuPosn + 74
PRINT CHR$(186)
NEXT Count
LOCATE , XMenuPosn
PRINT CHR$(200);
PRINT STRING$(56, CHR$(205));
PRINT CHR$(207);
PRINT STRING$(16, CHR$(205));
PRINT CHR$(188)
LOCATE YMenuPosn + 21, XMenuPosn
PRINT "Use the TAB key to move between fields"
PRINT
END SUB
SUB FillMenu
'*** Fill in the variable menu items ***
DIM XFilePosn AS INTEGER ' X Positon of file columns
XFilePosn = XMenuPosn + 2
'*** The user writable part of the menu ***
LOCATE YMenuPosn + 3, XMenuPosn + 15
PRINT CurrDrive$
LOCATE YMenuPosn + 5, XMenuPosn + 15
PRINT CurrDir$
'*** the scrolling file menu ***
LOCATE YMenuPosn + 9, XFilePosn
FOR Count = 1 TO 40
PRINT FileName$(Count)
LOCATE CSRLIN, XFilePosn
IF Count MOD 10 = 0 THEN
XFilePosn = XFilePosn + 14
LOCATE YMenuPosn + 9, XFilePosn
END IF
NEXT Count
'*** The scrolling directory menu ***
LOCATE YMenuPosn + 9, XMenuPosn + 59
FOR Count = 1 TO 10
PRINT DirName$(Count)
LOCATE CSRLIN, XMenuPosn + 59
NEXT Count
END SUB
SUB FindDrives
'*** Find what drives are present in the PC ***
ON ERROR GOTO DriveErr
FOR Count = 65 TO 90
DrvErr = 0
Drive$ = CHR$(Count) + ":\"
FILES Drive$
IF DrvErr = 0 THEN Drive$ = Drive$ + CHR$(Count)
NEXT Count
END SUB
SUB GetCurrent
'*** Get the files from the current drive and directory ***
DIM Num AS INTEGER 'General number variable
DIM FileInfo AS STRING 'Line from ZFileDir.tmp
'*** Clear the current contents of the file and directory arrays ***
ERASE FileName$, DirName$
'*** Open a temporary file to hold the DIR information ***
'*** Unfortunately, I can't find a way of getting ***
'*** the location of the temporary file folder ***
```

```
FileNo = FREEFILE
SHELL "dir > c:\ZFileDir.tmp"
OPEN "C:\ZFileDir.tmp" FOR INPUT ACCESS READ LOCK READ WRITE AS FileNo
DO
LINE INPUT #FileNo, FileInfo$
IF EOF(FileNo) THEN EXIT DO
LOOP UNTIL INSTR(FileInfo$, "Directory of ") > 1
Num = INSTR(FileInfo$, ":")
Num = Num - 1
CurrDrive$ = MID$(FileInfo$, Num, 2)
CurrPath$ = MID$(FileInfo$, Num)
Num = Num + 2
CurrDir$ = MID$(FileInfo$, Num)
NumDirs = 0
NumFiles = 0
DO
LINE INPUT #FileNo, FileInfo$
IF EOF(FileNo) THEN EXIT DO
IF INSTR(FileInfo$, "file(s)") > 0 THEN EXIT DO
IF INSTR(FileInfo$, "<DIR>") > 1 THEN
NumDirs = NumDirs + 1
Num = INSTR(FileInfo$, " ")
Num = Num - 1
DirName$(NumDirs) = LEFT$(FileInfo$, Num)
IF DirName$(NumDirs) = "." THEN
DirName$(NumDirs) = ""
NumDirs = NumDirs - 1
END IF
ELSE
IF LEN(FileInfo$) > 0 THEN
NumFiles = NumFiles + 1
Num = INSTR(FileInfo$, " ")
Num = Num - 1
FileName$(NumFiles) = LEFT$(FileInfo$, Num) + "."
FileName$(NumFiles) = FileName$(NumFiles) + MID$(FileInfo$, 10, 3)
IF UCASE$(FileName$(NumFiles)) = "ZFILEDIR.TMP" THEN
FileName$(NumFiles) = ""
NumFiles = NumFiles - 1
END IF
END IF
END IF
LOOP UNTIL INSTR(FileInfo$, "file(s)") > 1
CLOSE
KILL "C:\ZFileDir.tmp"
END SUB
SUB ReadSpec
CLS
DIM i AS INTEGER
i = 1
PRINT
PRINT "Press any key to acquire spectrum"
PRINT
DO
LOOP UNTIL INKEY$ <> ""
PRINT #3, "(P)"
B$ = INPUT$(LOC(3), #3)
DO
PRINT #1, i, B$
LOOP UNTIL B$ = E
RETURN
END SUB
SUB SortArrays (SortArray$(), Low AS INTEGER, High AS INTEGER)
```

```
'*** This is a QuickSort routine ***
DIM Lower AS INTEGER
DIM Higher AS INTEGER
DIM RandIndex AS INTEGER
'QuickSort works by picking a random "pivot" element in SortArray, then
'moving every element that is bigger to one side of the pivot, and every
'element that is smaller to the other side. QuickSort is then called
'recursively with the two subdivisions created by the pivot. Once the
'number of elements in a subdivision reaches two, the recursive calls end
'and the array is sorted.
IF Low < High THEN
' *** Only two elements in this subdivision ***
' *** Swap them if they are out of order, then end recursive calls: ***
IF High - Low = 1 THEN
IF SortArray$(Low) > SortArray$(High) THEN
SWAP SortArray$(Low), SortArray$(High)
END IF
ELSE
'*** Pick a pivot element at random, then move it to the end ***
RandIndex = INT(RND * (High - Low + 1)) + Low
SWAP SortArray$(High), SortArray$(RandIndex)
Partition$ = SortArray$(High)
DO
'*** Move in from both sides towards the pivot element ***
Lower = Low
Higher = High
DO WHILE (Lower < Higher) AND (SortArray$(Lower) <= Partition$)
Lower = Lower + 1
LOOP
DO WHILE (Higher > Lower) AND (SortArray$(Higher) >= Partition$)
Higher = Higher - 1
LOOP
'*** If pivot element not reached, it means that ***
'*** two elements on either side are out of order, ***
'*** so swap them ***
IF Lower < Higher THEN
SWAP SortArray$(Lower), SortArray$(Higher)
END IF
LOOP WHILE Lower < Higher
'*** Move the pivot element back to its proper place in the array ***
SWAP SortArray$(Lower), SortArray$(High)
'*** Recursively call the SortArray sub ***
'*** Pass the smaller subdivision first to use less stack space ***
IF (Lower - Low) < (High - Lower) THEN
SortArrays SortArray$(), Low, Lower - 1
SortArrays SortArray$(), Lower + 1, High
ELSE
SortArrays SortArray$(), Lower + 1, High
SortArrays SortArray$(), Low, Lower - 1
END IF
END IF
END IF
END SUB
SUB WriteSpec
PRINT #3, "(P)"
OPEN Message$ FOR OUTPUT AS #1
PRINT #1, "Written"
CLOSE
END SUB
```